Phase and Polarization Pulse Shaping for Nonlinear Microscopy.

Peter Schön

Université Paul Cézanne - Aix-Marseille III

THÈSE

pour obtenir le grade de **Docteur en Sciences**
de l'Université Paul Cézanne - Aix-Marseille III

Discipline : Optique électromagnétique et image

Phase and Polarization Pulse Shaping for Nonlinear Microscopy.

(Mise en forme d'impulsions en phase et polarisation pour la microscopie non-linéaire.)

soutenue publiquement le **4 Octobre 2010** par

Peter Schön

École Doctorale : Physique & Sciences de la Matière

Rapporteurs :	Dr. Béatrice Chatel
	Prof. Andreas Zumbusch
Examinateurs :	Dr. Pablo Loza-Alvarez
	Dr. Hervé Rigneault
Directeur de thèse :	Dr. Sophie Brasselet

Institut Fresnel — CNRS UMR 6133 — Équipe Mosaic

Acknowledgements

The present work would not have been possible without the help of many people and it would have been far less pleasant without the presence of many others.
In particular I want to thank:

Claude Amra and Hugues Giovannini for the opportunity to do my PhD at the Institut Fresnel.

Hervé Rigneault for his very warm welcome upon my arrival at the MOSAIC group, many fruitful discussions, and his willingness to preside over the jury of this thesis.

The further members of the jury: Dr. Béatrice Chatel, Prof. Dr. Andreas Zumbusch and Dr. Pablo Loza-Alvarez for their interest in the subject of this thesis, the careful reading of the manuscript and for having made the journey to Marseille.

Above all Sophie Brasselet for supervising this thesis, for being of immeasurable help throughout these three years and for her great scientific insight.

Servane Lenne without whose support I would not have surmounted the pitfalls of the French bureaucracy in the beginning of my stay in Marseille.

Martin Behrndt for his help with the experimental setup.

Thomas Ebbesen and his group for the fabrication of the metallic nano-apertures that were studied in this work.

Yaron Silberberg and Ori Katz for welcoming and accompanying me at the Weizmann Institute of Science and teaching me a lot about single-pulse CARS.

David Gachet for sacrificing lots of his time for me both in Israel and in France and for never getting tired of the ever increasing number of questions during the writing of this manuscript.

Dora Aït-Belkacem for her help with the collagen measurements.

Alicja, Fabiana, Alla, Pierre B. et Pierre G., Pascal, Heykel, Stéphane et Christophe and many others. It would go far beyond the scope of this work to list all the ways in which they made these three years an unforgettable and great experience.

All other members of the MOSAIC group.

Maria.

The members of the Église Protestante Évangélique de Saint Just for their warm welcome, the discovery of French hospitality and the introduction to pétanque.

The Ensemble Musical Méditerranéen.

My parents.

Contents

Introduction **7**

1 Nonlinear Optics **11**
1.1 Introduction to Nonlinear Optics 11
1.2 Second-order nonlinear processes 15
1.2.1 Second-Harmonic Generation (SHG) 15
1.2.2 Sum Frequency Generation (SFG) 19
1.2.3 Further second-order nonlinear processes 20
1.3 Third-order nonlinear processes 21
1.3.1 Basic third-order nonlinear processes 21
1.3.2 Coherent anti-Stokes Raman Scattering (CARS) 23
1.4 Incoherent nonlinear processes: Two-Photon Fluorescence (TPF) 31

2 Pulse shaping **37**
2.1 Introduction 37
2.2 Spectral phase 38
2.3 $4f$-line 42
2.4 Amplitude, phase and polarization shaping 44
2.4.1 Amplitude and phase shaping 47
2.4.2 Polarization shaping 49
2.5 Experimental Setup 50
2.5.1 Excitation path 50
2.5.2 Detection path 54
2.6 Pulse shaper calibration 54
2.7 Compensation of phase distortions 60
2.7.1 Pre-compensation by chirped mirrors 60
2.7.2 Characterization of the pre-compensated pulse by autocorrelation . 61
2.7.3 Correction of remaining phase distortions by an evolutionary strategy 62
2.7.4 Limitations of Evolutionary algorithms 67
2.8 Single-beam homodyne SPIDER 69
2.8.1 Principle of single-beam homodyne SPIDER 71
2.8.2 Correction of phase distortions using single-beam homodyne SPIDER 74
2.8.3 Limitations of this technique 77

2.8.4 Control of arbitrary phase profiles at the focal point of the objective using single-beam homodyne SPIDER 82

3 Polarization distortion effects in polarimetric two-photon microscopy 89
3.1 Introduction to polarization-resolved microscopy 89
3.2 Polarization distortion from optics probed by two-photon fluorescence . . . 94
3.3 Measurement of dichroic parameters 101
3.4 Polarization distortion by high NA focussing 108

4 Amplitude, phase and polarization pulse shaping for structural investigations of (bio-)molecular media in SFG microscopy 112
4.1 Introduction 112
4.2 Single $\chi^{(2)}$ component readout 115
4.2.1 Principle 115
4.2.2 Experimental realization on known crystals 117
4.3 Effect of the Z-direction coupling under high NA focussing 120
4.4 Molecular order imaging using polarization pulse shaping 125
4.5 Single SFG tensorial component contrast by phase and polarization pulse shaping 133
4.6 Conclusion 135

5 Single pulse Coherent anti-Stokes Raman Spectroscopy (CARS) 140
5.1 Introduction 140
5.2 Principle 142
5.3 Measurement of basic resonance characteristics 146
5.4 Determination of the Raman depolarization ratio ρ_R 152
5.5 Conclusion 160

6 Enhancement of nonlinear signals by photonic structures 163
6.1 Introduction 163
6.2 SHG enhancement from metallic nano-apertures 165
6.3 CARS enhancement from dielectric microspheres 173
6.4 Conclusions 177

Conclusion et perspectives 180

A Weighted linear fit 183

B Orientation measurement with fluorescence anisotropy 185

C Field propagation in high NA optics 188
C.1 Focussing of the exciting field 188
C.2 Collection of the generated signal 191

Bibliography **193**

Introduction

When the laser was invented 50 years ago, it was considered as "a solution looking for a problem" [1]. Since then it has seen a remarkable success and is now indispensable in science, industry and entertainment. There has been great progress in the development of new laser types and modes of operations. One of the latter is the pulsed regime where the energy of the laser is not anymore equally distributed in time but confined to short time intervals leading to very high electromagnetic field strengths. During the last 30 years the duration of these pulses has been decreased continuously. Nowadays pulses in the visible and infrared have been compressed down to several femtoseconds, and in the ultraviolet even attosecond pulses have been achieved by the generation of high-order harmonics [2].

The high energy densities in picosecond and femtosecond pulses have opened up the field of nonlinear optics where the response of a medium ceases to be proportional to the incident field but rather exhibits a higher-order dependency on it. These nonlinear processes can be of a coherent nature like Second Harmonic Generation (SHG), Third Harmonic Generation (THG) and Coherent anti-Stokes Raman Scattering (CARS), or they can be incoherent like Two-Photon Fluorescence (TPF). First these techniques were used for spectroscopy [3, 4, 5] but soon their potential for microscopy became evident [6, 7, 8, 9, 10]. Because these nonlinear contrasts appear in different wavelength regions thus permitting to combine them easily, and because many of them do not require a sample staining, they are by now in many cases standard techniques in the imaging of biological media [11, 12, 13, 14, 15].

Ultrashort pulses in the femtosecond domain are characterized by broad spectra in the frequency domain. The field of each wavelength present within the pulse is characterized by its amplitude, its phase relative to the fields of the other pulse wavelengths, and its polarization. Not only do these spectral characteristics influence the temporal shape of the pulse, but they are also reflected in the nonlinear signals generated by it. Therefore the knowledge of a pulse's amplitude, phase and polarization is often required for the interpretation of nonlinear optics experiments. While amplitude and polarization can be easily measured by spectrometers, polarizers and wave plates, the determination of the phase is more demanding. Yet, several methods like frequency-resolved optical gating (FROG) [16], spectral phase interferometry for direct electric-field reconstruction (SPIDER) [17], single-pulse reconstruction by interferometry [18, 19], and multiphoton intrapulse interference phase scan (MIIPS) [20, 21] have been developed to achieve this.

For many applications just knowing what are the pulse characteristics is not sufficient,

ways to actively control them are necessary. This is the domain of pulse shaping. Controlling optical pulses can strongly affect the intrinsic behavior of matter. For instance, the selectivity of photo-induced chemical reactions can be controlled by varying the delay between several pulses [22]. Pulse shaping as the direct manipulation of a single pulse's amplitude, phase, polarization or a combination of any of these was started by Weiner *et al.* in 1988 [23]. They spatially dispersed and recombined the pulse in a $4f$-line (see section 2.3) consisting of two gratings and two lenses where amplitude and phase masks were inserted in the dispersed beam to control those two parameters. While the $4f$-line remains a central part in the majority of today's pulse shapers, the fixed masks were soon replaced by programmable ones so that a dynamic amplitude and phase shaping became possible.

In the mid-nineties several device classes were proposed and implemented for this goal (see section 2.4). They have in common that a refractive index pattern gets created in the device which - in combinations with polarizers - leads to amplitude and/or phase control. In acousto-optic modulators (AOM) this pattern is induced by a radio-frequency wave [24, 25], in multiple quantum wells (MQW) it is written as a hologram by two continuous wave (cw) laser beams [26], and in liquid crystal spatial light modulators (LC-SLM) it arises from an externally applied voltage [27]. A different route for phase shaping has been taken by the use of deformable mirrors as the shaping device in the $4f$-line. Here, the modulation of the optical path length is not achieved by a control of the refractive index, but by an alteration of the physical distance the beam has to pass within the shaper [28]. These techniques have led to a large number of works on coherent control, which is the way to drive atoms or molecules towards specific pathways by manipulating the excitation field characteristics [27, 29, 30, 31, 32].

While these first studies mainly focussed on the mechanisms allowing pulse shaping in amplitude and phase towards coherent control experiments, subsequent works attempted to apply these new capabilities to nonlinear optical experiments, as their outcome depends strongly on the characteristics of the incident pulse. Because nonlinear optics involves the interaction of multiple fields, a nonlinear optical excitation is composed of several possible pathways where the fields' components combine. The phase profile of a large spectral pulse has therefore a considerable influence on the interferences between the different excitation pathways, which can be constructive or destructive depending on the phase combinations of the different participating wavelengths. In particular, maximizing a nonlinear signal can be achieved by compressing the pulses of a given laser in the temporal domain as much as possible. This condition is reached when their spectral phase is flat (λ-independent), which is usually not the case in a setup, as all optical elements in the beam path distort the phase profile. The Gerber group developed evolutionary learning algorithms for this purpose [33, 34, 35]. The SHG signal of a nonlinear crystal was measured for different phase configurations in a SLM and the phase mask was changed in an intelligent way until an optimal signal was obtained. Other phase control algorithms like MIIPS that also lead to a flat phase have strongly improved the image quality in nonlinear microscopy of biological samples such as HeLa cells and mouse kidney tissue [36].

The applications of phase pulse shaping are much broader than realizing flat phases. By shaping a sinusoidal phase into a laser pulse the Silberberg group could control two-photon transitions in a caesium gas [29], and obtained a single pulse CARS spectrum as well as depth-resolved CARS microscopy images [37, 38]. The latter was also possible when a spectrally narrow phase jump was added to a flat phase [39]. As ever spectrally broader laser sources become available, similar amplitude and phase shaped field profiles permit the rapid acquisition of CARS spectra covering the whole fingerprint region of organic molecules [40], and detection efficiencies of down to 300 molecules for CARS [41] and 50 molecules for near-degenerate four wave mixing processes [42] have been reached.

While single pulse amplitude and phase shaping was developed as soon as shaping technologies became available, single pulse polarization shaping was neglected for a long time. Only in 2001 was the first femtosecond polarization pulse shaping study published by Brixner and Gerber [43]. They used an LC-SLM in a $4f$-line to control the degree of ellipticity as well as the orientation of the elliptical principal axes. Later they improved their method to create arbitrary polarization-controlled pulses in the time domain [44, 45]. With such shaped pulses it was possible to control the photoisomerization of the cyanine dye NK88 [46], increase the ionization yield of potassium dimer molecules [47] and to influence the charges carried by iodine ions [48].

By then polarization shaping schemes based on a LC-SLM were also developed both in the Silberberg and the Leone group for their investigation of single pulse CARS [49, 50] to suppress the non-resonant background, and of multiphoton absorption processes [51] to control the angular momentum distribution of molecules in their final state. Furthermore a pulse shaping scheme based on two consecutive $4f$-lines was realized to permit full control over the polarization state of ultrashort pulses [52].

Polarization shaping schemes where the $4f$-line forms part of an interferometer has also been developed recently. Different polarization components of the incident beam pass different regions of the shaping device, thus allowing for independent amplitude and phase shaping. In this way polarization shaping can be achieved when the beam is recombined. If they are operated in a transmissive setup [53, 54] interferometric stability issues come into play that are avoided by an operation in a reflective setup [55], and of course by single pulse shaping geometries.

The combination of femtosecond pulses shaped simultaneously in amplitude, phase and polarization in combination with near-field microscopy has led to the emergence of nanoscopic ultrafast space-time-resolved spectroscopy [56]. Moreover, polarization pulse shaping allows controlling the electromagnetic near-field distribution in the vicinity of nanostructures, in particular the creation and positioning of hot spots with nanometric dimensions [32, 57, 58]. This achievement is based on the ability of metallic nanostructures to exhibit different plasmon resonance modes at different positions at nanometric distances, and that are polarized differently. Similarly to coherent control, different interferences between excitation pathways therefore create localization at the nano-scale. With the help of an evolutionary learning algorithm it is for example possible to locate the field at a specific bow-tie nanostructure while excluding it from another bow-tie close-by [59]. Thus

polarization pulse shaping has become an important tool in the quest to create nanometric light sources.

The experiments presented in this manuscript cover different topics and the connection between them may not always be evident at first glance. Yet they all contribute to explaining the capabilities of single pulse polarization pulse shaping for nonlinear microscopy.

In order to summarize the properties of the different nonlinear processes described throughout this work, chapter 1 describes the context of nonlinear optical contrasts. The basic formalism is introduced and all nonlinear processes relevant for this thesis are explained in detail.

Chapter 2 is devoted to pulse shaping as performed in this work. The experimental setup is explained with particular emphasis on the pulse shaper and its calibration. For the interpretation of nonlinear optical signals the knowledge of the phase profile of the exciting pulse is indispensable. That is why the second half of the chapter deals with the measurement of the spectral phase and the compensation of phase distortions to guarantee a spectrally flat phase in the sample plane. We concentrated here on the specific configuration of nonlinear microscopy which brings more stringent instrumental constraints. This is why here mostly "single pulse" techniques have been explored.

Because polarization shaping experiments only show their full potential when the relationship between the polarization state at the exit of the pulse shaper and the entrance of the microscope is known, chapter 3 is dedicated to the characterization of polarization distortions in a microscopy setup. And even though no pulse shaping is involved in this chapter, the obtained results are a prerequisite for a meaningful interpretation of subsequent polarization shaping experiments.

Chapter 4 is a first instrumental application of polarization shaping for nonlinear microscopy imaging. It demonstrates the potential of combined amplitude, phase and polarization shaping by simultaneously reading out the components of the second-order nonlinear susceptibility tensor $\chi^{(2)}$. Applications are presented in imaging local order and orientation of molecular and biomolecular samples.

In chapter 5 the performance of single pulse CARS is tested and a new method for the measurement of the Raman depolarization ratio of vibrational molecular transitions based on phase and polarization pulse shaping is proposed.

Finally, in chapter 6 the enhancement of nonlinear optical signals by photonic structures - both nano-apertures within a metal film and dielectric microspheres - is assessed. This last chapter, although of a different topic than the previous ones, describes first attempts in specific structures that could potentially lead to future studies combining pulse shaping, nonlinear contrasts and enhancements.

Chapter 1

Nonlinear Optics

All experiments presented in this work rely on nonlinear optical processes. In this chapter the nonlinear susceptibility will be introduced as a handy tool to describe and categorize these processes. Those that are used later on will be explained in more detail. Since the frame of this work is mostly dedicated to imaging, the specificity of nonlinear contrasts in microscopy will be derived.

1.1 Introduction to Nonlinear Optics

All electromagnetic phenomena follow Maxwell's equations for the electric and magnetic fields $\mathbf{E}(\mathbf{r},t)$ and $\mathbf{B}(\mathbf{r},t)$ [60, 61]:

$$\begin{aligned} \nabla \times \mathbf{E} &= -\frac{1}{c}\frac{\partial \mathbf{B}}{\partial t}, \\ \nabla \times \mathbf{B} &= \frac{1}{c}\frac{\partial \mathbf{E}}{\partial t} + \frac{4\pi}{c}\mathbf{J}, \\ \nabla \cdot \mathbf{E} &= 4\pi\rho, \\ \nabla \cdot \mathbf{B} &= 0 \end{aligned} \tag{1.1}$$

with $\mathbf{J}(\mathbf{r},t)$ and $\rho(\mathbf{r},t)$ the current and charge densities, related to each other by the charge conservation law:

$$\nabla \cdot \mathbf{J} + \frac{\partial \rho}{\partial t} = 0 \tag{1.2}$$

These source terms can be separated into

$$\mathbf{J} = \mathbf{J}_{dc} + \frac{\partial \mathbb{P}}{\partial t} \tag{1.3}$$

a dc current density $\mathbf{J}_{dc}$ and a time-dependent generalized polarization $\mathbb{P}$. Maxwell's equations transform then to:

$$\begin{aligned} \nabla \times \mathbf{E} &= -\frac{1}{c}\frac{\partial \mathbf{B}}{\partial t}, \\ \nabla \times \mathbf{B} &= \frac{1}{c}\frac{\partial}{\partial t}(\mathbf{E} + 4\pi\mathbb{P}) + \frac{4\pi}{c}\mathbf{J}_{dc}, \\ \nabla \cdot (\mathbf{E} + 4\pi\mathbb{P}) &= 0, \\ \nabla \cdot \mathbf{B} &= 0 \end{aligned} \tag{1.4}$$

with $\mathbb{P}(\mathbf{r}, t)$ as the only time-dependent source term. Taking the curl of $\nabla \times \mathbf{E}$ leads to the propagation equation:

$$\nabla \times (\nabla \times \mathbf{E}) = -\frac{1}{c}\frac{\partial}{\partial t}(\nabla \times \mathbf{B}) = -\frac{1}{c}\frac{\partial}{\partial t}\left(\frac{1}{c}\frac{\partial}{\partial t}(\mathbf{E} + 4\pi\mathbb{P}) + \frac{4\pi}{c}\mathbf{J}_{dc}\right) \tag{1.5}$$

As $\mathbf{J}_{dc}$ is time-independent Eq. (1.5) changes to:

$$\nabla \times (\nabla \times \mathbf{E}) + \frac{1}{c^2}\frac{\partial^2}{\partial t^2}\mathbf{E} = -\frac{4\pi}{c^2}\frac{\partial^2}{\partial t^2}\mathbb{P} \tag{1.6}$$

In the case of an external field $\mathbf{E}$ which gets applied to a material not possessing any electric field sources itself ($\nabla \cdot \mathbf{E} = 0$), $\nabla \times (\nabla \times \mathbf{E}) = \nabla(\nabla \cdot \mathbf{E}) - \triangle\mathbf{E}$ simplifies to:

$$\triangle\mathbf{E} - \frac{1}{c^2}\frac{\partial^2}{\partial t^2}\mathbf{E} = \frac{4\pi}{c^2}\frac{\partial^2}{\partial t^2}\mathbb{P} \tag{1.7}$$

$\mathbb{P}$ describes the response of the medium to the external field and is thus a function of $\mathbf{E}$.

For low field strengths the induced polarization follows the field in a linear way, so that

$$\mathbb{P}(\mathbf{r}, t) = \int_{-\infty}^{\infty} \chi^{(1)}(\mathbf{r} - \mathbf{r}', t - t') : \mathbf{E}(\mathbf{r}', t') \mathrm{d}\mathbf{r}' \mathrm{d}t' \tag{1.8}$$

where $\chi^{(1)}$ is the linear susceptibility, for which causality demands $\chi^{(1)}(\mathbf{r}, t) = 0$ for $t < 0$ [61, 62]. In the case of a monochromatic plane wave $\mathbf{E}(\mathbf{r}, t) = \mathbf{E}(\mathbf{k}, \omega) = \mathbf{E}_0\, e^{i(\mathbf{k}\cdot\mathbf{r} - \omega t)}$ a Fourier transformation of Eq. (1.8) leads to

$$\mathbb{P}(\mathbf{r}, t) = \mathbb{P}(\mathbf{k}, \omega) = \chi^{(1)}(\mathbf{k}, \omega) : \mathbf{E}(\mathbf{k}, \omega) \tag{1.9}$$

with

$$\chi^{(1)}(\mathbf{k}, \omega) = \int_{-\infty}^{\infty} \chi^{(1)}(\mathbf{r}, t) e^{-i(\mathbf{k}\cdot\mathbf{r} - \omega t)} \mathrm{d}\mathbf{r}\mathrm{d}t \tag{1.10}$$

the familiar expression of linear optics. Under the electric dipole approximation that will be used throughout this work, $\mathbb{P}$ becomes a local function of $\mathbf{E}$, meaning that a polarization at point $\mathbf{r}$ depends exclusively on the field $\mathbf{E}$ at that point. $\chi^{(1)}(\mathbf{r} - \mathbf{r}', t)$ and $\chi^{(1)}(\mathbf{k} - \mathbf{k}', \omega)$ are then independent of $\mathbf{r}'$ and $\mathbf{k}'$ respectively and $\mathbb{P}$ reduces to the electric dipole polarization

$\mathbf{P}(\mathbf{r},t)$. It should be noted that $\chi^{(1)}$ can also be derived quantum mechanically as the product of an annihilation and a creation operators that correspond to the product of two transition dipole moments [61].

This linear relationship between $\mathbf{P}$ and $\mathbf{E}$, however, does not hold anymore for strong fields $\mathbf{E}$. In general $\mathbf{P}(\mathbf{E}(\mathbf{r},t))$ can be a very complicated function. To approach this dependence, $\mathbf{P}$ can be expanded in a power series of $\mathbf{E}$, under the assumption that the field is sufficiently weak so that magnetic dipoles and higher-order electric and magnetic multipoles can still be neglected (Fig. 1.1). The formalism above then yields [62]:

$$\begin{aligned}\mathbf{P}(\mathbf{r},t) &= \int_{-\infty}^{\infty}\chi^{(1)}(t-t'):\mathbf{E}(\mathbf{r},t')\mathrm{d}t' \\ &+ \int_{-\infty}^{\infty}\chi^{(2)}(t-t_1,t-t_2):\mathbf{E}(\mathbf{r},t_1)\mathbf{E}(\mathbf{r},t_2)\mathrm{d}t_1\mathrm{d}t_2 \\ &+ \int_{-\infty}^{\infty}\chi^{(3)}(t-t_1,t-t_2,t-t_3):\mathbf{E}(\mathbf{r},t_1)\mathbf{E}(\mathbf{r},t_2)\mathbf{E}(\mathbf{r},t_3)\mathrm{d}t_1\mathrm{d}t_2\mathrm{d}t_3 \\ &+ \ldots\end{aligned} \tag{1.11}$$

with the $(n+1)^{th}$-rank tensor $\chi^{(n)}$ as the n-th order nonlinear susceptibility. If the electric

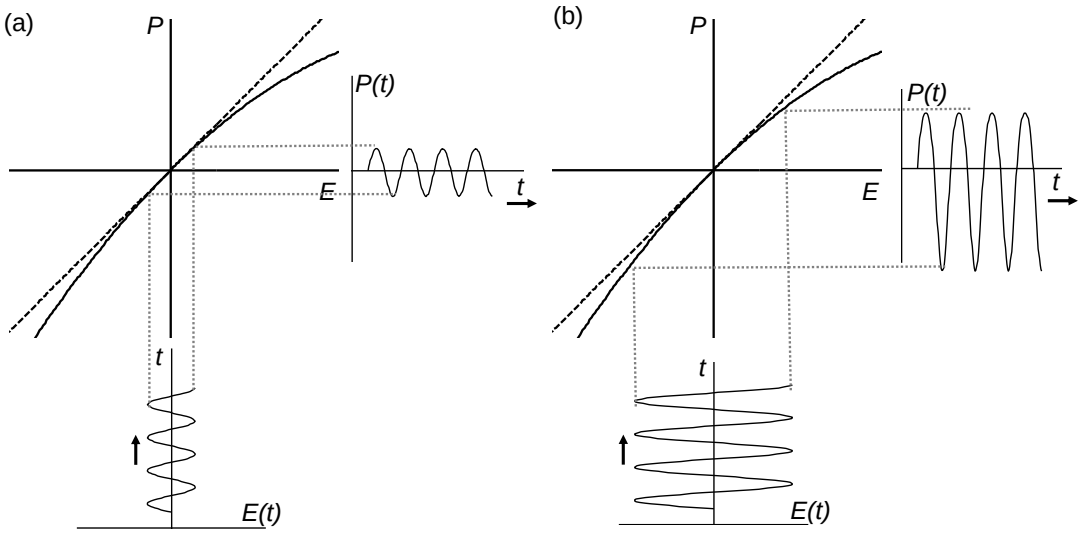

Figure 1.1: $\mathbf{P}(\mathbf{E})$-dependence (solid line) and its linear approximation (dashed line) [63]. For small field amplitudes (a) $\mathbf{P}$ follows $\mathbf{E}$ in a linear way (linear optics) while this does not hold for larger electric field amplitudes (b) when higher-order contributions appear in the polarization $\mathbf{P}$ (nonlinear optics). Grey dotted lines as a guide to relate the incoming field $\mathbf{E}(t)$ and the generated polarization $\mathbf{P}(t)$.

field can be expressed as a superposition of monochromatic plane waves

$$\mathbf{E}(\mathbf{r},t) = \sum_i \mathbf{E}(\mathbf{k}_i,\omega_i) \tag{1.12}$$

a Fourier transformation of Eq. (1.11) results in

$$\mathbf{P}(\mathbf{k},\omega) = \mathbf{P}^{(1)}(\mathbf{k},\omega) + \mathbf{P}^{(2)}(\mathbf{k},\omega) + \mathbf{P}^{(3)}(\mathbf{k},\omega) + ... \tag{1.13}$$

with

$$\begin{aligned} \mathbf{P}^{(1)}(\mathbf{k},\omega) &= \chi^{(1)}(\omega){:}\mathbf{E}(\mathbf{k},\omega) \\ \mathbf{P}^{(2)}(\mathbf{k}=\mathbf{k}_i+\mathbf{k}_j,\omega=\omega_i+\omega_j) &= \chi^{(2)}(\omega_i+\omega_j){:}\mathbf{E}(\mathbf{k}_i,\omega_i)\mathbf{E}(\mathbf{k}_j,\omega_j) \\ \mathbf{P}^{(3)}(\mathbf{k}=\mathbf{k}_i+\mathbf{k}_j+\mathbf{k}_l,\omega=\omega_i+\omega_j+\omega_l) &= \chi^{(3)}(\omega_i+\omega_j+\omega_l){:}\mathbf{E}(\mathbf{k}_i,\omega_i)\mathbf{E}(\mathbf{k}_j,\omega_j)\mathbf{E}(\mathbf{k}_l,\omega_l) \end{aligned} \tag{1.14}$$

and

$$\begin{aligned} \chi^{(n)}(\omega=\omega_1+\omega_2+...+\omega_n) &= \int_{-\infty}^{\infty} \chi^{(n)}(t-t_1,t-t_2,...,t-t_n) \\ &\times\ e^{i[\omega_1(t-t_1)+\omega_2(t-t_2)+...+\omega_n(t-t_n)]}\mathrm{d}t_1\mathrm{d}t_2...\mathrm{d}t_n \end{aligned} \tag{1.15}$$

The physical origin of the polarization in dielectric materials is the displacement, induced by an external field, of the electron charge density with respect to the nuclei charge density. For small electric field strengths at optical frequencies, the electrons will oscillate in the lower parts of the nucleus' potential where it can be treated as a harmonic well. Therefore only the linear part of the susceptibility is present in the polarization. If however the field is strong enough not to be neglected anymore compared to the internal atomic field E_a between the core and the electron shell, the harmonic approximation fails and nonlinear terms of the susceptibility come into play. E_a is on the order of $3 \cdot 10^{10}\,\mathrm{Vm}^{-1}$ [63]. For fields of such magnitudes, intensities of about $10^{14}\,\mathrm{Wcm}^{-2}$ have to be provided. Normal sunlight shines with up to $0.07\,\mathrm{Wcm}^{-2}$ in Central European latitudes. Even focused standard continuous wave (cw) lasers do not reach such magnitudes. That is why nonlinear optics depends on the use of picosecond or even shorter pulsed lasers, where the laser energy is temporally confined into these tiny intervals, resulting in huge field strengths. Upon further increase of the field strength the electric dipole approximation breaks down due to several different effects like ionization or the oscillation of the nuclei themselves in the external field as can be observed when using attosecond pulses.

The different contributions to the nonlinear polarization are best studied in the frequency domain rather than in the time domain because they can be easily classified by using Eqs. (1.13) and (1.14) not only according to their order of nonlinearity but also according to the frequencies at which the corresponding fields radiate. In the following will be presented in detail all nonlinear processes that constitute a part of the experiments performed for this work while others will only be mentioned briefly to give a general overview. In these sections $\chi^{(n)}(\omega;\omega_1,\omega_2,...,\omega_n)$ will denote the susceptibility associated to a process of n-th order that creates a field of frequency ω out of the generating frequencies $\omega_1+\omega_2+...+\omega_n$. At this stage we treat the problem as a scalar one, the tensorial analysis follows in later chapters. Whenever the tensorial nature of $\chi^{(n)}$ is considered in this chapter it is stated explicitly.

1.2 Second-order nonlinear processes

1.2.1 Second-Harmonic Generation (SHG)

The simplest of all nonlinear processes is the generation of the second harmonic, in which two fields of frequency ω create a polarization field with twice their frequency in the nonlinear medium $\chi^2(2\omega;\omega,\omega)$ (Fig. 1.2). Decomposition of the second-order susceptibility

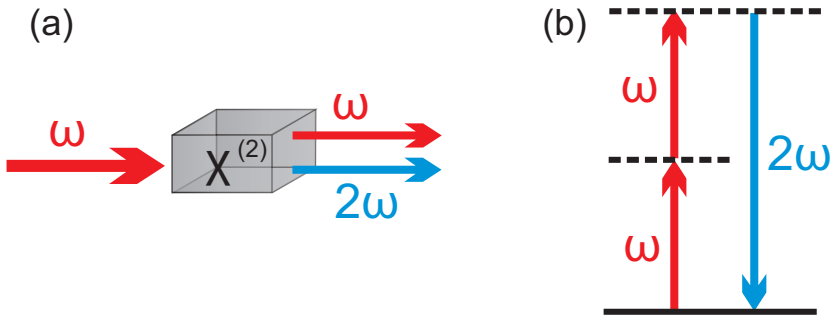

Figure 1.2: Second-harmonic generation. (a) geometry of the process; (b) SHG energy-level diagram (solid black line: energy ground level; dashed lines: virtual energy levels).

tensor in Eq. (1.14) results in (accounting for the tensorial nature of $\chi^{(2)}$):

$$P_I(2\omega) = \sum_{JK} \chi^{(2)}_{IJK}(2\omega) E_J(\omega) E_K(\omega) \tag{1.16}$$

Each tensorial element $\chi^{(2)}_{IJK}$ couples the fields polarized in directions J and K to generate a SHG field in direction I ($(I,J,K) = (X,Y,Z)$). The final field P_I is then the superposition of all these couplings.

SHG only occurs in non-centrosymmetric media. This is easily seen under spatial inversion ($\mathbf{r} \to -\mathbf{r}$). Eq. (1.16) then transforms to:

$$\begin{aligned} \mathbf{P}^{(2)}_I(-\mathbf{r}) &= \sum_{JK} \chi^{(2)}_{IJK}(-\mathbf{r}) \mathbf{E}_J(-\mathbf{r}) \mathbf{E}_K(-\mathbf{r}) \\ = -\mathbf{P}^{(2)}_I(\mathbf{r}) &= \sum_{JK} \chi^{(2)}_{IJK}(-\mathbf{r})(-\mathbf{E}_J(\mathbf{r}))(-\mathbf{E}_K(\mathbf{r})) = \sum_{JK} \chi^{(2)}_{IJK}(-\mathbf{r}) \mathbf{E}_J(\mathbf{r}) \mathbf{E}_K(\mathbf{r}) \end{aligned} \tag{1.17}$$

Writing this for every single coupling (I,J,K) and comparing it with Eq. (1.16) leads to $\chi^{(2)}_{IJK}(-\mathbf{r}) = -\chi^{(2)}_{IJK}(\mathbf{r})$. In centrosymmetric media the material properties do not change under room inversion, so that $\chi^{(2)}_{IJK}(-\mathbf{r}) = \chi^{(2)}_{IJK}(\mathbf{r})$ from which follows $\chi^{(2)}_{IJK} = 0$ for all (I,J,K). The same reasoning applies to all other even-ordered nonlinear processes.

SHG is a coherent process, based on the pure scattering of a harmonic photon, without necessitating an absorption event such as in fluorescence (see section 1.4). The photons

pass via virtual levels so that the SH generation occurs instantaneously. The created wave therefore has a fixed phase relation to the generating field **E**. As **E** propagates through the nonlinear material more and more nonlinear dipoles start to radiate the second harmonic in a coherent way. Was the medium's refractive index n a constant, all these radiated SHG fields emitted in the propagation (forward) direction of the incident radiation would be in phase or phase matched and the total signal would build up over the whole length of the medium (Fig. 1.3b). In this way measurable signals could be detected even with very small laser intensities provided the material was thick enough, and the SH generation would occur over a sufficiently large distance. However, due to the fact that the refractive index of a material is generally wavelength-dependent ($n = n(\omega)$), a wave vector mismatch between created and propagating harmonic waves $\Delta\mathbf{k}_{fwd} = \mathbf{k}_{2\omega} - 2\mathbf{k}_{\omega}$ occurs in the forward direction (with $\mathbf{k}_{\omega} = n(\omega)\frac{2\pi}{\lambda}$ the wave vector of the driving field **E**, and $\mathbf{k}_{2\omega}$ the one of the generated field **P**, where λ denotes the wavelength). Consequently the radiation of the dipoles at a certain sample thickness is not any longer in phase with the radiation of the dipoles somewhat in front of or behind them (Fig. 1.3c). As long as the phase mismatch is

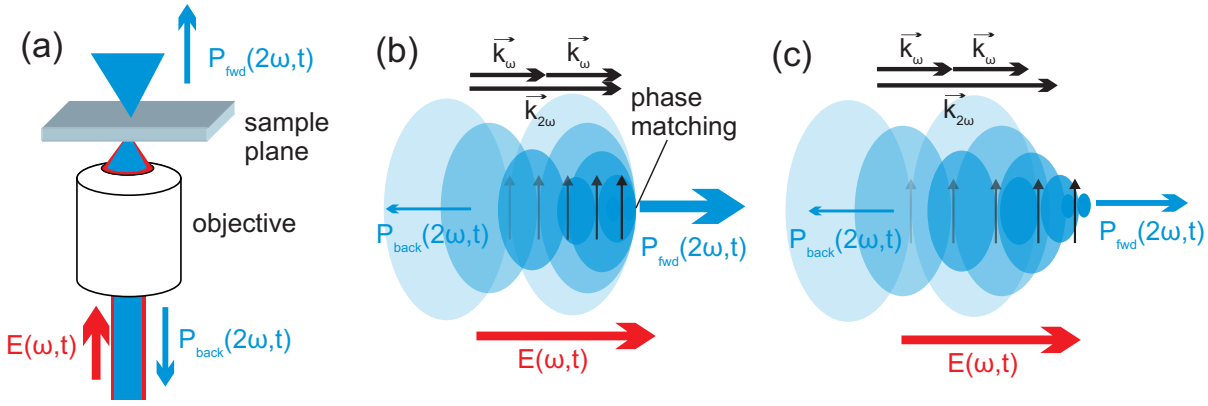

Figure 1.3: Illustration of phase matching (the blue areas represent the wavefronts of the dipole emission). (a) Microscopy setup with forward and backward scattered signal. (b) Perfect phase matching. The emission of all nonlinear dipoles is in phase in the forward direction and coherent buildup creates a huge field. (c) Slight phase mismatch. The dipoles' emission fields are slightly out of phase in the forward direction resulting in only partial constructive interference and consequently a smaller field. In both cases the SHG backward emission is strongly phase mismatched.

smaller than π, the signal can still be considered phase matched which leads to a coherence length of

$$l_{c,fwd} = \frac{\pi}{\Delta k_{fwd}} = \frac{\lambda}{4(n(2\omega) - n(\omega))} \tag{1.18}$$

Microscopy samples for example in biology contain a lot of water. At room temperature its refractive index for light with $\lambda = 800\,\text{nm}$ is 1.329, while at the corresponding SHG wavelength it increases to $n(\lambda_{SHG} = 400\,\text{nm}) = 1.344$ [64]. Thus $\Delta k_{fwd} = 0.24\,\mu\text{m}$ and $l_{c,fwd} = 13\,\mu\text{m}$.

To obtain the high energy densities required for nonlinear optics it is necessary to tightly focus the laser beam which is done by objectives with high numerical apertures (NA). Under these conditions the beam acquires an additional phase, the Gouy phase shift Δk_{ϕ_G} [65, 66], over the focussing region. The wave vector mismatch increases to:

$$\Delta k_{fwd} = |k_{2\omega} - 2(k_\omega + \Delta k_{\phi_G})| \tag{1.19}$$

For high NA focussing this Gouy phase shift amounts to around π over a distance of 2λ. For $\lambda = 800\,\text{nm}$ this results in $\Delta k_{\phi_G} = 2\,\mu\text{m}^{-1}$, which is much larger than the mismatch due to the wavelength dependence of the refractive index and the coherence length becomes:

$$l_{c,fwd} = \frac{\pi}{\Delta k_{fwd}} \approx \frac{\pi}{2\Delta k_{\phi_G}} = \frac{\pi}{\pi/\lambda} = \lambda \tag{1.20}$$

This means that the SHG signal generated in the forward direction by the nonlinear dipoles in a sample will buildup coherently for a distance about the size of the wavelength. Because the SHG signal is only generated in considerable quantities at the center of the laser focus due to the quadratic dependence on the electric field, a region itself comparable in size to λ in the propagation direction of the laser [67], the SHG emitted in the forward direction is coherent over the whole generation length. The dipoles of course radiate in the backward (epi) direction, too (see Fig. 1.3a), but then $\mathbf{k}_{2\omega}$ and $\mathbf{k}_\omega$ are opposite and the wave vector mismatch increases to:

$$\Delta k_{epi} = |k_{2\omega} + 2(k_\omega + \Delta k_{\phi_G})| \approx |4k_\omega + 2\Delta k_{\phi_G}| \tag{1.21}$$

under the assumption that $2k_\omega$ and $k_{2\omega}$ are similar. Consequently the coherence length reduces significantly to:

$$l_{c,epi} = \frac{\pi}{\Delta k_{epi}} = \frac{\pi}{4n\frac{2\pi}{\lambda} + \frac{\pi}{\lambda}} = \frac{\lambda}{8n+1} \approx \frac{\lambda}{12} \tag{1.22}$$

for an aqueous medium with $n \approx 1.33$. Therefore only very thin samples radiate backwards. In addition this mode can also be used to study interfaces of thick nonlinear samples as only dipoles in immediate interface vicinity contribute to the backward emitted signal. The use of high NA objectives for focussing facilitates the detection of the backscattered light, which is extensively used in imaging of biological samples like cells or tissues where many different small structures like collagen fibers lead to epi-detectable SHG signals [68, 14, 69]. Bulk investigations, on the other hand, can only be performed with forward emitted SHG. The cross sections for SHG are generally very small, typically four orders of magnitude smaller than those for two-photon fluorescence (section 1.4). For example for the dye Di-6-ASPBS $\sigma_{SHG} \approx 10^{-3}\,\text{GM}$, while $\sigma_{TPF} \approx 30\,\text{GM}$ with $1\,\text{GM}$ (Goeppert-Mayer) $= 10^{-50}\,\text{cm}^4\text{s}$ [11] for a driving wavelength of 880 nm. Despite these tiny cross sections of the individual dipoles the coherent buildup especially in the forward direction allows for the creation of quite large signal strengths. To understand this let us consider a focal volume with N emitters each radiating a field P_{rad}. In the case of an incoherent process like fluorescence the total signal

will be the sum of the individual intensities $I_{fluo} \propto N|P_{rad}|^2$ while in the case of SHG to total field is the sum of the individual fields and therefore $I_{SHG} \propto |NP_{rad}|^2 = N^2|P_{rad}|^2$ (this is only a rough calculation not accounting for phase retardation effects between dipoles as will be discussed in section 6.2). The square dependence on the number of emitters within the coherence length allows the detection of nonlinear signals even with lasers giving much less field strengths than the internal atomic field E_a.

Not specifying the spatial extension of the object that can induce phase-retardation effects related to phase-matching as described before, the SHG intensity analyzed along a direction i is a coherent sum:

$$I_i^{2\omega} \propto \left| \int\int\int \left[\mathbf{k} \times \underbrace{\left(\mathbf{k} \times \mathbf{p}^{2\omega}(\mathbf{\Omega}, \mathbf{r}) \right)}_{\mathbf{E}_i^{2\omega}(\mathbf{\Omega},\mathbf{r})} \right]_i \mathrm{d}\mathbf{\Omega}\mathrm{d}\mathbf{r}\mathrm{d}\mathbf{k} \right|^2 \tag{1.23}$$

with

$$\mathbf{p}^{2\omega}(\mathbf{\Omega}, \mathbf{r}) = \chi^{(2)}(\mathbf{\Omega}, \mathbf{r}) : \mathbf{E}^{\omega}(\mathbf{r})\mathbf{E}^{\omega}(\mathbf{r}) \tag{1.24}$$

over the orientation $\mathbf{\Omega}$, position $\mathbf{r}$ and emission direction $\mathbf{k}$ of the nonlinear induced field. It is therefore clear that the measured intensity will be dependent on the incident polarization $\mathbf{E}^{\omega}$ and the $\chi^{(2)}$ tensorial properties of the explored material. It is the basis of the "nonlinear polarimetric" approach further developed in chapter 3. Note that since $\chi^{(2)} = N\beta$ with β the molecular-scale hyperpolarizability, the retrieved signal is indeed proportional to N^2.

That was also the reason why Franken *et al.* were able to detect SHG [70] already in 1961 shortly after the invention of the laser which were still quite weak back then. It was the first experimental observation of a nonlinear optical process. Since then second-harmonic generation has found numerous applications. Early works of Chen *et al.* [71] and Roth *et al.* [72] showed its potential as a analytical and structural measurement tool in molecular and biomolecular media. Soon SHG microscopy was developed, applied both to crystals [7] and tissues [8]. Because SHG arises exclusively from non-centrosymmetric media, it offers a structural contrast by nature which has led to a wide use in bio-imaging with prospectives for biomedical diagnostics. As other multiphoton imaging techniques SHG microscopy also benefits from the use of excitation wavelengths in the near infrared. In this region biological tissues are more transparent than in the visible spectrum. Consequently the laser excitation is less subject to illumination scattering, allowing for deeper optical penetration. Furthermore SHG offers a very good intrinsic resolution (typically 300 nm lateral) because the signal only arises with exploitable intensities from the focal point due to the quadratic dependence on the electric field.

Examples for SHG imaging range from labeled artificial and cell membranes [73, 74] and molecular monolayers [75, 76] down to single micro- and nano-crystals [77, 78, 79]. Currently intrinsic SHG responses from biomolecular assemblies such as in collagen [80, 69, 81], microtubules [82] and skeletal muscles [83] are exploited with the ultimate goal of developing diagnostics of pathological effects related to tissues and cell architecture. As opposed

to fluorescence these techniques do not require a previous labeling of the desired structure and thus biological material can be imaged in its natural unaltered state.

In this work we will concentrate essentially on the exploitation of the polarization dependence of the SHG signal. By controlling the excitation polarization state in nonlinear microscopy it is possible better understand the 3D light-matter SHG interactions [84, 85, 86]. Polarization resolved SHG imaging has allowed retrieving information on molecular orientations in highly ordered materials such as crystals [77, 78, 79, 87, 88, 89], oriented molecular systems [90, 76] and biological samples [91, 92, 93, 94, 95, 96]. This kind of information can play an important role in nano-material engineering as well as in biological imaging.

1.2.2 Sum Frequency Generation (SFG)

Very closely related to SHG is Sum Frequency Generation (SFG). It differs only in the fact that both coupled fields may have different frequencies. Eq. (1.16) then changes to

$$P_I(\omega = \omega_1 + \omega_2) = \sum_{JK} \chi^{(2)}_{IJK}(\omega) E_J(\omega_1) E_K(\omega_2) \tag{1.25}$$

This can for example be achieved by coupling two monochromatic lasers (Fig. 1.4a). In this work we use SFG that is excited by ultra-short laser pulses with pulse durations up to several tens of femtoseconds. These lasers are spectrally broad and consequently in a medium exhibiting a $\chi^{(2)}$ nonlinear susceptibility sum frequency generation will occur instead of pure SHG, because all different frequencies present within the pulse will get coupled. In general there will be many frequency combinations leading to the same SFG frequency (Fig. 1.4b). Thus Eq. (1.25) expands to:

$$P_I(2\omega) = \int_{-\infty}^{\infty} \sum_{JK} \chi^{(2)}_{IJK}(\omega, \Omega) E_J(\omega - \Omega) E_K(\omega + \Omega) \mathrm{d}\Omega \tag{1.26}$$

where the integration accounts for all these frequency pairs. Having all these couplings present simultaneously means that a large band of virtual energy levels is involved in the SFG process. Therefore chances increase that some of them coincide or lie close by to real atomic or molecular energy levels, either vibrational or electronic. Passage via these levels will of course modify the SFG probabilities of these pathways. To account for this the second frequency dependence (Ω) of $\chi^{(2)}$ has been introduced in Eq. (1.26). In the absence of all intermediate real energy levels, in other words when all two-photon pathways leading to the same SFG frequency have the same probability, $\chi^{(2)}$ is again independent of Ω.

An excitation pulse containing frequencies within the $[\omega_{min}, \omega_{max}]$-interval will generate a sum frequency spectrum confined to $[2\omega_{min}, 2\omega_{max}]$. The shape of the SFG pulse will depend on the spectral characteristics of the generating laser. Not only do the intensity and polarization of each frequency therein influence the final SFG spectrum, also the phase relationship of all spectral components with respect to each other plays an important role

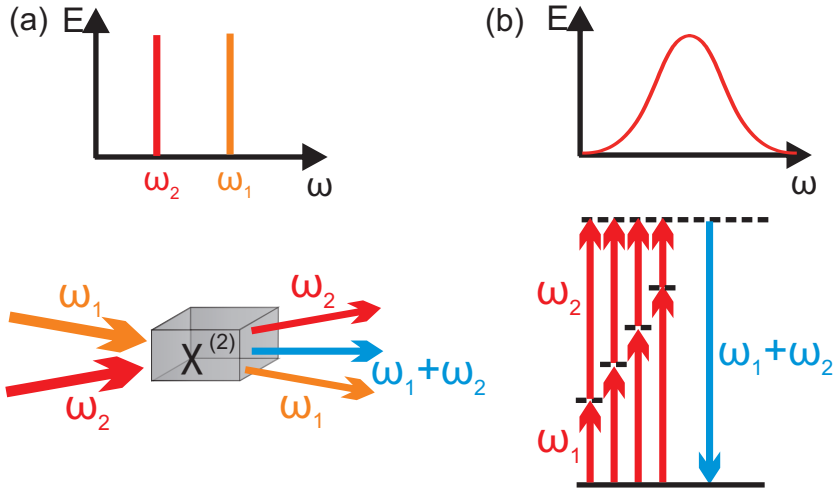

Figure 1.4: Sum Frequency Generation. (a) geometry of the process in the case of only two discrete wavelengths; (b) SFG energy-level diagram for a spectrally broad excitation pulse (solid black line: energy ground level; dashed lines: virtual energy levels).

because all pathways leading to the same SFG frequency will interfere, either constructively or destructively (see sections 2.2 and 4.5) [30, 31]. The ability to control amplitude, phase and polarization of the excitation laser pulse is therefore crucial to understand the SFG signal.

Because SHG is just a particular case of SFG, the latter possesses the same kind of applications as the former. In chapter 4 we present a new method to read out the second order nonlinear susceptibility tensor $\chi^{(2)}$ by combining SFG microscopy with amplitude, phase and polarization pulse shaping (see section 2.4).

1.2.3 Further second-order nonlinear processes

There are several other processes that are governed by the second-order nonlinear susceptibility $\chi^{(2)}$. Quite similar to sum frequency generation is difference frequency generation ($\chi^{(2)}(\omega_3 = \omega_1 - \omega_2; \omega_1, -\omega_2)$). Here the generated signal is the difference between the two incident frequencies (Fig. 1.5a). This means a high-energy photon (ω_1) gets split up into one of the lower incident energy (ω_2) and the remaining difference (ω_3). The result is a amplification of the laser at ω_2, hence the alternative name for this process: optical parametric amplification. This mechanism can also be used to create a tunable infrared radiation when a frequency- tunable visible laser is combined with another visible laser of a fixed frequency.

A special case of difference frequency generation arises, when there is only one frequency available in the incident field ($\chi^{(2)}(0; \omega, -\omega)$). A static electric field is created in the nonlinear medium, which is an optical rectification effect (Fig. 1.5b).

Also the opposite can occur: When sending an optical field through a nonlinear medium

under the presence of a static electric field ($\chi^{(2)}(\omega;\omega,0)$), a term following the optical field and proportional to the static field appears in the nonlinear polarization, leading to a dependence of the refractive index at the frequency ω of the optical field on the static field. This is the Pockels effect, used in optical modulators that behave similarly to those presented in section 2.4 (Fig. 1.5c).

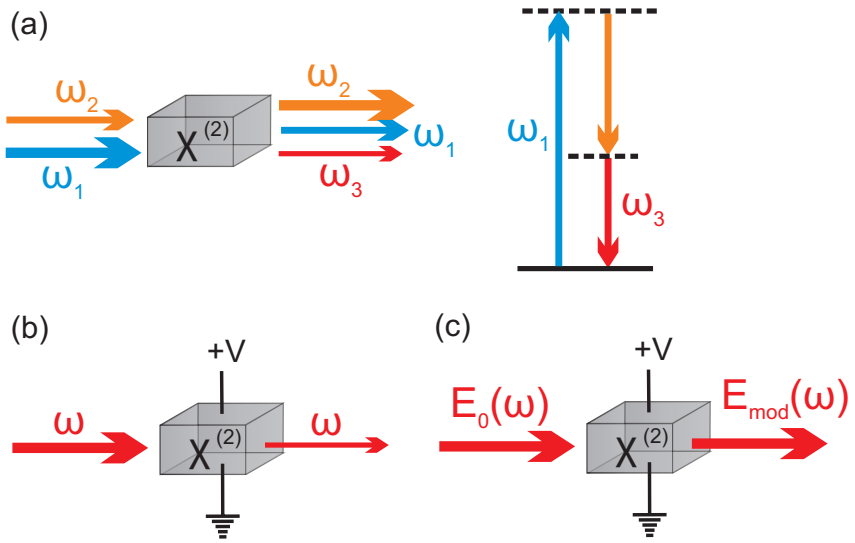

Figure 1.5: Further second-order nonlinear processes. (a) difference frequency generation, geometry and energy-level diagram (solid black line: energy ground level; dashed lines: virtual energy levels); (b) optical rectification: static electric field gets created under the action of an incident field; (c) Pockels effect: field gets modified under the action of a static electric field.

1.3 Third-order nonlinear processes

Because a third-order nonlinear susceptibility couples three electric fields, the number of possible processes is greater than for the second-order case.

1.3.1 Basic third-order nonlinear processes

In analogy to SHG three photons of the same frequency can be combined in a medium to create one photon thrice as energetic ($\chi^{(3)}(3\omega;\omega,\omega,\omega)$). This process is called third harmonic generation (THG)(1.6a,b). Symmetry considerations as presented above for SHG (page 15) show that THG is not restricted to non-centrosymmetric media. In fact, every medium has a non-zero third-order nonlinear susceptibility and will therefore produce a THG signal. However, phase matching is less favored for this process, because the wave

vector mismatch in the propagation (forward) direction of the exciting beam amounts to (in analogy to the argumentation in section 1.2.1):

$$\Delta k_{fwd} = |k_{3\omega} - 3(k_\omega + \Delta k_{\phi_G})| \approx 3\Delta k_{\phi_G} = 3\frac{\pi}{2\lambda} \tag{1.27}$$

resulting in a coherence length of

$$l_{c,fwd} = \frac{\pi}{\Delta k_{fwd}} \approx \frac{2}{3}\lambda \tag{1.28}$$

which is less than for SHG. The signal emitted against the propagation direction (epi), however, accumulates a phase mismatch of:

$$\Delta k_{epi} = |k_{3\omega} + 3(k_\omega + \Delta k_{\phi_G})| \approx 6k_\omega + 3\Delta k_{\phi_G} = 6\frac{2\pi n}{\lambda} + 3\frac{\pi}{2\lambda} \approx \frac{35\pi}{2\lambda} \tag{1.29}$$

for a typical refractive index n around 1.33, reducing the coherence length to:

$$l_{c,epi} = \frac{\pi}{\Delta k_{epi}} \approx 0.06\lambda \tag{1.30}$$

Thus no signal arises from homogeneous media. A constructive interference between the radiated fields from different nonlinear dipoles is only possible when the sample is heterogeneous within the focal volume, i.e. when there are interfaces or inclusions, which will induce an additional index mismatch in the focal volume [97]. Consequently THG microscopy is used mainly for surfaces and has been combined with SHG imaging of cells for example, because both processes give spectrally separable signals arising from different parts of the cell, SHG from non-centrosymmetric fibers, most commonly microtubules, and THG from lipid body surfaces [98]. It is also suited to detect inhomogeneities in an otherwise homogeneous medium [99]. A combination of polarization and phase pulse shaping has recently allowed to improve the spatial resolution in THG microscopy [100, 101].

When an intense optical field traverses a medium in the presence of a static electric field, the quadratic electrooptic Kerr effect arises. The refractive index of the medium gets then modified proportional to the square of the static field ($\chi^{(3)}(\omega;\omega,0,0)$).

One of the most important nonlinear optical processes is the optical Kerr effect $\left(\chi^{(3)}(\omega;\omega,-\omega,\omega)\right)$, producing a response of the medium of frequency ω to the incident field of that same frequency. It is of the form

$$\mathbf{P} = \chi^{(1)}\mathbf{E} + 3\chi^{(3)}\mathbf{E}\mathbf{E}^*\mathbf{E} = (\chi^{(1)} + 3\chi^{(3)}I)\mathbf{E} \tag{1.31}$$

containing a linear term and one of third order proportional to the field's intensity $I = \mathbf{E}\mathbf{E}^*$ whose factor 3 is due to the possible permutations of the fields. The propagation equation (Eq. 1.7) then transforms to:

$$\triangle\mathbf{E} - \frac{1}{c^2}(1 + 4\pi\chi^{(1)} + 12\pi\chi^{(3)}I)\frac{\partial^2}{\partial t^2}\mathbf{E} \tag{1.32}$$

Assuming a plane wave and solving the time derivative results in:

$$\triangle \mathbf{E} + \frac{\omega^2}{c^2}(1 + 4\pi\chi^{(1)} + 12\pi\chi^{(3)} I(\mathbf{r}, t))\mathbf{E} \tag{1.33}$$

where $1 + 4\pi\chi^{(1)} + 12\pi\chi^{(3)} I(\mathbf{r}, t)$ plays the role of the squared refractive index consisting of the ordinary part $n_0^2 = 1 + 4\pi\chi^{(1)}$ and an intensity-dependent nonlinear component. As this term is usually small the refractive index can be approximated as $n = n_0 + n_2 I(\mathbf{r}, t)$. This effect has several consequences: Because the transverse beam profile of a typical laser usually resembles more or less a Gaussian, there is more energy in its center than at the edges. Different parts of the beam profile therefore see different refractive indices with the maximum in the center. The result is the autofocussing of the beam within the medium (1.6c). If the original beam profile is not smooth but contains several perturbations (local maxima), every one of them suffers from the autofocussing process resulting in a filamentation of the beam. The optical Kerr effect also modifies the temporal form of the pulse envelope. The temporal center of the pulse experiences a higher refractive index due to its higher intensity than the temporal edges. It thus propagates somewhat slower through the medium. This leads to a pulse where the intensity increases slowly in the beginning and drops rapidly after the maximum has been reached. Additionally the spectral phase (see section 2.2) is affected (self phase modulation). For a plane wave propagating along z it is expressed as:

$$\phi(t, z) = kz - \omega t = \phi(t, 0) + 2\pi n \frac{z}{\lambda} = \phi(t, 0) + 2\pi n_0 \frac{z}{\lambda} + 2\pi n_2 \frac{z}{\lambda} I(t, 0) \tag{1.34}$$

In analogy to the derivation of the arrival time of a certain frequency within a spectrally broad pulse in section 2.2 the instantaneous frequency $\omega_{inst}(t)$ of such a pulse is related to its spectral phase via: $\omega_{inst}(t) = -\frac{\partial \phi}{\partial t}$. Thus follows:

$$\omega_{inst}(t) = \omega_0 - \frac{2\pi n_2 L}{\lambda} \frac{\partial I(t)}{\partial t} \tag{1.35}$$

where ω_0 denotes the central frequency of the pulse before entering the nonlinear medium of length L. Before the intensity maximum is reached $\frac{\partial I(t)}{\partial t}$ is positive and therefore the instantaneous frequency will be lower than ω_0. But because the pulse envelope gets also shifted as explained above the intensity rises only gradually and the effect is very small. On the other hand once the maximum has been passed, the intensity falls abruptly thus creating a large negative derivative $\frac{\partial I(t)}{\partial t}$ and a great number of frequencies higher than ω_0 appear in the pulse. In this way the self phase modulation not only rearranges the frequencies within the pulse putting the lower ones to the beginning and the higher ones to the end, it also creates new frequencies on the high-frequency side of the pulse spectrum that were not present before the passage of the nonlinear material (1.6d).

1.3.2 Coherent anti-Stokes Raman Scattering (CARS)

All processes presented so far do not take into account the energy level structure of matter. The medium's role was to provide the nonlinear susceptibility that allows for photon

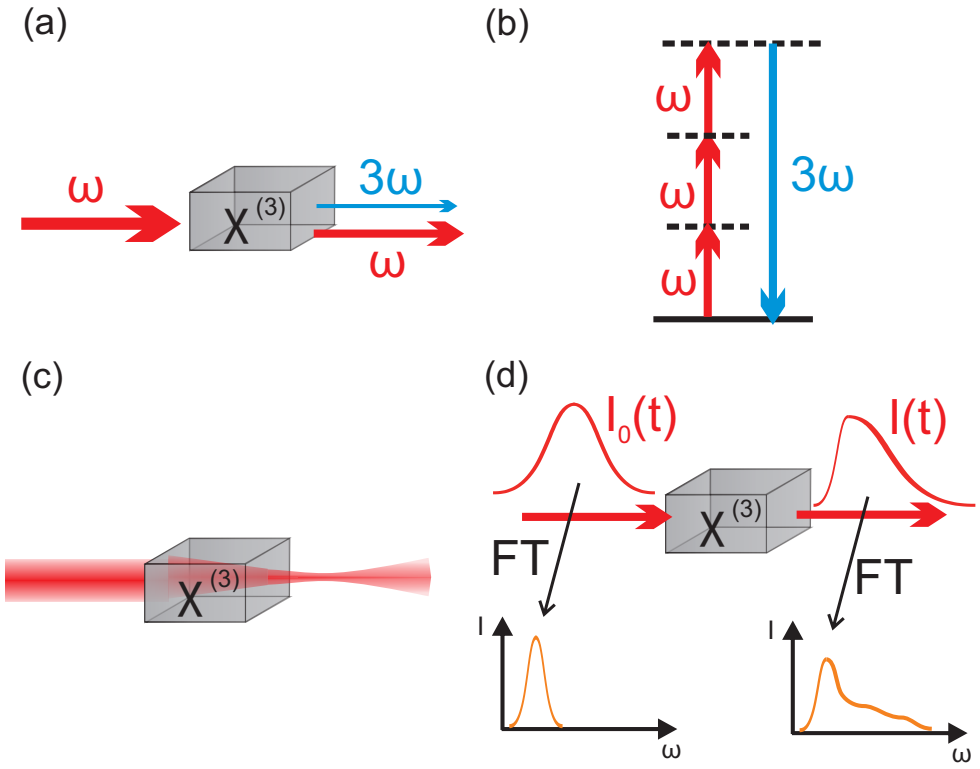

Figure 1.6: Basic third-order nonlinear processes. (a,b) Third-harmonic generation (THG): (a) geometry of the process; (b) energy-level diagram (solid black line: energy ground level; dashed lines: virtual energy levels). (c,d) Optical Kerr effect. (c) autofocalisation; (d) self-phase modulation: intensity maximum gets temporally delayed, and higher frequencies appear in the spectrum (FT: Fourier transformation).

coupling and frequency rearrangements. But the medium itself was never affected, all processes passed via virtual energy levels. This of course is a very incomplete picture, because any material has a large number of energy levels describing electronic, vibrational or rotational states of its constituents. Rotational transitions require only very small energies in the meV-range. Considering that room temperature corresponds already to about 25 meV, these rotational states are almost evenly populated and any rotational transitions induced by external sources such as lasers would be completely masked by the thermal motion. Thus these states can be neglected for the study of nonlinear optics. Transitions that change the vibrational state of a molecule's or crystal's nuclei relative to one another require energies in the 0.1 eV-range, less than contained in optical fields. They can however be addressed by a combination of fields as explained further down. To cause an electronic transition that changes the energy level of the valence electrons finally necessitates energies in the eV-range, about the same amount as provided by optical fields (for example the photons in a laser with a wavelength of 800 nm carry 1.5 eV). Given this abundance of vibrational and electronic levels it is clear that they cannot be discarded when dealing

with nonlinear processes especially when the order of nonlinearity increases and more and more fields get coupled giving access to more and more coupling frequencies. As the energy levels are characteristic for a medium, using them in nonlinear experiments opens up paths for material detection and identification.

One process that attempts to do exactly this is Coherent anti-Stokes Raman Scattering (CARS). It is a combination of two Raman scattering processes. In this mechanism, first discovered in 1928 independently by Landsberg and Mandelstam [102] in the Soviet Union and by the Indians Raman and Krishnan [103], light undergoes a frequency change when scattered in matter. This frequency change can be either positive or negative depending on the state of the scatterer. If the scattering particle is in its ground state, the incident photon can trigger a transition to an excited vibrational state and the energy of the scattered photon will be that of the incident one, reduced by the transition energy, it will be red-shifted. This regime is called Stokes scattering. If on the other hand the scatterer is already in an excited vibrational state, the incoming photon can take up this energy in the scattering process, leaving the particle in its ground state while the scattered photon gets blue-shifted, the anti-Stokes scattering regime. As at room temperature almost all particles are in their vibrational ground states, anti-Stokes scattering is extremely rare compared to Stokes scattering. And in any case, both forms of Raman scattering are much unfavored compared to elastic (or Rayleigh) scattering where neither the photon undergoes a frequency change nor the scattering particle a vibrational transition (Fig. 1.7a).

The cross sections for Raman scattering can however be greatly increased by stimulating these processes. When two optical fields with frequencies ω_p and ω_S are simultaneously present in a nonlinear medium they will couple to generate a field with the difference frequency $\Omega = \omega_p - \omega_S$ (see Fig. 1.5a). If Ω matches a vibrational transition, this transition will be stimulated and the difference field gets absorbed, pumping a great number of molecules into the excited state. The two incident fields are called *pump* and *Stokes* fields because the first lifts the molecule to a virtual energy level from which the second, lower energetic, field then triggers the transition as it would occur in a Stokes scattering process. If then a third, the *probe*, field (at frequency ω_{pr}) interacts with the medium, the anti-Stokes process occurs, resulting in a signal field at ω_{as}. Taken together this is the CARS process (Fig. 1.7b). It is a third-order nonlinear process described by: $\chi^{(3)}(\omega_{as} = \omega_p - \omega_S + \omega_{pr}; \omega_p, -\omega_S, \omega_{pr})$. Although it involves a transition of the molecule through a real state, the process is nonetheless coherent because the anti-Stokes emission is radiated in a coherent way by the probe field and not spontaneous.

As with all non-linear processes, cross sections for CARS are very small and high field strengths are required to generate a detectable signal. These are only provided by pulsed lasers with pulse durations in the picosecond or even femtosecond range. Immediately the difficulty arises to synchronize the three exciting fields so that the pulses from all of them overlap in time, a task far from being trivial given the extremely short pulse durations. This and the general effort to reduce experimental setup complexity have let to the widespread use of the pump laser for the probe field as well ($\omega_{pr} = \omega_p$), so that only two lasers need to be synchronized.

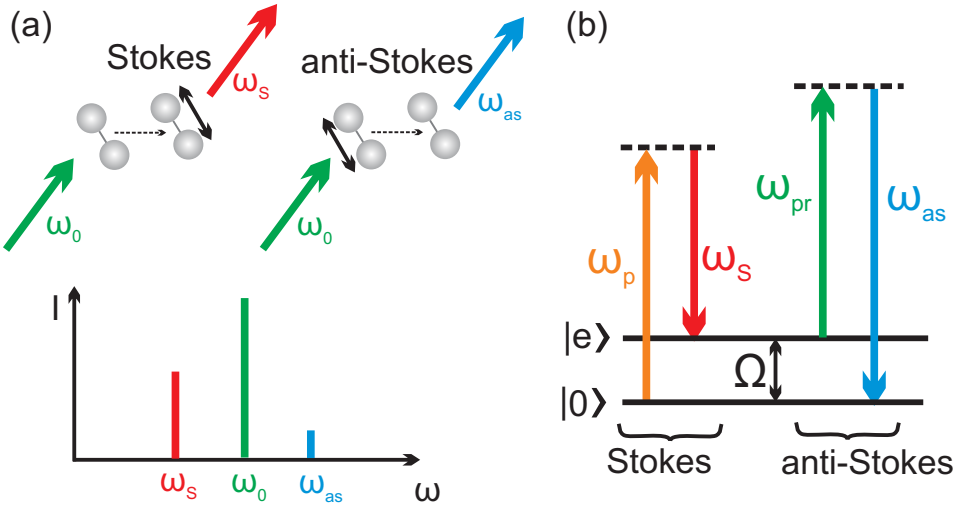

Figure 1.7: Raman scattering and CARS. (a) Raman scattering. Upper left: Stokes scattering; upper right: anti-Stokes scattering (a double arrow designates the vibrational excited state); below: frequency and intensity comparison of Rayleigh (ω_0), Stokes (ω_S) and anti-Stokes (ω_{as}) scattering signals. (b) CARS energy level diagram. $|0>$: energy ground state; $|e>$: excited vibrational state; Ω: vibrational energy; dashed lines: virtual energy levels; incident fields: pump (ω_p), Stokes (ω_S) and probe (ω_{pr}); anti-Stokes signal field ω_{as}.

Beyond that another source of difficulties arises in the CARS process: the non-resonant background. The frequency combination depicted in Fig. 1.7b is not the only one possible. Even if $\omega_p - \omega_S$ equals Ω, a coupling of ω_p,ω_S and $\omega_{pr} = \omega_p$ does not have to pass via the vibrationally excited level $|e>$ as shown in Fig. 1.8a. This combination produces a coherent field at the same anti-Stokes frequency ω_{as} as in the resonant case. A non-resonant process also occurs when $\omega_p - \omega_S$ does not match the resonance frequency Ω (Fig. 1.8b). Both processes constitute the commonly known non-resonant CARS signal, through strictly speaking no anti-Stokes Raman scattering occurs because the scatterers never change their vibrational states during the process. But because these signals always accompany any resonant CARS signal they are treated and named as an ensemble. The total CARS signal can therefore be written, based on Eq. (1.14), as:

$$I_{CARS} = |\chi_R^{(3)}(\omega_{as}):\mathbf{E}_p\mathbf{E}_p\mathbf{E}_S^* + \chi_{NR}^{(3)}(\omega_{as}):\mathbf{E}_p\mathbf{E}_p\mathbf{E}_S^*|^2 \tag{1.36}$$

with $\chi_R^{(3)}$ and $\chi_{NR}^{(3)}$ as the resonant and non-resonant nonlinear susceptibilities, and $\mathbf{E}_p$ and $\mathbf{E}_S$ the pump/probe and Stokes fields.

As the virtual energy levels in these non-resonant processes are usually far away from real vibrational or electronic states of the nonlinear material, $\chi_{NR}^{(3)}$ is frequency-independent. Since it is not involved in any absorption of light, it does not contain an imaginary part. That is of course not true for the resonant nonlinear susceptibility. Because the energy levels in molecules are of a Lorentzian line shape, $\chi_R^{(3)}$ will follow the same behavior,

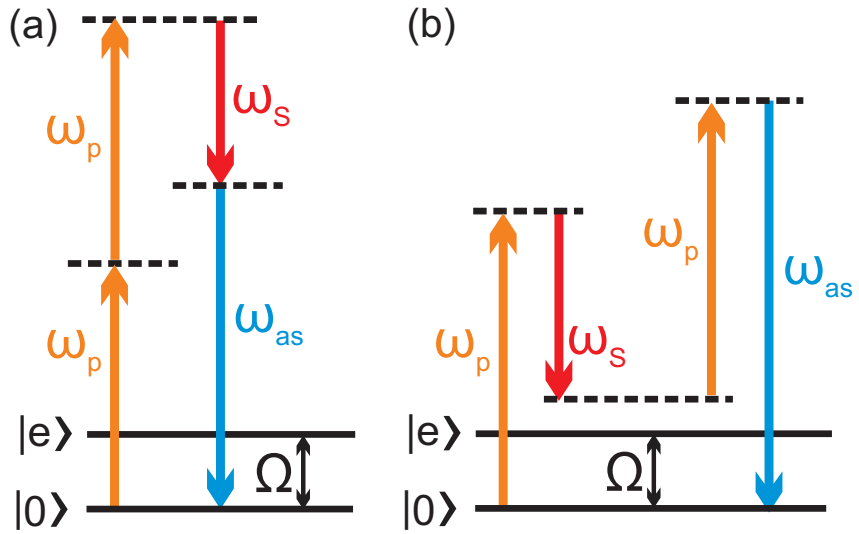

Figure 1.8: Non-resonant CARS energy level diagrams. (a) $\omega_p - \omega_S = \Omega$, but only virtual energy levels (dashed lines) are involved in the creation of the signal at ω_{as}; (b) $\omega_p - \omega_S \neq \Omega$. $|0>$: energy ground state; $|e>$: excited vibrational state; Ω: vibrational energy; incident fields: pump/probe (ω_p), Stokes (ω_S).

resulting in:

$$\chi_R^{(3)} = \frac{a}{(\omega - \Omega_R) + i\Gamma} \tag{1.37}$$

where ω is the beating frequency $\omega_p - \omega_S$ between the pump and the Stokes field. In the resonance case, when ω equals the vibrational transition frequency Ω_R, $\chi_R^{(3)}$ gets maximized, its finiteness assured by the absorption term described by the imaginary part of the expression, where Γ corresponds to the half width at half maximum (HWHM) of the Lorentzian curve. a is the oscillator strength, specific for each vibrational transition. Inserting Eq. (1.37) in Eq. (1.36) then gives:

$$\begin{aligned} I_{CARS} &\propto |\chi_R^{(3)} + \chi_{NR}^{(3)}|^2 = |\chi_R^{(3)}|^2 + 2|\chi_{NR}^{(3)}|\mathfrak{Re}\{\chi_R^{(3)}\} + |\chi_{NR}^{(3)}|^2 \\ &= \frac{a^2}{(\omega - \Omega_R)^2 + \Gamma^2} + 2|\chi_{NR}^{(3)}|\frac{a(\omega - \Omega_R)}{(\omega - \Omega_R)^2 + \Gamma^2} + |\chi_{NR}^{(3)}|^2 \end{aligned} \tag{1.38}$$

The superposition of the fields arising from the resonant and the non-resonant coupling leads to three terms contributing to the measured CARS intensity. The first term in Eq. (1.38) contains the purely resonant term derived from the Lorentzian shape of the resonant nonlinear susceptibility, corresponding thus to the signal in ordinary Raman spectroscopy. It contains all information on the vibrational mode. The second term, proportional to the real part of $\chi_R^{(3)}$, comprises the interference of the resonant and non-resonant contributions. Because both signals are coherent, this term can be considered as heterodyning the resonant contribution with a local oscillator created by the non-resonant field. As opposed to

the resonant term in Eq. (1.38) which is symmetric to the resonance frequency Ω_R, the heterodyne term shows an antisymmetric dependence. The third term, containing exclusively the non-resonant contribution, acts only as a constant offset. The resulting CARS signal from these three terms is depicted in Fig. 1.9a. Typically CARS spectra are obtained by fixing either the pump or the Stokes laser at a certain frequency and tuning the frequency of the other one, thus continuously changing the addressed beating frequency $\omega = \omega_p - \omega_S$. ω is usually expressed in wave numbers (cm^{-1}), which is the inverse wavelength of the molecular vibration. An example of a CARS spectrum is shown in Fig. 1.9b and compared with the corresponding Raman spectrum (Fig. 1.9c). While the Raman spectrum

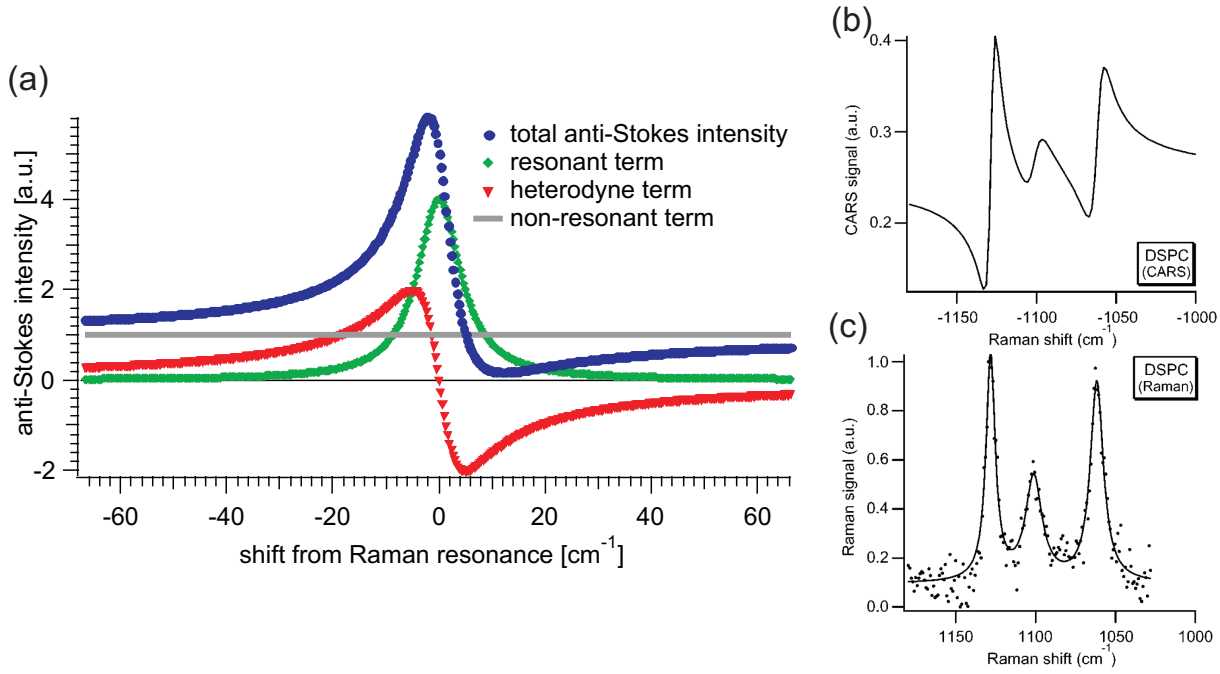

Figure 1.9: CARS spectrum. (a) Different contributions to a CARS spectrum [104]; (b) CARS spectrum of the lipid 1,2-distearoyl-sn-glycero-3-phosphocholine (DSPC) between 1000 and 1200 cm^{-1} with three resonances; (c) Raman spectrum of DSPC in the same wave number range [105].

only contains the resonant contribution, the typical peak-dip structure is clearly visible in the CARS spectrum due to the influence of the non-resonant pathway.

Typical high energetic vibrations, like the C-H stretching mode around 3000 cm^{-1} or the C=O stretching mode around 1750 cm^{-1} often appear as relatively isolated peaks in Raman and CARS spectra. They are exhibited by many substances since they only involve two atoms. To identify an organic compound one has to look into the fingerprint region ($< 1000\,\mathrm{cm}^{-1}$), where low-energetic vibrations can be found that involve more constituents and are therefore characteristic for a certain molecule. Because the number of possible vibrations increases rapidly with the number of participating atoms, this fingerprint region is usually very crowded in vibration bands. To obtain the Raman spectrum, the sample

gets illuminated by a fixed frequency and the Raman scattered photons are detected. Since there is no stimulated process in this case and the underlying cross sections are very tiny, the whole procedure can take very long times, making it unsuitable for microscopy imaging applications. CARS offers a much faster alternative. However, due to the complex signal generation process, CARS spectra are much harder to interpret. Not only do they contain the non-resonant background, the signal shows also a quadratic dependence to the pump power and a linear one to the Stokes beam power. Adding the uncertainties arising for example from unperfect focal volume superposition of the two lasers, it is very difficult to extract quantitative information on scatterer concentrations from CARS measurements, that are immediately accessible in classical Raman spectroscopy. Nevertheless, successful experiments in CARS microscopy have opened up the way to new perspectives, based on different schemes that will be described below an in chapter 5.

As is the case for the nonlinear processes presented so far, the intensity of the CARS emission in a certain direction is strongly tied to phase matching considerations. In analogy to Eq. (1.19) for SHG, the total wave vector mismatch for CARS emitted in the forward direction reads as:

$$\begin{aligned} \Delta k_{fwd} &= |k_{as} - 2(k_p + \Delta k_{\phi_G,p}) + (k_S + \Delta k_{\phi_G,S})| \\ &= |k_{as} - 2k_p + k_S - 2\frac{\pi}{2\lambda_p} + \frac{\pi}{2\lambda_S}| \\ &\approx \frac{\pi}{\lambda_p} - \frac{\pi}{2\lambda_S} \end{aligned} \tag{1.39}$$

with k_p, k_S, k_{as} the wave vectors of pump, Stokes and anti-Stokes beams respectively. As in the case of forward emitted SHG (see page 17) the wave vector mismatch due to the frequency dependence of the refractive index ($k_{as} - 2k_p + k_S$) can be neglected compared to the mismatch caused by the Gouy phase shift. Because $\mathbf{k}_S$ is directed opposite to $\mathbf{k}_p$, the total wave vector mismatch for forward emitted CARS is much smaller than for example in the case of THG. The correspondent coherence length then becomes:

$$l_{c,fwd} = \frac{\pi}{\Delta k_{fwd}} = \frac{1}{\frac{1}{\lambda_p} - \frac{1}{2\lambda_S}} \tag{1.40}$$

The concrete value of $l_{c,fwd}$ depends on the pump and Stokes frequencies used, but it will be contained between λ_p (for $\lambda_S \gg \lambda_p$) and $2\lambda_p$ (for $\lambda_S \to \lambda_p$). In any case this is larger than the distance over which the CARS signal is generated due to the third-order nonlinearity of the process. Therefore CARS is always phase matched in the forward direction. In the epi direction the phase mismatch is stronger:

$$\begin{aligned} \Delta k_{epi} &= |-k_{as} - 2k_p + k_S - 2\frac{\pi}{2\lambda_p} + \frac{\pi}{2\lambda_S}| \approx |2(k_S - 2k_p) - 2\frac{\pi}{2\lambda_p} + \frac{\pi}{2\lambda_S}| \\ &= |2(\frac{2\pi n}{\lambda_S} - 2\frac{2\pi n}{\lambda_p}) - 2\frac{\pi}{2\lambda_p} + \frac{\pi}{2\lambda_S}| = \pi(8n+1)\left|\frac{1}{2\lambda_S} - \frac{1}{\lambda_p}\right| \end{aligned} \tag{1.41}$$

and the coherence length is reduced to:

$$l_{c,epi} = \frac{\pi}{\Delta k_{epi}} = \frac{1}{(8n+1)\left(\frac{1}{\lambda_p} - \frac{1}{2\lambda_S}\right)} \tag{1.42}$$

For a refractive index of $n = 1.33$ it ranges from $l_{c,epi} = 0.09\lambda_p$ (for $\lambda_S \gg \lambda_p$) to $l_{c,epi} = 0.17\lambda_p$ (for $\lambda_S \to \lambda_p$). This means that, as for THG, there is no CARS signal in the epi direction for thick samples (except from backscattering) and only a small one for extremely thin ones.

CARS was first presented by Maker and Terhune in 1965 [106] as a process resulting from the third-order nonlinear susceptibility, though not yet under this name (which does not lack a certain irony considering them working for the Ford Motor Company). In 1973 it was proposed as a concentration measurement tool in gas spectroscopy [107] and shortly afterwards the first successful implementation in liquids was achieved by Begley *et al.* [5]. They profited from the blue shift of the CARS signal relative to the exciting lasers. This allowed them to neatly separate it from the fluorescence background in their samples that is always red-shifted with respect to the excitation. Since the traditional Raman signal appears in the same frequency range as the fluorescence, it would be masked by the latter and thus the use of CARS instead of spontaneous Raman scattering allowed much more precise concentration measurements. Soon, the interest also turned towards CARS microscopy, first proposed in 1982 by Duncan *et al.* [108], but progress was slow due to experimental difficulties. Only in 1999 was the field restarted when Zumbusch *et al.* [9] could benefit from more stable femtosecond laser sources. Since then CARS microscopy has experienced a remarkable growth. The ability of CARS to give an intrinsic contrast in biological samples, especially of lipids, which is, moreover, chemically specific, without the need of prior staining with fluorophores [109, 110] shows its potential for medical diagnostics. It can also be easily combined with techniques like two-photon fluorescence (see section 1.4) due to signal appearance in different spectral regions [111, 112, 113].

To extract quantitative information from a CARS image the resonant part of the signal has to be discriminated against the non-resonant background. Only a selection of all the different possibilities proposed so far will be presented here; for a more complete list the reader can refer to the PhD thesis of D. Gachet [104]. Several approaches attempt to eliminate the non-resonant background altogether. One possibility is to polarize the pump and Stokes beams in different directions (polarization CARS), resulting in differently polarized resonant and non-resonant signal parts that can be selected by a subsequent analyzer [114, 115]. One can also profit from the fact that the non-resonant pathway is instantaneous while in the resonant pathway the system rests for a certain time in the excited vibrational level. By delaying the probe photon with respect to the first pair of pump and Stokes photons the resonant contribution will be generated at a later time than the non-resonant one, and a detector with good temporal resolution can discriminate between these signals (temporal CARS) [116, 117]. Unfortunately these techniques result also in a much weaker resonant signal, so that they are not suited for small concentrations of

scatterers or weak vibrational modes. Therefore it is often not desirable to suppress the non-resonant signal. Instead the extraction of the resonant signal can also be performed by a heterodyne detection, where the CARS signal is mixed with a local oscillator at the same frequency. Modulating the phase of this oscillator allows retrieval of the resonant component [118, 119, 120].

So far CARS was considered as a process, where two lasers at specific frequencies ω_p and ω_S generated the anti-Stokes signal at one specific ω_{as}. To obtain a whole CARS spectrum, it is thus necessary to tune one or both of the incident laser frequencies so that many $\omega = \omega_p - \omega_S$ can be probed. The process is therefore very time-consuming. The availability of spectrally broad lasers in the femtosecond pulse range has offered new possibilities to overcome this limitation. If a spectrally narrow pump pulse is combined with a broad Stokes pulse - multiplex CARS -, the probed CARS region will have the same spectral width as the Stokes pulse with a spectral resolution limited by the width of the pump pulse [105, 121]. If two broadband pulses are used, problems with the spectral resolution of the CARS signal arise, that can be addressed by shaping the pulses. In the easiest case, a linear chirp (see section 2.2) in both pulses can recover some of the resolution because different frequency differences $\omega = \omega_p - \omega_S$ will act on the sample at different times and thus the CARS spectrum can be reconstructed from the signal time trace on the detector [122]. The work of Knutsen *et al.* [123, 124] and Andresen *et al.* [125] followed the same idea. Since femtosecond lasers provide broad spectra, just one single laser can serve simultaneously as pump, Stokes and probe - single pulse CARS -, reducing greatly the experimental complexity by removing the obligation for pulse synchronization and focal volume overlap. On the other hand additional steps have to be taken to spectrally resolve the resonant contribution. Via pulse shaping (see section 2.4) amplitude, phase or polarization features have to be introduced into the excitation spectrum, leading to exploitable signatures in the CARS signal. This approach was first taken by the group of Silberberg [126, 127, 38, 49, 39]. Others followed and developed data treatment algorithms to obtain Raman-like spectra [50, 40]. We used this approach in combination with polarization pulse shaping to measure the Raman depolarization ratio (see chapter 5, where these techniques are more thoroughly described) and to investigate the enhancement of the CARS signal of a solvent in the presence of micrometric dielectric spheres (see chapter 6).

1.4 Incoherent nonlinear processes: Two-Photon Fluorescence (TPF)

While CARS passes via a real vibrational energy level of the nonlinear medium, it remains a coherent process because the final transition again involves a virtual state and thus the emitted signal is coherent to the exciting field. However, as soon as the last traversed level is real, the corresponding process becomes incoherent. This is due to the fact that the system stays for a stochastically distributed time in the real state and thus looses memory of the

exciting conditions, particularly of the phase state of the incident field. All luminescence processes belong into this category. They exist in linear and nonlinear versions. A nonlinear one playing an important role in this work is two-photon fluorescence (TPF). The name is a bit misleading, because it involves a two-photon excitation, followed by an emission of fluorescence. The two-photon absorption step is modeled by $\chi^{(3)}$ and thus TPF can be considered as a third-order nonlinear process as well, which will be explained further down.

But let us first focus on the one-photon excitation fluorescence. When a molecule absorbs a photon it can emit a red-shifted photon some time later, a process called luminescence, encompassing both fluorescence and phosphorescence. Since at room temperature almost all molecules are in their ground states $|S_0\rangle$, the absorption lifts the molecule from the ground state to the first excited electronic state $|S_1\rangle$ [128]. In the excited state, however, the atom cores of the molecule have a slightly larger equilibrium distance R_1 than in the ground state (R_0). Due to the much smaller mass of the electrons compared to the cores, the electronic transition can be considered to be instantaneous compared to the motion of the nuclei, the Franck-Condon principle [129, 130]. This means right after the absorption the nuclei are closer than R_1 and will consequently commence a vibration around the new equilibrium distance. Thus an electronic transition is always accompanied by a vibrational transition. In the case of liquid media, the molecule will relax very rapidly into the lowest vibrational state of the excited electronic state, where the core distance will be R_1, via internal conversion, a radiationless process. From this state the molecule can relax further to its ground state by emission of a photon: fluorescence. Now the transition starts from the core distance R_1, so after the emission the nuclei will vibrate around the new equilibrium distance R_0 which they reach again through internal conversion. Therefore also the fluorescence emission is accompanied by a vibrational transition. The energy of the emitted photon is thus the energy of the absorbed photon minus the energies of the vibrations triggered by the absorption and emission and that is the reason why fluorescence is red-shifted compared to the excitation (Fig. 1.10). Because the internal conversion, occurring on time scales in the picosecond range, is much faster than typical fluorescence lifetimes that amount to tens of nanoseconds, the molecule will have relaxed to the lowest vibrational state before fluorescence occurs. Therefore no matter which is the excitation frequency, the fluorescence almost always originates from this lowest state, making the fluorescence spectrum more or less independent from the excitation frequency (Kasha's rule [131]). But still transitions to many different vibrational levels remain possible resulting in a spectrally broad fluorescence signal.

Quantum mechanical selection rules require that the electron spin configuration of the molecule does not change when absorbing or emitting photons. Because the ground state $|S_0\rangle$ is a singlet state, the various traversed excited states $|S_1\rangle$ are singlet states as well. However, due to strong spin-orbit interaction, transitions into an excited triplet $|T_1\rangle$ state are possible, though they occur very seldom compared to the fluorescence pathway remaining in the singlet system. After this intersystem crossing the molecule will again relax via internal conversion into the lowest vibrational mode of the excited electronic triplet state. A subsequent radiative transition to the ground state requires once more an intersystem

crossing. Because this process is unlikely the lifetimes of excited triplet states are much longer (milliseconds to seconds) compared with those of singlet states. The photons emitted from such a transition are referred to as phosphorescence. Fig. 1.10 gives an overview over both fluorescence and phosphorescence.

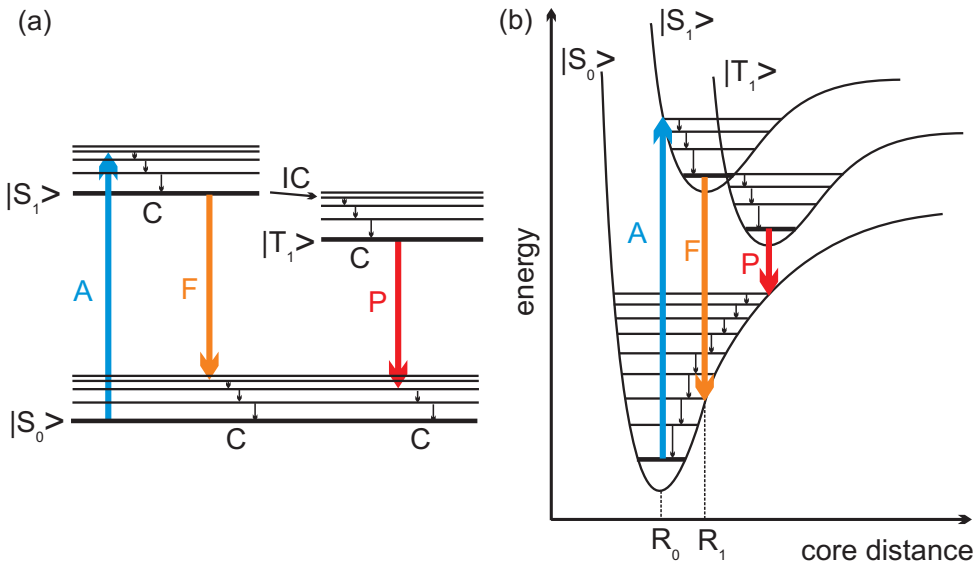

Figure 1.10: Luminescence. (a) energy level diagram. $|S_0\rangle$: ground state; $|S_1\rangle$: first electronic excited singlet state; $|T_1\rangle$: first electronic excited triplet state (all with associated vibrational levels); A: absorption, C: internal conversion, F: fluorescence, IC: intersystem crossing, P: phosphorescence. (b) Illustration of the Franck-Condon principle with potential well model (molecular states as in (a)). Electronic transitions (A,F,P) trigger vibrational transitions due to different core distances for different states (R_0 and R_1: equilibrium core distances for ground state and first excited singlet state respectively).

In one-photon excitation fluorescence a single photon is absorbed by the molecule. The absorption probability A^{1ph} can then be written as:

$$A^{1ph} = |\boldsymbol{\mu}^{01}\mathbf{E}^{\omega}|^2 \tag{1.43}$$

where $\mathbf{E}^{\omega}$ is the incident field at frequency ω and $\boldsymbol{\mu}^{01}$ the molecular absorption dipole oriented in space, describing an electronic transition from the ground state $|0\rangle$ to the first excited state $|1\rangle$. Expressing $\boldsymbol{\mu}^{01}$ in terms of its components leads to:

$$A^{1ph} = |\sum_i \mu_i^{01} E_i^{\omega}|^2 = \sum_{ij} \mu_i^{01}\mu_j^{01} E_i^{\omega} E_j^{-\omega} = (\boldsymbol{\mu}^{01} \otimes \boldsymbol{\mu}^{01}) \cdot (\mathbf{E}^{\omega} \otimes \mathbf{E}^{-\omega}) \tag{1.44}$$

The right part of this equation translates the process into a tensorial expression where $\otimes$ refers to a tensorial product. The product of the absorption dipoles $(\boldsymbol{\mu}^{01} \otimes \boldsymbol{\mu}^{01})$ is a second-rank tensor, the one-photon absorption cross section α, whose components are formed as

$\alpha_{ij} = (\boldsymbol{\mu}^{01} \otimes \boldsymbol{\mu}^{01})_{ij} = \mu_i^{01}\mu_j^{01}$. One-photon absorption is thus governed by the same kind of tensor as the other linear optical processes (see Eq. (1.14)). α is therefore directly related to the linear susceptibility $\chi^{(1)}$. Consequently one-photon absorption is proportional to the intensity of the exciting field, as is also evident from Eq. (1.43).

An electronic excitation can, however, also be achieved by absorbing two photons simultaneously whose combined energy corresponds to the transition energy. The system will pass from the ground state $|0\rangle$ via a virtual state $|v\rangle$ to the excited state $|1\rangle$ (Fig. 1.11a). The two-photon absorption probability thus reads:

$$A^{2ph} = |\boldsymbol{\mu}^{0v}\mathbf{E}^{\omega}|^2|\boldsymbol{\mu}^{v1}\mathbf{E}^{\omega}|^2 \tag{1.45}$$

An analogous treatment as above results in [79]:

$$\begin{aligned} A^{2ph} &= (\boldsymbol{\mu}^{0v} \otimes \boldsymbol{\mu}^{0v} \otimes \boldsymbol{\mu}^{v1} \otimes \boldsymbol{\mu}^{v1}) \cdot (\mathbf{E}^{\omega} \otimes \mathbf{E}^{-\omega} \otimes \mathbf{E}^{\omega} \otimes \mathbf{E}^{-\omega}) \\ &= \gamma \cdot (\mathbf{E}^{\omega} \otimes \mathbf{E}^{-\omega} \otimes \mathbf{E}^{\omega} \otimes \mathbf{E}^{-\omega}) \end{aligned} \tag{1.46}$$

with the fourth-rank tensor γ defined as the two-photon absorption cross section, showing that two-photon absorption is a third-order nonlinear process (see again Eq. (1.14)). To derive the relationship between γ and the third-order nonlinear susceptibility $\chi^{(3)}$:

$$\gamma = \frac{8\pi^2}{c^2\varepsilon}\mathfrak{Im}\{\chi^{(3)}\} \tag{1.47}$$

with the speed of light c and the dielectric constant ε, quantum theory and second-order perturbation theory need to be used as demonstrated by Shen [61].

One and two-photon absorptions follow different selection rules due to the fact that photons are bosons that therefore carry a spin of 1. In one-photon transitions the initial and final state therefore need to show a difference in angular momentum of ± 1, while in two-photon transitions the difference has to be 0 or ± 2. But no matter how the excitation occurred, whether by a one-photon or a two-photon transition, the emission part of the fluorescence process is the same in both cases. The emitted fluorescence field $\mathbf{E}^{em}$ in the propagation direction $\mathbf{k}$ arises from the emission dipole $\boldsymbol{\mu}^{em}$ (itself defined by the transition dipole $\boldsymbol{\mu}_{0F}$ between the ground and the fluorescing state) and follows the dipole radiation behavior:

$$\mathbf{E}^{em} \propto \mathbf{k} \times (\mathbf{k} \times \boldsymbol{\mu}^{em}) \tag{1.48}$$

The complete TPF process is the combination of the two-photon absorption and the one-photon emission parts (Fig. 1.11b and 1.11c), thus the TPF intensity is calculated as:

$$\mathbf{I} \propto |\boldsymbol{\mu}^{abs} \cdot \mathbf{E}|^4|\mathbf{E}^{em}|^2 \tag{1.49}$$

In a standard TPF measurement a great number of fluorophores is present within the focal volume, each at a position $\mathbf{r}$ with an orientation of the absorption and emission

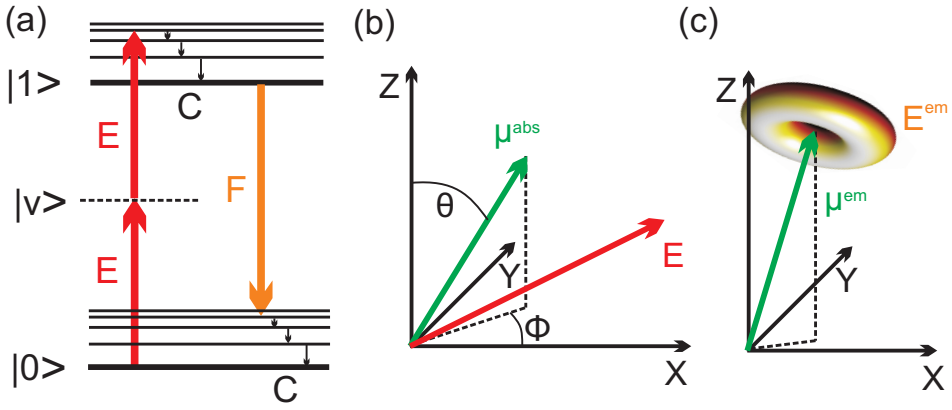

Figure 1.11: Two-photon fluorescence. (a) energy level diagram. $|0\rangle$: ground state; $|1\rangle$: first electronic excited state (both with associated vibrational levels); $|v\rangle$: virtual state; E: excitation field, C: internal conversion, F: fluorescence. (b) absorption: absorption dipole $\boldsymbol{\mu}^{abs}$ oriented along $\Omega = (\theta, \phi)$ in space (X, Y, Z) interacting with excitation field E. (c) emission pattern $\mathbf{E}^{em} \propto \mathbf{k} \times (\mathbf{k} \times \boldsymbol{\mu}^{em})$ from the emission dipole $\boldsymbol{\mu}^{em}$.

dipoles $\Omega = (\theta, \phi)$, described by the orientation distribution function $f(\Omega)$. The TPF intensity in the analyzing direction i (expressed by the unit vector in that direction $\mathbf{u}_i$) is the superposition of all individual intensity contributions:

$$I_i = \int\int\int \overline{|\boldsymbol{\mu}^{abs}(\boldsymbol{\Omega}, \mathbf{r}) \cdot \mathbf{E}(\mathbf{r})|^4} |\mathbf{E}^{em}(\boldsymbol{\Omega}, \mathbf{r}, \mathbf{k}) \cdot \mathbf{u}_i|^2 f(\boldsymbol{\Omega}) \mathrm{d}\boldsymbol{\Omega} \mathrm{d}\mathbf{r} \mathrm{d}\mathbf{k} \tag{1.50}$$

with $\mathbf{E}(\mathbf{r})$ the excitation field vector calculated at the position $\mathbf{r}$. Because the signal gets measured during a fixed time, the average absorption over this period ($\overline{...}$) has been included as well. Note that the summation is exclusively done over intensities, never over fields. This is a consequence of the incoherent nature of the TPF process. The absorption and subsequent internal conversion plus the emission after a stochastically distributed dwell time in the excited state lead to a complete memory loss of the excitation conditions and the emission becomes completely uncorrelated from the state of the excitation field and also the emission from one fluorophore will be uncorrelated from that of another. A coherent buildup, as can occur in coherent nonlinear processes is thus not possible and the TPF signal scales with the number of fluorophores N rather than with its square as in SHG or its cube as in CARS.

The first demonstration of TPF was performed by Kaiser and Garrett in 1961 [132]. Soon afterwards it was used for spectroscopic measurements [3, 4]. In 1990 Denk et al. showed the potential of TPF in microscopy imaging [10]. Since then it has become a standard technique in imaging of biological samples [11, 12, 13, 14, 15]. Many of these applications profit from the fact that TPF can be nicely combined with other nonlinear contrast methods such as SHG. While a laser at frequency ω yields a SHG signal at 2ω, the corresponding TPF signal is red-shifted due to the internal conversion processes within

the fluorophore (Fig. 1.12). Both signals are thus easily separated spectrally. Furthermore

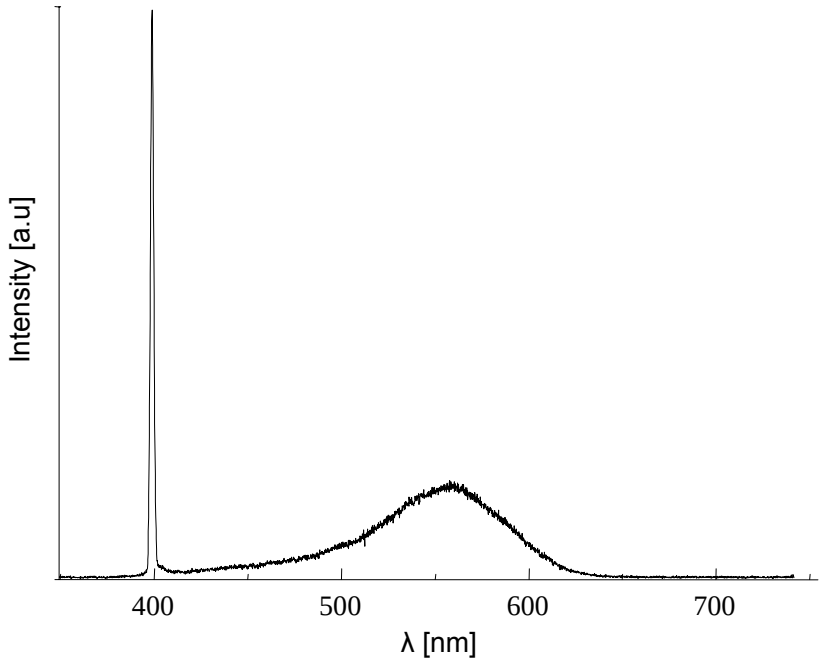

Figure 1.12: SHG and TPF responses of a metallic nanoparticle with a size of 100 nm. Laser illumination at $\lambda = 800$ nm. Strong SHG peak at $\lambda_{SHG} = \lambda/2 = 400$ nm and broad TPF spectrum. The steep right part of the spectrum is due to a bandpass filter cutoff.

TPF active molecular species are often not the same as those radiating strong SHG fields, providing molecular contrast in complex samples.

TPF imaging has also been combined with anisotropy measurements (see chapter 3). In this way the width of the orientation distribution of lipids within the plasma membrane could be determined [133] and it was possible to measure the chirality in collagen fibers [134]. Finally, more complex polarimetric studies (see chapter 3 as well) have allowed retrieving the orientation of molecular samples with complicated symmetries [90] where traditional anisotropy methods fail.

Chapter 2

Pulse shaping

2.1 Introduction

To reach the high energy densities needed to generate nonlinear signals in detectable intensities, the samples are usually excited by pulsed lasers. As opposed to continuous wave (cw) lasers which yield a temporally constant intensity output, in pulsed lasers all the energy is confined into tiny intervals in the picosecond or femtosecond range. To achieve this, thousands of spectral modes within the laser cavity have to be placed in a fixed phase relationship to one another, they have to be mode-locked. Then for most of the time they interfere destructively and the laser output is zero, but at regular intervals (given by the laser repetition frequency) all these modes interfere constructively and produce a short but very intensive burst. Therefore within that pulse all contributing frequencies are present. They can be obtained by calculating the Fourier transform of the temporal pulse profile $\tilde{\mathbf{E}}(t)$:

$$\mathbf{E}(\nu) = \int_{-\infty}^{\infty} \tilde{\mathbf{E}}(t) e^{i\nu t} \mathrm{d}t \tag{2.1}$$

where $\mathbf{E}(\nu) = |E(\nu)|\mathbf{u}(\nu)e^{i\phi(\nu)}$. Each frequency component $\nu = \frac{\omega}{2\pi}$ is described by an amplitude $|E|$, its polarization direction $\mathbf{u}$ and its phase ϕ relative to the other frequencies. In the same way the knowledge of the spectral profile leads directly to the temporal shape of the pulse by an inverse Fourier transformation:

$$\tilde{\mathbf{E}}(t) = \frac{1}{2\pi} \int_{-\infty}^{\infty} \mathbf{E}(\nu) e^{-i\nu t} \mathrm{d}\nu \tag{2.2}$$

Temporal and spectral width are inversely proportional. In the case of a Gaussian temporal profile $\tilde{\mathbf{E}}(t) = E_0 e^{-\frac{t^2}{2\sigma_t^2}} e^{i\nu_0 t}$ around a central frequency ν_0 and a temporal width σ_t the frequency spectrum is a Gaussian as well with a width σ_ν fulfilling the condition $\sigma_\nu \approx \frac{0.16}{\sigma_t}$ (or for full width at half maximum intensity values: $\Delta\nu_{FWHM} \approx \frac{0.44}{\Delta t_{FWHM}}$, where $\Delta t_{FWHM} = 2\sigma_t\sqrt{ln2}$). For a pulse with a width of $\sigma_t = 10\,\mathrm{fs}$ around $\lambda_0 = 800\,\mathrm{nm}$ this corresponds to a spectral width of $\sigma_\nu = 15\,\mathrm{THz}$ or $\Delta\lambda_{FWHM} \approx 80\,\mathrm{nm}$.

Pulse shaping consists in the control of either a pulse's amplitude, its phase, its polarization or a combination of any of these in the time or in the spectral domain. There exist several passive ways to alter the pulse: in an interferometer the pulse can be split in two and the delay between both after the recombination can be controlled. It is also possible to insert an optically transparent material like glass into the beam path which leads to a strong dispersion effect and therefore to the acquisition of a quadratic frequency-dependent phase (see section 2.2) whose magnitude depends on the thickness of the material and its refractive index. While this always leads to a positive quadratic phase (positive dispersion) in a standard dielectric medium, the use of two prisms, two gratings or two chirped mirrors (see section 2.7.1) also allows the introduction of negative dispersion [135]. But none of these techniques allow a refined control of the pulse.

Though active shaping can also be achieved in an interferometric [136] or telescopic [137] setup, most shaping geometries rely on a $4f$-line (see section 2.3) in combination with a spatial light modulator (SLM) based on the birefringence tuning of liquid crystal elements [43, 44, 54, 53, 52, 138, 139] (see section 2.4). Pure phase shaping has also allowed to develop a method for scanningless vertical sectioning in microscopy [137] by temporal focussing of the exciting beam rather than traditional spatial focussing. Amplitude pulse shaping of broadband pulses can be used to selectively excite dyes with different absorption spectra without having to tune the laser emission [36]. Simultaneous phase and amplitude shaping has led to chemical selectivity in single pulse CARS experiments [37, 40]. Polarization shaping was first introduced in coherent control for the optimization of two-photon excitation processes in gases [136, 47, 48], as the sharp spectral bands of anisotropic or aligned atomic transitions are especially adapted to polarized coherent control operations. Soon it was combined with amplitude and phase shaping [140]. But combined amplitude, phase and polarization shaping is not limited to the study of two-photon processes. It has also been used in the correction of polarization distortions in fiber propagation [141], CARS non-resonant background rejection [49], field localization on plasmonic nanostructures [59] and resolution enhancement of THG microscopy [101]. Specific works performed on polarization pulse shaping and single-pulse shaped CARS will be more thoroughly developed in chapters 4 and 6.

2.2 Spectral phase

Because the temporal and the spectral profile of the pulse are directly related by a Fourier transformation, a change in one of them, e.g. in the spectral phase, will automatically affect the other. To gain a better understanding of this relationship let us look at the mean arrival time $\langle t \rangle$ of the pulse:

$$\langle t \rangle = \int t|\varepsilon(t)|^2 \mathrm{d}t = -i \int \varepsilon^*(t) it \varepsilon(t) \mathrm{d}t \tag{2.3}$$

where $\varepsilon(t)$ is the normalized pulse so that $\int |\varepsilon(t)|^2 \mathrm{d}t = \frac{1}{2\pi}\int |\varepsilon(\omega)|^2 \mathrm{d}\omega = 1$. Using the Parseval-Plancherel theorem

$$\int_{-\infty}^{\infty} f^*(t)g(t)\mathrm{d}t = \frac{1}{2\pi}\int_{-\infty}^{\infty} f^*(\omega)g(\omega)\mathrm{d}\omega \tag{2.4}$$

which relates the integrated product of two functions to the one of their Fourier transforms, Eq. (2.3) becomes:

$$\langle t\rangle = \frac{-i}{2\pi}\int \varepsilon^*(\omega) it \varepsilon(\omega)\mathrm{d}\omega = \frac{-i}{2\pi}\int \varepsilon^*(\omega)\frac{\mathrm{d}\varepsilon(\omega)}{\mathrm{d}\omega}\mathrm{d}\omega \tag{2.5}$$

Expressing $\varepsilon(\omega)$ as $\varepsilon(\omega) = |\varepsilon(\omega)|e^{i\phi(\omega)}$ - with $\phi(\omega)$ being the spectral phase - leads to:

$$\langle t\rangle = \frac{-i}{2\pi}\int |\varepsilon(\omega)|\frac{\mathrm{d}|\varepsilon(\omega)|}{\mathrm{d}\omega}\mathrm{d}\omega + \frac{1}{2\pi}\int |\varepsilon(\omega)|^2\frac{\mathrm{d}\phi(\omega)}{\mathrm{d}\omega}\mathrm{d}\omega \tag{2.6}$$

The second term of this expression is real while the first one is purely imaginary. For the mean arrival time of the pulse, which is a real quantity, we can therefore neglect the first term and $\langle t\rangle$ becomes the mean of the spectral phase derivative:

$$\langle t\rangle = \frac{1}{2\pi}\int |\varepsilon(\omega)|^2\frac{\mathrm{d}\phi(\omega)}{\mathrm{d}\omega}\mathrm{d}\omega = \left\langle \frac{\mathrm{d}\phi(\omega)}{\mathrm{d}\omega}\right\rangle \tag{2.7}$$

This means that the arrival time of a specific frequency $\tau(\omega)$ is the spectral phase derivative:

$$\tau(\omega) = \frac{\mathrm{d}\phi(\omega)}{\mathrm{d}\omega} \tag{2.8}$$

Now it is easy to see how a specific spectral phase will change the temporal profile of the pulse. Fig. 2.1 shows a number of phase profiles $\phi(\omega)$, the associated arrival times $\tau(\omega)$ and the corresponding temporal pulse profile $E(t)$. In the easiest case of a constant phase, $\tau(\omega)$ remains unchanged and the pulse envelope is not affected, only the oscillations $e^{i\omega_0 t}$ within are shifted. If the spectral phase is linear ($\phi(\omega) = a(\omega - \omega_0)$), $\tau(\omega) = a$ and all frequencies arrive at time a, so the whole pulse gets shifted in time but its form remains unchanged. A quadratic phase $\phi(\omega) = b(\omega - \omega_0)^2$ results in a linear variation of the arrival times for the different pulse frequencies $\tau(\omega) = 2b(\omega - \omega_0)$. As a consequence the pulse gets stretched in time, meaning that the peak field strength diminishes. This can have very detrimental effects on the efficiency of nonlinear processes as they depend on high field strengths. Quadratic phases are referred to as linear chirp, inspired by birds' songs which also often exhibit fast frequency sweeps. A cubic phase $\phi(\omega) = c(\omega - \omega_0)^3$ has even stronger effects on the temporal pulse shape. Let's assume that c is positive; $\tau(\omega)$ will be a parabola. For $t < 0$ no part of the pulse arrives. Around $t = 0$ a large number of central frequencies appear. Since they carry the largest spectral intensities, the field at that time will be very strong. Later on the frequencies on both sides of the spectrum show up, but they carry less and less energy and the field strength drops. Moreover there are always

two frequencies from different sides of the spectrum present simultaneously, resulting in an interference that will be constructive or destructive depending on the spectral difference. Thus the field's decrease is modulated by the interference's oscillation pattern. More complex phase profiles can be investigated in the same way. It is worthwhile to note that all temporal profiles presented in Fig. 2.1 are created by the same spectral intensity. Just a difference in the spectral phase leads to the substantial modifications in the temporal domain.

The most used of these phases is the quadratic phase. It is acquired by the beam whenever it passes through a dispersive material like glass. As the refractive index is in general wavelength-dependent, different spectral components of the pulse traverse the material with slightly different velocities resulting in a stretched pulse where the frequencies are ordered, red light being faster than the blue, provided the material is normally dispersive. This is nothing else than the acquisition of a quadratic phase. To calculate how strong the stretching will be for a specific quadratic phase let us first consider a Gaussian pulse spectrum with a flat phase: $E(\omega) \propto e^{-\frac{(\omega-\omega_0)^2}{2\sigma^2}}$. A Fourier transformation gives the pulse in the time domain, where it still has a Gaussian envelope of the form $E(t) \propto e^{-\frac{t^2}{2\tau_0^2}} = e^{-\frac{\sigma^2 t^2}{2}}$. Thus $\tau_0 = \frac{1}{\sigma}$. The temporal intensity profile of the pulse is consequently $I_0 = |E(t)|^2 \propto e^{-\frac{t^2}{\tau_0^2}}$. On the other hand, if the pulse possesses a purely quadratic phase:

$$E(\omega) = |E(\omega)|e^{i\phi(\omega)} \propto e^{-\frac{(\omega-\omega_0)^2}{2\sigma^2}} e^{ib(\omega-\omega_0)^2} = e^{-\frac{(\omega-\omega_0)^2}{2}\left(\frac{1}{\sigma^2}-2bi\right)} \tag{2.9}$$

its temporal envelope becomes:

$$E_p(t) \propto e^{-\frac{t^2}{2\left(\frac{1}{\sigma^2}-2bi\right)}} \tag{2.10}$$

and its intensity profile in the time domain calculates as:

$$I_p = |E_p(t)|^2 \propto e^{-\frac{t^2}{\tau_p^2}} = e^{-\frac{t^2}{2\left(\frac{1}{\sigma^2}-2bi\right)}} e^{-\frac{t^2}{2\left(\frac{1}{\sigma^2}+2bi\right)}} = e^{-\frac{t^2}{\frac{1}{\sigma^2}+(2b\sigma)^2}} \tag{2.11}$$

from which follows:

$$\tau_p^2 = \frac{1}{\sigma^2} + (2b\sigma)^2 = \tau_0^2\left(1+\left(\frac{2b}{\tau_0^2}\right)^2\right) \tag{2.12}$$

Replacing the Gaussian variances of the fields with full-width-half-maximum values of the intensities ($\Delta t = 2\tau\sqrt{\ln 2}$) results in:

$$\Delta t_p = \Delta t_0 \sqrt{1+\left(\frac{8b\ln 2}{\Delta t_0^2}\right)^2} \tag{2.13}$$

Figure 2.2 illustrates this relationship for a number of different quadratic phases b. It can

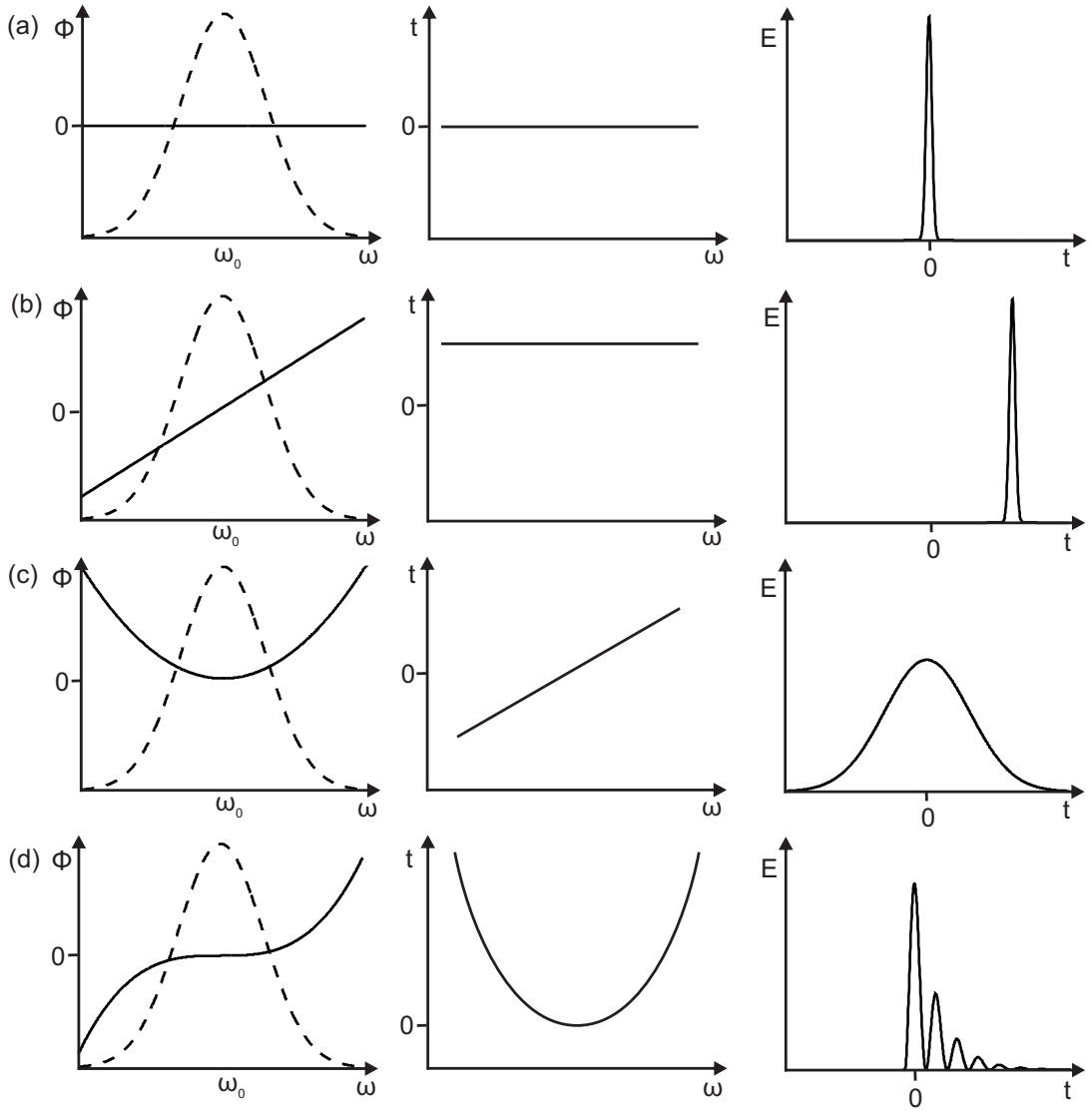

Figure 2.1: Dependence of the temporal pulse profile on the spectral phase. Left column: spectral phase $\phi(\omega)$ (continuous line) and spectral intensity (dashed line); middle column: frequency arrival time $\tau(\omega) = \frac{\mathrm{d}\phi(\omega)}{\mathrm{d}\omega}$; right column: temporal pulse profile $E(t)$ (only the pulse envelope is shown, $e^{i\omega_0 t}$ oscillations are within). (a) flat phase ($\phi(\omega) = 0$); (b) linear phase with positive slope ($\phi(\omega) = a(\omega - \omega_0)$); (c) quadratic phase ($\phi(\omega) = b(\omega - \omega_0)^2$); (d) cubic phase with positive coefficient ($\phi(\omega) = c(\omega - \omega_0)^3$).

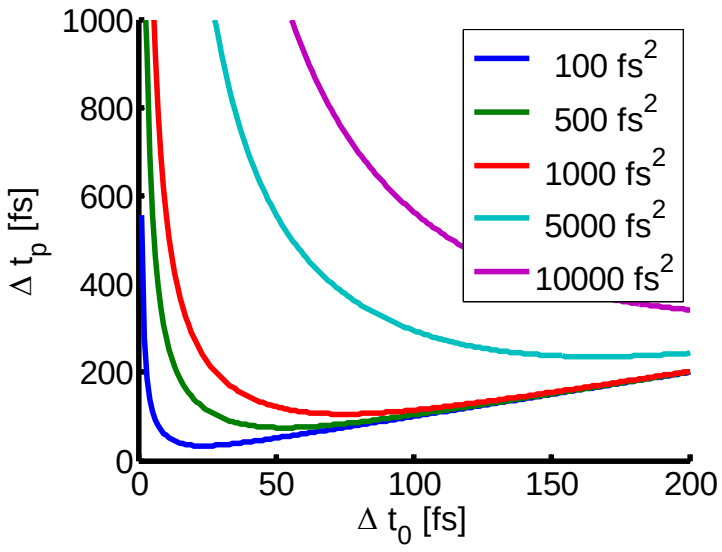

Figure 2.2: Effect of a quadratic phase b on the temporal pulse width Δt_p compared to a the width Δt_0 of a pulse with the same spectral intensity but a flat phase (see Eq. (2.13)).

be seen that the effect is rather small for long pulses ($\Delta t_0 > 200\,\mathrm{fs}$), but very severe for extremely short ones even for small quadratic phase values. While for example a pulse of $\Delta t_0 = 100\,\mathrm{fs}$ only experiences a minimal stretch to $\Delta t_p = 104\,\mathrm{fs}$ when a quadratic phase of $b = 500\,\mathrm{fs}^2$ gets added to it, the same phase will elongate a pulse of $\Delta t_0 = 15\,\mathrm{fs}$ to $\Delta t_0 = 185\,\mathrm{fs}$.

Combining phase shaping with polarization pulse shaping adds a new degree of complexity. When the whole pulse spectrum contains both a polarization component along one axis (X) and another one along a perpendicular axis (Y), a phase can be shaped independently for these two directions ($\phi_X(\omega)$ and $\phi_Y(\omega)$) and thus:

$$\mathbf{E}(\omega) = \begin{pmatrix} |E_X(\omega)|\, e^{i\phi_X(\omega)} \\ |E_Y(\omega)|\, e^{i\phi_Y(\omega)} \end{pmatrix} \tag{2.14}$$

In this way it is possible to encode an arbitrary temporal pulse, where both the polarization and the instantaneous wavelength can be controlled for each instant during the pulse's duration which has been demonstrated by the Brixner group [44, 47, 142] (see Fig. 2.3).

2.3 $4f$-line

If one wishes to spectrally shape a broad laser pulse it is necessary to gain individual access to each spectral component. This is most commonly done by separating them spatially in a $4f$-line [143]. Here, $4f$ designates the total distance a beam has to travel through the shaper, namely four times the focal length f of a lens or curved mirror (Fig. 2.4). In one

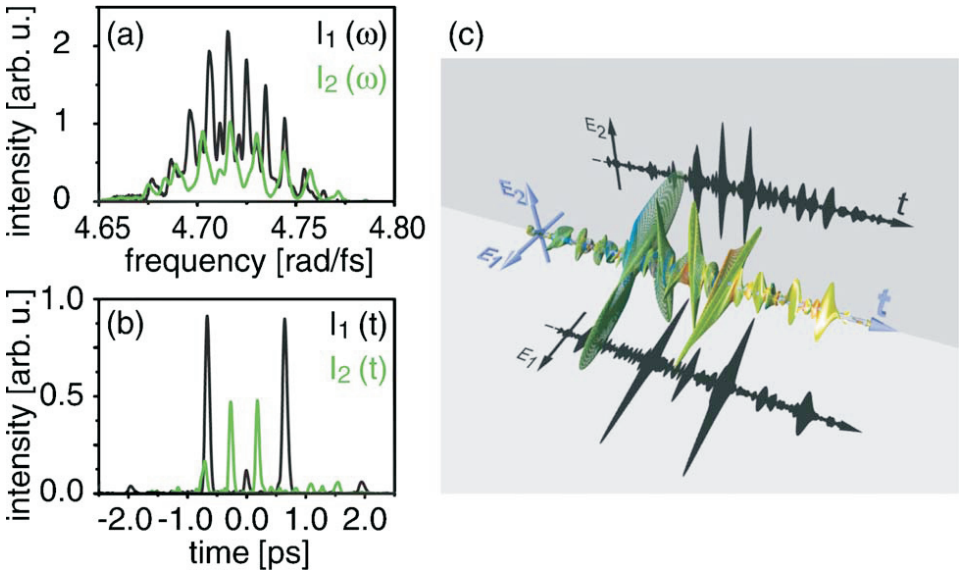

Figure 2.3: Arbitrary temporal pulse profile (c) created by phase and polarization shaping [142]; at each instant during the pulse duration, the instantaneous polarization and frequency (here represented by the color) are controlled. The spectral and temporal profiles are shown in (a) and (b) for both polarization components.

of their foci a grating spatially diffracts the incoming beam and each spectral component gets focused onto a different point in the plane of the opposite focal point, the Fourier plane. Afterwards an identical arrangement recombines the beam again. The result is the exact same beam as at the start; that is why such a configuration is also called a *zero dispersion line*. Beam shaping devices can then be placed in the Fourier plane. The $4f$-line can either be set up with lenses [52] or with curved mirrors (spherical or cylindrical) [43]. A lens-based shaper requires a much longer space ($4f$) for its setup than a mirror-based one ($2f$) making the former often impractical for experimentalists that have to deal with limited space. On the other hand a mirror-based configuration often necessitates the use of additional plane mirrors and leads to beam paths with non-right angles difficult to set up (see Fig. 2.4b) and that can also influence the polarization state in a non-desired way. Due to the large beam surface after the grating, a large collimating element is needed, which favors the use of mirrors, as large mirrors are easier to fabricate and thus much cheaper than lenses of the same size. Additionally, mirrors suffer less from aberrations.

In any case, however, the setup of a $4f$-line is quite tricky because even slight asymmetries between the expanding and recombining parts of the line cause unwanted artifacts in the exiting beam, e.g. different spectral content in different parts of the beam area. This can be avoided by placing a mirror in the Fourier plane to thus using the same optical path for both parts of the $4f$-line [141]. Additionally the whole arrangement gets more compact and less vulnerable to perturbations. On the downside, the reflective configuration is not an option in every case. As will be shown later on, amplitude and phase shaping requires

an exit polarizer while polarization shaping must avoid it. Shall all these properties be controlled, the non-reflection configuration has to be employed.

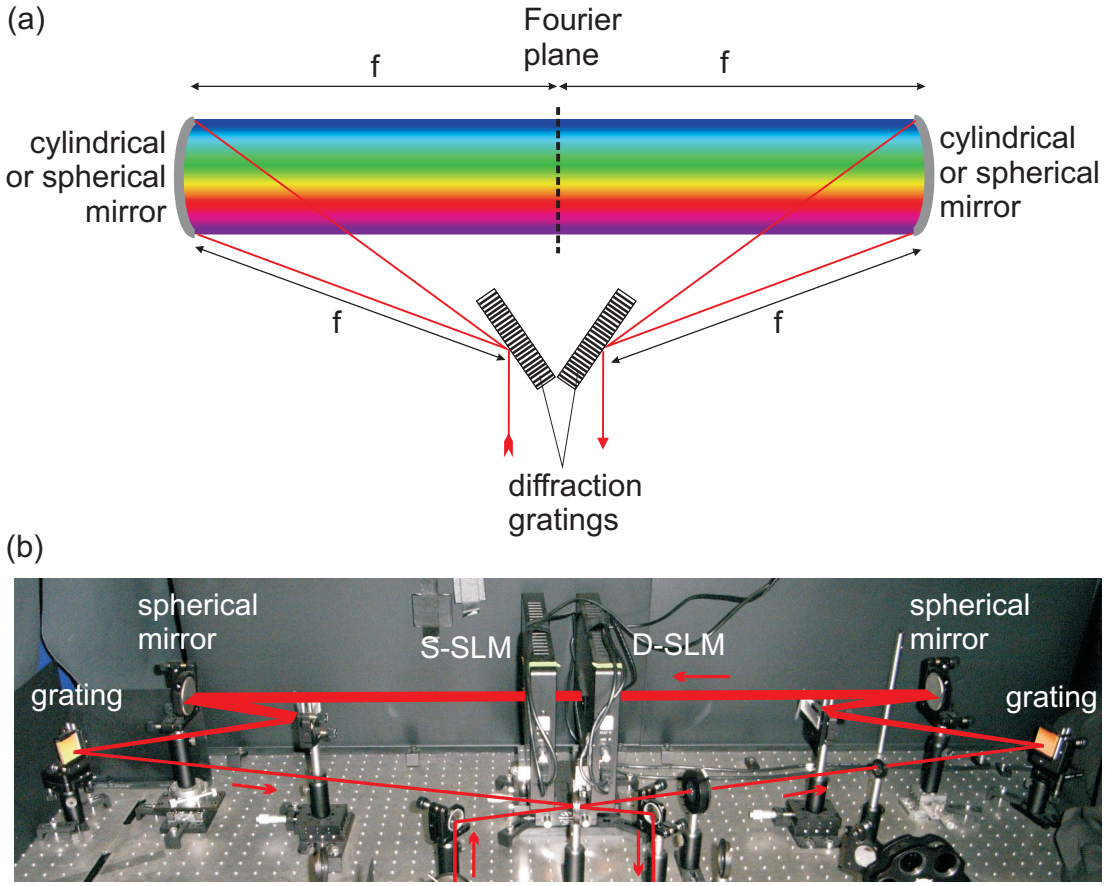

Figure 2.4: $4f$-line. (a) sketch with diffraction gratings and curved mirrors; (b) photograph of the experiment setup used in this work with a drawing of the beam path. For details to the shaping device in the Fourier plane (D-SLM and S-SLM) see section 2.4.

2.4 Amplitude, phase and polarization shaping

Once the beam is spectrally dispersed, a shaping device can be placed in the Fourier plane of the $4f$-line. There exist many different types of shaping devices, Steinmeyer [144], Weiner [145] and Monmayrant *et al.* [146] wrote extensive reviews of them. In the case of a reflective $4f$-line the shaping can be done by a deformable mirror [28] (Fig. 2.5a). Different frequencies have then paths of different lengths resulting in a spectral phase shift. Another option is to insert a phase plate, but this is only a static shaping as the phase plate is fix. For a dynamic shaping it can be replaced with a programmable hologram [26] (Fig. 2.5b). A more frequently used option are acousto-optic modulators. An arbitrary

waveform, synchronized with the repetition rate of the laser is sent into an acousto-optical crystal where it creates a refractive index pattern. This determines the amplitude and phase of the part of the pulse diffracted into the first order of the acousto-optic deflector [24, 25] (Fig. 2.5c). While in a standard acousto-optical device the acoustic wave propagates perpendicular to the optical wave, both are collinear in a variant, the Dazzler [147], that moreover does not need the Fourier plane as the shaping is done in the temporal and not in the spectral domain. The optical wave entering along one of the axes of the acousto-optical crystal is transferred by the acoustic wave to the perpendicular axis. The efficiency of this transfer and thus the amplitude and the phase at the exit of the Dazzler is again controlled by the profile of the acoustic wave.

The most frequently used shaping device are however liquid crystal (LC) spatial light modulators (SLM) [145]. Though they exist in many variations they all function on the same basis: an array or matrix of nematic LC elements. These are birefringent materials. By applying a voltage at two electrodes - usually indium tin oxide (ITO) on a glass substrate - at the sides of the pixel, the LCs alter their orientation and thus change the refractive index along the extraordinary direction while the index along the ordinary direction is not affected (Fig. 2.5d). These proper axes of the liquid crystals may be along the macroscopic horizontal and vertical axes X and Y [52] or form an angle with them of $\pm 45°$ depending on the LC-SLM configuration used [44]. Light traversing the LC therefore acquires a voltage-dependent phase. If a line SLM - consisting of a 1D array of LC elements - is placed at the center of a $4f$-line, each pixel will manipulate one specific spectral component of the pulse. On this basis amplitude, phase and polarization can be controlled.

A problem encountered in LC-SLMs is the pixelation of the device. Usually between the pixels there are small gaps where the light passes unshaped. In the temporal domain this results in a residual peak a $t = 0$ [149] (Fig. 2.6a). Moreover some other undesired effects arise from the pixelation. Even in the Fourier plane of the pulse shaper where the SLM is located, each wavelength present with the pulse occupies a finitely small space so that it happens that certain wavelengths pass more than just one pixel. This causes problems as soon as the voltages applied to neighboring pixels vary considerably. In an amplitude mask for example where one pixel is transparent and its neighbor is not, a frequency component arriving at both of them is not anymore distributed everywhere throughout the beam diameter after passage of the shaper. Thus several wavelengths within the pulse may not spatially overlap anymore [150] (Fig. 2.6b). As a consequence each frequency might be focused differently by an objective which could influence experiments that depend on the absorption of both of these frequency components by the same dipole. At last, the frequency sampling from the pixelation also results in the creation of time replicas of the shaped pulse. These replicas are separated by an interval of $T_0 = \frac{2\pi}{\delta\omega}$, where $\delta\omega$ is the frequency difference between the light traversing neighboring SLM pixels. The intensity of the replicas follows a sinus cardinalis with a period of $\frac{T_0}{1-r}$ where r denotes the space occupied by the SLM pixels relative to the total space (pixels plus gaps) [149, 151]. The pixel gaps lead to time replicas of the residual pulse at $t = 0$, too, but all of these have the same intensity (Fig. 2.6c). Whether these time replicas pose a problem or not in pulse

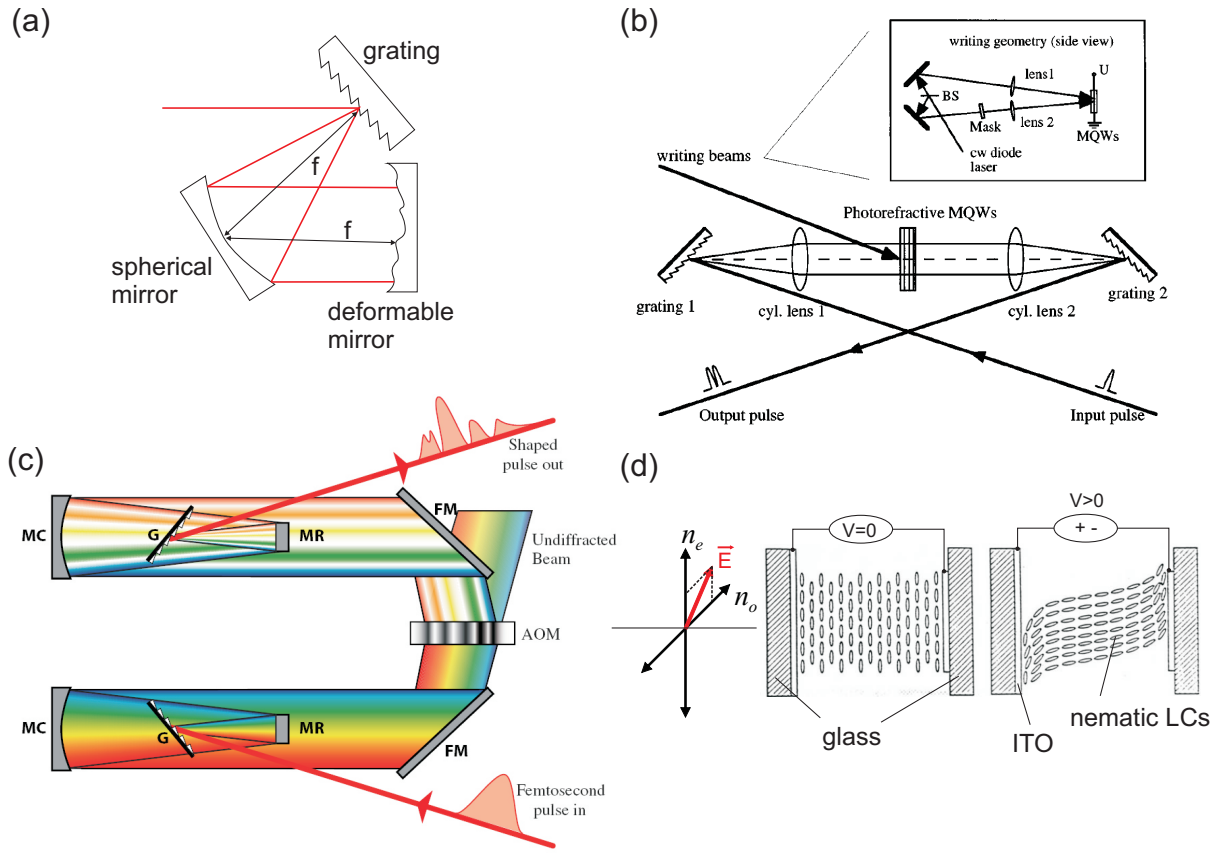

Figure 2.5: Pulse shaping devices in a $4f$-geometry. (a) Deformable mirror in a reflective $4f$-line; (b) programmable holograms created in photorefractive multiple quantum wells (MQW) [26]; (c) acousto-optic device addressed by a radio frequency (RF) generator [146]; (d) nematic liquid crystals (LC) between two electrodes: their orientation and thus the refractive index in the extraordinary direction (n_e) depends on the applied voltage while the index in the ordinary direction (n_0) remains unaltered [148].

shaping experiments depends on the time window T accessible by the shaper. As described above, a linear phase moves the pulse in time, but only within limits due to spatial filtering of the shaper. The width of this accessible window depends on the frequency dispersion in the $4f$-line and is given by [149]:

$$T = \frac{\Delta x_{in} \lambda_0}{cd \cos |\theta_i|} \tag{2.15}$$

where θ_i is the incident angle of the beam with central wavelength λ_0, and Δx_{in} is the lateral dimension of the incident beam (fixed by the diaphragm placed at the entrance of the shaper) on the first diffraction grating with line density $1/d$. c denotes the speed of light. T describes the FWHM of a Gaussian envelope around $t = 0$ that modulates the intensity of shaped beams depending on their temporal shifts (Fig. 2.6d). In our shaper T is smaller than T_0 as calculated in section 2.5.1. Thus time replicas do not concern us

in our shaping experiments.

A LC light valve [152, 153] allows profiting from the pulse shaping capability of liquid crystals without the inconvenience of a pixelation [154]. Instead of a large number of LC elements, only one big liquid crystal gets inserted between the optically transparent electrodes together with a layer of photoconductive $Bi_{12}SiO_{20}$ (BSO) (Fig. 2.6e). The latter changes its conductivity when illuminated with blue/green light, the magnitude of this change depending on the light intensity. This modification alters the tension seen by the LC when a voltage is applied to the electrodes. Thus a light intensity pattern on the BSO induces a spectral phase pattern into the passing laser pulse.

2.4.1 Amplitude and phase shaping

Consider first two line-LC arrays one after the other between two horizontal polarizers which form together a dual SLM (D-SLM). Assume further that the crystal axes of these LC arrays are inclined $\pm 45°$ to the polarizer's direction, so that the ordinary axis of the first array corresponds to the extraordinary axis of the second and vice versa (Fig. 2.7a). In the frame of the optical axes of the liquid crystal the amplitude of the incident electric field $\mathbf{E}_i$ can then be expressed as

$$\mathbf{E}_i \propto \frac{E_0}{\sqrt{2}} \begin{pmatrix} 1 \\ 1 \end{pmatrix} \tag{2.16}$$

after having passed the entrance polarizer, where E_0 denotes the magnitude of the horizontally polarized field. In the LC arrays both field components see different refractive indices n_0 and $n_e(V)$, depending on the applied voltage V that alters the refractive index along the extraordinary axis, and consequently the field acquires a phase proportional to the refractive index difference $\Delta n = n_e - n_0$:

$$\begin{aligned} \Delta\Phi' &= \frac{2\pi}{\lambda} l \Delta n(V') \\ \Delta\Phi'' &= \frac{2\pi}{\lambda} l \Delta n(V'') \end{aligned} \tag{2.17}$$

Here, l is the depth of the LC pixel, $\Delta\Phi'$ and $\Delta\Phi''$ refer to the phases acquired in the first, respectively second LC array and V' and V'' denote the voltages applied to both arrays. Thus the field after both arrays can be written as:

$$\overset{1.\,LC\,array}{\Longrightarrow} \mathbf{E}' \propto \frac{E_0}{\sqrt{2}} \begin{pmatrix} 1 \\ e^{i\Delta\Phi'} \end{pmatrix} \overset{2.\,LC\,array}{\Longrightarrow} \mathbf{E}'' \propto \frac{E_0}{\sqrt{2}} \begin{pmatrix} e^{i\Delta\Phi''} \\ e^{i\Delta\Phi'} \end{pmatrix} \tag{2.18}$$

The fact that the extraordinary axes of both LC array are perpendicular to each other leads to phases $\Delta\Phi'$ and $\Delta\Phi''$ along perpendicular axes as well. The exit polarizer, parallel to the one at the input, projects the field again on the input polarizer direction, which leads to the following expression for the final field E_f:

$$E_f \propto \frac{E_0}{2}(e^{i\Delta\Phi''} + e^{i\Delta\Phi'}) \tag{2.19}$$

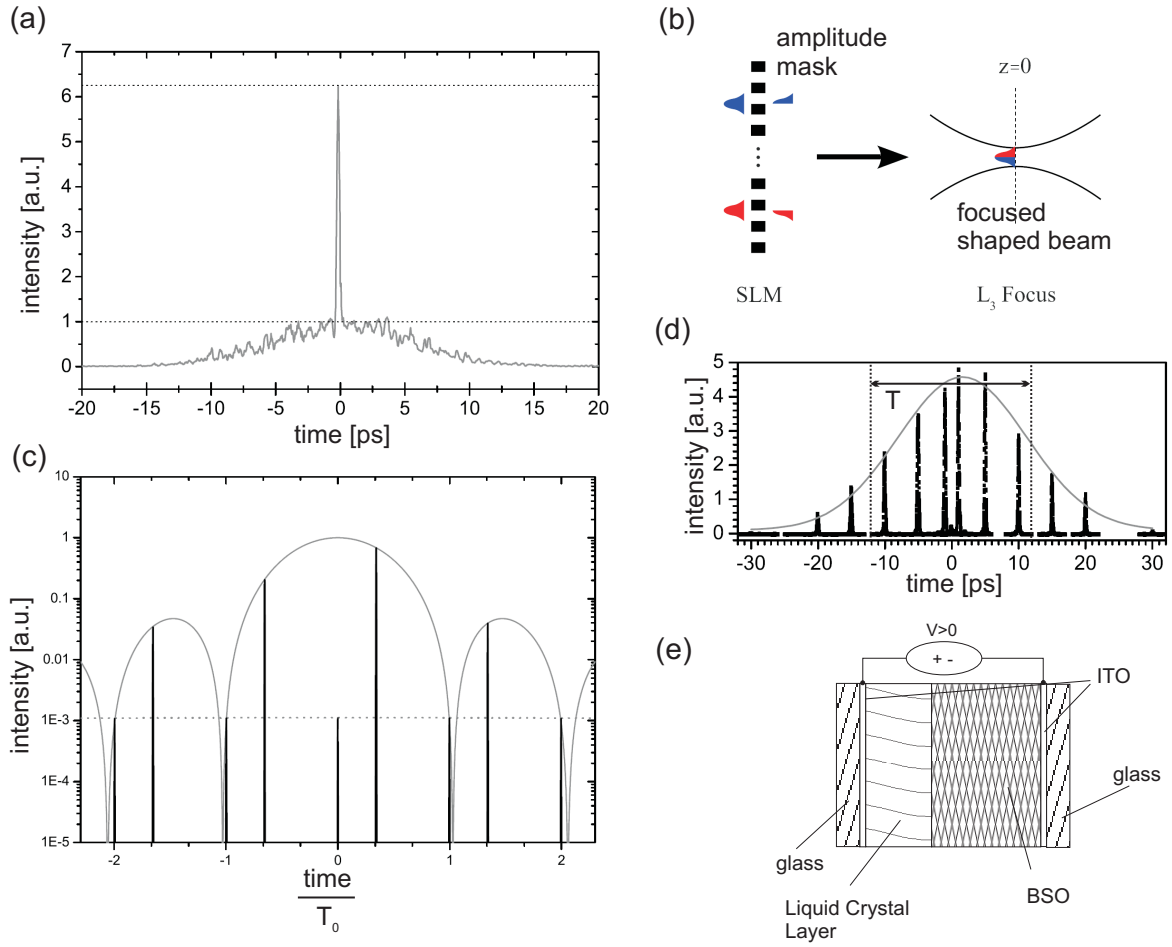

Figure 2.6: Pulse shaper pixelation effects. (a) Peak at $t = 0$ due to the gaps between the SLM pixels (a strong quadratic phase ($7 \cdot 10^5\,\mathrm{fs}^2$) was shaped into the pulse) [149]; (b) frequency do not overlap anymore when they traverse neighboring pixels with strongly varying conditions (here: amplitude mask) [150]; (c) time replicas (black lines) both of the shaped pulse (linear phase to achieve a time shift of 12 ps), modulated by a sinus cardinalis (grey line), and of the residual pulse at $t = 0$ due to the pixel gaps with constant intensity (grey dotted line); $T_0 = 35.8\,\mathrm{ps}$ and $r = 0.97$ [149]; (d) Gaussian envelope (grey) with FWHM T modulating the intensity of shaped pulses (black) shifted in time with respect to the original pulse; here a number of linear phases were applied to realize the time shift [149]; (e) light valve: non-pixelated LC pulse shaper device (explanation in the text).

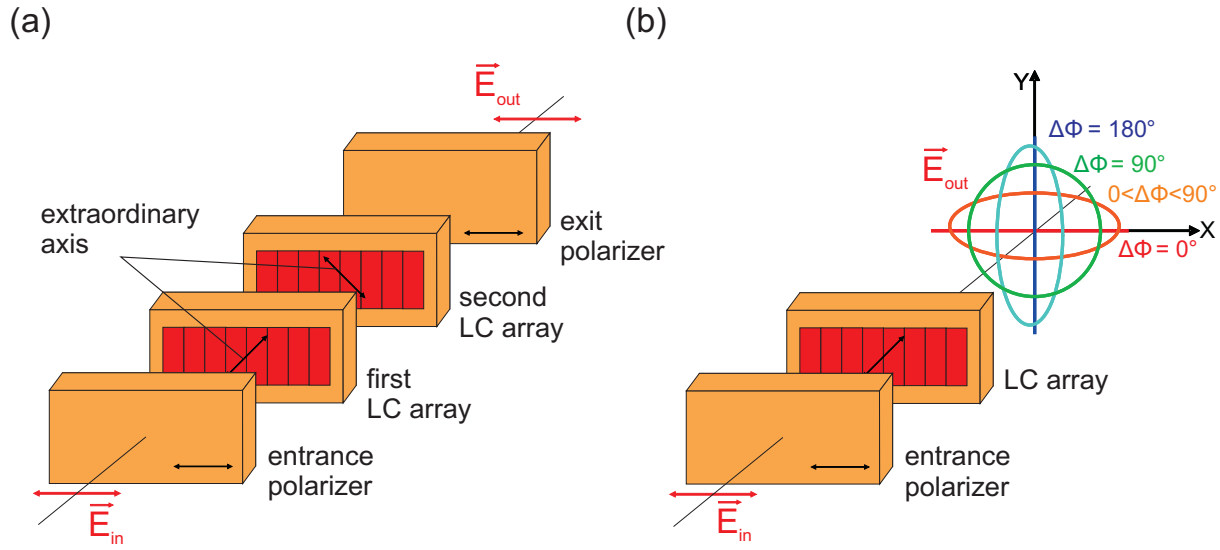

Figure 2.7: LC-SLM device sketch. (a) sketch of a D-SLM for amplitude and phase shaping: between parallel polarizers, two LC arrays are placed, their axes being inclined 45° to the polarizer direction; (b) sketch of a S-SLM for polarization shaping: behind a polarizer only one LC array is placed, its axes as in (a). The different output polarizations mentioned in the text are sketched at the exit.

that can also be written as:

$$E_f \propto E_0 \cos\left(\frac{\Delta\Phi'' - \Delta\Phi'}{2}\right) e^{i\frac{\Delta\Phi'' + \Delta\Phi'}{2}} \tag{2.20}$$

This last expression contains an amplitude term that depends on the difference of the phases introduced in the D-SLM and a phase term containing their sum. Thus independent amplitude and phase shaping is achieved.

2.4.2 Polarization shaping

For polarization shaping a single SLM (S-SLM) with only one LC array is needed whose axes are again inclined 45° to the horizontal polarizer's direction at the entrance, but without an additional polarizer at the exit (Fig. 2.7b). Again a phase $\Delta\Phi$ is acquired by the incoming field E_{in}. In the frame of the optical axes of the liquid crystal, the output field can be written as:

$$\mathbf{E}_{out} \propto \frac{E_{in}}{\sqrt{2}} \begin{pmatrix} e^{i\Delta\Phi} \\ 1 \end{pmatrix} \tag{2.21}$$

Achievable polarization states for the exiting field $\mathbf{E}_{out}$ range successively from linear along the horizontal axis X for $\Delta\Phi = 0°$, elliptical with a major axis along X ($0° < \Delta\Phi < 90°$), circular ($\Delta\Phi = 90°$), elliptical with a major axis along Y ($90° < \Delta\Phi < 180°$), and finally linear along the vertical axis Y ($\Delta\Phi = 180°$).

This scheme allows in particular the creation of pulse profiles with regions of frequencies that are linearly polarized perpendicular to one another. The combination of a D-SLM and a S-SLM therefore permits to manipulate independently amplitude, phase and polarization of the excitation field. A way to characterize the polarization state at the exit of the pulse shaper will be presented on page 106.

As already mentioned polarization shaping can also be preformed in a different configuration. Polachek *et al.* use two consecutive $4f$-line where in the first one amplitude and phase shaping is performed with a D-SLM as described above, while in the second one for polarization shaping the LC-mask is oriented parallel to the incident beam [52]. Together with a waveplate after the shaper a fuller control over the spectral polarization is achieved. In particular it allows achieving elliptical polarizations oriented in directions different from only X or Y.

2.5 Experimental Setup

2.5.1 Excitation path

Our experimental setup is shown in Fig. 2.8a. To be able to perform spectral pulse shaping for the applications described in the following chapters of this work, a laser bandwidth of at least 50 nm is necessary. For this we employ a Ti:Sa laser (Micra, Coherent, Santa Clara, CA) delivering pulses around $\lambda = 800\,\text{nm}$ with a FWHM of up to 100 nm (adjusted by a pair of prisms in the cavity). The repetition rate of the laser is 80 MHz and its typical averaged power 400 mW. A spectrum of this laser is shown in Fig. 2.8b. Note that regular care of the Ti:Sa crystal was required to ensure a stable 80 nm bandwidth, which was our standard working conditions. The spectral phase at the laser exit gets distorted by all following elements in the beam path. This effect is partially compensated by a pair of chirped mirrors (see section 2.7.1). A lens after the laser exit serves to minimize the beam divergence at the entrance of the pulse shaper.

In a $4f$ geometry, a diffraction grating with $n = 600\,\text{lines/mm}$ spatially separates the spectral components that are reflected by a planar mirror onto a spherical one, again creating a parallel beam. The grating period chosen here is relatively low comparing to other existing systems, however it allows a better balance of its polarization response, since we necessitate polarization control in addition to a phase and amplitude one. Around the Fourier plane of the shaper we insert two LC devices (CRI, Woburn, MA): a D-SLM for phase and amplitude control and a S-SLM for polarization control. All three arrays contain 640 nematic LC pixel elements. Each pixel has a width of $98\,\mu\text{m}$ and they are separated by a gap of $2\,\mu\text{m}$. Their height is 5 mm. Afterwards the shaped beam gets recombined by an identical arrangement of spherical mirror, planar mirror and diffraction grating. The spherical mirrors possess focal lengths of $f = 500\,\text{mm}$ and have a diameter of 5 cm.

The dispersion angle of the diffraction grating is given by its line density n. For a blazed grating as used here the sum of the sine of the angle of the incident beam (α) and the angle of the reflected first order beam (β) relative to the grating normal equals $n\lambda$.

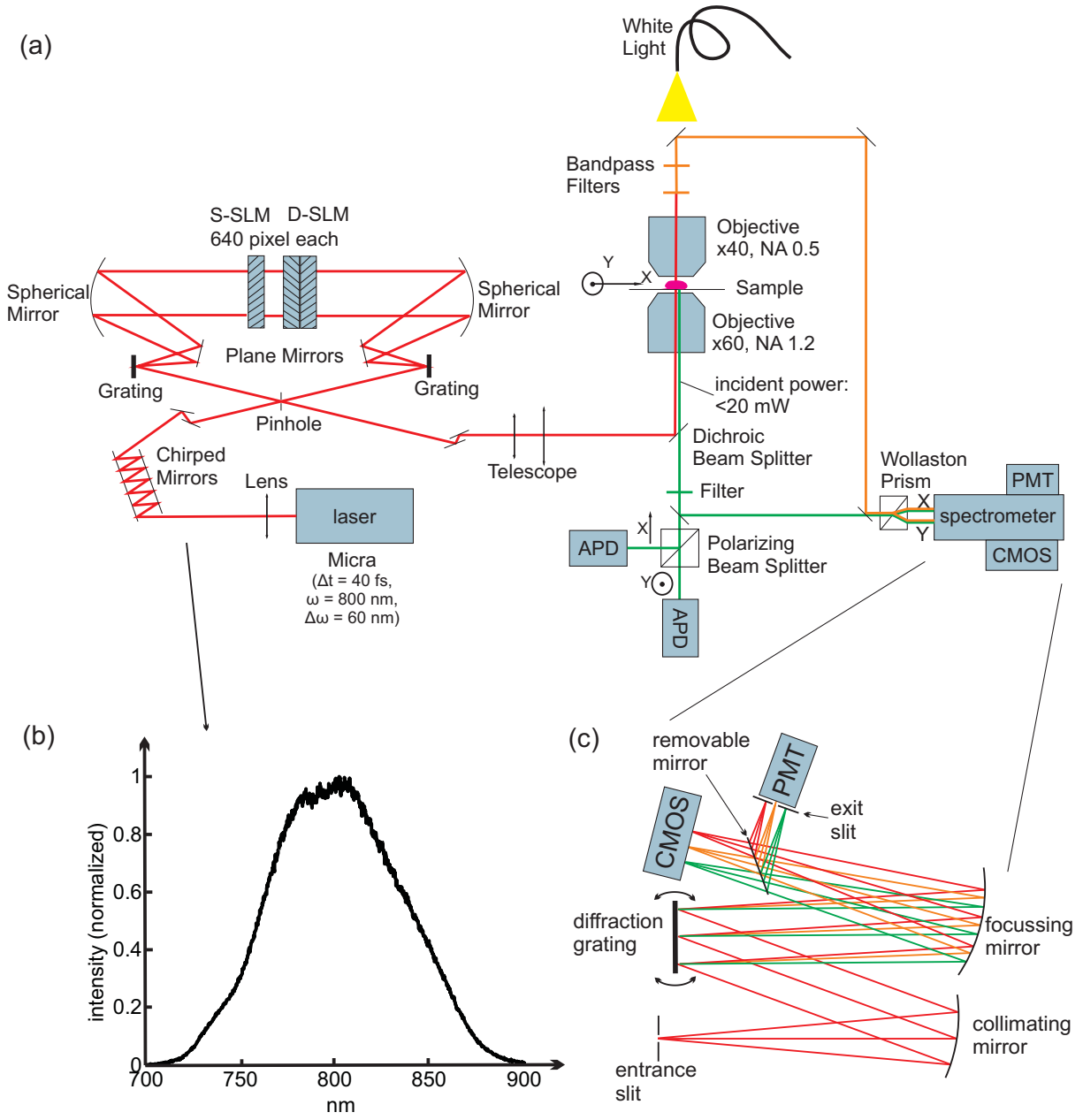

Figure 2.8: Experimental setup. (a) Overview of the whole setup: excitation and detection paths; (b) spectrum at the laser exit; (c) sketch of the spectrometer; a removable mirror allows detecting the signal either with a CMOS camera for whole spectral detection or with a PMT to only detect the central wavelengths around λ_0; λ_0 can be adjusted by slightly rotating the diffraction grating.

As α is the same for all incident wavelengths, only β changes with λ. Between 700 nm and 900 nm, the limiting wavelengths of our pulse, $\Delta\beta$ amounts to 6.9°. For a propagation length of $f = 500\,\text{mm}$ until the spherical mirror this results in a lateral dispersion Δx of $\Delta x = f\,\Delta\beta \approx 6\,\text{cm}$. Given the mirror diameter of 5 cm this means a portion of the pulse spectrum gets lost and only the wavelength region between around 720 nm and 880 nm is directed towards the SLMs. This loss is however not a problem, as in these spectral regions there is hardly any energy present as can be seen in Fig. 2.8b. The lateral extension of the remaining beam of 5 cm corresponds to 500 SLM pixels that get traversed out of the total of 640. Thus the spectral resolution of our shaper is around 0.32 nm per SLM pixel which corresponds to $\delta\omega = 0.9\,\text{ps}^{-1}$.

From this value the expected time period where pulse replicas are expected is $T_0 = \frac{2\pi}{\delta\omega} = 7\,\text{ps}$. On the other hand the time shift accessible by our shaper according to Eq. (2.22) is:

$$T = \frac{\Delta x_{in} n \lambda_0}{c \cos|\theta_i|} \approx 3\,\text{ps} \tag{2.22}$$

as the beam hits the grating at an angle of 5° and has a diameter of about 2 mm. Therefore $T < T_0$, meaning that time replicas do not concern us in our shaping experiments.

Placing both a D-SLM and a S-SLM in this setup requires a considerable distance of about 10 cm in the propagation direction. Therefore a large focal length of the spherical mirrors is necessary to ensure a large Rayleigh distance around the Fourier plane. The spatial resolution in the lateral and axial directions in this plane depends on the numerical aperture (NA) [155]. With $\text{NA} = \sin\theta \approx \theta = \frac{\Delta x_{in}}{2f}$ (the approximation is valid for small angles) and a focal length of $f = 500\,\text{mm}$ this results in NA = 0.002 and thus:

$$\begin{aligned} d_{lat} &= \frac{\lambda}{2\text{NA}} \approx 200\,\mu\text{m} = 2\,\text{SLM pixels} \\ d_{ax} &= \frac{2\lambda}{\text{NA}^2} \approx 40\,\text{cm} \end{aligned} \tag{2.23}$$

calculated for the central wavelength of our pulses of $\lambda = 800\,\text{nm}$. Therefore the large focal length of the mirrors guarantees us enough space in the propagation direction to place both shaping devices without compromising the spectral resolution of the $4f$-line. A consequence of the lateral resolution of almost three SLM pixels is that at least this number of neighboring pixels needs to be addressed to assure a certain amplitude, phase and polarization state of a certain pulse wavelength at the exit of the shaper. This is demonstrated in Fig. 2.9 where it was attempted to eliminate a number of wavelengths from the laser spectrum by amplitude shaping with a variable number of consecutive pixels. At three pixels upward the extinction is seen to be quite good while for one and two pixels there still remains a non-negligible portion of the intensity from the targeted wavelength.

As mentioned above, the relatively low line density of the gratings is chosen to ensure a similar reflectivity for horizontally and vertically polarized light. We measure a 15% reflectivity difference between those components. On the downside this low line density also

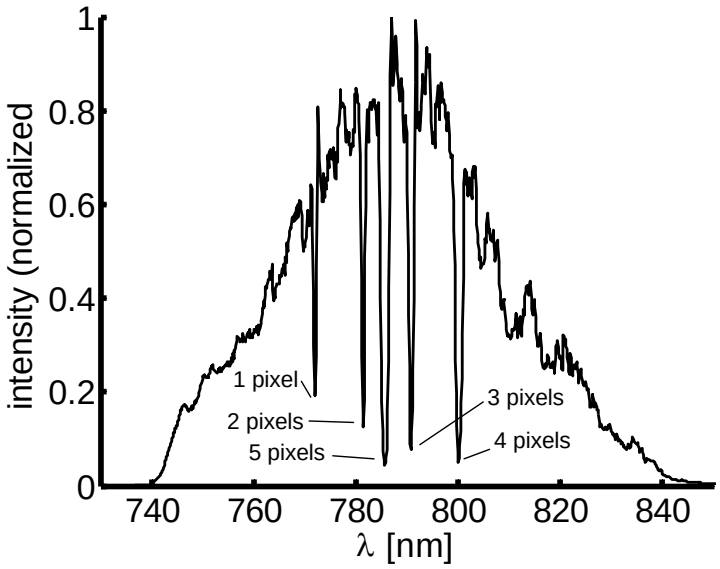

Figure 2.9: SLM resolution. Via amplitude shaping certain wavelengths are removed from the spectrum; when only one or two neighboring SLM pixels are involved in the shaping, the extinction is only partial, from three pixels upward the result is much better.

results in a lower reflectivity of the grating as a whole, we only reach 65%. But because gratings with higher line densities have very different reflectivities for different polarizations, which makes them unsuited for polarization shaping geometries, we opted against them. As a consequence, the overall transmission of the pulse shaper for horizontally polarized light is only 15%, but which is still largely sufficient for many applications. The calibration procedure of the pulse shaper is described in detail in section 2.6 where also spatio-temporal coupling issues are addressed.

Before being sent through the objective to the sample a telescope of two lenses enlarges the beam to completely fill the objective's back aperture. As objectives we either use a high numerical aperture water immersion objective (NA = 1.2, ×60) as in chapter 3 or one with a lower NA of 0.5 (×20) as in chapter 5 (both Nikon, Tokyo, Japan). The incident power, integrated over the whole spectrum can be varied to reach values of up to 20 mW in the sample plane. The sample is placed on a piezoelectric stage (PI, Karlsruhe, Germany) so that it can be scanned in all three dimensions. The dwell time per pixel is 20 ms which translate to an acquisition time of 50 s for an image with 50×50 pixel.

For several experiments in this work spectrally narrow wavelength-tunable laser pulses are required, notably for the calibration measurements in chapter 3 and in the first half of chapter 6. In these cases a different Ti:Sa laser is used (Chameleon by Coherent, Santa Clara, CA). This mode-locked laser produces 150 fs pulses with a repetition rate of 80 MHz, whose center wavelength can be tuned between 680 nm and 1050 nm. This pulse duration corresponds to a spectral FWHM of about 20 nm if the emission is centered around 800 nm.

Additionally an achromatic half waveplate mounted on a step rotation motor serves to rotate the incident polarization direction. See page 101 and Fig. 3.4 for details.

2.5.2 Detection path

For signal detection several contrasts were investigated:

SFG and TPF signals are generally collected in the backward direction through the same objective. Due to their large spectral distance to the excitation beam they can be easily separated from it by a dichroic beam splitter (FF720-SDi01, Semrock, Rochester, NY) and subsequent filters. The dichroic beam splitter is chosen for its low group velocity dispersion as well as its low polarization dichroism factor in the $720 - 880\,\mathrm{nm}$ spectral region (see chapter 3). The signal gets then detected by avalanche photo diodes (APD, PerkinElmer, Waltham, MA) after a polarizing beam splitter divides it into its two polarization components that correspond to the X- and Y- axes in the sample plane. Alternatively the detection can also be performed by an imaging spectrometer (iHR320, Horiba Jobin Yvon, Kyoto, Japan) where a Wollaston prism in front of the entrance performs the polarization splitting. Additional to the spectral detection on a CMOS camera chip, specific wavelengths ($\Delta\lambda \leq 2$ nm) can be detected by a photomultiplier tube (PMT - Hamamatsu Photonics, Hamamatsu, Japan) placed after a mono-channel exit slit (Fig. 2.8c).

CARS signals, on the other hand, have to be collected in the forward direction for two reasons: first, due to phase mismatching only for very small samples (≤ 100 nm) a considerable portion of the generated signal is emitted backwards (see page 29). As soon as the sample gets thicker backward emission is suppressed. Second, single-pulse generated CARS is spectrally very close to the exciting beam and is difficult to separate from it by the dichroic beam splitter (see chapter 5). A spectrally extremely sharp splitter would be needed that at the same time does not affect the phase structure of the reflected incoming laser light. An objective (NA = 0.5, $\times 40$, Zeiss, Oberkochen, Germany) collects the signal and transfers it via several sharp bandpass filters for laser light rejection to the spectrometer entrance where again a Wollaston prism performs the polarization splitting.

Additionally in this microscope, white light illumination is used to identify and position macroscopic objects in the sample plane.

2.6 Pulse shaper calibration

The above described pulse shaper only reaches its full potential when it is carefully calibrated. This consists of two major parts: first, the $4f$-line needs to be well aligned to assure a parallel beam at the shaper exit where all pulse wavelengths are homogenously distributed within the beam diameter (and well recombined by the second grating), and second it has to be established which wavelength traverses which pixel and which applied voltage to this pixel leads to which acquired phase by the beam.

A perfect $4f$-alignment is a challenging task. Not only both gratings need to be positioned exactly in the focal points of the spherical mirrors, but also both the expanding

and the recombining branches of the shaper must be perfectly symmetric. Considering the numerous non right-angled reflections in the setup (see Fig. 2.4b), achieving this symmetry is far from trivial. The joined diaphragm that the beam has to pass before entering and after leaving the shaper facilitates the task. The low divergence of the beam is established by measuring the beam diameter on the whole path from the pulse shaper exit to the microscope and adjusting the positions of the gratings and mirrors in the $4f$-line until the beam diameter stays constant.

Even in a well collimated exiting beam there may be remaining inhomogeneities in that different wavelengths show different spatial distributions within the beam diameter. This is usually the effect of an imperfect positioning of the second diffraction grating. We checked the beam homogeneity in several ways. First we sent the beam after the pulse shaper exit to a screen several meters away and expanded it with lens with a high focal length. In this way a spot with a diameter of more than 10 cm is seen. Then we continuously moved an absorbing plate in the Fourier plane of the shaper, thus selectively cutting an increasing wavelength region. A well aligned $4f$-line is characterized in this case by a homogeneous extinction of the spot on the screen over its whole area. Were the wavelengths distributed differently relative to one another, the extinction would sweep over the spot from one side to the other. The position of the second grating (and partially the alignment of the mirrors in the recombining part of the shaper) was then adjusted to obtain the best homogeneity.

For a finer alignment we repeated the procedure, but this time not with a far away screen, but at the focus of the microscope objective. There we put a thin glass slide and sent the reflected laser light to a camera for detection. When the objective is focused on the glass surface only a bright spot is seen. But as soon as the focal plane is a bit below or above the glass slide a ring pattern appears. Now the extinction is observed again when an absorbing plate gets moved into the Fourier plane of the objective. The grating's position is readjusted so that the extinction is uniform and not moving from one side of the pattern to the other. After these steps the $4f$-alignment should be sufficient.

In a last test we measured the point-spread functions (PSF) of our beam as a whole and of various narrow spectral regions therein. The PSF of an imaging system describes the response to a point source. It is thus the size of the focal volume that is governed both by the numerical aperture (NA) of the objective and by the illumination profile of the beam. For an ideal PSF the beam needs to overfill the objective's back aperture. Should it only fill a part of it, the PSF increases compared to the ideal case. By measuring the PSF for different spectral regions within the pulse it is possible to obtain an information on the spatial distribution of different wavelength regions within the beam diameter and thus assess the quality of the alignment of the $4f$-line.

To image a PSF one needs a point source compared to the size of the PSF itself. An ideal PSF is diffraction limited and has therefore transverse dimensions of the size of half the used wavelength which in our case are several hundred nanometers. Nanometric objects below 50 nm can therefore considered to be point sources for our purpose. We use two-photon fluorescent nanospheres with a diameter of 20 nm dispersed on a glass slide. The emitted TPF signal is collected by the APDs mentioned above. We perform a XY- and

a XZ-scan of a single nanosphere (Z refers to the propagation direction of the beam and X and Y are the transverse dimensions). The question arises how a single nanosphere can be identified as their sizes are far below the diffraction limit. In the case of several nanospheres that are close to one another the recorded signal does not resemble that of a PSF which can be approximated by a 3D-Gaussian but often shows different forms in one of several dimensions. Additionally, the more nanospheres are present within the focal volume, the higher is the emitted TPF signal. Thus by singling out weaker isolated spots it can be assumed with high certainty that only one nanosphere is present therein.

The scanning is done for different wavelength regions. They are selected by blocking the unwanted wavelengths with black cardboard in the Fourier plane of the pulse shaper. Fig. 2.10 shows both the XY- and the XZ-scans for an illumination with light between 790 nm and 810 nm. Additionally the sections through the center of the spot and the corresponding Gaussian fits are depicted for all three dimensions. Table 2.1 gives the widths

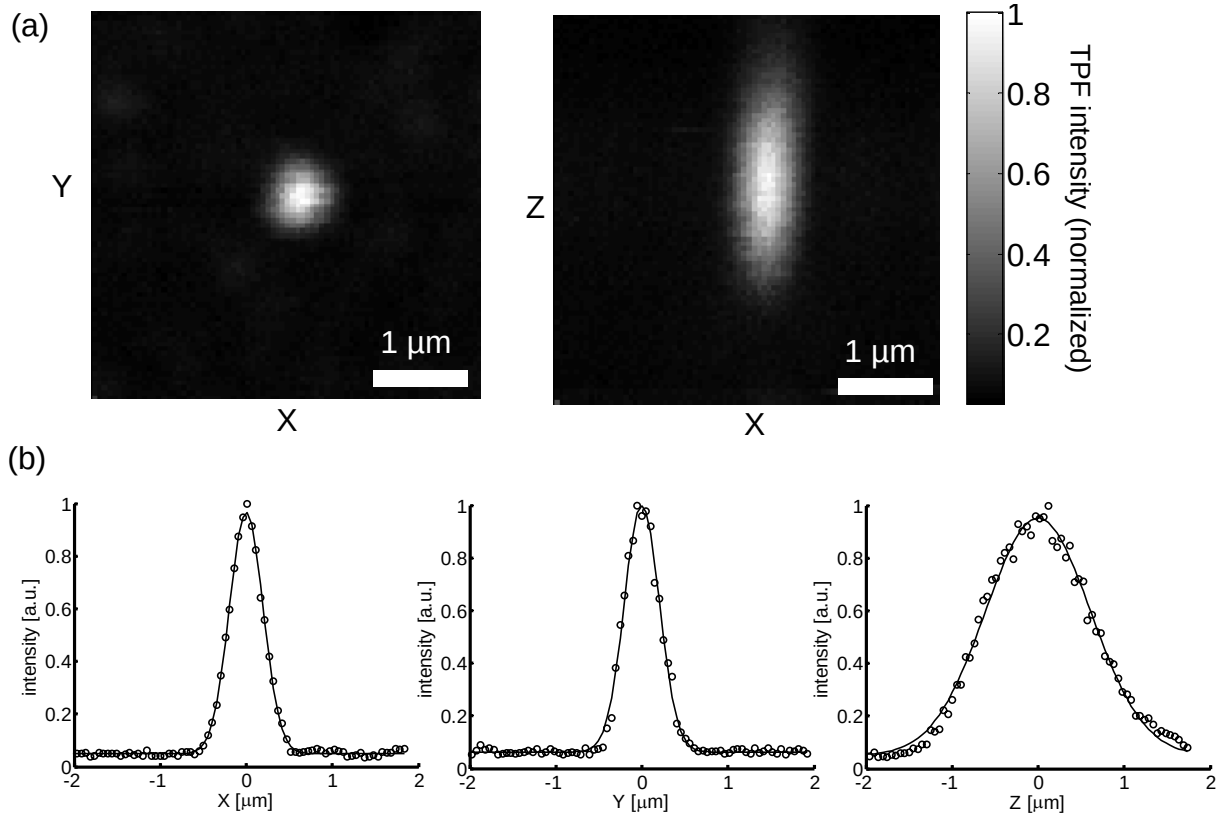

Figure 2.10: Measurement of the PSF. (a) XY- and XZ-scanning images of a fluorescent nanosphere with a diameter of 20 μm. (b) Sections through the center of the spot in (a) in all three dimensions (circles) and the corresponding Gaussian fit (solid line).

of the Gaussian fits of Fig. 2.10b as well as for those at all other tested wavelength regions. The values between 770 nm and 830 nm are well in accordance with each other and also correspond to the size of a ideal PSF for an objective with NA = 1.2 and an illumination

$\lambda\,[nm]$	$\sigma_X\,[\mu m]$	$\sigma_Y\,[\mu m]$	$\sigma_Z\,[\mu m]$
770-790	0.29	0.33	0.89
790-810	0.28	0.29	0.86
810-830	0.27	0.32	0.88
830-850	0.27	0.43	1.10

Table 2.1: Gaussian widths σ of the PSF for several wavelength regions present within the laser spectrum.

around 800 nm. This indicates that these wavelength are homogenously distributed within the transverse beam profile. For larger wavelengths, σ_Y and σ_Z increase, showing that at this spectral side the spatial distribution is less perfect. But because in this region there is only very little power remaining, it does not significantly influence the experiments that will be described in this thesis.

After the $4f$-line is well aligned the SLMs need to be calibrated. For this we only regard the S-SLM in a first step. A polarizer is placed at its exit that has the same orientation as the one at the entrance. In this way we transform the polarization shaping SLM into an amplitude shaper as only those exit polarizations along X in Fig. 2.7b can pass. This is expressed mathematically when the field in Eq. (2.21) gets multiplied with a projection function $\mathbf{u}$ of the polarizer, which in the frame of the optical axes of the LC array (that are inclined $\pm 45°$ to the polarizer's direction (X)) reads as $\mathbf{u} = \frac{1}{\sqrt{2}} \begin{pmatrix} 1 \\ 1 \end{pmatrix}$. Consequently the final field E_f becomes:

$$E_f = \mathbf{E}_{out} \cdot \mathbf{u} \propto \frac{E_{in}}{\sqrt{2}} \begin{pmatrix} e^{i\Delta\Phi} \\ 1 \end{pmatrix} \cdot \frac{1}{\sqrt{2}} \begin{pmatrix} 1 \\ 1 \end{pmatrix} = \frac{E_{in}}{2} \left(1 + e^{i\Delta\Phi}\right) \tag{2.24}$$

The corresponding field intensity I_f is expressed as:

$$\begin{aligned} I_f = |E_f|^2 &\propto \frac{E_{in}^2}{4} \left(1 + e^{i\Delta\Phi}\right)\left(1 + e^{-i\Delta\Phi}\right) = \frac{E_{in}^2}{4} \left(2 + e^{i\Delta\Phi} + e^{-i\Delta\Phi}\right) \\ &= \frac{E_{in}^2}{2} \left(1 + \cos i\Delta\Phi\right) \end{aligned} \tag{2.25}$$

Thus induced phase shifts of $0, 2\pi, 4\pi, ...$ lead to maximal transmission while it is minimal for phase shifts of $\pi, 3\pi, 5\pi, ...$ Now we continuously change the applied voltage to all pixels in the same way and record a spectrum of the transmitted beam. The voltage can be varied between 0 and 10 V in discrete steps, the so-called drivecounts, with one drivecount corresponding to 2.44 mV. Fig. 2.11a shows an exemplary response of a SLM pixel when the drivecounts are varied between 0 and 4000. The graph has been normalized so that it fills the interval [0 1] which corresponds to the division by the incident field intensity $|E_{in}|^2$. For each wavelength this curve looks slightly different because the refractive index n is wavelength dependent and therefore the conditions when a certain phase shift is reached

are different for each wavelength. The two maxima correspond to $\Delta\Phi = 2\pi, 4\pi$ and the two minima to $\Delta\Phi = \pi, 3\pi$. From this curve it is clear that $\Delta\Phi$ does not follow the drivecounts in a linear way. For example between 2000 and 4000 drivecounts there is no extrema, while there are four of them between 500 and 2000 drivecounts.

The phase shifts can be extracted from these graphs by Eq. (2.25), setting E_{in} to 1:

$$\Delta\Phi = \arccos\left(2I_{norm} - 1\right) \tag{2.26}$$

where I_{norm} is the normalized intensity as explained above. Fig. 2.11b depicts $\Delta\Phi$ for the same λ as in Fig. 2.11a. To obtain this curve $\Delta\Phi$ in Eq. (2.26) still has to be unwrapped as the arccos operation only gives values in the interval $[0\ \pi]$. As mentioned before the attainable values of $\Delta\Phi$ differ slightly for each λ, but for all wavelengths within our laser pulse the phase shift range $[0.6\pi\ 4.3\pi]$ can be achieved.

So far we only looked at a certain spectrometer pixel to produce the curves in Fig. 2.11a and 2.11b which give the λ-drivecount-$\Delta\Phi$-relationship. Now it still needs to be related to the pixels of the SLM. We achieve this by using again the amplitude shaping capabilities of the S-SLM. All SLM pixels are put to the same drivecount value of 1300. In this region most of the field can pass for all wavelengths (see 2.11a). Of course this does not mean that there is maximal transmission for this value, but this is not necessary. Now we change the drivecounts for a number of isolated pixels in such a way that the transmission drops for these pixels. Fig. 2.11c shows the resulting spectral measurement. Again it is not necessary that the transmission gets minimal, it suffices that a clear drop is seen in the spectrum. From the knowledge of the spectral position of these drops and the SLM pixel numbers where the drivecounts were changed, we calculate the pixel-λ-relationship of our shaper as shown in Fig. 2.11d and fit it with a linear function. In the depicted case the fit gives:

$$\text{pixel} = m\lambda + n = -3.13\,\text{nm}^{-1}\,\lambda + 2841 \tag{2.27}$$

from which follows that between two neighboring SLM pixels a wavelength difference $\Delta\lambda$ of $\Delta\lambda = \frac{1}{m} = 0.32\,\text{nm}$ exists as already deduced before.

Once the S-SLM is placed and calibrated the D-SLM has to be aligned. Because both LC arrays therein are identical to the one in the S-SLM, the λ-drivecount-$\Delta\Phi$-relationship of the S-SLM applies as well for the D-SLM. To place the D-SLM correctly into the Fourier plane a similar procedure is performed as the one that determines the pixel-λ-relationship. For the same pixel position in the D-SLM and the S-SLM the drivecount value is varied so that a drop in the laser spectrum can be seen. Then the lateral position of the D-SLM in the Fourier plane is adjusted by a micrometer screw so that both drops coincide at the same spectral position. Once this is done, the exit polarizer on the S-SLM is removed to switch from amplitude shaping to polarization shaping mode and the pulse shaper is ready for operation.

It should be noted that the pixel-λ-relationship may change during time. Each setup has slight instabilities and the numerous optical elements from the laser up to the Fourier

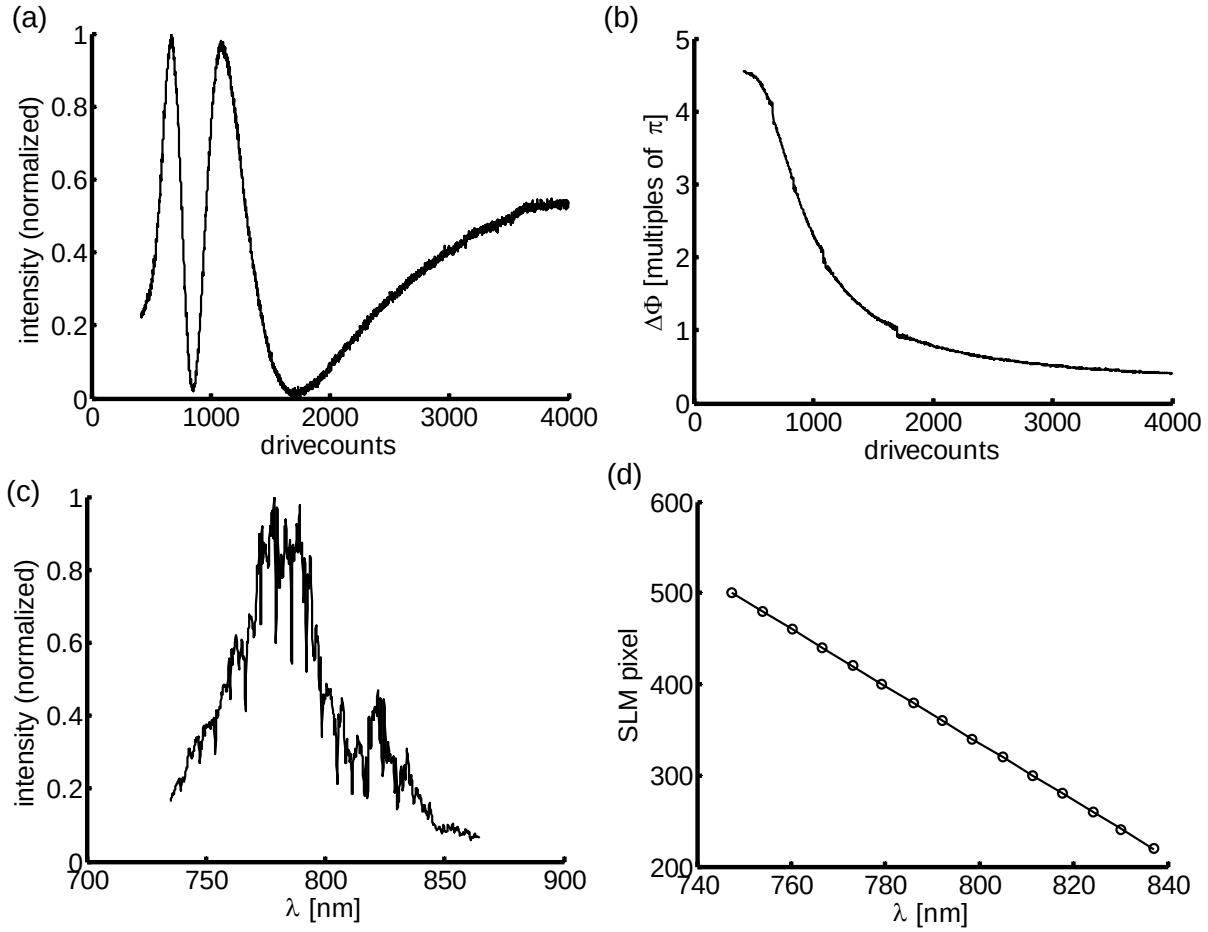

Figure 2.11: SLM calibration. (a) Transmission dependence for a wavelength in the spectral center of the pulse on the applied voltage (drivecounts) on the SLM pixel. (b) Associated phase shifts $\Delta\Phi$ for the same case. (c) Laser spectrum when when the drivecounts for certain SLM pixels are chosen such that a drop in transmission occurs. Note that even while the transmission pattern above $\lambda = 800\,\mathrm{nm}$ is far from optimal, these drops are still easily visible. (d) pixel-λ-dependence for the spectrum in (c) (circles) and its linear fit (solid line).

plane of the $4f$-line may minimally move resulting in a different beam path. Just a lateral shift of $100\,\mu$m leads to a change in the pixel-λ-relationship by one pixel. From one day to another it was seen that the alignment changes, sometimes only slightly, sometimes a beam displacement in front of the shaper entrance of up to several millimeters was observed. Thus the SLM-calibration has to be established again before each experiment. There are two possibilities to do so. Of course the procedure of Fig. 2.11c and 2.11d could be repeated but this takes a not negligible amount of time. An easier way consists in shaping an amplitude drop into the pulse for example in the way that one side of the spectrum gets suppressed while the other one is maintained. Even if this is done with a pixel-λ-relationship that does not completely reflect the actual passage of the shaper, the amplitude shaping will still be nearly perfect as the drivecount-$\Delta\Phi$-relationship as seen in Fig. 2.11a does not change considerably for wavelengths in close proximity. The alignment of the $4f$-line is then adjusted so that the amplitude drop appears at the expected spectral position.

2.7 Compensation of phase distortions

2.7.1 Pre-compensation by chirped mirrors

An optical pulse has its shortest duration and consequently its highest peak power if its spectral phase is flat, the pulse is then said to be *Fourier transform limited*. When such a pulse passes an optical material like glass in which the refractive index is wavelength-dependent, its phase profile gets distorted, mostly by the acquisition of a quadratic phase, leading to a stretched pulses (see section 2.2). Since all nonlinear optical processes we are interested in depend quadratically or cubically on the electric field, a temporally stretched pulse with corresponding lower field strengths is highly detrimental in the generation of those phenomena and has to be avoided. In our setup the dominating source of this phase distortion is the objective in which a large distance of glass has to be traversed by the pulse; but of course all other optical elements in the path play a role as well. As a first order compensation we use a parallel pair of chirped mirrors (Femtolasers, Vienna, Austria) in a multiple reflection scheme (Fig. 2.12a). These are multilayer mirrors in which each wavelength penetrates up to a different depth, red light farther than blue light, thus creating an increasing time delay in longer wavelengths that counteracts the delay accumulated by the shorter wavelengths in the passage through glass (Fig. 2.12b). To find the best number of reflections on both mirrors it is sufficient to measure the intensity of any nonlinear optical process since it will be highest if the spectral phase is flat. We chose the two-photon fluorescence (TPF) of a Rhodamine 6G (Rh6G) solution. Such a solution measurement has the advantage that it is insensitive to slight changes of the focal spot position which can cause problems in surface signal measurements. We found the signal maximum at 19 reflections on each mirror which - assuming an added phase of $-200\,\mathrm{fs}^2$ per reflection (Fig. 2.12c) - amounts to a total compensation of around $19 \cdot 2 \cdot (-200\,\mathrm{fs}^2) = -7600\,\mathrm{fs}^2$ which corresponds to about 18 cm of BK7 glass, taking a

value of 420 fs^2/cm [156] which indicates that there are already some phase distortions at the laser exit as the beam traverses less than 18 cm of glass between this point and the sample plane. Because the added phase is wavelength dependent (Fig. 2.12c), the mirrors,

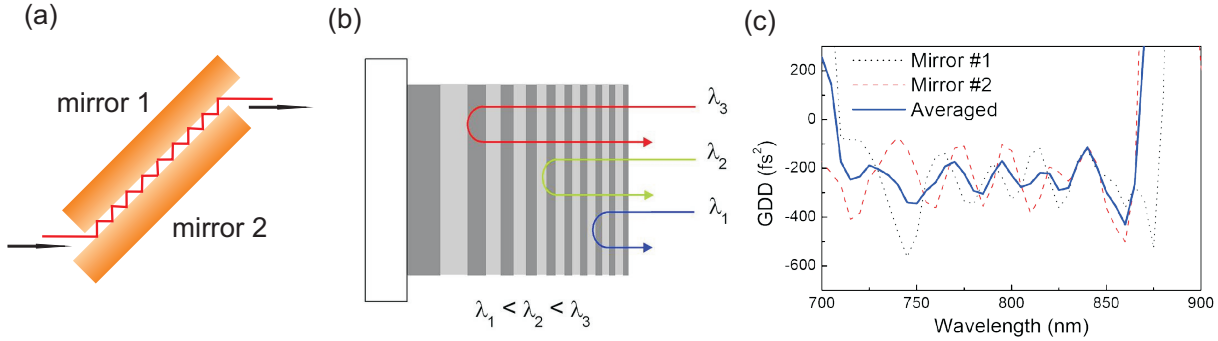

Figure 2.12: Chirped mirrors. (a) setup with multiple reflections; (b) sketch of the light path within the mirror for different wavelengths [157]; (c) added quadratic phase (group delay dispersion - GDD) per reflection [157].

while compensating the predominant phase distortions, add new ones on a smaller scale. The effect of all remaining distortions can be seen in an autocorrelation measurement.

2.7.2 Characterization of the pre-compensated pulse by autocorrelation

To determine the temporal shape of a phenomenon one needs a measurement process of a least the same if not a much better temporal sensitivity. Femtosecond laser pulses being about the shortest events man can produce, the only possibility to measure them temporally is to employ the pulse itself or a reference pulse. The easiest way to do so is by autocorrelating the pulse [158]. In an interferometer setup the beam gets split in two paths, both beam parts travel along their respective branches before they get recombined again (Fig. 2.13a). By varying the length of one of the branches the time delay τ between both pulses can be controlled. For a visualization of this delay a nonlinear optical process should be used. We excited again the TPF of a Rh6G solution, a process that depends quadratically on the field intensity. In the frame of an autocorrelation it is expressed as [159]:

$$I_{TPF}(\tau) \propto \int_{-\infty}^{\infty} |E(t) + E(t-\tau)|^4 \, \mathrm{d}t \tag{2.28}$$

Let's suppose that the interferometer splits the beam exactly in two so that in each branch there is half of the intensity I_0 of the original beam. If now both pulse halves arrive one after the other at the sample, they excite the TPF independently and the measured signal I_{TPF} will be $I_{TPF} \propto 2(I_0/2)^2 = {I_0}^2/2$. If on the other hand both pulses halves are perfectly superposed, $I_{TPF} \propto {I_0}^2$ will be the same as that of the unsplit pulse. In between these two cases both pulses will interfere either constructively or destructively. The form

and width of this interference pattern is therefore a measure of the pulse's temporal shape and width. After optimizing the number of reflections on the chirped mirrors we obtained the autocorrelation trace shown in Fig. 2.13b. Its central maximum can be fitted nicely

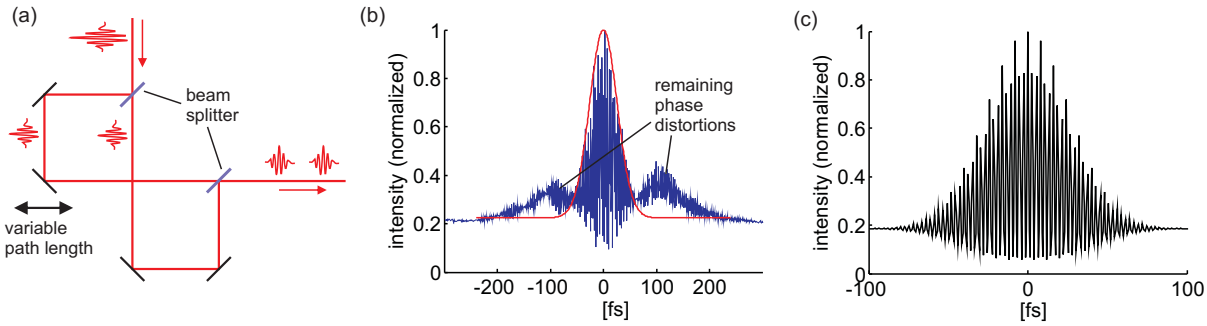

Figure 2.13: Autocorrelation. (a) interferometric setup; (b) blue: TPF autocorrelation trace of the laser pulse with optimal dispersion compensation with chirped mirrors; red: fit with the Gaussian envelope of a transform limited pulse with $\Delta\tau_{FWHM} = 40$ fs; (c) theoretical autocorrelation function for a Fourier transform limited pulse: no side peaks appear.

with the Gaussian envelope of a pulse with $\Delta\tau_{FWHM} = 40\,\text{fs}$, which is to be expected from a near infrared Fourier transform limited pulse with a bandwidth of about 25 nm. This is much lower than the about 50 nm we disposed of for this experiment. Additionally there remain some side peaks a transform limited pulse cannot produce (Fig. 2.13c). Together they indicate the presence of remaining phase distortions and clearly show that chirped mirrors alone are not sufficient to reestablish a flat phase throughout the pulse spectrum and consequently a further compensation step is needed.

The success of an autocorrelation measurement depends to a large extent of the recombination quality of both interferometer paths. If there are slight misalignments both beams will not perfectly overlap in space even for $\tau = 0$. Here, we additionally use a microscopy setup with a high NA objective to focuss the beams in order to reach sufficiently high energy densities in the focal volume for the generation of nonlinear optical signals. Under these conditions a perfect alignment is even more crucial as slight imperfections are enhanced by focussing and the nonlinear signal generation reacts very sensitive to them. In particular the height of the autocorrelation peak relative to the baseline diminishes for an imperfect spatial overlap thus making it harder to extract meaningful information from such an measurement. In the case presented in Fig. 2.13b we estimate a spatial overlap of 45 %.

2.7.3 Correction of remaining phase distortions by an evolutionary strategy

For the removal of all remaining phase distortions a pulse shaper is very suitable (see Eq. 2.20). If the distortions are known they can be directly eliminated. Unfortunately an

autocorrelation measurement does not permit to deduce the actual spectral phase in the focal plane of the objective, it only allows to visualize the possible presence of a non-flat phase. In general it is quite tricky to determine the phase out of an intensity measurement, in particular when it is a spectral phase. Nonetheless several methods have been proposed to accomplish exactly this [30]:

Frequency-resolved optical gating (FROG), developed by Trebino [160], uses an interferometric setup, in which the time-delay τ of the pulses in both branches of the interferometer can be varied, to induce a nonlinear process in a material where both pulses are recombined [16]. A spectrum of the nonlinear signal is then measured for each τ. A typical two-dimensional FROG trace is shown in Fig. 2.14b. Via an iterative algorithm the spectral phase of the pulse can be reconstructed out of this graph. By now a large number of different FROG variants have been developed, for example SHG FROG [161] as depicted in Fig. 2.14a. The SHG signal S generated by both pulse copies in the second-order nonlinear medium calculates as:

$$S(\tau,\omega) \propto \left| \int E(t)E(t-\tau)e^{i\omega t}\mathrm{d}t \right|^2 \tag{2.29}$$

Other FROG variants include polarization gate FROG, self-diffraction FROG, third-harmonic generation FROG and transient grating FROG [16]. Though the signal $S(\tau,\omega)$ is calculated differently for each of these variants, the spectral phase is always retrieved by an appropriate algorithm. Most of these variants are performed in a non-collinear geometry. This limits their use for microscopy applications where both beams would have to pass the same objective therefore accepting a reduced spatial resolution when both beams reach the objective with an angle. We verified the proper functioning of our pulse shaper by setting up a FROG experiment before the microscope entrance but did not use it to characterize the pulse state at the focal spot of the objective due to the extra complexity brought by the high NA focussing and the collinear geometry. Other groups avoided the collinear-geometry issue by developing new collinear FROG variants [162, 163, 164].

In spectral phase interferometry for direct electric-field reconstruction (SPIDER) - introduced by Iaconis and Walmsley [17] - two copies of the pulse with varying time delay τ - again created in an interferometer - interact with a chirped longer pulse in a nonlinear medium (Fig. 2.14c). The chirp is usually achieved by sending the pulse through a thick plate of glass. Because in the chirped pulse the instantaneous frequency changes in time, the nonlinear signals - most commonly SHG pulses - resulting from each of the two copies of the original pulse with the chirped one also have different frequencies. Both signal pulses interfere in a spectrometer to create a spectrogram of the form $E^*(\omega-\Omega_1)\,E(\omega-\Omega_2)\,e^{i\omega t}$ where Ω_1 and Ω_2 are the instantaneous frequencies of the chirped pulse at the times it interferes with both copies of the original pulse. From the spectrogram the phase difference

$$\phi(\omega-\Omega_1) - \phi(\omega-\Omega_2) \tag{2.30}$$

is obtained that is related to $\frac{\mathrm{d}\phi}{\mathrm{d}\omega}$ which then allows reconstruction of the spectral phase of the original pulse.

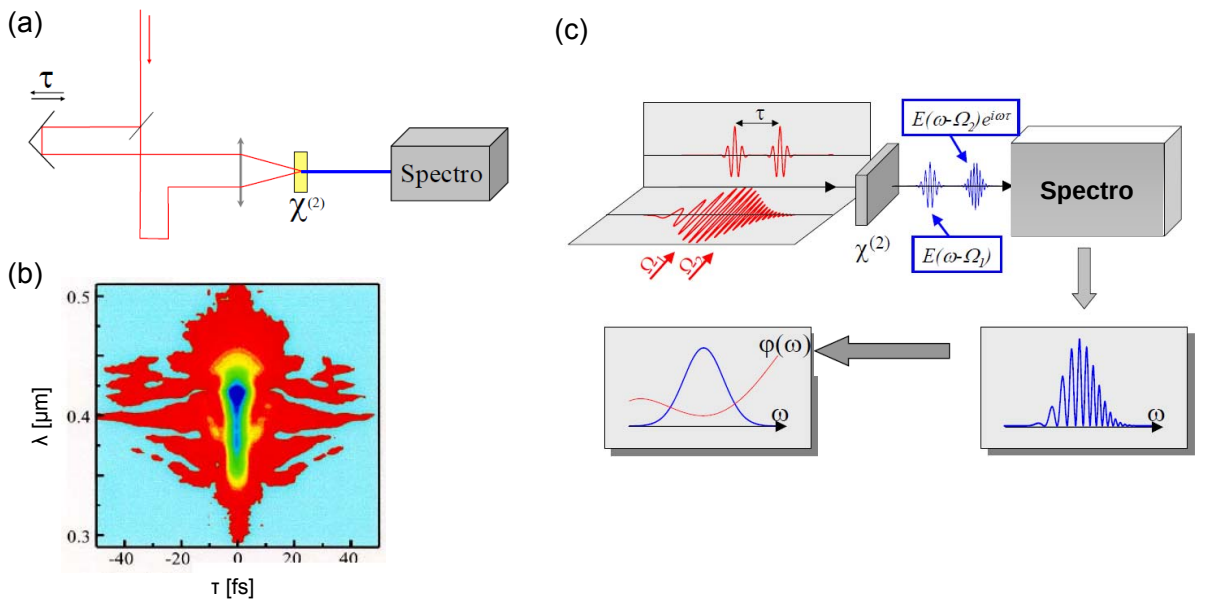

Figure 2.14: Phase measurement techniques. (a) FROG (here SHG FROG): two pulse copies pass an interferometer with variable delay τ and interact with a second-order nonlinear sample. From the spectrally resolved SHG signal for all τ the spectral phase is recovered in an iterative algorithm [165]. (b) Typical FROG trace [166]. (c) SPIDER: two pulse copies separated by τ interact with a stretched pulse in a second-order nonlinear sample, and from the spectral interferogram the phase gets calculated [165].

Note that in microscopy both methods are difficult to implement. FROG requires an interferometric setup with all related difficulties like interferometric stability and good spatial overlap after recombination as well as considerable computational capacities. SPIDER, though less demanding in computational power, depends on an even more advanced setup. Some of the many SPIDER variants that have been developed will be described further down in section 2.8.

Fortunately one does not depend on a *a priori* knowledge of the spectral phase to compensate for its distortions with the help of a pulse shaper. It is for example possible to develop the spectral phase in a Taylor series around a central frequency ω_0:

$$\phi(\omega) = \phi(\omega_0) + \frac{\mathrm{d}\phi}{\mathrm{d}\omega}|_{\omega_0}(\omega-\omega_0) + \frac{\mathrm{d}^2\phi}{\mathrm{d}\omega^2}|_{\omega_0}(\omega-\omega_0)^2 + \frac{\mathrm{d}^3\phi}{\mathrm{d}\omega^3}|_{\omega_0}(\omega-\omega_0)^3 + \ldots \qquad (2.31)$$

and write a series of quadratic and cubic phases in the pulse shaper (absolute and linear phases do not alter the pulse envelope (see section 2.2)) to optimize a nonlinear signal. We tried this but did not succeed because probably numerous phase distortions are present which can not be adequately described by a combination of quadratic and cubic terms.

Another way to reduce phase distortions with the help of a pulse shaper are evolutionary strategies (ES). They do not require any insertions into the beam path. Evolutionary strategies were developed in 1965 by Rechenberg *et al.* to optimize the shape of a flexible body in a wind channel to minimize its drag [167]. Further shape optimizations of engineering problems followed [168, 169]. Evolutionary learning algorithms designed for the phase shaping of ultrashort pulses were realized in the Gerber group [33, 34, 35] to maximize nonlinear signals. They used LC-SLM phase masks as in this work. It is also possible to employ evolutionary strategies to achieve certain experimental goals where the *a priori* phase and polarization shape of the pulse is unknown. Aeschlimann *et al.* for example succeeded in locating the electric field in a sub-diffraction limited area at a bow-tie structure while excluding it from others close-by [59].

An ES draws its inspiration from evolutionary processes in biology that lead to optimal adaptation to the surrounding environment. Standard evolutionary factors are *mutation*, that creates new genes in a random manner, *selection* that keeps only those individuals exhibiting an advantage or increased fitness compared to the rest of the population while at the same time eliminating individuals with less perfect adaptation, and *recombination*, the mixing of genes between individuals as occurs during sexual reproduction.

An analogous approach is possible in optimization problems in computation. First a merit or fitness function has to be defined that describes the degree of adaptation and shall be maximized. In our specific case we want to create a flat spectral phase in the focal plane of the objective. This is characterized by maximal efficiency of nonlinear optical processes. As in the earlier sections of this chapter we choose to optimize the TPF signal of a Rh6G solution which serves as merit function. Individuals to be investigated are D-SLM configurations that show only phase modifications but don't change the spectral amplitude (see Eq. 2.20). Hundred of them form a population. A configuration is an array of voltage values applied to the SLM pixels that translates into a certain induced phase profile. In the first generation the whole population is created randomly (Fig. 2.15a). For each member its TPF response is measured, the fifteen that give the highest signal are kept as parents for the next generation while the 85 remaining configurations get discarded (selection). In a second step hundred pairings are randomly formed out of the fifteen parents. Each pairing creates a child by randomly taking the voltage value for each pixel either from one or the other parent (recombination). All children form the next generation and the parents are discarded. After that a normally distributed noise in form of small drivecount values is added to each configuration (mutation). This is necessary to jump out of local extrema that doubtlessly exist numerously in the 470-dimensional configuration space (the D-SLM has 640 pixels of which around 470 are passed by spectral pulse components with non-negligible intensity). For a good performance of the ES the width σ of this Gaussian noise distribution needs to be self-adaptive. In the beginning of the algorithm it is desirable to search over a very large region of the configuration space while later on, once the presumable global minimum has been approached, the search should be narrowed. We start with an initial mutation width of $\sigma = 50$ drivecounts which corresponds to a voltage of 122 mV or 1% of the total available voltage region. After the mutation every member of

the population is measured and the fifteen best form as basis for the next generation and the process repeats itself till a stable value in the TPF intensity is reached.

It is clear that such a procedure contains a large number of free parameters like the total number of individuals in the population, the fraction kept as parents, the modalities of the recombination - whether it is performed pointwise or in larger sections, whether the parents form part of the next generation or not -, the width of the Gaussian for the creation of the mutation noise - especially its temporal variability -, whether additional boundary conditions like continuity of the phase function are included or not, etc. The choice of all these parameters will decide whether the ES succeeds or fails. We followed the work of groups employing evolutionary strategies in similar fields [170, 33, 171] to make these choices. Of particular importance is the self-adaptive mutation width. We reach good results in accordance with the work of Zeidler [172] by decreasing the mutation width for the next generation by 10% whenever 60% of the current population give a higher signal than their parents and by increasing it by the same percentage otherwise. In a typical ES experiment performed in this way σ increases rapidly in the beginning up to 200 drivecounts before slowly decreasing towards 0. Fig. 2.15b shows this development.

After about 300 generations a stable maximum in the TPF intensity is seen to be reached (Fig. 2.15c). Writing a configuration into both masks of the D-SLM takes around 250 ms. Together with a measurement acquisition time of 100 ms this results in a total of about 350 ms per configuration as the time for all calculations performed during the ES can be neglected in comparison with these two limiting factors. Thus an ES over 300 generations with 100 configurations per generations takes about three hours. Therefore the TPF measurement of an fluorescent solution is much more convenient than for example the SHG detection from a nonlinear crystal where the positional stability - especially in Z - would have to be maintained over the whole period. In a solution the sample position is not crucial because the system behaves the same everywhere. The resulting configuration after the ES can be considered to correct for the remaining phase distortions and to lead to a spectrally flat phase (Fig. 2.15d). Though the corrected phase distortions are still dominated by the quadratic term responsible for the linear chirp - its parabola seen here folded up due to the restriction of the phase interval that can be reached by our SLM (see page 58) - it can by no means adequately describe the complete rather complex shape and demonstrates the insufficiency of simple compensation devices like chirped mirrors. At both sides of the spectrum the shape of the phase function is naturally more noisy and less reliable because of the lack of energy in these spectral regions, but on the other hand even an imperfect phase compensation there does not considerably alter the pulse as a whole.

Fig. 2.16 shows the SHG spectrum obtained from a nonlinear crystal - $KTiOPO_4$ (KTP) (for more information on it, see section 4.2.2) - placed with its main axis along X and excited by the phase corrected laser field, also oriented along X. Also seen is the expected SHG response from our excitation laser spectrum if the phase was really flat. Though the overall form of the measured spectrum corresponds quite well with the expected one, the signal bandwidth is somewhat reduced. This indicates that despite the ES, there are still some phase distortions present in the pulse. For a more detailed analysis

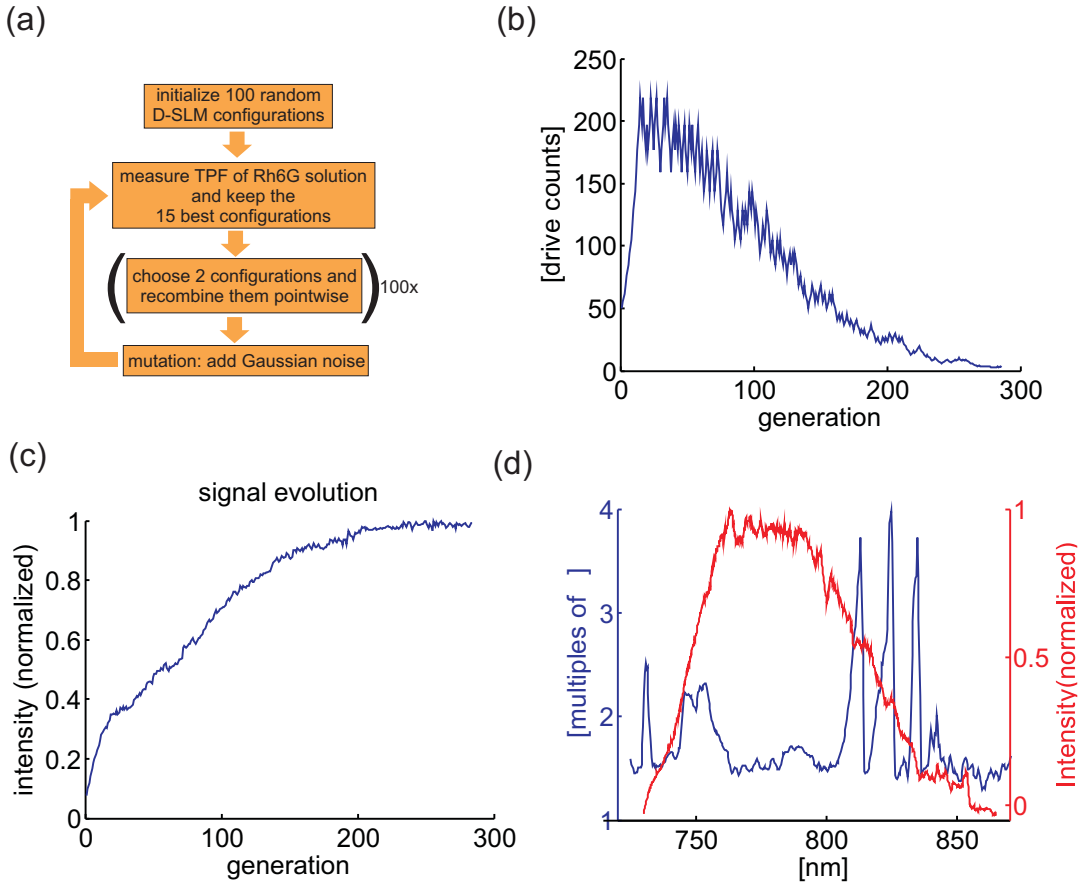

Figure 2.15: Evolutionary strategy. (a) procedure; (b) evolution of the self-adaptive mutation width σ during the algorithm; (c) signal evolution: average of the TPF intensity of the fifteen best configurations; (d) phase corrections; blue: final D-SLM phase that leads to a flat phase at the focal plane of the objective, red: normalized laser spectrum.

on how the phase profile influences the SHG spectrum, see section 4.5.

2.7.4 Limitations of Evolutionary algorithms

So far we only attempted to compensate for phase distortions to obtain a flat phase at the focal point of the objective by maximizing nonlinear processes. Though this is a very important task, phase pulse shaping offers a much greater potential. The capability to create arbitrary phase profiles allows actively controlling nonlinear processes. Certain pathways can for example be suppressed while others remain unaffected. An example of such a situation is presented in section 4.5. However, an ES is not able to create or measure such profiles for lack of adequate merit functions. In the case of flat phase recovery the choice of the merit function is trivial: the intensity of any nonlinear optical process. Once it is maximized, the phase will be flat. But if the task is for example to

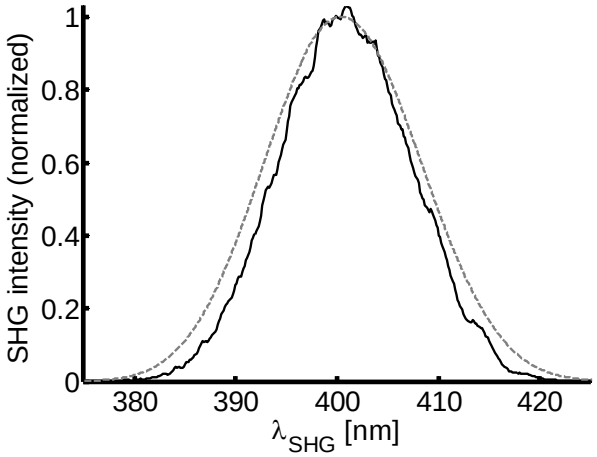

Figure 2.16: SHG spectrum (black solid line) after the evolutionary strategy. Both the nonlinear sample (KTP) and the incident field are oriented along X. The expected SHG spectrum from our laser pulse with a flat phase is shown as a grey dashed line. The lower bandwidth of the measured spectrum indicates the presence of some phase distortions.

create a sinusoidal phase profile, no merit functions springs to mind. Since a sinusoidal phase results in a SHG pattern with minima and maxima depending on the position of symmetric and antisymmetric phase points (see section 4.5), one could think of maximizing the ratio between the SHG intensities at the maximum and minimum position. But there are a number of other, non sinusoidal, phase profiles that would achieve the same. Thus, such a merit function is ill fitted. Other choices are accompanied by similar difficulties.

In many cases it should not be necessary to measure an arbitrary phase, even if it is applied on the SLM. One could start from the SLM configuration corresponding to a flat phase at the sample plane as found by the ES described in the previous section, and then add the desired phase. If the shaper is carefully calibrated, meaning it is known which frequency traverses which SLM pixel and the relationship between the applied voltage and its effect on the phase of that particular frequency has been established previously, writing a certain phase in the shaper will yield exactly that phase at the end plus the initial phase of the pulse. As this initial phase is just the phase corrected by the ES, any phase could be created in a controlled way. The main question is therefore, how reliable is the flat phase found by the ES?

As the ES maximizes the TPF response of a Rh6G solution it is safe to assume, that even if the phase it not entirely flat at the end the remaining distortions would hardly affect the overall signal intensity. This means that in spectral regions with high energy content, i.e. in the central region, the found phase is very reliable. However, at both sides of the spectrum where only a tiny portion of the pulse's energy resides, the ES is less accurate, because these regions contribute only a very small portion to the overall signal and thus phase distortions there don't affect the signal considerably. This is true for all nonlinear processes that could be used for an ES, but the severity of the effect depends on the kind

of nonlinearity measured. For TPF and SHG the signal intensity scales with the square of the incident intensity, while for THG the relationship is cubic. As a result a THG-ES is even less sensitive than TPF and SHG to distortions at the sides of the spectrum.

Another problem arises from the fact that the SLM has only a limited range of phases ϕ that can be applied, in our case $\pi/2 \leq \phi \leq 3.5\pi$ (see section 2.6). However, the distortions that have to be corrected for, exceed this limit and phase wrappings get introduced. These wrappings pose a problem for the ES algorithm because it relies on a slow optimization of the phase which works nice if the target function is smooth. Jumps in the phase function, on the other hand, might result in trapping the algorithm at the jump frequency on one or the other side of the gap. In most cases a manual post treatment can resolve these issues. For a SLM pixel whose drivecounts value is very different from those of the neighboring pixels, it gets set to the average of its neighbors. Fig. 2.17 shows an example of an ES result before and after this post treatment. In the spectral center only little can be gained

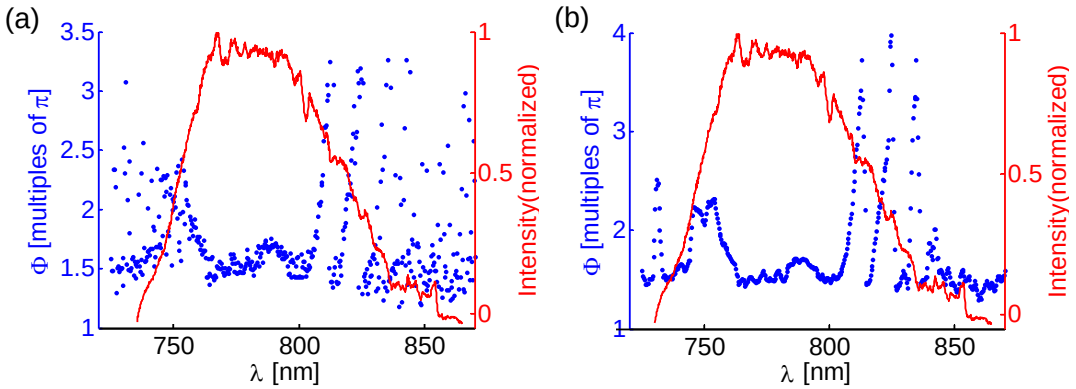

Figure 2.17: Post treatment of ES result. (a) final configuration found by the ES; (b) configuration after manual post treatment (phase as blue dots and spectral intensity as red line). Before treatment the phase is very noisy in regions with low spectral intensity while relatively smooth in the center of the spectrum.

by post treating the configuration, the ES having already nicely converged. The more one approaches the spectral borders the noisier the ES configuration gets and the bigger the effects of the treatment. Consequently in those regions the actual phase is very ill determined and has to be considered to be unknown. As already mentioned this does hardly affect the overall signal intensity, but it prevents the creation of arbitrary phase profiles in these regions.

2.8 Single-beam homodyne SPIDER

To prevent these problems one must have the possibility to reliably measure the phase in regions with low spectral intensity in a configuration that can work in a collinear geometry.

The disadvantages of the conventional methods FROG and SPIDER have already been mentioned earlier (section 2.7.3). It is however worthwhile to note that a few spectral phase measurement techniques can be performed in a collinear geometry, among them some new SPIDER variants. The time-domain homodyne optical technique (HOT) for SPIDER [173, 174] does not require anymore a spectral readout as it works exclusively in the time domain (Fig. 2.18a). The phase is recovered by varying the time delay τ between both pulses in the interferometer. In the shaper-assisted collinear (SAC) SPIDER [175] the pulse doublet is created in a pulse shaper. In a reference branch the original pulse gets stretched and after recombination it interacts with the shaper output. Both beams are focussed onto a nonlinear sample (a BBO crystal) and the spectrally resolved SHG signal gets analyzed according to standard SPIDER algorithms (Fig. 2.18b). As both methods work in a collinear way, they are suited for microscopy with high NA objectives, but they still depend on interferometric setups.

This constraint is avoided in the multiphoton intrapulse interference phase scan (MIIPS) method, developed by the Dantus group [20, 21]. Besides a pulse shaper and a spectrometer it does not require any additional elements (Fig. 2.18c). To retrieve the spectral phase $\phi(\omega)$ of a broadband pulse, a known sinusoidal phase profile $f(\omega) = \alpha \cos(\gamma\omega - \delta)$ is added to the unknown phase. α denotes the phase amplitude, γ its period (typically on the order of the pulse duration in the time domain) and δ the relative position of the added phase within the unknown phase of the pulse. A multiphoton signal (for example SHG) gets generated by this pulse and is measured by a spectrometer for a whole range of values δ. When the second derivative of both $\phi(\omega)$ and $f(\omega)$ add up to zero, the SHG signal gets maximized. Thus by scanning $f(\omega)$ for different δ the quadratic phase component of $\phi(\omega)$ can be determined. To compensate for the cubic component, the third derivative of $f(\omega)$ has to be considered and so on for all higher orders. A typical MIIPS trace, combining the SHG spectra for different δ is shown in Fig. 2.18d. A flat phase is characterized by parallel features. Different inclinations and spacings indicate non-flat spectral phases. Several variants of MIIPS have been developed, both in an iterative [176] and in a non-iterative fashion [177].

Recently the group of Lim [178] introduced a single-beam homodyne SPIDER method in which two narrow polarization jumps close to one another - of which one is additionally phase shifted with respect to the other - are shaped into a broadband pulse. This is done in a pulse shaper based on a LC-SLM as in this work. In the SPIDER variants mentioned so far two copies of the pulse interact with different parts of a stretched pulse. Here the non-polarization shifted pulse serves as both pulse copies at the same time, while the two almost monochromatic polarization jumps mirror two different wavelengths of the stretched pulse. The field from the polarization jump regions interferes in a second-order nonlinear medium with the field of the whole pulse thus creating two different SHG signals as in the SPIDER variants mentioned so far. From the interferences produced by these two signals a phase difference $\theta(\omega)$ in analogy to Eq. (2.30) is obtained:

$$\theta(\omega) = \phi(\omega) - \phi(\omega - \delta\omega) \tag{2.32}$$

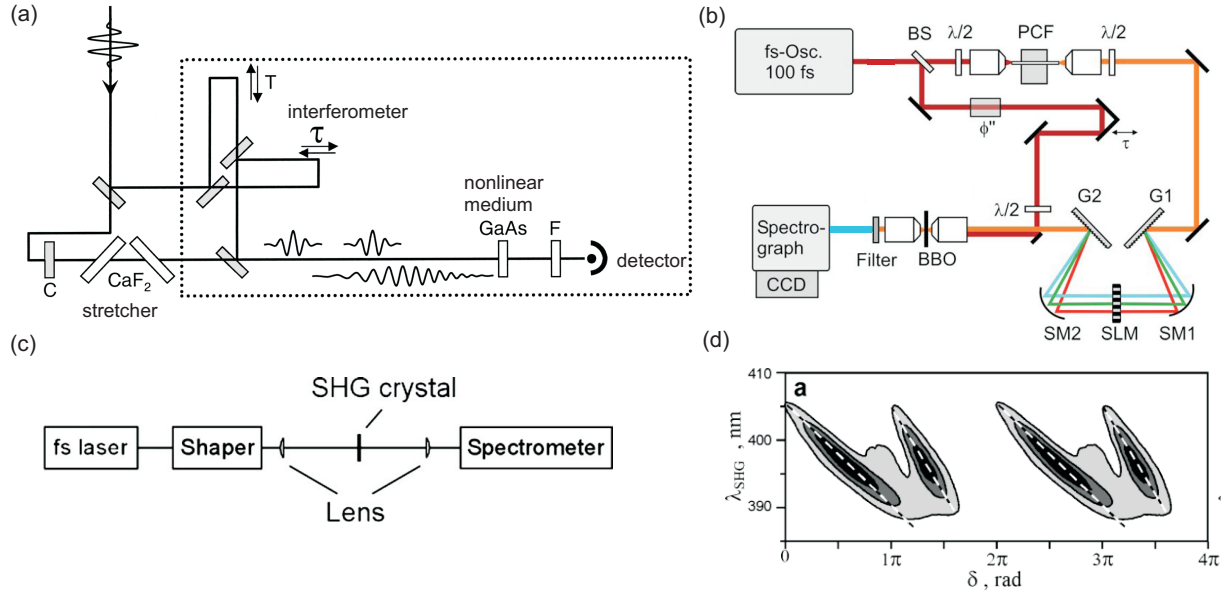

Figure 2.18: Collinear phase characterization methods. (a) time domain HOT SPIDER consisting of an interferometer and a stretcher whose outputs interfere in a nonlinear medium and the signal analysis leads to the spectral phase [174]. (b) SAC SPIDER consisting of a stretcher and a pulse shaper where the pulse doublet gets created. Both branches interfere in a nonlinear medium and the spectrally resolved SHG signal leads to the spectral phase [175]. (c) MIIPS setup [176]. (d) Typical MIIPS trace for a non-flat spectral phase [20].

where $\delta\omega$ is the spectral distance between both polarization jumps. From this result the spectral phase of the original pulse is recovered by the recursive formula:

$$\phi(\omega_0 + n\delta\omega) = \phi(\omega_0) + \sum_{k=1}^{n} \theta(\omega_0 + k\delta\omega) \tag{2.33}$$

where n is a positive integer. The spectral resolution of this method is $\delta\omega$. All these collinear techniques require a double shaping, either polarization/phase or amplitude/phase.

A subsequent development has led to the proposal of the single-beam homodyne SPIDER [179] where only a narrow phase jump gets inserted into the pulse without the need of shaping neither amplitude nor polarization.

2.8.1 Principle of single-beam homodyne SPIDER

When a narrow phase jump gets inserted into the spectral profile of the pulse, the electric field can be written as [179]:

$$E^0(\omega) = E_h(\omega) + E_{pr}(\omega) \tag{2.34}$$

where E_{pr} is the probe field at the phase jump position ω_{pr} and E_h the remaining pulse with a hole at the probe frequency (Fig. 2.19a). Under the assumption of a very narrow jump it is possible to write $E_{pr}(\omega) = E^0(\omega_{pr})\delta(\omega - \omega_{pr})$. The applied phase at ω_{pr} is denoted ϕ_{pr}. An SHG field created by such a pulse can then be expressed as (see section 1.2.2):

$$\begin{aligned} E_{SHG}(\omega) &\propto \int \mathrm{d}\Omega E^0(\omega-\Omega)E^0(\Omega) \\ &= \int \mathrm{d}\Omega[E_h(\omega-\Omega)+E_{pr}(\omega-\Omega)][E_h(\Omega)+E_{pr}(\Omega)] \\ &= \int \mathrm{d}\Omega[E_h(\omega-\Omega)+E^0(\omega_{pr})\delta(\omega-\Omega-\omega_{pr})][E_h(\Omega)+E^0(\omega_{pr})\delta(\Omega-\omega_{pr})] \\ &= \int E_h(\omega-\Omega)E_h(\Omega)\mathrm{d}\Omega + 2E^0(\omega_{pr})E_h(\omega-\omega_{pr}) + (E^0(\omega_{pr}))^2\delta(\omega-2\omega_{pr}) \end{aligned} \tag{2.35}$$

The first term $\int \mathrm{d}\Omega E_h(\omega-\Omega)E_h(\Omega) \equiv E^{LO}_{SHG}(\omega)$ couples E_h with itself and is independent of the probe phase ϕ_{pr}. It acts as a local oscillator. The second term $2E^0(\omega_{pr})E_h(\omega-\omega_{pr}) \equiv E^{(1)}_{SHG}(\omega)$ contains the interference between E_h and E_{pr} and has the same spectral phase as $E_h(\omega)$ with an offset ϕ_{pr} due to the narrow bandwidth of E_{pr}. In the original SPIDER this term corresponds to the interaction of one copy of the pulse (here: $E_h(\omega)$) with a certain part of the stretched pulse (here: E_{pr}). The third term $(E^0(\omega_{pr}))^2\delta(\omega-2\omega_{pr}) = E^{pr}_{SHG}(\omega)$ only influences the SHG spectrum at $\omega = 2\omega_{pr}$ and can therefore be neglected (Fig. 2.19b). The corresponding SHG intensity $I_{SHG}(\omega)$ is then:

$$\begin{aligned} I_{SHG}(\omega) &= |E^{LO}_{SHG}(\omega) + E^{(1)}_{SHG}(\omega)|^2 \\ &= |E^{LO}_{SHG}(\omega)|^2 + |E^{(1)}_{SHG}(\omega)|^2 \\ &\quad +2|E^{LO}_{SHG}(\omega)E^{(1)}_{SHG}(\omega)|cos(\phi^{LO}(\omega) - \phi_{pr} - \phi(\omega-\omega_{pr})) \end{aligned} \tag{2.36}$$

with $\phi(\omega)$ the phase of $E_h(\omega)$ and $\phi^{LO}(\omega)$ that of $E^{LO}_{SHG}(\omega)$. This is the implementation of the double quadrature spectral interferometry [180] applied to a single pulse. The first two intensity terms as well as the factor in front of the cosine are independent of the probe phase ϕ_{pr}. An operation of the form

$$\frac{I_{SHG}(\omega,\phi_{pr_1}) - I_{SHG}(\omega,\phi_{pr_2})}{I_{SHG}(\omega,\phi_{pr_3}) - I_{SHG}(\omega,\phi_{pr_4})} \tag{2.37}$$

eliminates all these summands and factors and keeps exclusively the cosines. Choosing $(\phi_{pr_1},\phi_{pr_2},\phi_{pr_3},\phi_{pr_4}) = (\pi/2,-\pi/2,0,\pi))$ in expression 2.37 results in a sine in the numerator while keeping the cosine in the denominator and the phase $\phi^{LO}(\omega) - \phi(\omega-\omega_{pr})$ can be extracted by:

$$\phi^{LO}(\omega) - \phi(\omega-\omega_{pr}) = \tan^{-1}\left[\frac{I^{(1)}_{SHG}(\omega,\phi_{pr}=\pi/2) - I^{(1)}_{SHG}(\omega,\phi_{pr}=-\pi/2)}{I^{(1)}_{SHG}(\omega,\phi_{pr}=0) - I^{(1)}_{SHG}(\omega,\phi_{pr}=\pi)}\right] \tag{2.38}$$

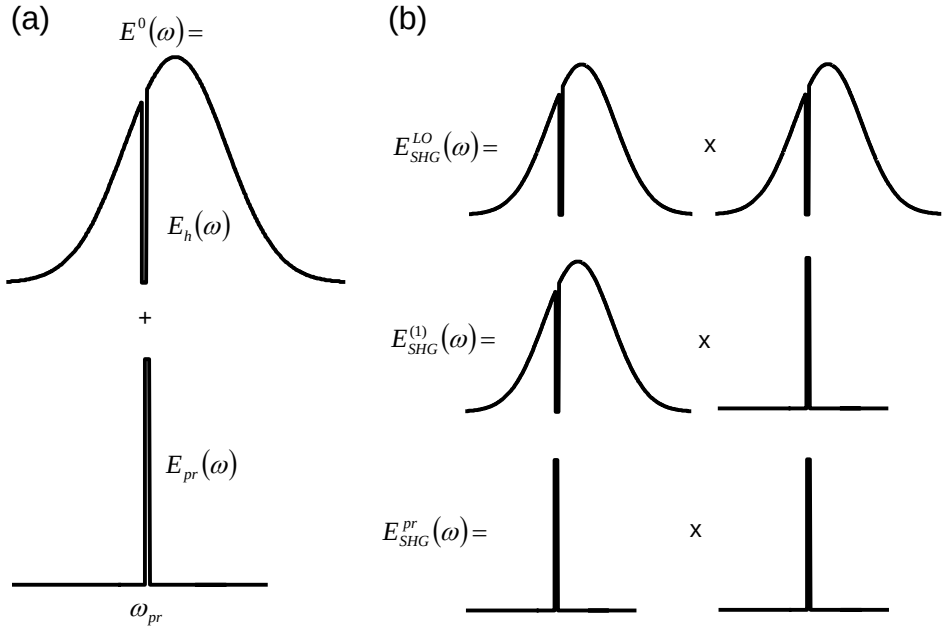

Figure 2.19: Single-beam homodyne SPIDER: principle. (a) incident electric field composed of probe field E_{pr} at ω_{pr} with the phase ϕ_{pr} and the rest of the field minus the probe field $E_h(\omega)$; (b) contributions to the SHG field $E_{SHG}(\omega)$: local oscillator field $E^{LO}_{SHG}(\omega)$ coupling of E_h with itself; interference field $E^{(1)}_{SHG}(\omega)$ coupling E_h with E_{pr}; and pure probe field contribution $E^{pr}_{SHG}(\omega)$.

To recover the original spectral phase $\phi(\omega)$ the remaining unknown phase $\phi^{LO}(\omega)$ must still be removed. This can be done by another series of measurements with phase jumps at a slightly different frequency $\omega_{pr}+\delta\omega$. The same procedure as above leads to:

$$\phi^{LO}(\omega)-\phi(\omega-\omega_{pr}-\delta\omega)=\tan^{-1}\left[\frac{I^{(2)}_{SHG}(\omega,\phi_{pr}=\pi/2)-I^{(2)}_{SHG}(\omega,\phi_{pr}=-\pi/2)}{I^{(2)}_{SHG}(\omega,\phi_{pr}=0)-I^{(2)}_{SHG}(\omega,\phi_{pr}=\pi)}\right] \quad (2.39)$$

$\phi^{LO}(\omega)$ in Eqs. (2.38) and (2.39) can be considered to be identical due to the narrow bandwidth of the probe. Thus subtracting one equation from the other gives, following the algorithm of the HOT SPIDER method [181]:

$$\begin{aligned}
&\phi(\omega-\omega_{pr})-\phi(\omega-\omega_{pr}-\delta\omega)\\
=\;&\tan^{-1}\left[\frac{I^{(2)}_{SHG}(\omega,\phi_{pr}=\pi/2)-I^{(2)}_{SHG}(\omega,\phi_{pr}=-\pi/2)}{I^{(2)}_{SHG}(\omega,\phi_{pr}=0)-I^{(2)}_{SHG}(\omega,\phi_{pr}=\pi)}\right]\\
-\;&\tan^{-1}\left[\frac{I^{(1)}_{SHG}(\omega,\phi_{pr}=\pi/2)-I^{(1)}_{SHG}(\omega,\phi_{pr}=-\pi/2)}{I^{(1)}_{SHG}(\omega,\phi_{pr}=0)-I^{(1)}_{SHG}(\omega,\phi_{pr}=\pi)}\right]\\
\equiv\;&\theta(\omega-\omega_{pr})
\end{aligned} \quad (2.40)$$

$\theta(\omega-\omega_{pr})$ is the phase difference between the two frequencies ω and $\omega+\delta\omega$ of the incident pulse. The offset ω_{pr} translates this difference in the pulse frequency range to the range of the measured SHG frequencies. Starting from the construction phase $\theta(\omega-\omega_{pr})$ the original phase is recovered by the recursive formula:

$$\phi(\omega_0+n\delta\omega)=\phi(\omega_0)+\sum_{k=1}^{n}\theta(\omega_0+k\delta\omega) \tag{2.41}$$

with n as a positive integer.

The single-beam homodyne SPIDER method requires therefore eight measurements: four different phase jumps at two different spectral positions. Thus it is much faster than a FROG measurement and avoids the complicated interferometry setup of a traditional SPIDER scheme. Forget *et al.* recently demonstrated the convergence of single-beam homodyne SPIDER results with those of other SPIDER variants [182]. As a disadvantage single-beam homodyne SPIDER does not offer the same spectral resolution as these other methods. FROG and SPIDER are only limited by the resolution of the spectrometer while the single-beam homodyne SPIDER resolution is given by the difference in phase jump positions $\delta\omega$. Still, this is usually enough. In our case each SLM pixel contains a spectral width of about 0.3 nm. As a particular pulse frequency will also have a finite width in the Fourier plane where the SLM is located, it may pass several neighboring pixels. To assure that the whole of a pulse frequency can be phase shifted, the phase jump region has to encompass several pixels, we chose four, corresponding to a spectral width of about 1.2 nm. $\delta\omega$ should then be chosen to be large enough, so that both phase jump positions are clearly distinct. This leads to a spectral resolution of this method of a few nm. As it is not expected that major phase distortions occur on such small scales, this resolution is sufficient for many purposes.

It should be noted, however, that the method requires spectra with very good signal to noise ratios, because it relies on quotients of differences of SHG spectra. As we will see below, even moderate noise levels would be detrimental for the phase recovery.

2.8.2 Correction of phase distortions using single-beam homodyne SPIDER

Before using the single-beam homodyne SPIDER method to create and measure arbitrary phase profiles, a first test should assess its capability to correct for phase distortions. As it relies on SHG we chose $KTiOPO_4$ (KTP) as a sample because of its high SHG cross section. The SHG spectra are measured as explained above (section 2.5.2). The phase steps were centered at 778 nm and 782 nm, resulting in a spectral resolution of our phase characterization of 4 nm. To obtain good signal to noise ratios of about 150, we averaged each spectrum over ten measurements of 2 s exposure time each. The opposite of the calculated phase is then applied to the D-SLM which should result in a flat phase at the sample plane. To test the performance of the method, the phase measurement is carried out again for this new found phase. Such an iterative approach (we went up to

the fourth iteration) should not only show the success of the phase compensation in the previous step, but also successively eliminate the remaining phase distortions. In Fig. 2.20 the results of such a measurement are presented. For each of the four iterations the construction phase $\theta(\omega)$ (Fig. 2.20a) and the calculated phase $\phi(\omega)$ (Fig. 2.20b) are displayed. Furthermore the SLM configuration is shown after the calculated phase has been subtracted from the previous configuration (Fig. 2.20c) and the SHG spectrum resulting from this SLM configuration (Fig. 2.20d).

It can be seen that a flat phase is not obtained after just one run of the procedure, as is especially clear from the shape of the SHG spectrum in Fig. 2.20d (blue curve) obtained after subtracting the calculated phase of the first run in the D-SLM (see section 4.5 on how the phase influences the SHG spectrum). During the next few iterations the SHG spectrum increases in bandwidth and exhibits a more Gaussian-like shape without local minima. The single-beam homodyne SPIDER theory does not require any iterations. The fact that the experimental implementation relies on them shows the sensitivity of the method on error sources. The importance of high signal to noise ratios was already stated, additionally the laser source has to be stable throughout the whole process that takes around a few minutes. Also the finite SLM resolution as well as the imperfect frequency separation in the SLM's plane affect the result quality since they lead to imperfect phase jumps that don't have the form of a δ-function as assumed in the theoretical derivation.

Caution has to be taken concerning another uncertainty of the method. Because it depends of the form of SHG spectra, single-beam homodyne SPIDER is only sensitive to phases that alter the SHG signal, which is also the case for all other SHG-based phase retrieval methods like SHG-FROG and the other SPIDER variants. As already explained in section 2.2 a constant phase only shifts the oscillations within the pulse envelope and a linear phase shifts the whole pulse in time, but both do not change the form of the pulse, thus they do not influence the SH generation and the method is consequently blind to these phases. A linear spectral phase would however result in a constant term in the construction phase $\theta(\omega)$ which is shown in Fig. 2.20a. The heavy fluctuations on both sides are generated by noise because almost no SHG intensity is present in these regions, but in the central portion of the SHG spectrum where $\theta(\omega)$ is more or less flat each iteration exhibits a different offset. One might argue that the presence of a linear phase does not pose a problem for nonlinear optical experiments as the results are unaffected by it, but this is not true when working with a pulse shaper with finite resolution. Because with a SLM it is only possible to apply phases within a certain range (in our case between 0.5π and 3.5π), a strong linear phase leads to phase wrappings in the SLM. As already mentioned in section 2.7.4 these phase jumps are detrimental to the control of the spectral phase, because the same frequency will pass the SLM on both sides of the jump leading to an ill-defined phase and being accompanied by an amplitude drop as well. The number of phase wrappings should therefore be reduced to a minimum which corresponds to the substraction of a suitable linear phase. If this phase is estimated by fitting a constant function to $\theta(\omega)$ in Fig. 2.20a or a linear function to $\phi(\omega)$ in Fig. 2.20b, the fit will be dominated by the huge phase values at the spectral fringes created by noise, thus leading

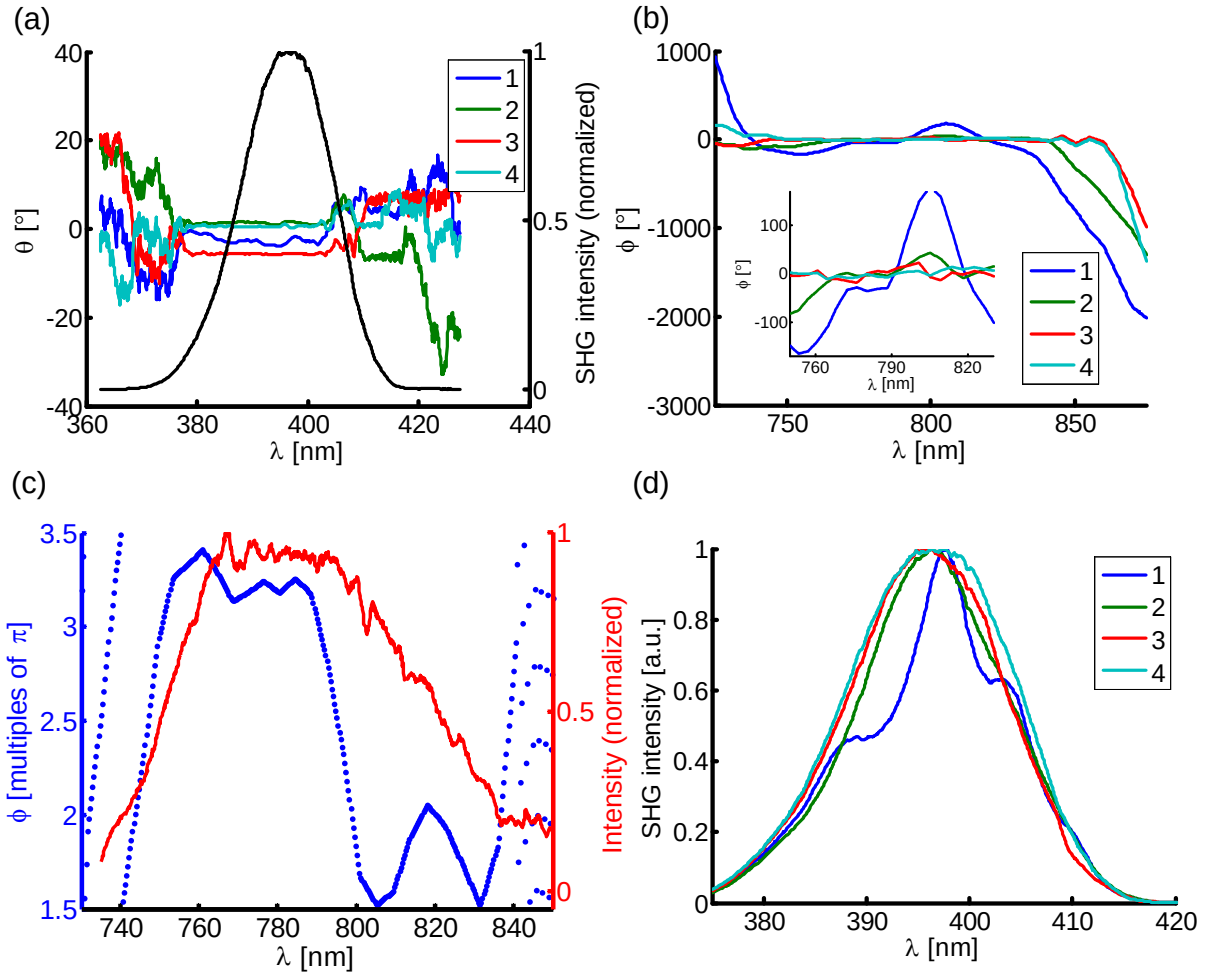

Figure 2.20: Single-beam homodyne SPIDER: Creating a flat phase. (a) construction phase $\theta(\omega)$ as defined in Eq. (2.41) for all four iterations, SHG spectrum after last iteration in black; (b) calculated phase $\phi(\omega)$ of the incident pulse (see Eq. (2.41)) for all four iterations (inset shows a zoom of the central region); (c) D-SLM configuration (blue dots) resulting from subtracting $\phi(\omega)$ from the previous D-SLM configuration (applied phase shifts are restricted between 1.5π and 3.5π, only the configuration after the fourth iteration is shown), and pulse spectrum (red line); (d) SHG spectrum of KTP when the D-SLM configuration is applied that compensates for phase distortions as seen in (b), for all four iterations.

to erroneous results. A better assessment of the linear phase is achieved when weighting the fit according to the spectral intensity of each contributing frequency (see appendix A). The results in Fig. 2.20 were obtained by following this procedure. Without the linear phase estimation, no convergence towards a flat phase was observed, on the contrary the spectral phase and the corresponding SHG spectrum became increasingly more distant from a flat phase configuration due to the ever increasing number of phase wrappings (data not shown).

2.8.3 Limitations of this technique

The experiments presented above demonstrate that it is possible to correct for distortions in the phase profile of a pulse which means the original phase can be measured. But the procedure requires a certain number of iterations, indicating that the phase measurement is not perfect. The question arises whether this is only due to experimental insufficiencies or whether there are also method-inherent limitations as to which kinds of phase profiles can be correctly determined and when the procedure starts to fail. We addressed this problem by a number of simulations. These were designed to correspond closely to our experimental conditions. The phase steps are centered at 778 nm and 782 nm with a width of 1.2 nm each and a Gaussian laser spectrum is assumed with a similar bandwidth to those provided by our laser. A certain phase is applied and from the SHG spectra we attempt to retrieve it according to the theory presented in section 2.8.1. From the obtained phase its linear component, weighted by the spectral importance of each frequency, is removed. The quality of the phase retrieval is then assessed by a mean square error calculation of the form:

$$\chi^2 = \int_\Omega (\phi_0(\omega) - \phi_r(\omega))^2 \mathrm{d}\omega \tag{2.42}$$

where $\phi_0(\omega)$ and $\phi_r(\omega)$ are the applied and the retrieved phase, respectively, and the integration is performed over the spectral support Ω of the laser pulse.

We can now explore the phase profiles for which the single-beam homodyne SPIDER method leads to a correct phase measurement and those regions where it fails to do so. As phase distortions in a typical pulse shaping microscopy setup usually contain a large quadratic phase contribution caused by the glass in the objective and many other smaller perturbations created by all the optical elements in the beam path, we represent them by a quadratic phase profile in which a sinusoidal phase is embedded: $\phi_0 = a(\omega-\omega_0)^2 + A\sin(b\omega)$ [183]. Fig. 2.21a shows the performance of the single-beam homodyne SPIDER for such phase profiles where $a = 300\,\mathrm{fs}^2$, $b = \frac{1}{4\pi}\,\mathrm{ps}$ and the amplitude A of the sinus is tuned between and 0 and 4π. Low χ^2 values correspond to a successful phase retrieval as seen in Fig. 2.21b, taken for $A = \pi$. But already relatively small deviations from this χ^2-baseline, as the one at $A = 1.7\pi$ indicate considerable errors in the phase retrieval process (Fig. 2.21c). The higher the values χ^2 (as for $A = 3.8\pi$ for example - Fig. 2.21d), the worse becomes the mismatch between original and applied phase.

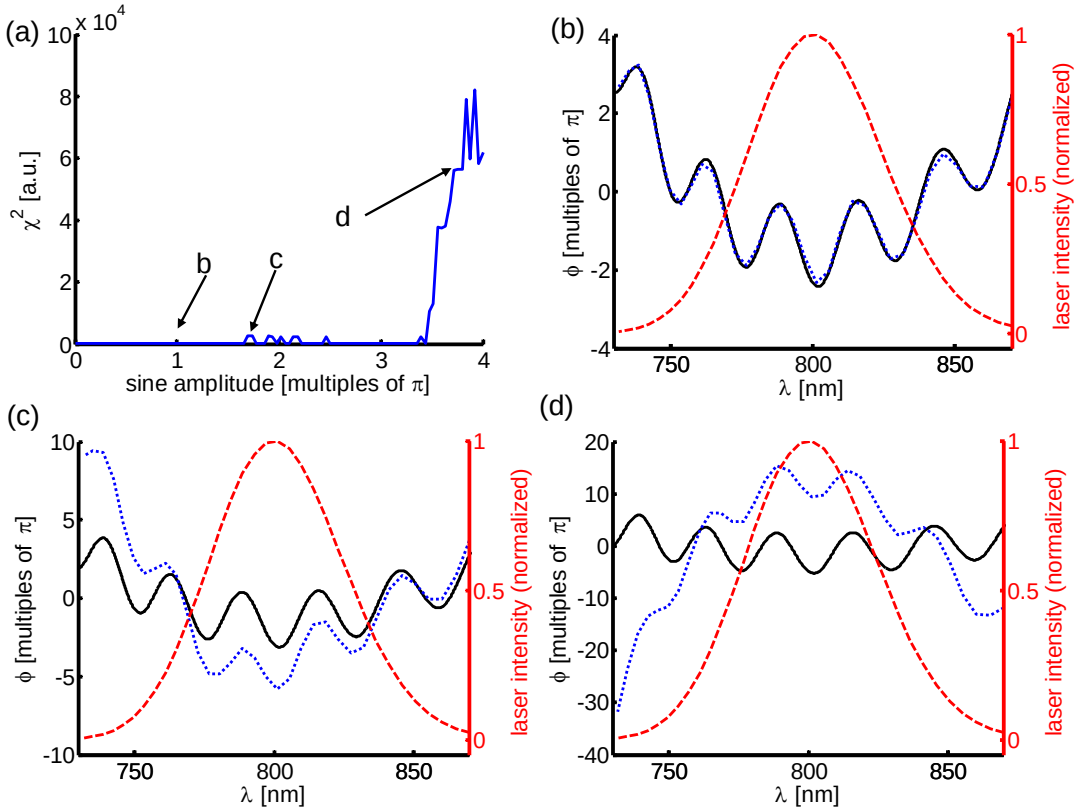

Figure 2.21: single-beam homodyne SPIDER: limitations. (a) phase retrieval mismatch χ^2 for the phase profile $\phi_0 = 300\text{fs}^2(\omega-\omega_0)^2 + A\sin(\frac{\omega[\text{ps}^{-1}]}{4\pi})$ with sinus amplitude $0 < A < 4\pi$. (b-d) retrieved phase for $A = 1$, $A = 1.7$ and $A = 3.8$ as indicated in (a); black solid line: applied phase ϕ_0, blue dotted line: retrieved phase ϕ_r; laser spectrum as dashed red line for orientation. Note the different vertical phase scales in (b-d) due to the increasing degree of phase mismatch; the quadratic part of ϕ_0 is the same in all three cases.

It can be clearly seen that the single-beam homodyne SPIDER is not universally successful. In order to gain a better understanding of when the method starts to fail we investigated a number of different types of phase profiles that are presented in Fig. 2.22 (the varied parameters will always be denoted as x). For a purely quadratic phase profile $\phi_0 = x(\omega-\omega_0)^2$ (Fig. 2.22a) the retrieval works fine even for very large quadratic phases such as $a = 5000\,\text{fs}^2$. Even though a rise is visible in the χ^2-graph, the mismatch values remain small, all the more as the phase values reach huge numbers at the sides of the spectrum. However, as soon as random perturbations are added, the method encounters huge difficulties. Fig. 2.22b contains profiles of the form $\phi_0 = 300\,\text{fs}^2(\omega-\omega_0)^2 + xN_G$ where N_G is a normally distributed noise with zero mean and a standard deviation of 1. A quadratic phase of $300\,\text{fs}^2$ corresponds to a point far to the left in the χ^2-graph in Fig. 2.22a, where the phase measurement works perfectly. But already small perturbations of $x = \sigma = \frac{\pi}{10}$ lead to a break-down of the retrieval. Curiously for a number of larger perturbations, the

measurement gives again the correct result, but once $\sigma > 0.3\pi$ there are no more matches.

To gain further insight into the effect of small scale changes, we used a sinusoidal profile that offers more control parameters than normally distributed noise. We find that the method depends strongly on the amplitude of the phase variations (Fig. 2.22c - $\phi_0 = x\sin(\frac{\omega[\mathrm{ps}^{-1}]}{4\pi})$). As soon as these surpass around $x = \frac{\pi}{3}$ the retrieval fails while it works for all lower values. Based on this finding we fixed the amplitude at $\frac{\pi}{3}$ and varied the period: $\phi_0 = \frac{\pi}{3}\sin(x\omega)$ (Fig. 2.22d). While the method works quite stable under these conditions for shortening periods up to the resolution limit (the distance $\delta\omega$ between the two phase step frequency positions), there are some isolated cases where difficulties are encountered. As soon as the sine amplitude is slightly increased, for example to 0.4π, a very different situation arises and only for some specific sine periods the retrieval leads to the correct result (data not shown). If the sine is overlaid by even moderate noise ($\phi_0 = 0.3\pi\sin(\frac{\omega[\mathrm{ps}^{-1}]}{4\pi}) + xN_G$ - Fig. 2.22e), the phase measurement only succeeds for values up to $x = \sigma = 0.07\pi$ and for the some isolated cases above. Even the spectral position of the sine's minima and maxima plays a role in the phase retrieval performance, though not an important one (Fig. 2.22f). For $\phi_0 = \frac{\pi}{3}\sin(\omega/(\frac{\omega[\mathrm{ps}^{-1}]}{4\pi} + x)$ retrieval fails only in two isolated cases while it works, although with slightly different accuracies, in all other cases.

Finally we looked at the behavior of a combined quadratic and sinusoidal phase. Fig. 2.22g investigates the retrieval performance influence on the sine amplitude within the quadratic profile, as already seen and analyzed in Fig. 2.21 ($\phi_0 = 300\,\mathrm{fs}^2(\omega - \omega_0)^2 + x\sin(\frac{\omega[\mathrm{ps}^{-1}]}{4\pi})$). Note that while in the case of a pure sine the retrieval only works up to amplitudes of $x = \frac{\pi}{3}$, the addition of a quadratic phase allows the correct measurement of sine phases with ten times the amplitude, though not over the whole range. On the other hand the addition of a quadratic phase imposes severe restrictions on the period of the sine ($\phi_0 = 300\,\mathrm{fs}^2(\omega - \omega_0)^2 + \pi\sin(x\omega)$ - Fig. 2.22h). Over the whole range between 0 and 4 sine periods within a spectral interval of 50 nm, regions where the retrieval succeeds alternate with those where it fails.

In summary we deduce that single-beam homodyne SPIDER is able to measure phases that do not exhibit large oscillations on small scales. That explains its success with quadratic phases, even though they may contain strong slopes at the spectral edges, but the phase remains monotonous is these regions. As soon as strong phase variations occur on small scales, the method quickly starts to fail as demonstrated by the sinusoidal phase profiles. In these cases the method has probably difficulties to differentiate the induced phase step from the rapid phase variations close-by. However, if these variations are added to a dominant slowly varying phase they can be better retrieved. In any case, the retrieval only works when it is done as an iterative process, something the theory does not predict. The reason for this lies most probably in the need for very noiseless spectra and the fact that the phase jump regions do not have the form of a δ-function as in the theoretical derivation thus blurring the SHG response and leading to difficulties in the phase retrieval. All in all it is very difficult if not impossible to predict the success or failure of single-beam

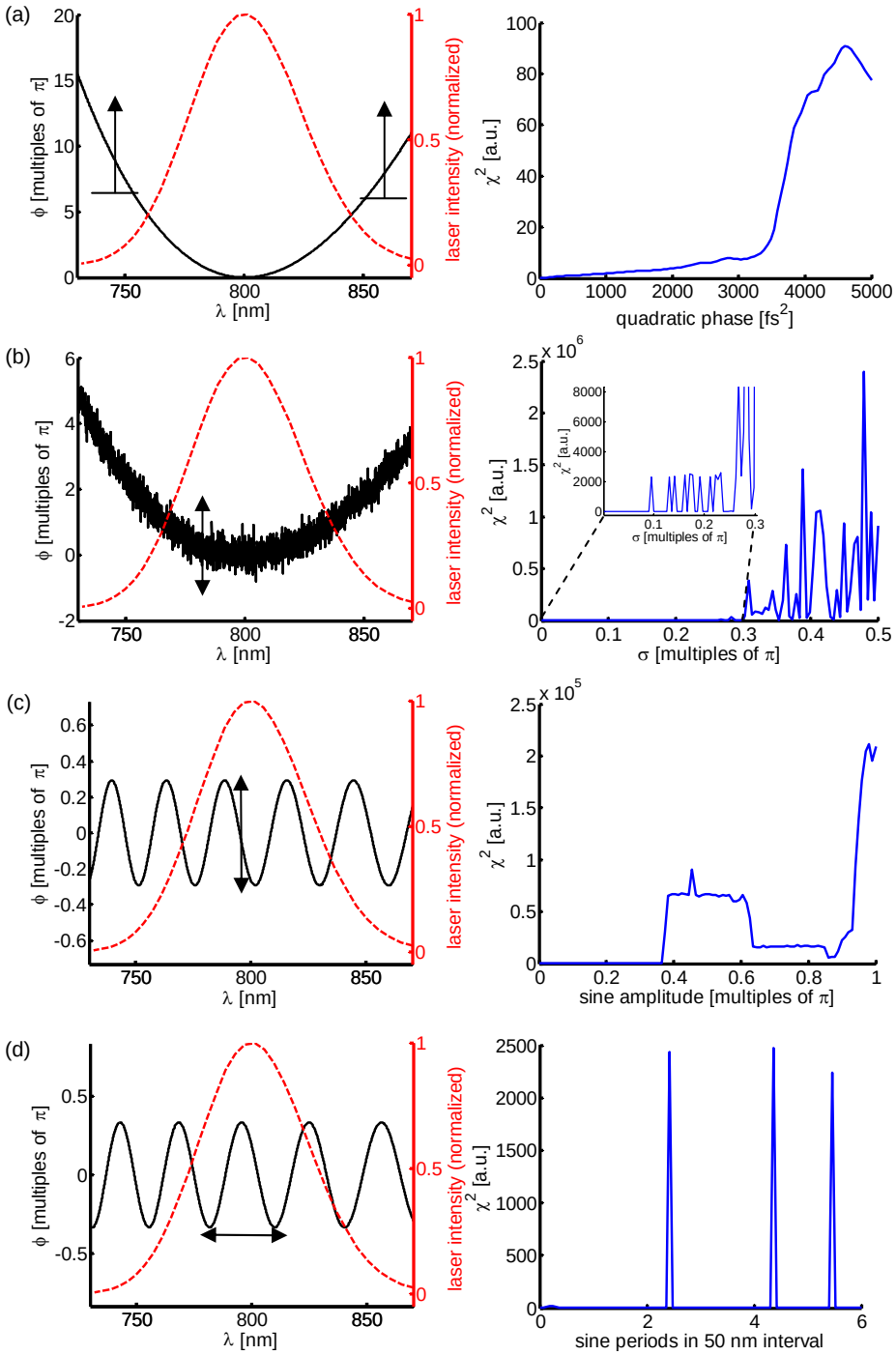

Figure 2.22: Single-beam homodyne SPIDER: phase retrieval simulations. (a) varying quadratic phase $\phi_0 = x(\omega - \omega_0)^2$; (b) quadratic phase with varying normally distributed noise $\phi_0 = 300\,\mathrm{fs}^2(\omega - \omega_0)^2 + xN_G$; (c) sine with varying amplitude $\phi_0 = x\sin(\frac{\omega[\mathrm{ps}^{-1}]}{4\pi})$; (d) sine with varying period $\phi_0 = \frac{\pi}{3}\sin(x\omega)$; (e) sine with varying normally distributed noise $\phi_0 = 0.3\pi\sin(\frac{\omega[\mathrm{ps}^{-1}]}{4\pi}) + xN_G$; (f) sine with varying spectral center $\phi_0 = \frac{\pi}{3}\sin(\frac{\omega[\mathrm{ps}^{-1}]}{4\pi} + x)$; ...

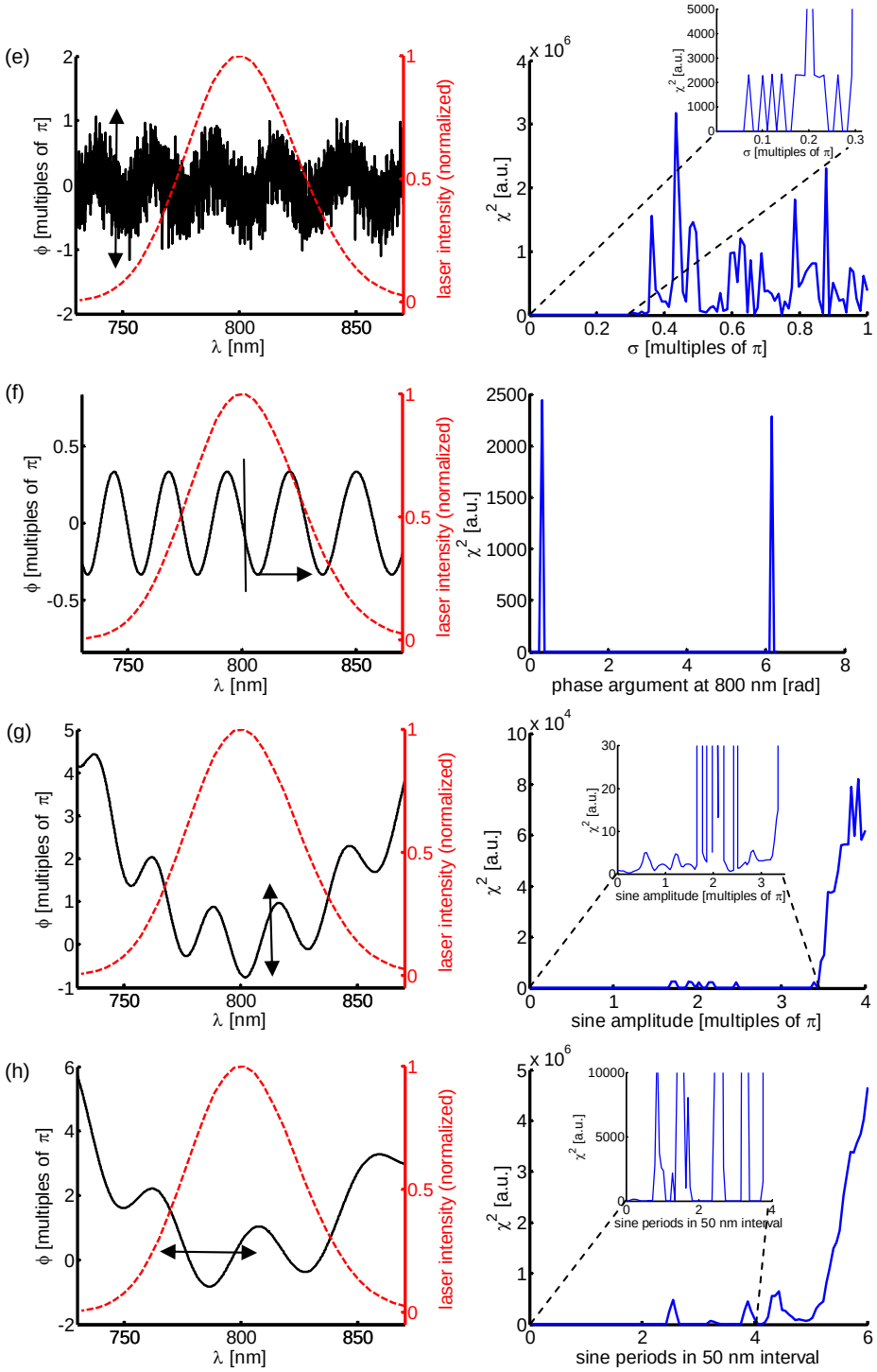

(g) quadratic phase and sine with varying amplitude $\phi_0 = 300\,\mathrm{fs}^2(\omega-\omega_0)^2 + x\sin(\frac{\omega[\mathrm{ps}^{-1}]}{4\pi})$; (h) quadratic phase and sine with varying period $\phi_0 = 300\,\mathrm{fs}^2(\omega-\omega_0)^2 + \pi\sin(x\omega)$. Left column: one example of each phase, laser spectrum as red dashed line for orientation; arrows indicate the varying parameter within each series. Right column: χ^2-graph for the series (insets are y-zooms of the graphs).

homodyne SPIDER without a proper simulation or a measurement. The elegant simplicity of the setup compared to the standard methods FROG and SPIDER clearly finds its trade-off in the strongly reduced number of phase profiles for which it is suited.

2.8.4 Control of arbitrary phase profiles at the focal point of the objective using single-beam homodyne SPIDER

Now that we know which kinds of phase profiles are accessible for single-beam homodyne SPIDER, the question arises whether we can also measure such phases with this method. To create a certain spectral phase at the focal point of the objective, first a flat phase is realized by compensating for phase distortions and then the desired phase is encoded in the SLM which is easily done, once the SLM is well calibrated (see section 2.6).

In practice there arises, however, the problem of the phase wrappings. As phase distortions can be quite large they can easily surpass the phases accessible by a SLM and therefore phase wrappings modulo 2π have to be introduced. If the desired phase profile gets then added to this phase the number of wrappings tends to increase. Each wrap presents a source of error due to imperfect frequency separation in the SLM plane of the pulse shaper. The actual spectral phase is thus ill defined at these positions and the spectral amplitude drops as well. It would therefore be desirable to create a specific phase profile directly without having to pass by the configuration that compensates for phase distortions. If these distortions would be due almost exclusively to a quadratic phase, they could be compensated quite successfully with chirped mirrors, but because they contain also higher-order contributions - including those introduced by the chirped mirrors themselves (see section 2.7.1) -, a pre-compensation by these mirrors is not always possible.

To measure an arbitrary phase in a first try we encoded this phase in the SLM after the phase distortions had been compensated. We used the single-beam homodyne SPIDER procedure to measure the so created phase. This was done in a non-iterative fashion. We tested it for sinusoidal and quadratic phases. Unfortunately this attempt failed. We attribute this to imperfections in the phase retrieval process. As in the case of a flat phase creation, where a good result only arrives after some iterations of the procedure, we expect that the same is true when other phase profiles are to be realized.

That is why to create a flat phase we need an iterative approach of the single-beam homodyne SPIDER. We start by measuring our phase without applying a specific profile in the SLM. The measurement result contains all the phase distortions. The retrieved phase is then subtracted in the SLM leading to a supposedly flat phase at the sample plane. A second phase measurement gives then all the remaining phase distortions that were not corrected for in the first measurement. The new phase is subtracted from the previously found SLM configuration and so on. This procedure can easily be adapted to create not a flat phase but an arbitrary phase profile (Fig. 2.23). For this we begin by writing the target phase in the SLM ignoring all knowledge about other phase distortions. A phase measurement thus gives the desired phase plus all distortions that are often much bigger

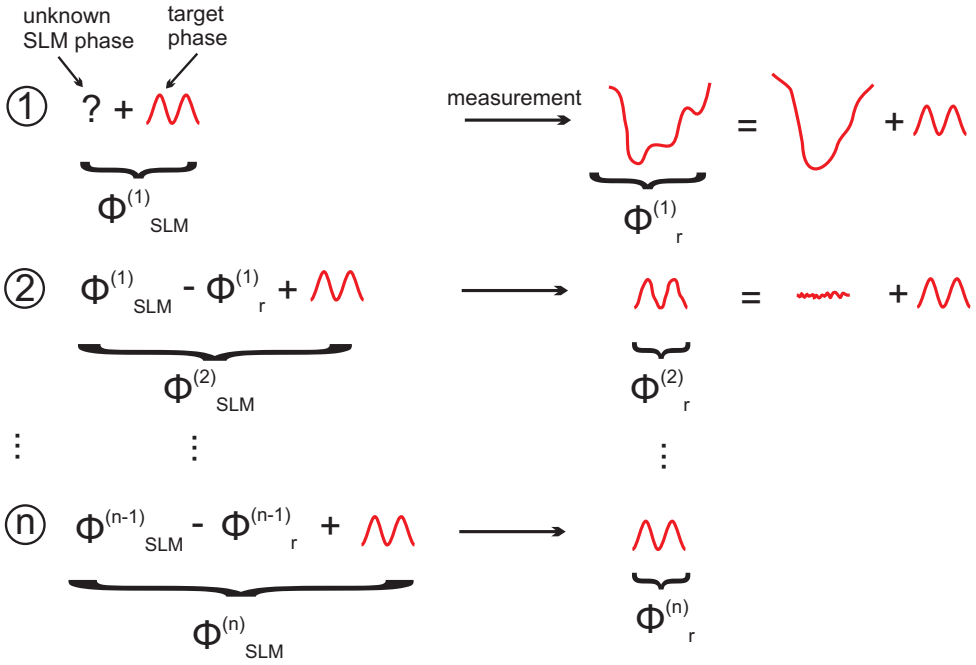

Figure 2.23: Algorithm to create arbitrary phase profiles with the single-beam homodyne SPIDER. In a first step the target phase gets applied to the SLM and the resulting phase ϕ_r^1 - containing all phase distortions - is measured. In a second step $\phi_r^{(1)}$ is subtracted from the previous SLM configuration and the target phase is added again, resulting in a new SLM phase $\phi_{SLM}^{(2)}$. Once this phase is measured only very few distortions from the target phase remain. After several iterations the target phase is established in the SLM.

than the target phase itself. In a second step we subtract the measurement result from the previous SLM configuration - supposedly leading to a flat phase at the sample plane - and add again the target phase. A second phase measurement should now be dominated by the target phase but will most likely still contain various small perturbations. After a few more cycles of this iterative process the target phase should be firmly established.

Fig. 2.24 shows a number of phases created in this way. This study aims at testing the robustness of the phase measurement technique described here. All profiles shown follow the form $\phi_0 = x_1\pi \sin(x_2 \frac{2\pi}{\Delta\omega}(\omega - \omega_0))$. The antisymmetric point of the phase is fixed at $\lambda_0 = \frac{2\pi c}{\omega_0} = 800\,\text{nm}$. The actual position of λ_0 is of minor importance as can be seen from Fig. 2.22f. Within an interval of $\Delta\lambda = 50\,\text{nm}$ around this point (which corresponds to $\Delta\omega$) the phase contains x_2 periods and it reaches a maximal value of $x_1\pi$. The shown phases thus correspond to the situation of Fig. 2.22c and 2.22d. As long as the phase amplitudes are small (0.3π) the phase creation and measurement works nicely (Fig. 2.24a-c). The quality of the measured phase is independent of the period of ϕ_0. As soon as the amplitude reaches values around $0.45\pi...0.5\pi$ the procedure starts to fail (Fig. 2.24d-e). Though the sinusoidal oscillations are still somewhat present, they are overlaid by strong linear or quadratic terms. For even higher amplitudes (0.6π) the method fails completely

(Fig. 2.24f). This is in very good agreement with the simulations presented in Fig. 2.22c and 2.22d. As the simulations also show a strong dependence of the quality of the phase measurement from the phase amplitude while the period of the phase profile plays only a very minor role. Even the amplitude value at which the procedure starts to fail is very similar in simulation and experiment.

This first result shows that even after four iterations the method is not robust for phase profile measurements. One might argue that with a longer iterative process it should in principle be possible to measure phases correctly whatever the phase profile complexity because even if the measured phase is wrong after the first try, subsequent iterations should sooner or later bring the phase to the desired form. We tested this by mimicking in our simulations some critical phase profiles that failed in the experiment. As before we tested sinusoidal profiles of the form $\phi_0 = x_1\pi\sin(x_2\frac{2\pi}{\Delta\omega}(\omega-\omega_0))$ and chose pairs of (x_1, x_2) where the experimental phase creation starts to fail, but where the desired phase shape can still be guessed by eye in the final measured phase. Fig. 2.25 shows two such cases ($(x_1, x_2) = (0.3, 4)$ and $(x_1, x_2) = (0.45, 2)$). For both of them the experimentally measured phase and the calculated phase of the simulation after each iteration are displayed. For both phase profiles neither experiment nor simulation converge on the desired phase. Although after certain iterations the main characteristics of the target phase were found, subsequent iterations show less good agreements. This might be due to the fact that each iteration introduces phase fluctuations on small scales. As the target phase is continuous while the calculated phase only has a spectral resolution of $\delta\omega$, the spectral difference between the two phase step positions, the disagreement between ϕ_0 and ϕ_r will show perturbations on the scale of $\delta\omega$. This is demonstrated in Fig. 2.26. The iterative single-beam homodyne SPIDER process is simulated for the target phase $\phi_0 = x_1\pi\sin(x_2\frac{2\pi}{\Delta\omega}(\omega-\omega_0))$ with $(x_1, x_2) = (0.3, 2)$, a condition, where both the experiment and the simulation lead to a correct phase measurement. However, as can be seen in Fig. 2.26a, ϕ_0 and the calculated phase ϕ_r are not identical due to the finite spectral resolution of ϕ_r. The disagreement between both is the strongest where ϕ_0 quickly changes its slope, i.e. in the region of the minima and maxima. Because the procedure subtracts ϕ_r in the SLM and adds again ϕ_0 to obtain the phase for the next iteration ϕ_n, this mismatch is preserved. With each subsequent iteration it gets accumulated (Fig. 2.26b). For phase profiles in regions where the method works reliably, this effect does not pose a problem as long as the number of iteration remains reasonably small, but it can be quite severe for phase profiles where the method has some trouble to measure the phase correctly. These additional perturbations will then considerably reduce the chances for success.

Another serious problem for single-beam homodyne SPIDER measurements is the signal to noise ratio in the spectral measurements. We dealt with a noise level of only about 0.6% which was reached by choosing long integration times (ten measurements of 2 s each per phase step value). The same amount was also included in our simulations depicted in Fig. 2.25. But even these minute values influence the outcome of our simulations considerably. For a number of phase profiles where both the experiment and the noiseless simulation lead

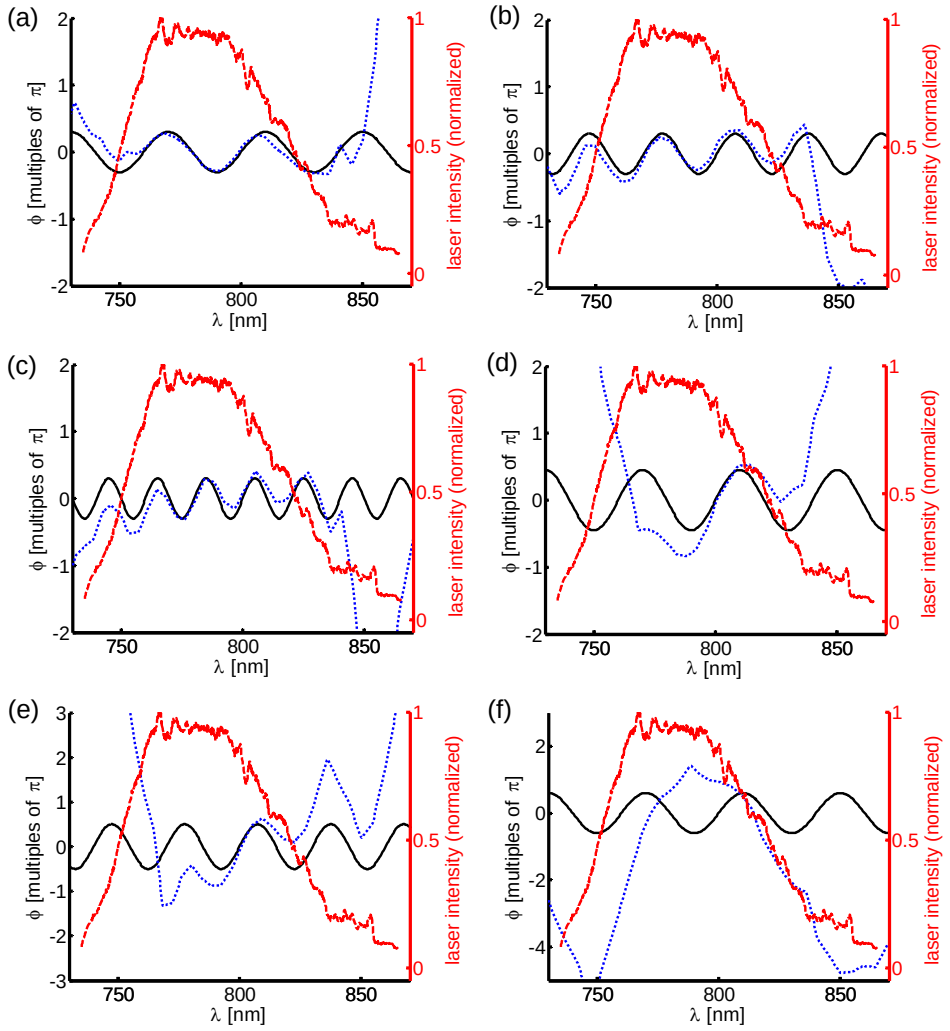

Figure 2.24: Single-beam homodyne SPIDER for phase creation. Desired phase profiles as solid black lines; retrieved phases after the fourth iteration (see text for details) as blue dotted lines; laser spectrum as dashed red curve for orientation. Sinusoidal phase profiles of the form $\phi_0 = x_1 \pi \sin(x_2 \frac{2\pi}{\Delta\omega}(\omega - \omega_0))$ (where $\Delta\omega$ corresponds to an interval of $\Delta\lambda = 50\,\text{nm}$ around $\lambda_0 = \frac{2\pi c}{\omega_0} = 800\,\text{nm}$) differ in amplitude ($x_1$) and periods per $\Delta\lambda$ (x_2). (a) $(x_1, x_2) = (0.3, 1.5)$; (b) $(x_1, x_2) = (0.3, 2)$; (c) $(x_1, x_2) = (0.3, 3)$; (d) $(x_1, x_2) = (0.45, 1.5)$; (e) $(x_1, x_2) = (0.5, 2)$; (f) $(x_1, x_2) = (0.6, 1.5)$.

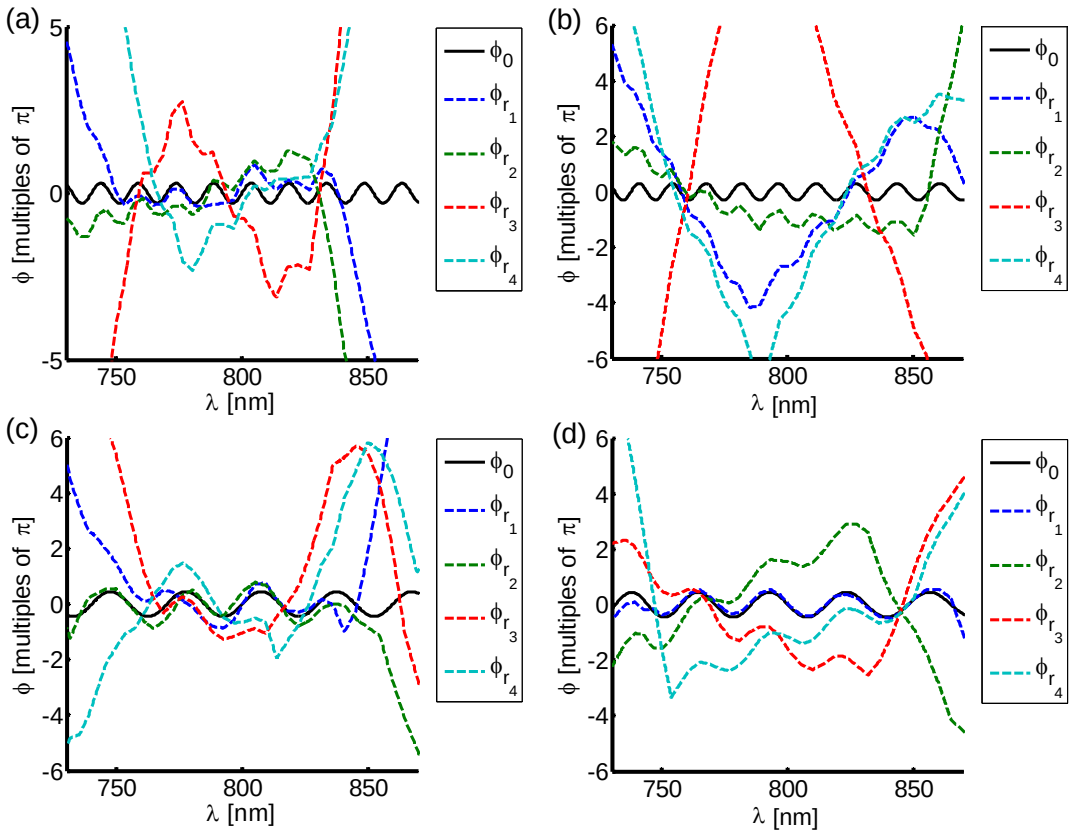

Figure 2.25: Single-beam homodyne SPIDER experiment and simulation for critical phase profiles. Sinusoidal phases of the form $\phi_0 = x_1\pi\sin(x_2\frac{2\pi}{\Delta\omega}(\omega-\omega_0))$. Left column: experiment, right column: simulation. Upper row: $(x_1, x_2) = (0.3, 4)$; lower row: $(x_1, x_2) = (0.45, 2)$. ϕ_0: target phase; ϕ_{r_n}: measured resp. calculated phase after the nth iteration.

to a correct phase determination, a simulation including noise may easily fail. That is also why we did not include any noise in the graphs in Fig. 2.26 to be able to show the effect just due to the finite ϕ_r-resolution. The extreme sensitivity to noise of single-beam homodyne SPIDER has its origin in the phase retrieval calculations (Eq. (2.38)) where the quotient of a difference of spectra is taken to exploit tiny changes in the SHG spectra created by slightly different excitation conditions. Therefore maximum care has to be taken to reduce the noise level as much as possible.

Finally we tested quadratic phase profiles experimentally ($\phi_0 = x(\omega-\omega_0)^2$). Fig. 2.27 shows two such profiles. Surprisingly, the single-beam homodyne SPIDER method has huge difficulties to create these phases even for very moderate quadratic phase coefficients ($x = 20\,\mathrm{fs}^2$ and $x = 100\,\mathrm{fs}^2$). At $x = 20\,\mathrm{fs}^2$ the correct phase is more or less found over most of the pulse's spectral range after some iterations while the method fails for $x = 100\,\mathrm{fs}^2$. However, in our simulations we always obtain the correct result (see Fig. 2.22a). One

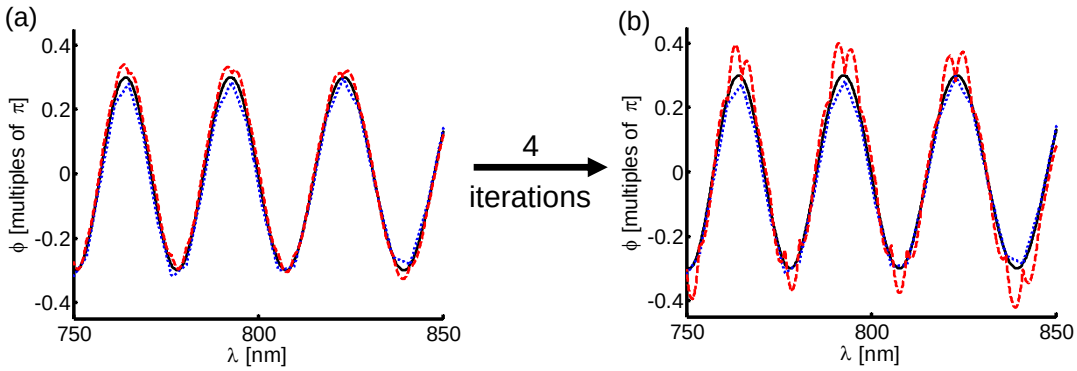

Figure 2.26: Effect of the finite spectral resolution $\delta\omega$ on single-beam homodyne SPIDER. Phase profile: $\phi_0 = x_1\pi\sin(x_2\frac{2\pi}{\Delta\omega}(\omega-\omega_0))$ with $(x_1, x_2) = (0.3, 2)$. Black solid line: target phase ϕ_0; blue dotted line: calculated phase ϕ_r; red dashed line: new SLM phase for the next iteration ϕ_n. (a) situation after the first iteration; (b) situation after the fourth iteration.

reason for this discrepancy might lie in the fact that the center of the quadratic phase ω_0 cannot be fixed by our method. Any quadratic phase centered at ω_0 can be expressed as a superposition of a quadratic phase around a different center ω_0' and a linear phase:

$$\begin{aligned}\phi &= x(\omega-\omega_0)^2 \\ &= x(\omega-\omega_0')^2 + x(\omega_0^2-\omega_0'^2) + 2x\omega(\omega_0'-\omega_0)\end{aligned} \tag{2.43}$$

Because single-beam homodyne SPIDER has no possibility to access absolute linear phases as detailed above, the phase center ω_0 is completely undetermined in a quadratic profile. As soon as ω_0' lies on one side of the laser spectrum the phases on the opposite side can assume large values resulting in multiple phase wrappings for the SLM to handle them. Once these perturbations are inserted a correct phase retrieval becomes much more difficult if not impossible.

In summary we showed that single-beam homodyne SPIDER is *a priori* a very elegant method to measure spectral phases. However, the range of accessible phase profiles is limited, though it is difficult to judge *a priori* whether a certain phase profile can be measured correctly [183]. As a general rule, on smaller scales phases should only contain moderate changes. Single-beam homodyne SPIDER is very successful in correcting for phase distortions and establishing a flat spectral phase. This confirms the results obtained in the Lim group [179]. Going beyond this, it is also possible to control certain well defined phase profiles by this method, but this procedure is very prone to errors resulting from even small levels of noise in the SHG spectra and from the iterative process, which is nonetheless mandatory to reliably measure a phase. As furthermore this technique is also limited in spectral resolution to the distance between the two phase jump positions, it is not applicable for a large number of phase profiles. Thus there is an interest to develop

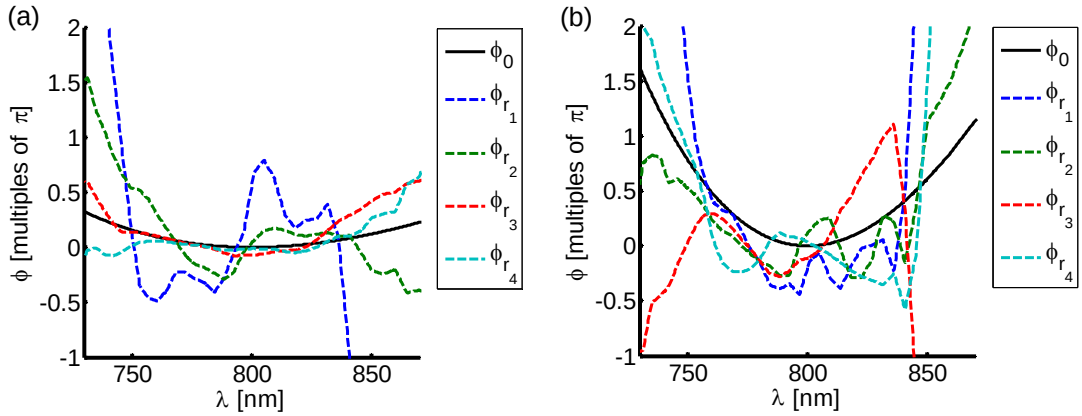

Figure 2.27: Creation of quadratic phase profiles ($\phi_0 = x(\omega - \omega_0)^2$) with single-beam homodyne SPIDER. (a) $x = 20$ fs^2; (b) $x = 100$ fs^2. ϕ_0: target phase; ϕ_{r_n}: measured phase after the nth iteration. See Fig. 2.24 for the spectral intensities of the pulse over the whole wavelength range.

new spectral phase retrieval methods or improve existing ones to be able to use them in microscopy. The next option could be to realize a collinear version of FROG. This would lead to a larger experimental complexity but would also be accompanied by a higher robustness in the phase retrieval.

Chapter 3

Polarization distortion effects in polarimetric two-photon microscopy

3.1 Introduction to polarization-resolved microscopy

In fluorescence and coherent nonlinear microscopy there exists a significant interest in the manipulation of the optical polarization through a microscope objective. This manipulation is a key ingredient in anisotropy imaging which attempts to gather information on the molecular order and organization in molecular and biomolecular media. Traditionally those studies are performed by using two states of incident polarization: s-polarized light where the electric field vector is directed perpendicular (s from the German *senkrecht*) to the plane of incidence and p-polarized light with the electric field vector in (or *parallel* to) the plane of incidence. They are sometimes also denoted H and V for horizontally and vertically polarized light with respect to a reference direction. The signal detection is as well performed according to two orthogonal directions, giving access to the parameters $I_{\parallel}$ and $I_{\perp}$, depending on the parallel or perpendicular configuration of the incident versus analyzed directions. But this scheme - because of its limited amount of accessible measurements - is only successful in cases where signal-emitting molecules possess an angular distribution of orientations with cylindrical symmetry, which reduces the amount of unknown parameters [184]. These are either the mean orientation or the width of the orientation distribution. Moreover, redundancies arise because of the impossibility to differentiate the case of an isotropic distribution from that of a molecular distribution at 45° relative to the s and p directions (see appendix B). However, despite these limitations fluorescence anisotropy imaging has led to functional contrasts in isotropic intracellular media [185, 186] and to the determination of the width of angular distributions of actin filaments [187] or lipids within the plasma membrane [188, 189, 133], both of which have a cylindrical symmetry. Also the mean molecular orientation angles of muscle fibers [190] and septin filaments [191] were measured in this way. But in general molecular and biomolecular media exhibit much more complex angular distributions that can differ strongly from pure cylindrical symmetries [192], and thus more refined polarimetric analyses are required.

In a complete polarimetric analysis, an incident linear polarization gets turned in the sample plane around an angle α relative to the X-axis, by rotating a half waveplate at the entrance of the microscope (Fig. 3.1a), and for each field orientation $\mathbf{E}(\alpha)$ the signal is recorded. Often it is additionally separated according to its components along the X- and the Y-axes, easily achieved by a polarization beam splitter. The resulting curve is usually displayed in a polar graph, where the radius corresponds to the signal intensity and the circumference to α (Fig. 3.1a). To get a better impression what kind of information gets communicated by this design let us consider several typical cases, exploring for instance the TPF contrast:

Fluorophores in an aqueous solution move and rotate quickly, so that in the time between the absorption and the subsequent fluorescence emission they completely changed their orientation and consequently the direction of the emission dipole moment becomes decorrelated from that of the absorption dipole and the emission pattern is isotropic. This is shown by a circle in the polar graph (Fig. 3.1b). Should the polarimetric response of such a fluorescent solution show other features as reduced signal intensities at certain angles α, it is an indication of distortions in the excitation field at those angles (this issue is discussed later in this chapter).

A very different kind of response is expected from samples made of *fixed dipoles*, where the emission dipoles cannot change their orientations with time. In a 1D crystal for example, all these dipoles are oriented parallel to each other along a certain direction ϕ_{dip}. The signal will be strongest when the field has the same orientation, that is $\alpha = \phi_{dip}$, and weakest when it is oriented perpendicular to the dipoles. Thus a two-lobe pattern can be seen (Fig. 3.1c). On the other hand for a sample of fixed dipoles but with random orientations such as a dried solution of fluorophores on a surface, there are always dipoles that get excited no matter which value α assumes and the total emitted signal will be constant. Contrary to the case of a solution, here the dipole positions are fixed and the signals I_X and I_Y are very different because of the polarized photoselection. Dipoles best excited by $E_X = E(\alpha = 0°)$ emit along X but not along Y and vice versa for dipoles best excited by $E_Y = E(\alpha = 90°)$. Therefore the polar graph shows two crossed two-lobe patterns (Fig. 3.1d), whose sum is still a circle as expected from isotropy.

Samples with fixed dipole positions but exhibiting a certain *disorder*, meaning that the individual dipole orientations do not coincide, but lie within a cone of possible orientations, show TPF polarimetric responses that reflect both the opening angle v of this cone and its orientation ρ within the sample plane. Thus these two parameters can be obtained from an analysis of the polarimetric data. Fig. 3.2 shows a number of TPF polarimetric responses for different (v, ρ)-pairs, where it is seen that polarimetric responses are quite sensitive to both the orientation and the degree of disorder of the molecular ensemble. For a more complete description of the model see appendix B.

The retrieval of orientational information from a polarimetric measurement is more accurate for nonlinear optical processes than for linear ones. Let us demonstrate this for fluorescence. As one-photon absorption is proportional to the square of the incident electric

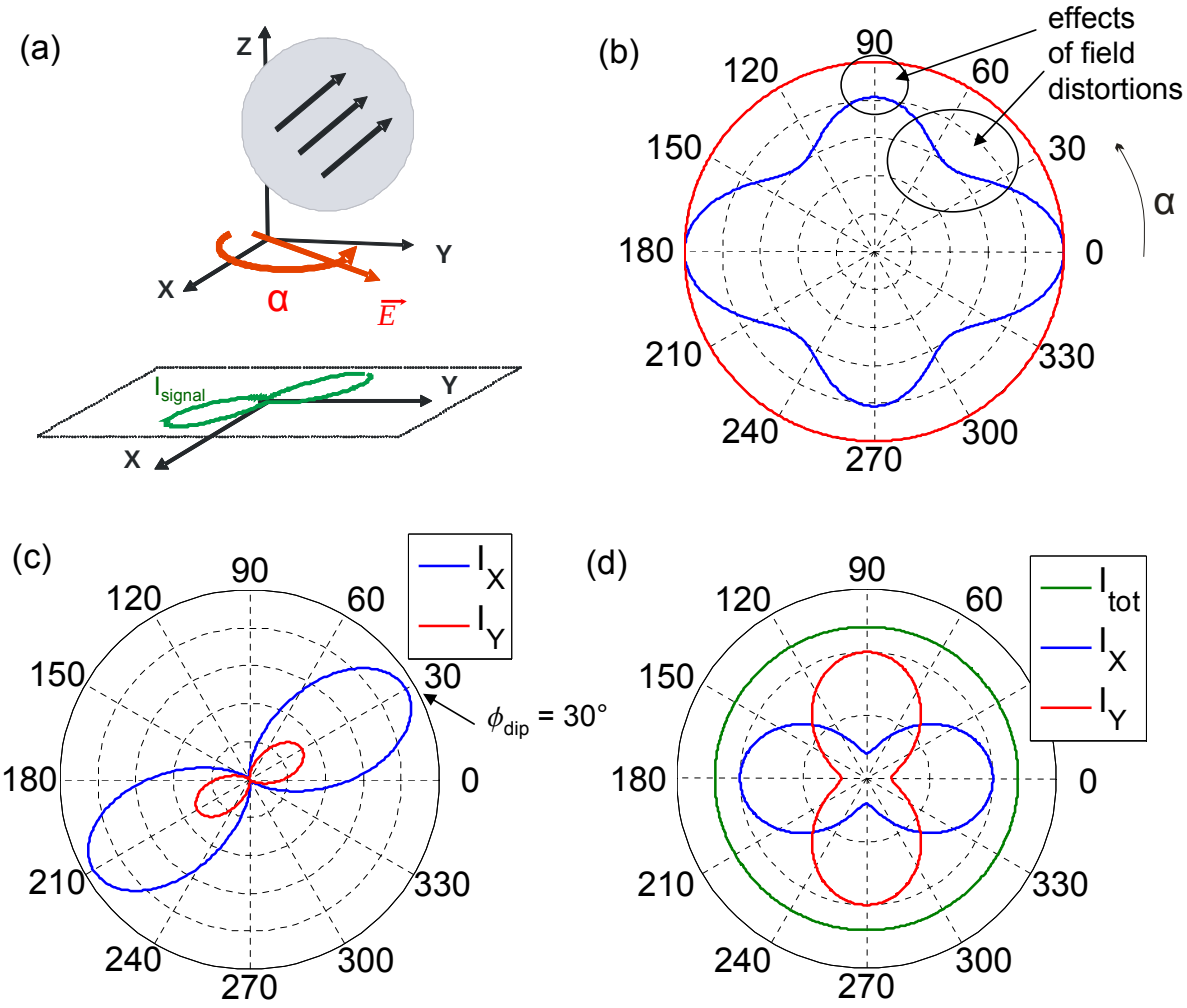

Figure 3.1: Typical polarimetric responses. (a) sketch of excitation conditions: the polarization of the incident field gets rotated in the (X, Y)-plane and the signal is recorded as a polar graph. (b) Polarimetric fluorescence response of a fluorophore solution: red line: no distortions of the incident field; blue line: typical response when distortions are present (see section 3.2). (c) Polarimetric fluorescence response of a sample with fixed dipoles oriented parallel to each other, for example a crystal: signal maximum at the orientation angle ϕ_{dip}. (d) Polarimetric fluorescence response of an assembly of fixed dipoles with random orientations. The total signal is α-independent, but its two components I_X and I_Y are strongly influenced by the field vector direction.

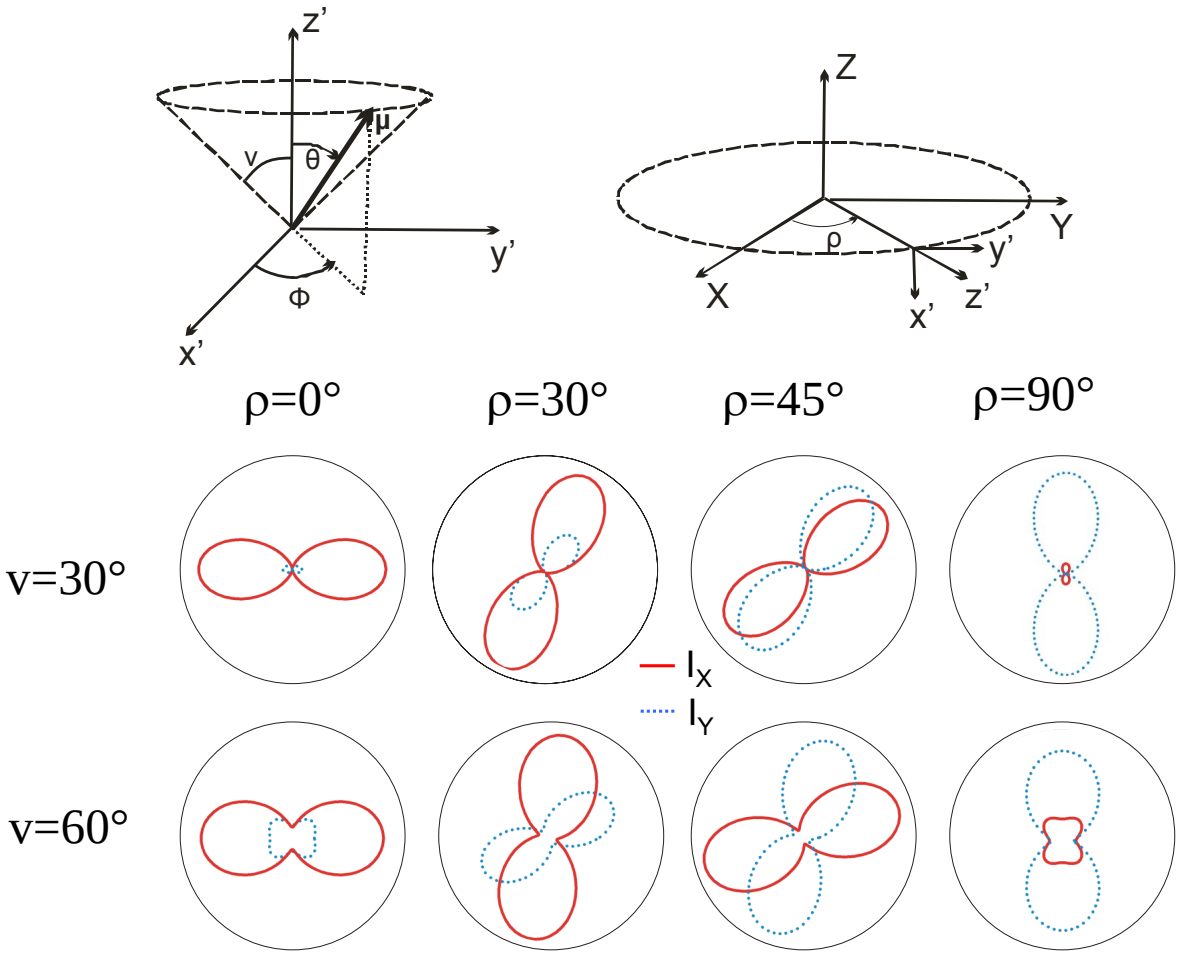

Figure 3.2: TPF polarimetric responses for a sample consisting of fixed nonlinear dipoles oriented along an angle ρ within the sample plane, exhibiting a certain disorder v (theoretical calculations) [184]. See appendix B for more information on the model.

field, the fluorescence of a fixed absorption dipole (at the angle ϕ_{dip}) will be proportional to the square of the cosine of the angle between this dipole and the polarization of the incident field α (as follows from Eq. (1.43)):

$$I^{1ph}(\alpha) \propto cos^2(\alpha - \phi_{dip}) \tag{3.1}$$

A two-photon absorption on the other hand is proportional to the fourth power of the incident field and thus the TPF response becomes:

$$I^{2ph}(\alpha) \propto cos^4(\alpha - \phi_{dip}) \tag{3.2}$$

The TPF polarimetric response is therefore more directional than that in the one-photon case as seen in Fig. 3.3, because of a more refined photoselection. A similar reasoning also

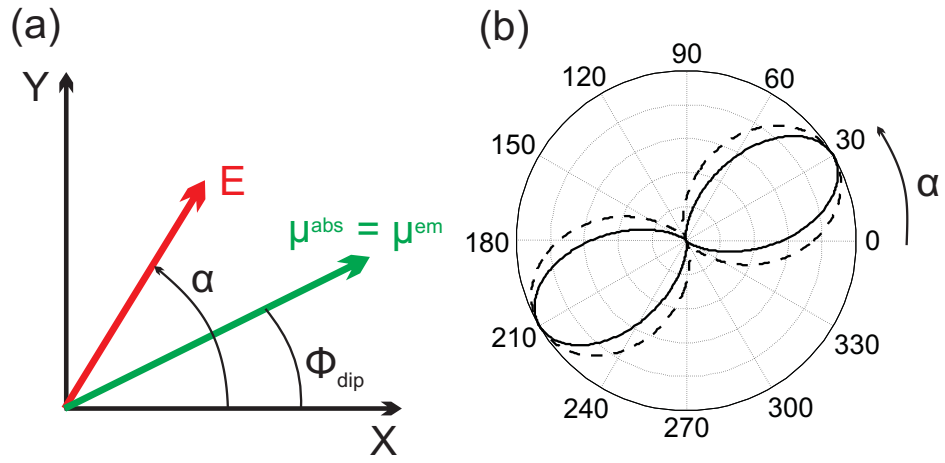

Figure 3.3: Polarimetric response of one and two-photon fluorescence. (a) sketch of excitation conditions: fixed absorption dipole $\boldsymbol{\mu}^{abs}$ at angle ϕ_{dip} and turning electric field polarization $\mathbf{E}(\alpha)$. (b) fluorescence intensity (radius) as a function of α ($\phi_{dip} = 30°$): dashed line: one-photon absorption ($\propto cos^2$); solid line: two-photon absorption ($\propto cos^4$).

holds for SHG and other nonlinear processes, where the directionality of the emitted signal becomes stronger with a higher order of the nonlinearity.

Nonlinear polarimetric studies also give access to more orientational information than standard anisotropy measurements [90, 76, 79, 89]. By controlling the polarization, THG signals emitted by birefringent crystals allow the determination of their orientation [99], and polarized CARS microscopy is capable to visualize the order of neuronal myelin [110]. With TPF and SHG it is possible to measure the chirality in collagen [134], determine the orientation of crystalline molecular systems [90] and of biological fibrils [95], and image the molecular order in lipid and cell membranes [184]. SHG polarimetry characteristics will be explained in more detail in chapter 4.

Apart from the measurement of molecular orientations polarimetric studies have also been used to improve imaging contrasts. When applied to scattering media such as biological tissues, the interpretation of the nonlinear signals will lead to techniques derived from ellipsometry such as the Mueller matrix formalism [193] or scattered light analysis based on Monte Carlo simulations [194], where the polarization analysis can potentially improve the image quality and resolution. For example, the auto-fluorescent background from biomolecules can be removed. Contrast enhancement of nonlinear microscopy has also been achieved by polarization pulse shaping [44, 49], however shaping techniques have not yet been applied (apart from the present work) to a full exploration of polarimetric responses.

All these polarization resolved microscopy techniques require that the excitation polarization state at the focal spot of the objective can be controlled, which is far from trivial. The polarization can be fixed without problems at a certain position within the excitation

beam path - for example by a linear polarizer -, but from there to the sample it may suffer from several perturbations that can significantly alter its state which in turn may lead to serious misinterpretations of the detected signals. This is particularly relevant for polarization shaping, where complex polarization states (see Fig. 2.3) have to be brought to the focal spot. In inverted microscopy, where the polarization gets fixed at the entrance of the microscope, there are two sources of these distortions: reflection optics - first and foremost the dichroic beam splitter that separates the excitation from the emitted signal (see Fig. 2.8) - and high numerical aperture (NA) focusing.

Here, we describe the effect of reflection optics and high NA focusing on the TPF polarization response in model samples. We present a simple and robust technique to retrieve the degree of dichroism and ellipticity in the sample plane of a nonlinear microscope. Additionally, the spatial distortions of the polarization induced by high NA focusing are assessed by numerical calculations (see appendix C).

3.2 Polarization distortion from optics probed by two-photon fluorescence

The effect of the beam splitter on the polarization state is described by a dichroism factor and an ellipticity. Both parameters can be measured by a direct analysis of the polarization state at the entrance of the objective [90]. Recently, an *in situ* characterization method has been developed using the direct measurement of the fluorescence from an isotropic sample made of fixed molecules of random orientations in a polymer film. This approach relied on the same type of polarimetric measurements as usually performed on a sample. While it is an *in situ* technique that does not require complete ellipsometric measurements, it suffered however from the possible contribution of partial depolarization in the signal, occurring from the homo-excitation energy transfer between molecules and their neighbors. The homo-FRET contribution furthermore depends on the molecular concentration. Another problem of this method is the possible angle between the excitation and emission dipoles of the fluorophores which depend on the employed molecules and on their concentration. Because this information is difficult to obtain, the method is not always suited. Here we will rely on the complete depolarization by a solution of fluorophores to circumvent these problems.

In standard polarimetry an incident linear polarization is rotated at the entrance of the microscope. The electric field in the sample plane can be decomposed on the (X, Y, Z) macroscopic frame (Fig. 3.4). As introduced in section 1.4, the TPF intensity analyzed along a given polarization direction i is proportional to the two-photon absorption probability multiplied by the one-photon emission probability in that direction which, in a molecular ensemble, can be written as (see Eq. (1.50)):

$$I_i(\alpha) \propto \int\int\int \overline{|\boldsymbol{\mu}_{abs}(\boldsymbol{\Omega}, \mathbf{r}) \cdot \mathbf{E}(\alpha, \mathbf{r})|^4} |\mathbf{E}_{em}(\boldsymbol{\Omega}, \mathbf{r}, \mathbf{k}) \cdot \mathbf{u}_i|^2 f(\boldsymbol{\Omega}) \mathrm{d}\boldsymbol{\Omega} \mathrm{d}\mathbf{r} \mathrm{d}\mathbf{k} \tag{3.3}$$

where $\overline{...}$ represents the time average, $f(\mathbf{\Omega})$ denotes the normalized molecular orientation distribution function with the angle set $\mathbf{\Omega} = (\theta, \phi)$ (Fig. 3.4), and $i = (X, Y)$ is the analyzed direction for a field propagating along Z. The proportionality sign in Eq. (3.3) allows omitting efficiency and collection factors that do not come into play in a relative polarization measurement which is the case in our studies. The incident electric field $\mathbf{E}(\alpha, \mathbf{r})$, polarized in the direction α (with respect to the X-axis) interacts at location $\mathbf{r}$ with the absorption dipole $\boldsymbol{\mu}_{abs}(\mathbf{\Omega}, \mathbf{r})$ whose orientation is given by the angle set $\mathbf{\Omega}$. The far

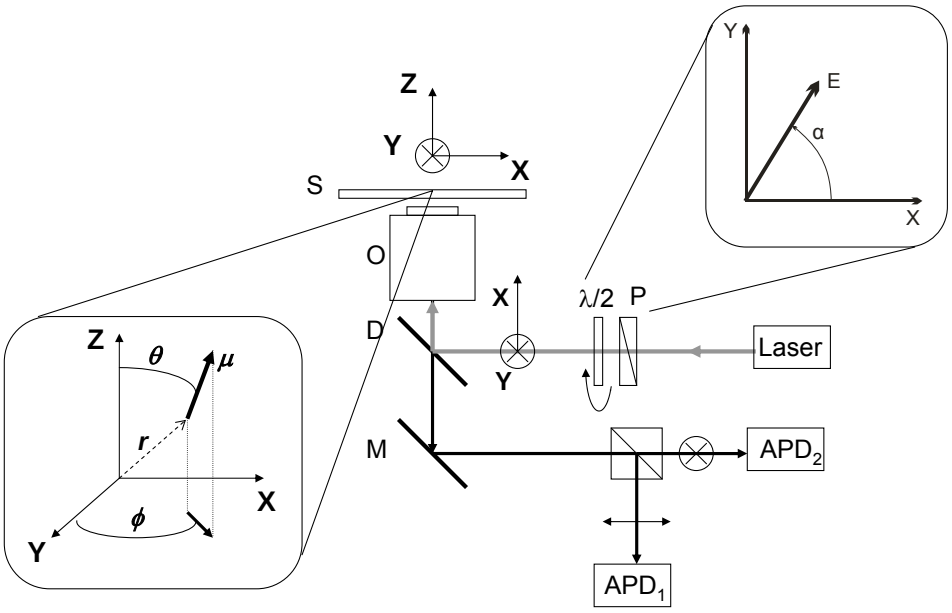

Figure 3.4: Geometry of the polarimetric two-photon fluorescence microscopy setup. O: objective (NA 1.2, x 60, Water Immersion); D: Dichroic mirror; M: mirror; APD1,2: avalanche photodiodes detecting respectively the X and Y components of the signal; P: polarizer; $\lambda/2$: rotatable half waveplate to turn the linear polarization within the (X, Y)-plane around the angle α; $\boldsymbol{\mu}$: fluorescence excitation dipole vector at position r and orientation $\Omega = (\theta, \phi)$.

field $\mathbf{E}_{em}(\mathbf{\Omega}, \mathbf{r}, \mathbf{k})$ is radiated by the emission dipole $\boldsymbol{\mu}_{em}(\mathbf{\Omega}, \mathbf{r})$ in the propagation direction $\mathbf{k}$, with $\mathbf{E}_{em}(\mathbf{\Omega}, \mathbf{r}, \mathbf{k}) \propto \mathbf{k} \times (\mathbf{k} \times \boldsymbol{\mu}_{em}(\mathbf{\Omega}, \mathbf{r}))$. $\mathbf{u}_i$ is a normalized vector in the analysis direction i. The incoherent summation of the fluorescence signal from individual molecules over all their positions and orientations is denoted by $\mathrm{d}\mathbf{\Omega}\mathrm{d}\mathbf{r}$. $\mathrm{d}\mathbf{k}$ on the other hand describes the integration over the emission propagation angles within the collection aperture. In a polarimetric measurement α is the tuning parameter, its continuous variation defining the polarization response from the sample from which information on the distribution function $f(\mathbf{\Omega})$ can be gained. This confirms that contrary to anisotropy measurements which rely on two excitation states $\left(\alpha = 0, \frac{\pi}{2}\right)$ and two analysis directions $(i = X, Y)$, the tunability in α allows providing more complete measurements of the orientation and symmetry of this distribution [87]. The incoherent nature of the fluorescence is reflected in the fact that the final integration over all possible molecular orientations $(\mathbf{\Omega})$, dipole positions within the

excitation volume ($\mathbf{r}$), and emission angles within the collection aperture ($\mathbf{k}$) is performed over the intensities of both the absorption and the emission part of the process. Coherent nonlinear processes such as SHG can also be derived from this approach, but then fields radiated from the induced nonlinear dipoles rather than intensities have to be summed up [87, 90] (see section 1.4).

For an isotropic liquid under two-photon excitation ($f(\mathbf{\Omega}) = 1$) the rotational diffusion time of the molecules is shorter than their typical fluorescence lifetimes and consequently the orientations of the emission dipoles are decorrelated from those of the absorption dipoles. Eq. (3.3) can then be written as:

$$I_i(\alpha) \propto \int\int \overline{|\boldsymbol{\mu}_{abs}(\mathbf{\Omega}, \mathbf{r}) \cdot \mathbf{E}(\alpha, \mathbf{r})|^4} \mathrm{d}\mathbf{\Omega}\mathrm{d}\mathbf{r} \int\int\int |\mathbf{E}_{em}(\mathbf{\Omega}', \mathbf{r}', \mathbf{k}) \cdot \mathbf{u}_i|^2 \mathrm{d}\mathbf{\Omega}'\mathrm{d}\mathbf{r}'\mathrm{d}\mathbf{k} \tag{3.4}$$

where the integration is performed over independent variables $\mathbf{\Omega}$ and $\mathbf{\Omega}'$ for the absorption and emission dipoles $\boldsymbol{\mu}_{abs}(\mathbf{\Omega}, \mathbf{r})$ and $\boldsymbol{\mu}_{em}(\mathbf{\Omega}', \mathbf{r}')$. Thus absorption and emission become independent and separable processes. Since the emission probability does not depend on the incident polarization angle α it contributes only as an multiplicative constant when the polarization gets turned. Therefore the collection aperture has no effect on the polarimetric response of the emitted signal and effects only its global efficiency. Eq. (3.4) therefore simplifies to:

$$I_i(\alpha) \propto C_i \int\int \overline{|\boldsymbol{\mu}_{abs}(\mathbf{\Omega}, \mathbf{r}) \cdot \mathbf{E}(\alpha, \mathbf{r})|^4} \mathrm{d}\mathbf{\Omega}\mathrm{d}\mathbf{r} \tag{3.5}$$

where the i-independent factor C_i, containing the emitted field radiation factor, may vary for different analyzing directions due to different efficiencies along X and Y. (I_X and I_Y measurements give therefore a direct access to this unbalanced collection factor.) For an isotropic solution $\boldsymbol{\mu}_{abs}$ of each dipole is expressed by a radial unit vector (see Fig. 3.4):

$$\boldsymbol{\mu}_{abs} = \begin{pmatrix} \sin\theta\cos\phi \\ \sin\theta\sin\phi \\ \cos\theta \end{pmatrix} \tag{3.6}$$

This decoupling of excitation and emission does not occur in materials of fixed molecules such as a polymer matrix [90]. Consequently, the polarimetric response can then be affected by correlation-related issues such as fluorescence energy transfer (FRET) or non-zero angles between the absorption and emission dipoles in the used molecules. By choosing an isotropic solution of fluorophores instead, we ensure that our results do not depend on the molecules and their concentration. Eq. (3.5) thus shows that measuring the fluorescence from a solution is an interesting way to provide information on the polarization distortion of an electric field independently from the used molecules.

As mentioned above, an incoming beam that originates from the rotation of a linear polarization is very likely to be affected by a degree of ellipticity and dichroism. Both effects arise from the reflections of the beam at mirrors and dichroic beam splitters, which are made of multilayer dielectric thin films usually not well controlled for field phases. In

the latter they can be strongly frequency dependent, especially as one approaches the cutoff frequency that separates the reflective and transmissive spectral regions of the dichroic. The incident amplitude of the field at the entrance of the objective can be written as [195]:

$$\mathbf{E}(\alpha, \delta, \gamma) \propto \begin{bmatrix} \cos\alpha \\ (1-\gamma)\sin\alpha\, e^{i\delta} \\ 0 \end{bmatrix} \tag{3.7}$$

with δ being the phase difference (ellipticity) and γ the amplitude factor (dichroism) between the two perpendicular polarization states s and p (defined by $\alpha = 0$, $\alpha = \frac{\pi}{2}$ corresponding to the X and Y directions in the sample plane) that arises from different reflectivities for these two states. Fig. 3.5 illustrates the effect of δ on the electric field. The two fundamental polarizations $\alpha = \left(0, \frac{\pi}{2}\right)$ are kept linear whatever the value of the

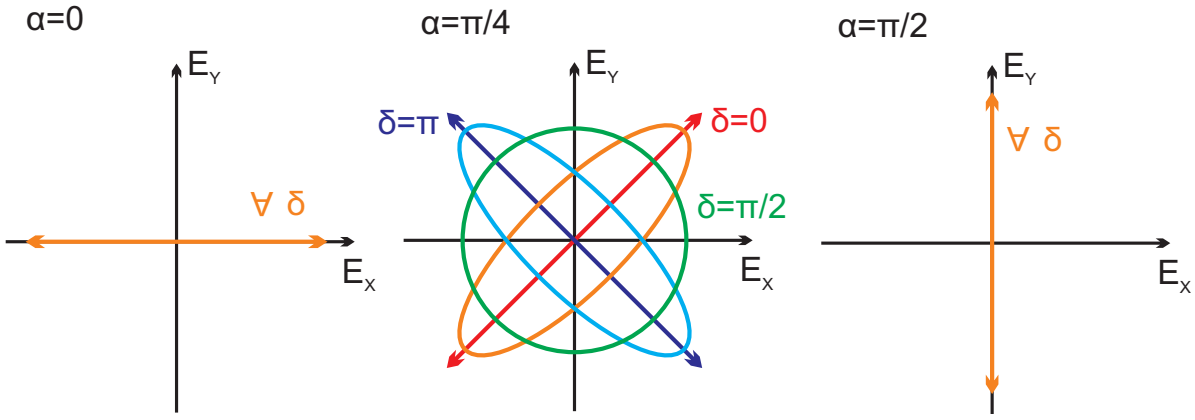

Figure 3.5: Effect of the ellipticity δ on the electric field $\mathbf{E}$ for different polarization angles α. Left: $\alpha = 0$ - the field is unaffected by δ and remains polarized along X. Middle: $\alpha = \frac{\pi}{4}$ - the field's polarization is strongly influenced by δ. Right: $\alpha = \frac{\pi}{2}$ - the field is unaffected again by δ and remains polarized along Y.

ellipticity. However, for intermediate polarizations, especially around $\alpha = \frac{\pi}{4}$ and $\alpha = \frac{3\pi}{4}$, the polarization state of the field strongly depends on the ellipticity. While for $\delta = 0$ it still remains linearly polarized along α, it becomes more and more elliptical around α when δ increases up to $\frac{\pi}{2}$. At this value the field can even become circularly polarized when $\alpha = \frac{\pi}{4}$. For higher values of δ up to π the ellipticity decreases, but the ellipse switches side and is oriented along $\pi - \alpha$. At $\delta = \pi$ the field is linear again, but along $\pi - \alpha$. The effect of γ is easier seen: for $\gamma > 0$ the field gets reduced in Y relative to X, while for $\gamma < 0$ the opposite holds.

An extra Z-axial component of the field will also be present in the focal plane of the objective, however the distortion by the high NA is not taken into account at this stage due to their invariance with respect to α. Section 3.4 addresses this issue in ordered samples.

As the fluorescence emission of an isotropic solution does not depend on the analysis direction, polarization state distortions brought by the reflection optics can be modeled by plane wave illumination based on Eqs. (3.5) and (3.7).

Figure 3.6 shows the effect of the ellipticity δ and the dichroism γ in a polar representation of the fluorescence intensity as a function of the incident polarization angle α in a fluorescent solution. In the case of a perfect system, where no ellipticity and dichroism

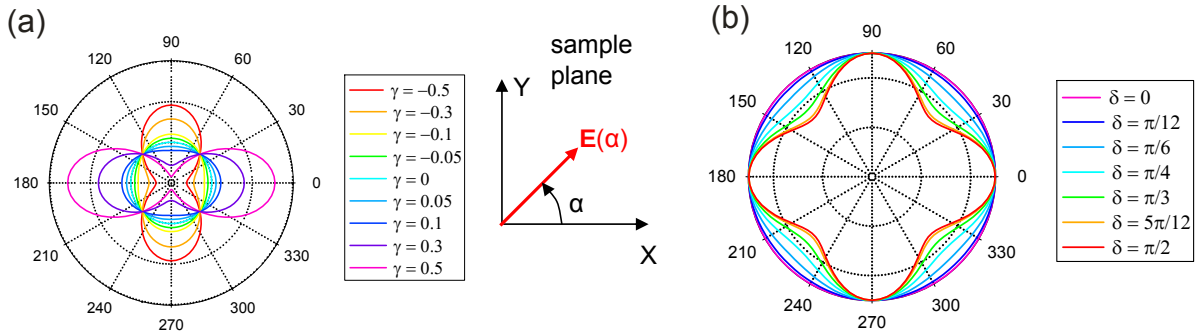

Figure 3.6: Effect of the dichroic mirror parameters δ (in rad) and γ on the TPF polarization response for a solution of Rh6G. (a) influence of the ellipticity δ for an amplitude factor $\gamma = 0$; (b) influence of γ for $\delta = 0$. Such polar plots are expected to be identical for the I_X and I_Y analysis directions.

factors arise, the TPF response is α-independent, as expected from an isotropic solution. Since the two principal polarizations ($\alpha = 0$ and $\alpha = \frac{\pi}{2}$) remain linear no matter which value δ assumes, the ellipticity cannot change the TPF signal at these positions. However, at intermediate polarization directions (especially around $\alpha = \frac{\pi}{4}$ modulo $\frac{\pi}{2}$) a non-zero δ leads to a more or less elliptic electric field (see Fig. 3.5) which in turn reduces the excitation efficiency at these angles. This is due to the fact that the two-photon excitation scales with the fourth power of the electric field (see Eq. (3.3)) and the field's amplitude reaches its maximum for a linear polarization while it gets more evenly distributed in time for elliptical polarizations, thus decreasing its peak value and consequently the efficiency of two-photon fluorescence excitation and nonlinear optical processes in general. On the other hand γ affects mainly the intensities in the X and Y polarization directions. A $\gamma > 0$ describes a system of reflection optics where the reflectivity in the Y direction is smaller than for X-polarized light, leading to a smaller electric field E_Y compared with E_X at the sample location and thus to a smaller TPF signal as well when the field is Y-polarized. The opposite situation is described by $\gamma < 0$. In general, mirrors and dichroic mirrors are made polarization independent in the sense that s (X) and p (Y) reflection efficiencies are almost identical. We will see later that the γ-values found experimentally are close to zero.

It should be noted that for an isotropic solution of fluorophores at $\gamma \approx 0$ the dependence of the polarimetric response on δ is $\frac{\pi}{2}$-periodic (see Fig. 3.6), therefore the deduction of δ is ambiguous. The TPF intensity is only affected by the amount of ellipticity present in the electric field but not on the orientation of the ellipse. For $\delta = 0$ for example a continuous

variation of α from 0 to 2π leads to a counterclockwise rotation of the polarization in the (X, Y)-plane. On the other hand for $\delta = \pi$ Eq. (3.7) transforms to:

$$\mathbf{E}(\alpha, \delta, \gamma) \propto \begin{bmatrix} \cos\alpha \\ (1-\gamma)\sin\alpha\, e^{i\pi} \\ 0 \end{bmatrix} = \begin{bmatrix} \cos\alpha \\ -(1-\gamma)\sin\alpha \\ 0 \end{bmatrix} \tag{3.8}$$

and thus to a clockwise rotation of a linear polarization under the increase of α (Fig. 3.7a). In both cases, however, the polarization remains linear and the TPF signal is identical. The same argument is true for all pairs of δ centered around $\frac{\pi}{2}$. This effect, due to the isotropic nature of the emitted fluorescence from a solution will however disappear in anisotropic media. Therefore only polarization responses from non-isotropic molecular angular distributions are able to remove the ambiguity of the $\left[0\ \frac{\pi}{2}\right]$ versus the $\left[\frac{\pi}{2}\ \pi\right]$ range for δ. This is illustrated in Fig. 3.7b where a fixed 1D fluorescent sample (such as a crystal made of parallel dipole molecules) is modeled with an intermediate orientation of $\frac{2\pi}{9}$ (40°) relative to X. In this case we used $f(\mathbf{\Omega}) = \delta(\mathbf{\Omega} - \mathbf{\Omega}_0)$ in Eq. (3.3) and fixed all dipoles within the excitation volume along the direction $\mathbf{\Omega}_0 = (\theta_0, \phi_0) = \left(\frac{\pi}{2}, \frac{2\pi}{9}\right)$. The resulting TPF polar-

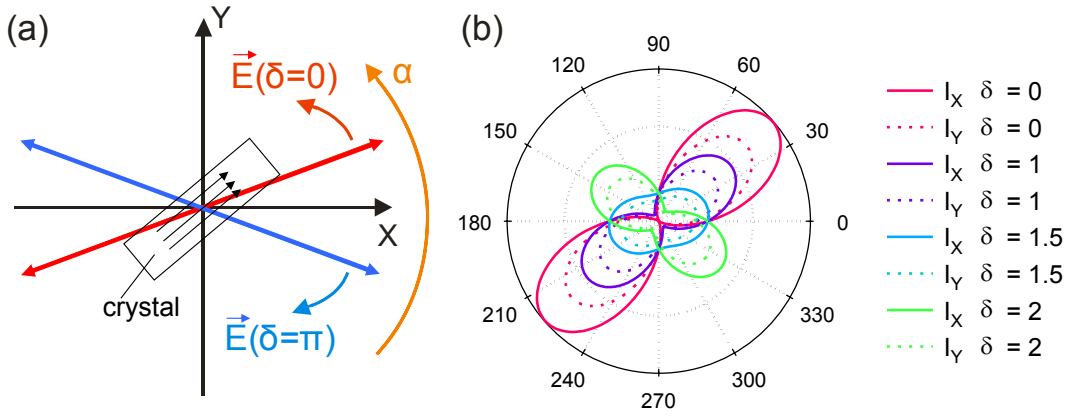

Figure 3.7: Ambiguity of dichroic parameter measurements. (a) actual rotation of the electric field under increase of α for $\delta = 0$ (red) and $\delta = \pi$ (blue). (b) removing the ambiguity: 1D fluorescent sample oriented at $(\theta_0, \phi_0) = \left(\frac{\pi}{2}, \frac{2\pi}{9}\right)$ in the sample plane (see Fig. 3.4 for angle definitions), $\gamma = 0$. Continuous lines: I_X, dashed lines: I_Y.

ization response is seen to be strongly dependent on the polarization parameters. When $\delta = 0$, the polarization response is anisotropic in the $\frac{2\pi}{9}$ (40°) direction as expected from the 1D symmetry of the sample. As the ellipticity increases, the polarization response changes its direction until reaching another quadrant for $\delta > \frac{\pi}{2}$. Thus an easy discrimination of the range of the ellipticity is possible: a polarization response stays in the quadrant of the sample orientation for $0 < \delta < \frac{\pi}{2}$, whereas it reaches the next quadrant for $\frac{\pi}{2} < \delta < \pi$, due to polarization rotation. This example also emphasizes the detrimental influence of in-plane polarization ellipticity when performing polarimetric measurements, the response

being strongly distorted for high ellipticities.

Due to the different angular regions of the polarization response in which the dichroic parameters γ and δ manifest themselves, a continuous rotation of the incident polarization allows the extraction of these parameters induced by the dichroic beam splitter with an ellipticity wrapped in the $\left[0\ \frac{\pi}{2}\right]$ range, whose ambiguity can eventually be removed with an anisotropic sample. The (γ, δ) determination requires in fact only three measurements $I(\alpha = 0)$, $I\left(\frac{\pi}{4}\right)$, $I\left(\frac{\pi}{2}\right)$ leading to a unique solution. Fig. 3.8 shows the cartographies of the ratios $\frac{I\left(\frac{\pi}{2}\right)}{I(0)}$ and $\frac{I\left(\frac{\pi}{4}\right)}{I(0)}$ in a (γ, δ) coordinate map. A given value of the ratio $\frac{I\left(\frac{\pi}{2}\right)}{I(0)}$ corresponds to a vertical line in the respective (γ, δ)-map (Fig. 3.8a), since these two polarization angles are not influenced by δ. On the other hand a given value of the ratio $\frac{I\left(\frac{\pi}{4}\right)}{I(0)}$ produces a (γ, δ)-dependent curve (Fig. 3.8b). The point of intersection between both of these traces then gives the only set of dichroic parameters to satisfy both ratios simultaneously, thus determining both δ and γ. However, taking into account experimental noise, the solution space for each ratio will no longer be a single line but rather a band with a certain margin of error, leading to a range of solution sets for the dichroic parameters (Fig. 3.8c). For a

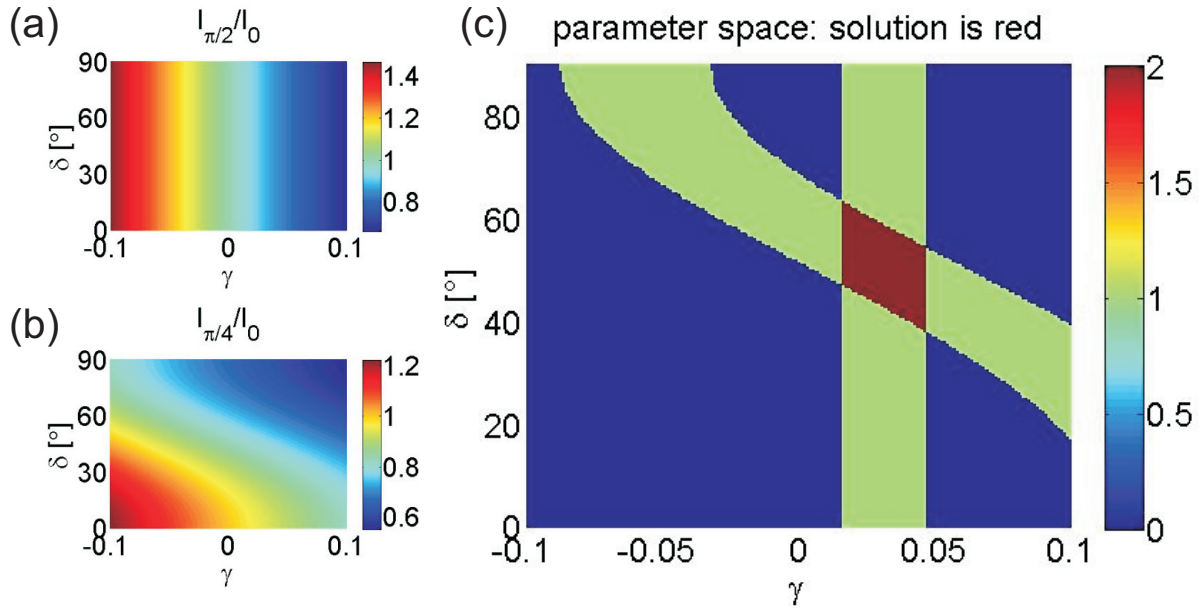

Figure 3.8: (γ, δ) coordinate maps. (a) ratio $\frac{I\left(\frac{\pi}{2}\right)}{I(0)}$; (b) ratio $\frac{I\left(\frac{\pi}{4}\right)}{I(0)}$; (c) solution (red space) including experimental error margins for a three-point fit based on a series of six measurements with $\lambda = 900\,\text{nm}$; $\frac{I\left(\frac{\pi}{2}\right)}{I(0)} = 0.89$, $\frac{I\left(\frac{\pi}{4}\right)}{I(0)} = 0.76$; the margin of error for both ratios was calculated to be 5.5%.

better experimental estimation a fit of the whole polarization dependent TPF-signal should be considered (see section 3.3) and not only one of three points.

Note that while the beam reflection on the dichroic mirror can lead to crucial effects, the backward detection of the emitted signal (either fluorescence or SHG) is not affected by the transmission of this signal through the dichroic mirror. Since its optical axes s and p also correspond to the analysis X and Y detection of the signal, any phase shift imposed to the detected field along these directions is invisible in the measured intensities which are the squares of the absolute field values and thus phase-insensitive. In addition, a dichroism factor in transmission only induces a difference in the magnitude of the X and Y responses that can be measured and later corrected for.

At last, note that this measurement is made in the same configuration as the other studies undertaken in this work; it therefore serves as a calibration step before any polarization shaping measurements are performed.

3.3 Measurement of dichroic parameters

As the performance of all reflection optics and in particular the dichroic mirror is wavelength-dependent, the calibration procedure described above has to be carried out at various λ. This is particularly relevant in the context of polarization shaping experiments, since a wavelength range of up to 100 nm can be explored in a single pulse made of complex polarization encoding. That is why we chose to measure $\gamma(\lambda)$ and $\delta(\lambda)$ with the help of a spectrally more narrow wavelength tunable laser (see page 54). The beam is propagated through the two-photon microscopy inverted set-up shown in Fig. 3.4. After the passage of a horizontal polarizer the field's polarization can be rotated by an achromatic half waveplate mounted in a step rotation motor. The incident beam is reflected by a dichroic beam splitter (650DCXP Chroma, Rockingham, VT) before being focused by a high NA (x 60, NA = 1.2) water immersion objective into a solution of free Rhodamine 6G (Rh6G) diluted in water (at a concentration of about $10^{-4}\,\frac{\text{mol}}{\text{l}}$). The generated TPF signal gets collected by the same objective, traverses the dichroic beam splitter and is finally divided by a polarization beam splitter according to its principal polarization axes and detected by two avalanche photodiodes (APD). For polarimetric measurements the APD signal integration time per orientation α of the half waveplate is 20 ms.

To determine the dichroic parameters γ and δ we opted against the three-point-fit explained in section 3.2 due to its rather large error margin but chose instead to fit the whole polarization dependent TPF signal. In a first step, theoretical polarimetric responses were calculated for a large variety of (γ, δ)-pairs and compared with our experimental data, the sum of mean squares

$$\chi^2(\gamma, \delta) = \sum_{\alpha} \left(I_{exp}(\alpha) - I_{theo}(\alpha, \gamma, \delta)\right)^2 \tag{3.9}$$

being an indication of the concordance.

Fig. 3.9a shows the dependence of χ^2 on γ and δ for a measurement at $\lambda = 900$ nm. Only one minimum exists. The same is true for all other tested cases. This allows the use of

a fitting procedure starting at an arbitrary point within the (γ, δ)-space that minimizes χ^2 by alternately varying both parameters until a stable minimum is found. There is no need for more advanced searching algorithms that for example include some addition of noise to allow jumping out of local minima or that work with multiple starting points to increase the chances to reach the global minimum [196], because in the (γ, δ) configuration space such local minima do not exist. The best fit for the presented case is depicted in Fig. 3.9b. Note that a slight asymmetry is observed in the experimental polarization response, which

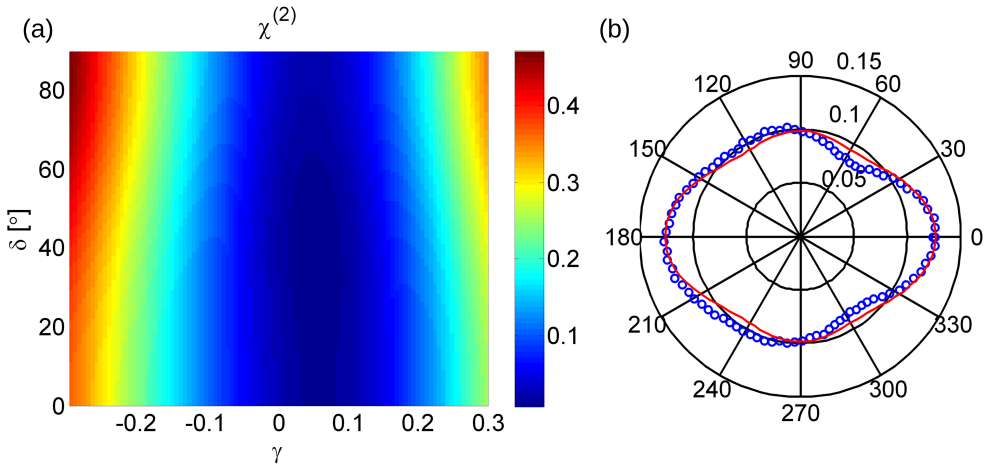

Figure 3.9: Experimental measurement of a polarimetric response from a Rh6G solution excited at $\lambda = 900\,\text{nm}$ using a 650DCXP (Omega Optical, Brattleboro, VT) dichroic mirror. (a) χ^2 parameter represented for a range of (γ, δ); (b) experimental points (dots) and corresponding best fit (continuous line).

is due to a slight misalignment of the beam path. The consequence is a slight increase in the ellipticity's error margin which still only amounts to $10^{-2}\,\text{rad}$.

The results of this approach for a large variety of wavelengths are shown in Fig. 3.10 together with some examples of the corresponding TPF signals. As stated above, the determination of δ is made within the $\left[0\ \frac{\pi}{2}\right]$ range. The obtained values for the dichroic parameters exhibit remarkably small error margins. δ can be determined with a precision of about 1° which is a great improvement to the three-point-fit presented above where the uncertainty was of the order of 10° (see Fig. 3.8). For γ, which describes the variation of the field strength compared to 1 (Eq. (3.7)), both fitting methods lead to error margins of less than 2%.

In order to confirm the retrieved parameters, we determined the expected γ and δ values from the dichroic mirror at 45° incidence by ellipsometry (GESP5, Sopralab, Courbevoie, France). This was done at the ENS Cachan, France. In ellipsometry measurements the reflection coefficients r for p- and s-polarized light (E_p and E_s) are measured. They are

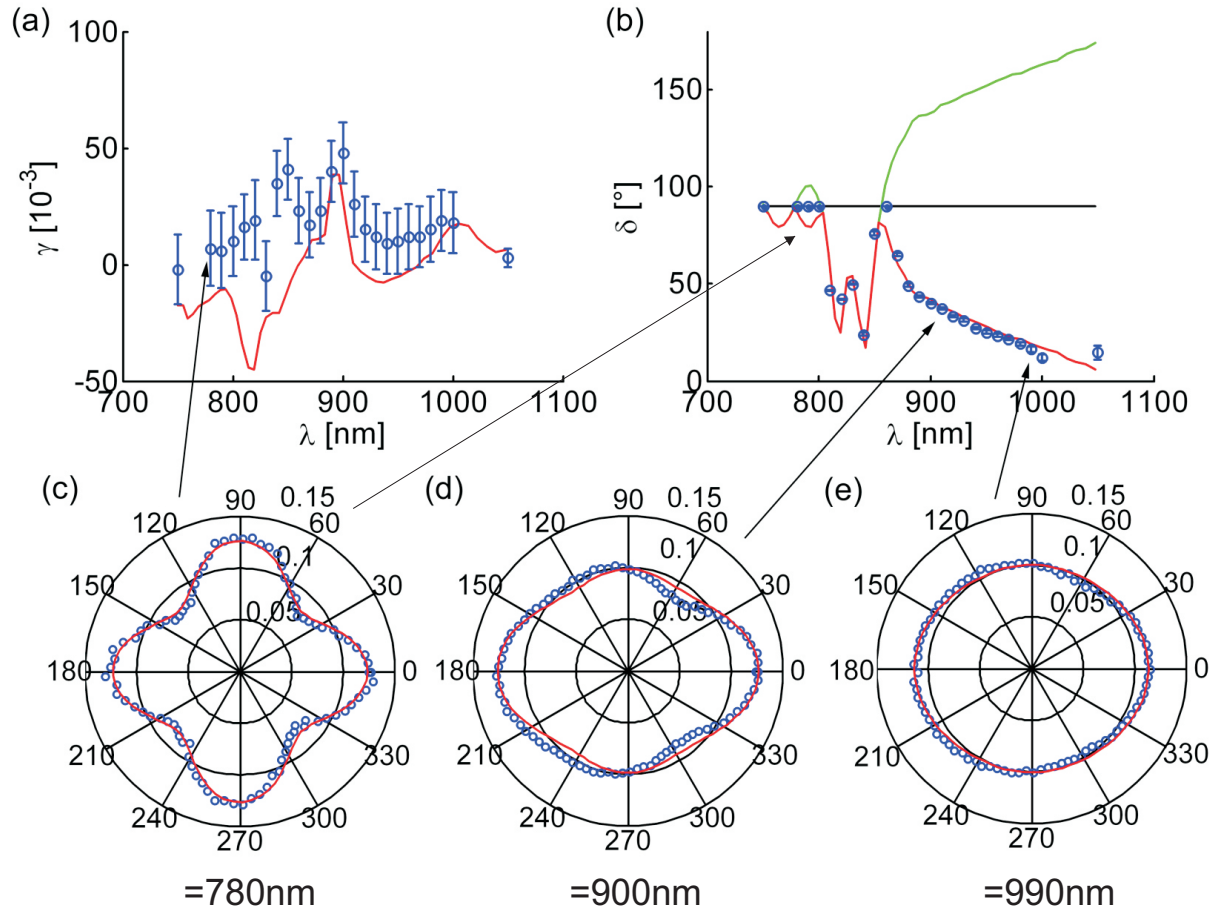

Figure 3.10: γ (a) and δ (b) parameters deduced from the TPF polarization responses (dots) and ellipsometry data (continuous line) of the dichroic mirror used for two-photon fluorescence (650DCXP), at various incident wavelengths. Each experimental point results from a series of 6 measurements. The green line in (b) corresponds to the δ ellipsometry data while the red one is wrapped in the $\left[0\ \frac{\pi}{2}\right]$ range for comparison with polarimetric measurements. (c-e) TPF polarization responses and fits (red curves) at three different wavelengths: (c) 780 nm; (d) 900 nm; (e) 990 nm.

defined as:

$$r_p = \frac{E_{pr}}{E_{pi}} = |r_p| e^{i\varphi_p}$$
$$r_s = \frac{E_{sr}}{E_{si}} = |r_s| e^{i\varphi_s} \tag{3.10}$$

with E_i as the incident and E_r the reflected fields. In practice the quotient:

$$\frac{r_p}{r_s} = \tan\psi e^{i\Delta} \tag{3.11}$$

is determined from which the two parameters $\tan\psi$ and $\cos\Delta$ can be retrieved [197]. They are directly related to γ and δ via:

$$\gamma = 1 - \tan\psi \tag{3.12}$$
$$\delta = \arccos(\cos\Delta) \tag{3.13}$$

Because Δ is accessed directly it does not suffer from any ambiguities. As can be seen in Fig. 3.10, the measured parameters in the two-photon fluorescence microscope are in very good agreement with the ellipsometry measurement for the whole wavelength range explored. The data comparison necessitated a phase wrapping of the ellipsometric data in the $\left[0\ \frac{\pi}{2}\right]$ range. This agreement confirms that γ and δ are almost exclusively caused by the dichroic itself. The slight overestimation of γ in Fig. 3.8a compared to the ellipsometry method probably arises from two effects: On the one hand, there may be small contributions of other optical components in the beam path other than the dichroic. And on the other hand the generated TPF signal has to pass the dichroic as well. While this has no effect on the measured δ as mentioned above, the signal is subject again to a dichroism factor as different polarizations may have different transmission efficiencies in the wavelength range of the signal. Because the form of the TPF emission spectrum is nearly independent of the excitation wavelength (Kasha's rule - see page 32) one would expect a constant offset over the whole excitation wavelength range, which is indeed observed. In any case the deviations between the accurate γ-values obtained by ellipsometry and those measured by our approach are nonetheless in very good agreement, as γ describes variations from 1, and thus the error remains below 5% even if this second interaction with the dichroic and the contributions of all other optical elements are neglected. Note that while the dichroic factor γ is seen to lie close to 0 (compared to 1), ensuring only small deviations of the amplitude $\frac{p}{s}$ from 1, the ellipticity caused by the dichroic mirror can reach high values far above $\frac{\pi}{2}$. This causes an intermediate incoming polarization to become elliptic and potentially rotated which strongly affects polarization responses (Fig. 3.7b). Other two-photon excitation dichroic mirrors studied with the same technique showed similar behaviors, especially close to their cut-off wavelength. To illustrate the dramatic changes brought by in-plane ellipticity on experimental polarization responses in anisotropic samples, we measured a 1D sample made of oriented fluorescent molecules along a macroscopic crystal

axis, whose orientation can be identified visually. This Perhydrotriphenylene (PHTP)-4-Dimethylamino-40-nitrostilbene (DANS) co-crystal, characterized in a previous work [89], was oriented in the (X, Y)-plane ($\theta_0 = 90°$) at an angle ϕ_0 close to 30° in the sample plane (Fig. 3.11). As these crystals have sizes in the millimeter range, their orientation angle can be determined without ambiguity. The fitting of the polarization responses with the 1D crystalline model using the previously determined parameters γ and δ leads to a crystal orientation of $(\theta_0, \phi_0) = (90°, 29°)$, which is in close agreement to the initially set orientation as seen in Fig. 3.11a. While at an excitation wavelength of $\lambda = 825\,\text{nm}$ the po-

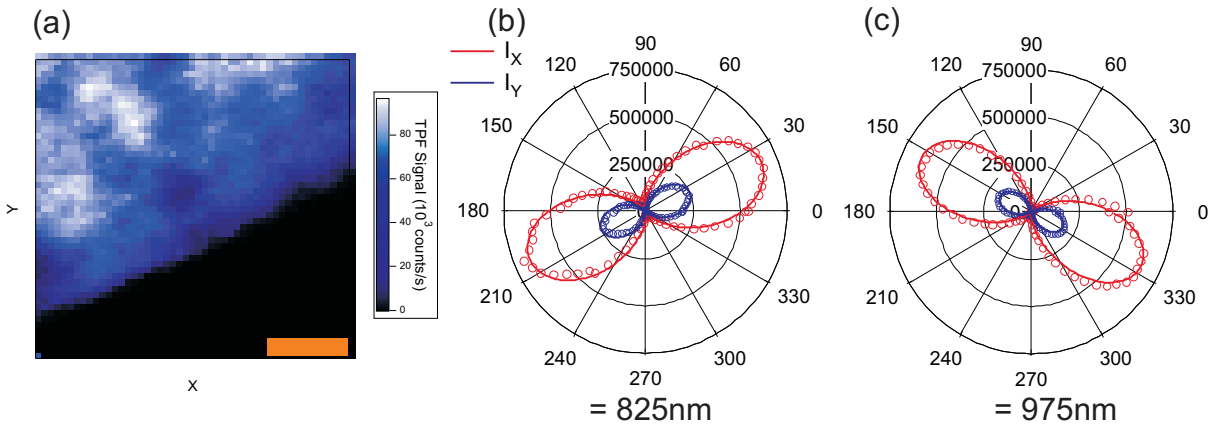

Figure 3.11: TPF polarization response of a 1D crystalline fluorescence sample made of DANS molecules in a PHTP crystalline host. (a) 2D scan (by a piezoelectric stage) of the sample showing the macroscopic crystal orientation (scale bar: 10 μm); the heterogeneity of the intensity observed in the image is due to an imperfect surface quality. (b,c) Experimental data (dots), and corresponding fits (continuous line) at (b) 825 nm excitation and (c) 975 nm excitation wavelengths. The fits account for the measured dichroic parameters and for the molecular orientation $(\theta_0, \phi_0) = (90°, 29°)$.

larization response is oriented in the same direction as the crystal, this is not anymore true for an excitation at $\lambda = 975\,\text{nm}$ where δ far exceeds $\frac{\pi}{2}$ (see Fig. 3.10b). However in both cases the same crystal orientation is found if the correct dichroic parameters are used. This example not only highlights the considerable influence of these parameters on polarimetric measurements but also demonstrates that reliable information can be extracted from these measurements even under the presence of strong dichroic perturbations provided that they have been characterized previously.

As the used dichroic (650DCXP, Omega Optical) induces strong and strongly varying ellipticities into the wavelength range we are interested in around 800 nm, it is not suited for polarimetric studies as almost no orientational information can be read out from the areas around $\alpha = 45°$ and $\alpha = 135°$. Therefore we switched to a different dichroic (FF720-SDi01, Semrock, Rochester, NY) that induces much less polarization distortions (Fig. 3.12). This dichroic is used for pulse shaping experiments because of its low dispersion properties.

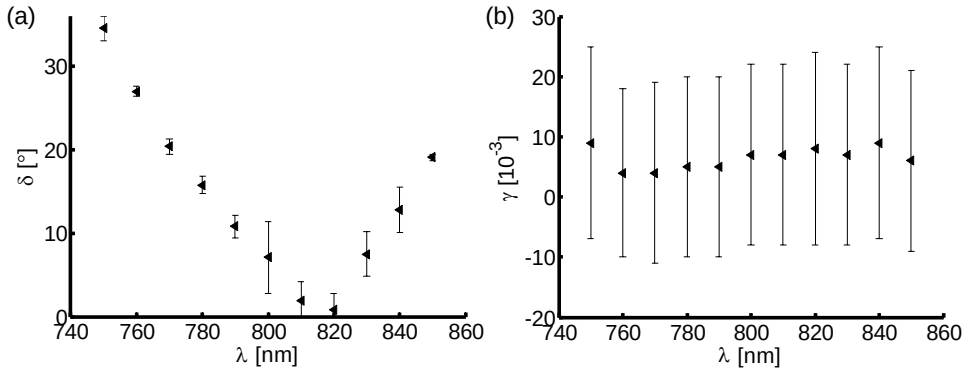

Figure 3.12: Polarization distortions for the dichroic mirror FF720-SDi01. (a) Ellipticity δ; (b) dichroism factor γ.

To characterize other optical elements in the beam path besides the dichroic mirror, it suffices to place the half waveplate (that turns the polarization) within the beam path at the right position for investigation. Of course the recorded TPF polarimetric response is then affected by all optical elements between the position of the waveplate and the focal spot of the microscope. But if the dichroic parameters of all but one element are already known, the contribution of the unknown one can be deduced.

To prepare our polarization shaping experiments we therefore characterized the beam path distortion components between the shaper and the microscope. For this we switched to the spectrally broad laser (see section 2.5.1) passing our pulse shaper. As a reminder Fig. 3.13a shows again the excitation path from Fig. 2.8. The five positions where we placed the rotatable half waveplate are denoted with A through E. Additionally all mirrors within the path that are required for space considerations and that offer additional degrees of freedom for the beam alignment - but which were excluded from Fig. 2.8 for clarity reasons - are indicated as well, because they also influence considerably the polarization state of the pulse.

It was already seen before that the dichroic parameters can be strongly wavelength-dependent. A pulse with a spectral bandwidth of 60 nm could therefore easily mask the true behavior of γ and δ. That is why we only chose spectral windows with a width of 20 nm that were controlled by blocking the unwanted spectral regions in the Fourier plane of the pulse shaper. For each of these regions and for each of the five positions A through E in the beam path (after the SLM, at the shaper exit, before the telescope, after the telescope, and at the microscope entrance) a polarimetric measurement was performed as described above and the corresponding dichroic parameters were retrieved. Fig. 3.13b and 3.13c present the results, the measurement at point A showing the global distortion undergone by the polarization through the whole setup.

It can be seen that different spectral regions of the pulse experience different polarization distortions which confirms their wavelength dependence. After the pulse shaper the dichroism factor remains very small and almost constant throughout the beam path.

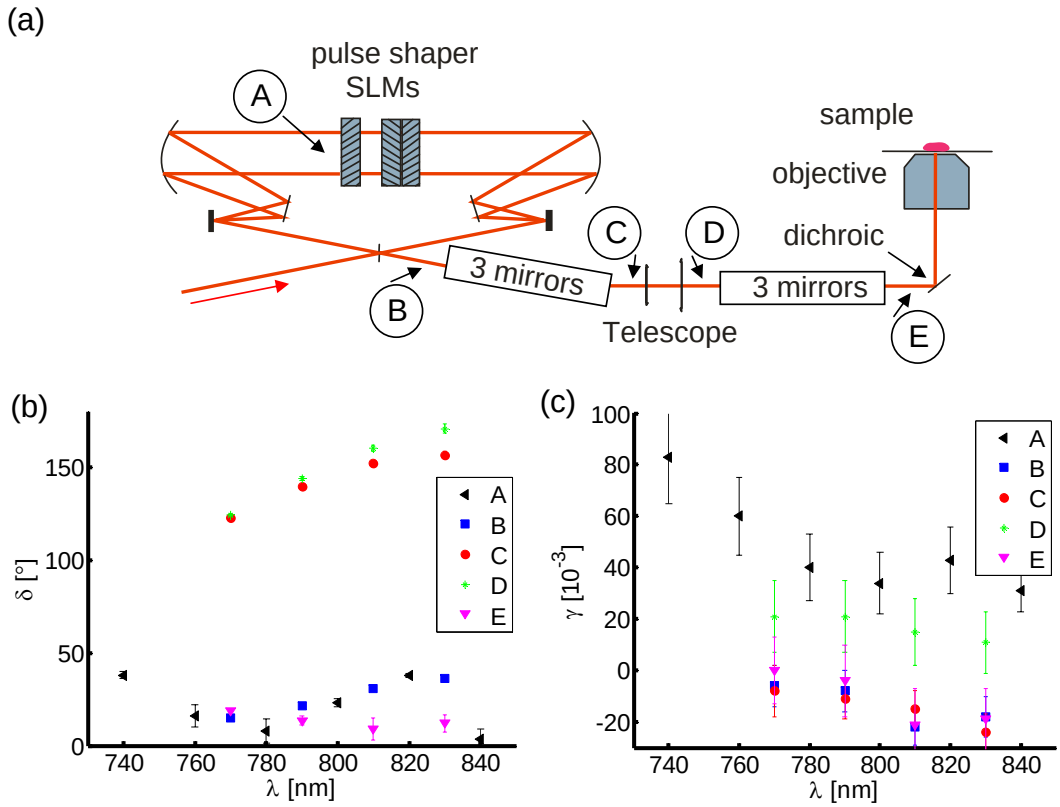

Figure 3.13: Characterization of polarization distortions throughout the beam path, part one. (a) Portion of the excitation path for pulse shaping described in section 2.5.1 with indication of all mirrors and the positions where the half waveplate was placed (A through E). (b) Ellipticity δ for all waveplate placements for different spectral regions of the ultrashort pulse. (c) Dichroism factor γ for all waveplate placements for these spectral regions.

The pulse shaper exit itself, however, influences it to a certain degree as is evident from a comparison between the values obtained a A and at B. This is the effect of the slightly different reflectivities of the second grating for *s*- and *p*-polarized light. But in any case γ stays small compared to 1.

A very different situation is found for the ellipticity. It changes dramatically during the beam propagation through the setup. While it is hardly changed by the recombing part of the pulse shaper (between A and B), a huge shift is induced by the three mirrors between the pulse shaper exit and the telescope. The telescope itself has a negligible effect (between C and D), but the three mirrors after it lead again to an equally large change in the opposite direction, therefore compensating for the previous distortions.

The overall distortion in the whole beam path is therefore rather weak. However, another issue occurs: the fluorescence polarimetric curves show a rotation of about 20° relative to X (Fig. 3.14), which is the signature of a rotation of one of the optical axes

in the path (probably due to a mirror reflection which is not perfectly at 45°). One might argue that once all polarization distortions are known they can be corrected for by the polarization pulse shaper. However, in our configuration this only works when the principal polarization axes do not change throughout the beam path, since the principal axes of the SLM have a fixed orientation. Without a polarization pulse shaper that can control the direction of the principal polarization axes [52], a correction is therefore not possible.

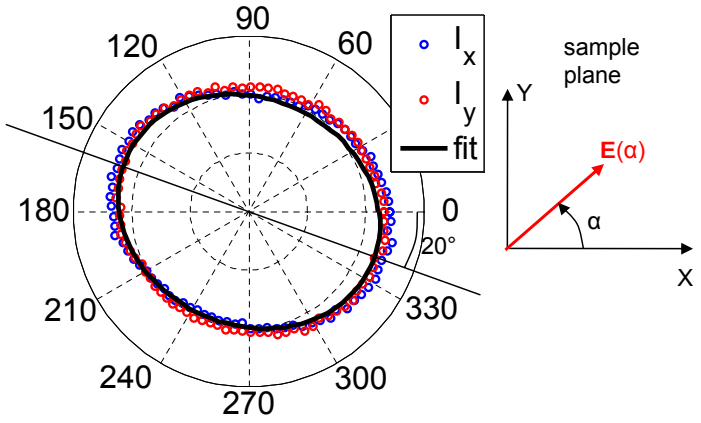

Figure 3.14: Characterization of polarization distortions throughout the beam path, part two. TPF polarimetric response for a polarization turned at point A in the pulse shaper after the SLM exit. The tilt of 20° indicates a rotation of the principal polarization axes by the second grating in the $4f$-line.

While these distortions do hardly influence a linear polarization, their effect is much more severe on elliptical or spherical ones. We illustrate this by creating a spherical polarization at the SLM exit (by shaping a phase of $\frac{\pi}{2}$ with the S-SLM, see Eq. (2.21)), placing a rotatable polarizer in the beam path either at position B or E and measuring the transmitted laser power. Instead of the expected circle the polar plots show a strong deformation. Since we restrict ourselves for the remainder of this work to polarization pulse shapes consisting of spectral regions with linear polarizations along the principal axes, this is not a detrimental issue here. Future implementations will require simplifying the excitation beam path and possibly using an extra polarization correction step, using a polarization shaper for arbitrary polarization generation [52].

3.4 Polarization distortion by high NA focussing

All calculations presented above were performed for a plane wave illumination which is justified when studying isotropic depolarized media since both 3D and 2D projections are isotropic. This is however not adapted for nonlinear microscopy experiments which require sub-wavelength resolution and very high field strengths, that use high NA objectives to

strongly focuss the incoming laser beam. This focussing results in a redistribution of the polarization components along the coordinate axes which can be assessed by the formalism presented in appendix C (see also Fig. 3.15). These polarization distortions come into play when the molecular excitation dipoles possess orientation components along the laser propagation direction. They couple with the axial component of the excitation field, an effect already been explained in detail by Yew *et al.* [198] for the case of SH generation from objects with known symmetries. In particular a field component along the propagation direction Z is created which can amount to up to 40% of the maximal field strength in the case of high NA objectives (Fig. 3.15). It can be seen that the polarization state

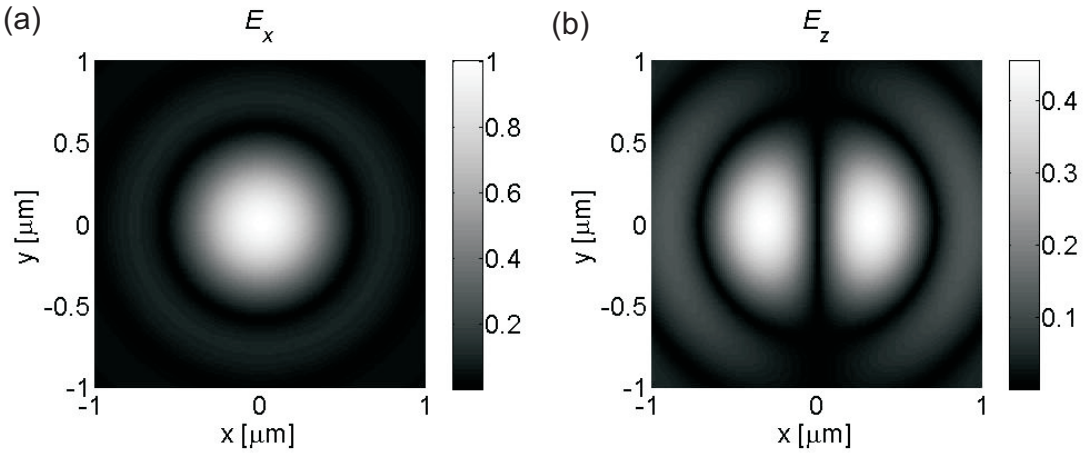

Figure 3.15: Map of the focalized incident electric field amplitude components along X and Z at the sample plane at $Z = 0$, for an incident polarization along X and focussed by an objective with NA = 1.2. (a) E_X; (b) E_Z (electric field normalized to the maximum of E_X).

of the incident beam now depends as well on the spatial coordinates within the excitation volume ($\mathbf{E}(\alpha, \delta, \gamma, \mathbf{r})$). To account for this in the calculation of the radiation from nonlinear materials, we filled the excitation volume with 300 evenly spaced dipoles at whose locations the vectorial excitation field is calculated. Eq. (3.3) then gives the TPF response of each of those dipoles. The radiating field then gets expressed for all angles encompassed by the collection aperture and is passed through the objective (see appendix C.2). In the present model, all dipole intensities are summed up due to the incoherent character of the fluorescence emission. We find that in a solution where the excitation process is randomized, the fluorescence polarimetric response is independent on the objective's numerical aperture both in the excitation and the collection modes (Fig. 3.16) which was expected as mentioned above. The calculations for the case of strong focalization (NA = 1.2) were carried out for a volume of $0.8\,\mu$m in the lateral directions (X and Y) and $1.6\,\mu$m in the axial direction (Z), homogeneously filled with $160 \times 160 \times 320$ dipoles. The weaker focalization case (NA = 0.9) is based on a focal volume of $1 \times 1 \times 2\,\mu\text{m}^3$ with $200 \times 200 \times 400$ dipoles.

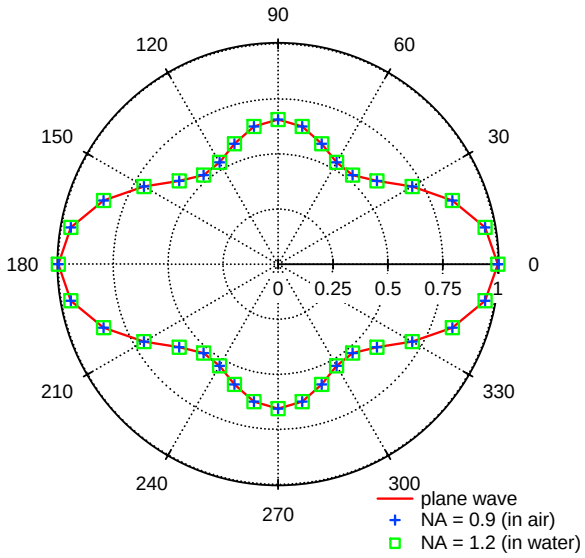

Figure 3.16: Dependence of the TPF response of fluorophores in a solution on the numerical aperture of the objective that is traversed both by the excitation beam and by the fluorescence signal detected afterwards. Three cases were simulated: very strong focalization (NA = 1.2 - green squares), medium focalization (NA = 0.9 - blue crosses) and plane wave illumination (NA = 0 - red line); $\gamma = 0.1$ and $\delta = \frac{\pi}{2}$. All calculations were performed for an excitation wavelength of 800 nm [199].

However, in the case of an anisotropic medium presenting out-of-plane orientation directions, a coupling in the Z direction cannot be neglected. To illustrate the role of the high NA used in two-photon microscopy, a model system of 1D symmetry was used in the calculations of Eq. (3.3) accounting for the complete vectorial form of the spatial excitation field. Fig. 3.17 depicts the polarization TPF response of a 1D sample made of fixed dipoles with small $\left(\theta = \frac{\pi}{3}\right)$ and strong $\left(\theta = \frac{\pi}{6}\right)$ orientation components along Z (see Fig. 3.4 for angle definitions). At low numerical aperture (NA = 0.1) the polarization response is only slightly deformed by an off-plane tilt. For high numerical apertures (NA = 1.2), however, strong deformations in the polarization response appear. Such a signal could easily be misinterpreted as originating from a non-1D sample in the (X, Y)-plane because some apparent perpendicular coupling occurs. Therefore great care has to be taken when dealing with polarization responses of non-anisotropic samples. (For more on sample symmetry and orientation investigation see chapter 4). Note that while the observed deformation exists even for $(\gamma, \delta) = 0$, it is enhanced with increasing ellipticities δ. In practice it is therefore crucial to account for high NA focussing in order to model the whole 3D picture of the distribution function of fluorescent molecules.

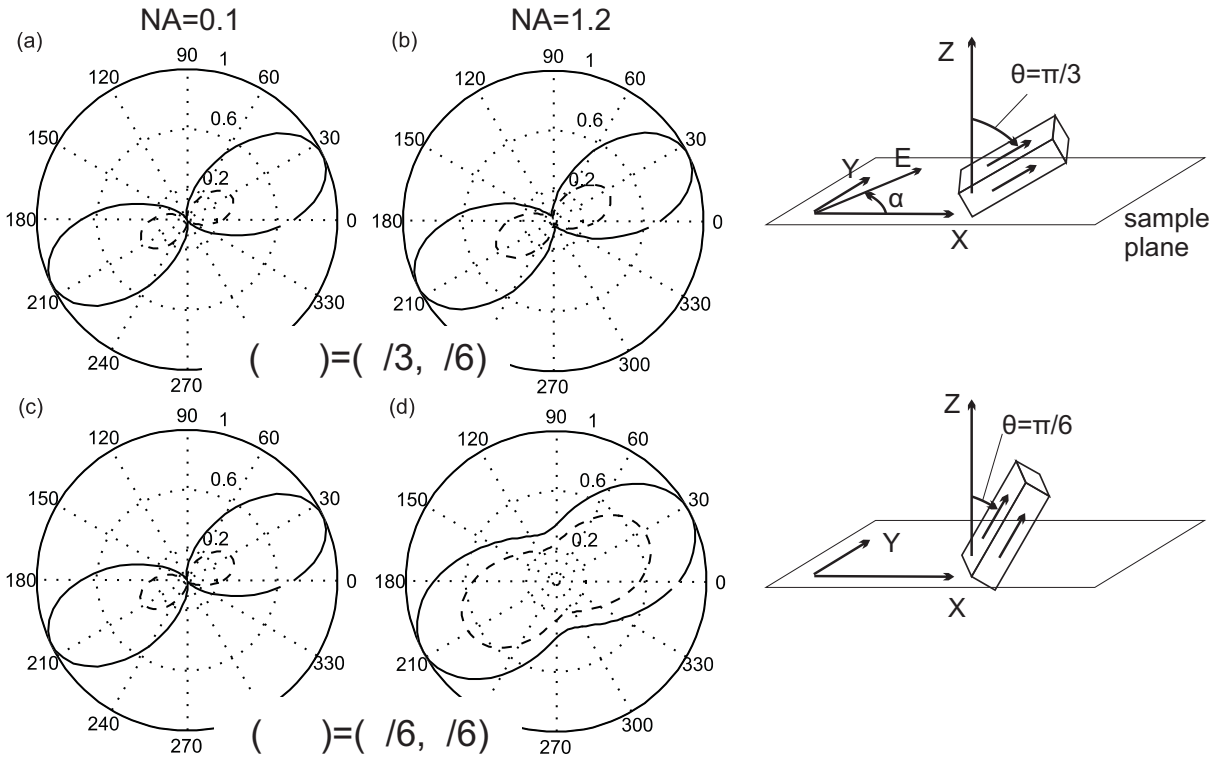

Figure 3.17: TPF polarization responses of a 1D fluorescence sample accounting for both reflection optics (using the parameters $\delta = \frac{\pi}{4}$, $\gamma = 0.01$) and high numerical aperture focussing. (a,c) NA = 0.1; (b,d) NA = 1.2. Sample orientation: (a,b) $(\theta, \phi) = \left(\frac{\pi}{3}, \frac{\pi}{6}\right)$; (c,d) $(\theta, \phi) = \left(\frac{\pi}{6}, \frac{\pi}{6}\right)$ - see drawings on the right. Continuous lines: I_X; dashed lines: I_Y. The polarization responses are normalized to a maximum value of 1.

Chapter 4

Amplitude, phase and polarization pulse shaping for structural investigations of (bio-)molecular media in SFG microscopy

4.1 Introduction

As seen in section 1.2.1, polarimetry can also be adapted to the SHG contrast. In this case, the retrieved information is directly related to the macroscopic $\chi^{(2)}$ tensor of the sample, probed within the excitation volume of a microscope. As we will see later, $\chi^{(2)}$ possesses orientation and symmetry information, contained in its tensorial components $\chi^{(2)}_{IJK}$.

In this chapter we develop a new method to read out these individual components. We use an excitation profile shaped in amplitude and polarization to generate a sum frequency signal where the contributions of different tensorial components get spectrally separated and subsequently detected by a spectrometer, allowing for a faster and more robust read-out than performed so far for example by polarimetry measurements. In a first step we test our approach on a well known nonlinear crystal (KTP). Afterwards it gets applied to microscopy to image both local order and disorder in a molecular crystalline sample, and local orientations in a collagen fiber on a sub-micrometric scale. Finally, we propose a related excitation scheme involving phase pulse shaping to avoid the spectral readout.

Sum Frequency Generation (SFG) is described, as explained in section 1.2.2, by the nonlinear induced dipole:

$$P_I(2\omega) = \int_{-\infty}^{\infty} \sum_{JK} \chi^{(2)}_{IJK}(\omega, \Omega) E_J(\omega - \Omega) E_K(\omega + \Omega) \mathrm{d}\Omega \tag{4.1}$$

where the fields E, polarized in directions J and K are coupled by the second-order nonlinear susceptibility $\chi^{(2)}_{IJK}$ of a nonlinear material to give a SHG polarization field P in

direction I. $\chi^{(2)}$ is in general a frequency dependent tensor. This dependence has its origin in vibrational or electronic energy levels in proximity to the virtual ones passed in the excitation process which alter the efficiencies or these pathways. When no one-photon resonances are involved in the excitation process, all two-photon excitation pathways leading to a certain SFG frequency ω have the same probability and $\chi^{(2)}_{IJK}(\omega,\Omega)$ reduces to $\chi^{(2)}_{IJK}(\omega)$ [200, 201, 202]. Any resonant one-photon situation would also lead to a perturbation of the SHG spectrum due to the introduction of additional phase terms in the competitive two-photon pathways leading to the two-photon excitation; this has been observed in atoms and other molecular systems investigated by TPF [201]. In addition, excitation conditions far from two-photon resonances lead to a ω-independent tensor $\chi^{(2)}_{IJK}$ where permutation of its three indices is allowed (Kleinman conditions) [203, 204]. We limit the present study to these cases. In the usual configuration of a two-photon excitation microscope, the sample lies in the (X,Y)-plane which contains the excitation polarization components.

For a crystal the $\chi^{(2)}_{IJK}$ coefficients depend on both its orientation in space defined by the set of Euler angles (ϕ,θ,ψ) (Fig. 4.1a) and its symmetry specified by the whole of its microscopic $\chi^{(2)}_{ijk}$ components expressed in the unit-cell coordinate frame x,y,z:

$$\chi^{(2)}_{IJK}(\phi,\theta,\psi) = \sum_{ijk=(x,y,z)} (\overrightarrow{I}\cdot\overrightarrow{i})(\overrightarrow{J}\cdot\overrightarrow{j})(\overrightarrow{K}\cdot\overrightarrow{k})(\phi,\theta,\psi)\chi^{(2)}_{ijk} \tag{4.2}$$

where the $(\overrightarrow{I}\cdot\overrightarrow{i}),(\overrightarrow{J}\cdot\overrightarrow{j}),(\overrightarrow{K}\cdot\overrightarrow{k})$ factors are the (ϕ,θ,ψ)-dependent cosine directors of the microscopic frame relative to the macroscopic one. They are formed as follows:

$$\begin{bmatrix} (X.x) & (X.y) & (X.z) \\ (Y.x) & (Y.y) & (Y.z) \\ (Z.x) & (Z.y) & (Z.z) \end{bmatrix} \tag{4.3}$$

$$= \begin{bmatrix} \cos\phi\cos\theta\cos\psi - \sin\phi\sin\psi & \sin\phi\cos\theta\cos\psi + \cos\phi\sin\psi & -\cos\psi\sin\theta \\ -\cos\phi\cos\theta\sin\psi - \sin\phi\cos\psi & -\sin\phi\cos\theta\sin\psi + \cos\phi\cos\psi & \sin\psi\sin\theta \\ \cos\phi\sin\theta & \sin\phi\sin\theta & \cos\theta \end{bmatrix}$$

The measurement of individual $\chi^{(2)}_{IJK}$ components therefore allows deducing the crystal's orientation in space if its nonlinear tensorial components are known in the microscopic frame. Several studies, undertaken in nanocrystals SHG using polarimetry, have allowed to deduce their orientation and crystalline quality, assuming that their nonlinear optical crystal coefficients were known from bulk crystals [79, 205]. In the reverse case, for an unknown crystal the retrieval of its macroscopic $\chi^{(2)}_{IJK}$ components under several known (ϕ,θ,ψ)-sets leads to the knowledge of its microscopic frame and thus to crystal symmetry identification. These polarimetric studies require long acquisition times and an *a posteriori* extensive data treatment [87, 88, 89].

Note that in a microscopy measurement, the efficient coupling fields lie along the X and Y-directions, therefore only six coefficients $\chi^{(2)}_{IJK}$ come into play. This reduces the retrieval of microscopic coefficients (knowing (ϕ,θ,ψ)) to only six independent ones (see Fig.

4.1b). In many crystal symmetries, the tensor actually contains less than six independent components [204].

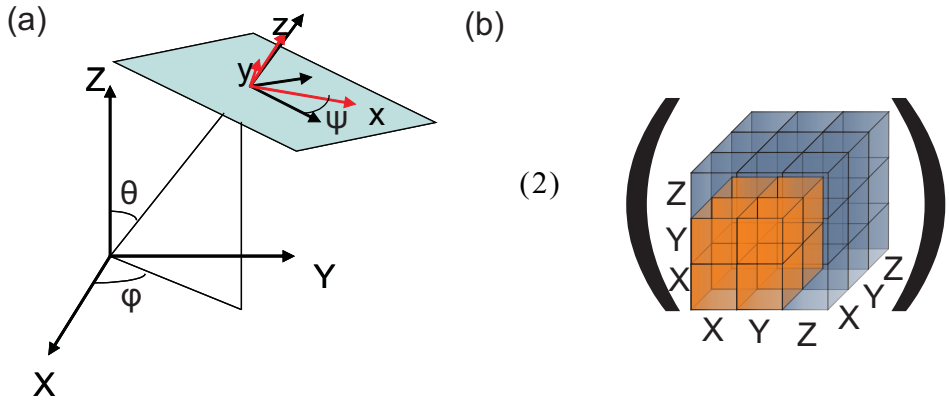

Figure 4.1: (a) Euler angles (ϕ, θ, ψ) for the transformation of the microscopic frame (x, y, z) for the nonlinear crystal or molecules into the macroscopic laboratory frame (X, Y, Z); (b) illustration of the second order nonlinear susceptibility tensor $\chi^{(2)}$ and its accessible components (orange) under low NA illumination.

The signal in a typical microscopy measurement arises from a very large number of nonlinear dipoles within the excitation volume. In a crystal they will all be perfectly aligned, but in more complex molecular media as encountered for example in biology this is not expected to be the case. There will rather be a preferential direction around which the individual nonlinear dipoles are oriented. This can be expressed as the coherent superposition of nonlinear dipoles within a distribution of orientations (ϕ, θ, ψ) leading to new macroscopic tensorial coefficients:

$$\chi^{(2)}_{IJK} = N \int\int\int_{(\phi,\theta,\psi)} \beta_{IJK}(\phi,\theta,\psi) f(\phi,\theta,\psi) \sin\theta \mathrm{d}\phi \mathrm{d}\theta \mathrm{d}\psi \tag{4.4}$$

with $f(\phi, \theta, \psi)$ as the normalized orientational distribution probability function of the molecular unit cells in the sample, N the molecular density of the sample, and β_{IJK} the molecular second-order nonlinear susceptibility tensor projected in the macroscopic frame. This formulation shows that in the case of a purely 1D crystalline sample (with only one non-vanishing coefficient $\chi^{(2)}_{zzz}$ in the microscopic frame) oriented along a macroscopic axis, the presence of orientational disorder can lead to significant non-diagonal macroscopic coefficients (such as $I = J \neq K$) [89]. From the measurement of the individual $\chi^{(2)}_{IJK}$ components the amount of disorder can then be deduced in a similar way as for TPF (see Fig. 3.2), but nevertheless complementary since SHG is additionally sensitive to asymmetry as it does not arise from centrosymmetric structures.

In this chapter we explore new ways of measuring macroscopic nonlinear optical coefficients using a simpler and faster scheme than previous polarimetry analysis. While

for a complete polarimetric study an intensity measurement has to be performed at each excitation angle α and only a subsequent fit of the polarization response leads to the knowledge of the nonlinear tensorial coefficients, our pulse shaping based scheme obtains these coefficients in a single-shot measurement without the need of a fit.

4.2 Single $\chi^{(2)}$ component readout

4.2.1 Principle

Let us first consider a monochromatic laser $E(\omega) = E_0\delta(\omega - \omega_0)$ with a linear polarization along a direction forming an angle α with the X-axis (Fig. 4.2a). For a measurement of the tensorial components $\chi^{(2)}_{IJJ}$ it suffices to polarize the laser in direction $J = (X, Y)$ and to measure the SFG intensity $\hat{I}$ in direction $I = (X, Y)$. For example a linear polarization along X $\left(\mathbf{E}_{0^\circ} = E_0 \begin{pmatrix} 1 \\ 0 \end{pmatrix}\right)$ leads to a SHG intensity of $\hat{I}_{I,0^\circ} = \left(\chi^{(2)}_{IXX} E_0^2\right)^2$ and allows the retrieval of $\chi^{(2)}_{IXX}$ by:

$$\chi^{(2)}_{IXX} \propto \sqrt{\hat{I}_{I,0^\circ}} \tag{4.5}$$

The proportionality reflects the fact that in these measurements we are interested in $\chi^{(2)}_{IJK}$-values relative to one another rather than in absolute values. A pure Y-polarization (90°) leads to the knowledge of $\chi^{(2)}_{IYY}$ in the same way.

The measurement of the mixed tensorial terms $\chi^{(2)}_{IJK}$ with $J \neq K$, i.e. $\chi^{(2)}_{XXY} = \chi^{(2)}_{XYX}$ and $\chi^{(2)}_{YXY} = \chi^{(2)}_{YYX}$, on the other hand causes substantial difficulties. To get a signal from them the excitation field needs both a X- and a Y-component, so a polarization along $\alpha = 45^\circ$ seems the obvious choice, but additionally to the SFG field arising from the mixed components $\chi^{(2)}_{IXY} = \chi^{(2)}_{IYX}$ also the components $\chi^{(2)}_{IXX}$ and $\chi^{(2)}_{IYY}$ will contribute (Fig. 4.2a). In particular $\mathbf{E}_{45^\circ} = \frac{E_0}{\sqrt{2}} \begin{pmatrix} 1 \\ 1 \end{pmatrix}$ generates a SH intensity of

$$\begin{aligned} \hat{I}_{I,45^\circ} &= \left(\frac{E_0^2}{2}\chi^{(2)}_{IXX} + 2\frac{E_0^2}{2}\chi^{(2)}_{IXY} + \frac{E_0^2}{2}\chi^{(2)}_{IYY}\right)^2 \\ &= \left(E_0^2\chi^{(2)}_{IXY} + \frac{1}{2}\left(\sqrt{\hat{I}_{I,0^\circ}} + \sqrt{\hat{I}_{I,90^\circ}}\right)\right)^2 \end{aligned} \tag{4.6}$$

From this it is possible to obtain the value of the mixed component by:

$$\chi^{(2)}_{IXY} \propto \sqrt{\hat{I}_{I,45^\circ}} - \frac{1}{2}\left(\sqrt{\hat{I}_{I,0^\circ}} + \sqrt{\hat{I}_{I,90^\circ}}\right) \tag{4.7}$$

but the error margin increases due to the fact that three measurements are required compared to the components $\chi^{(2)}_{IJJ}$ that can be determined by a single one. The additional noise induced by successive discrete measurements is also a reason why a complete polarimetric analysis with subsequent fit is preferred to this measurement scheme.

Alternatively two lasers with different wavelengths can be used, one polarized along X and the other along Y. Three couplings are possible in such a scheme (Fig. 4.2b): Both lasers can couple with themselves giving rise to signals with frequencies $2\omega_x$ and $2\omega_y$ (ω_x and ω_y being the frequencies of the lasers polarized along the corresponding directions). Both depend solely on the tensorial components $\chi^{(2)}_{IXX}$ and $\chi^{(2)}_{IYY}$ respectively. Additionally a third signal arises from the coupling of one laser with the other at $\omega_x + \omega_y$, exclusively generated by $\chi^{(2)}_{IXY} = \chi^{(2)}_{IYX}$. Therefore the contributions of all six tensorial components (three for each detection direction) are not only spectrally well separated from one another, but they can all be obtained in a single measurement. However, to reliably compare the intensities of the mixed terms with those of the others and determine the magnitude of the underlying $\chi^{(2)}$-components, one depends on a perfect or at least perfectly known overlap of the focal volumes of both lasers, a challenge in practice. More importantly, such measurements would require perfectly coherent lasers, synchronized in order to produce a coherent buildup of the crossed nonlinear signal.

To avoid both the need for multiple measurements as well as necessity to superpose focal volumes of several lasers, we propose a solution based on pulse shaping. Amplitude shaping selects only two narrow regions out of a spectrally broad pulse, the rest being suppressed. Polarization shaping polarizes one of these regions along X, the other along Y (Fig. 4.2c) [206]. Thus two lasers get simulated whose focal volumes overlap perfectly,

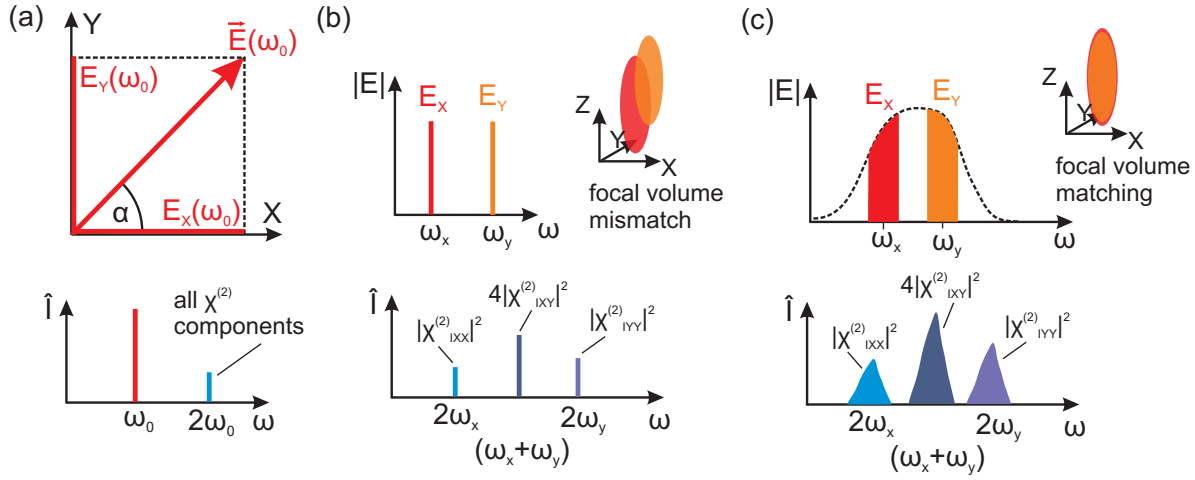

Figure 4.2: $\chi^{(2)}$-component read-out schemes. (a) one laser with linear polarization: signals from different components get mixed; (b) two synchronized lasers at ω_x and ω_y with perpendicular polarizations: for each detection direction I, components $\chi^{(2)}_{IJK}$ get spectrally separated, but mismatch of the focal volumes of both lasers is very probable ; (c) two amplitude windows with perpendicular polarizations shaped out of spectrally broad pulse: $\chi^{(2)}$-components get separated without focal volume mismatch.

provided that the spatial dispersion in ω is perfectly controlled after the shaper (which

has been verified as explained in section 2.6). Since SFG depends quadratically on the incoming intensity it is not desirable to narrow the amplitude windows too much wasting the majority of the laser energy. Instead the maximal width should be chosen that still gives completely spectrally separated SFG peaks (see Fig. 4.2c).

4.2.2 Experimental realization on known crystals

To demonstrate the capabilities of a single $\chi^{(2)}$-component read-out by amplitude and polarization pulse shaping we use a crystal with a size of several millimeters in all three dimensions, $KTiOPO_4$ (KTP), of known symmetry and orientation. In the epi-microscopy geometry only the signal from above the surface is imaged, as explained in chapter 1. There aren't any resonances within the incident wavelength range, and in this regime KTP has three independent tensorial components, that in the crystal frame (x, y, z) are $\chi^{(2)}_{zzz} = 33.8\,\mathrm{pm/V}$, $\chi^{(2)}_{zxx} = 5.08\,\mathrm{pm/V}$ and $\chi^{(2)}_{zyy} = 8.7\,\mathrm{pm/V}$ [207]. It is placed with the (x, z) crystallographic plane in the microscope's (X, Y) sample plane and can be rotated around its y-axis which corresponds to the propagation direction Z of the incident laser, therefore allowing a variation of the macroscopic nonlinear coefficient as detailed in Eq. 4.2 (with $\theta = 90°$, $\psi = 90°$ and ϕ variable, ϕ being defined as the angle between the crystal axis z and the X axis of the laboratory frame).

Two laser profiles are tested: in the first case the whole spectral width of the pulse is sent to the sample with a flat spectral phase and polarized either along X or Y, which corresponds to the case of Figure 4.2a only with a broad pulse instead of a monochromatic one. In the second case both spectral amplitude and polarization are shaped according to Figure 4.2c where the two spectral windows with a width of 10 nm each are centered on $\lambda_X = 780\,\mathrm{nm}$ and $\lambda_Y = 820\,\mathrm{nm}$ for X- and Y-polarized light. The SFG spectra for these profiles are taken for different crystal orientations, which are measured independently using white light illumination imaging (see Fig. 2.8). Fig. 4.3 shows a sketch of the corresponding signals on the CMOS chip in the spectrometer. The X- and Y-polarized signals appear as thin lines on the chip. In the case of the two-peak excitation these lines consist only of three separated regions. By just reading out one of them the strength of the corresponding coupling component $\chi^{(2)}_{IJK}$ can be determined.

Figure 4.4 displays the experimental results normalized to the maximal value of $\chi^{(2)}_{XXX}$, compared with calculations based on Eqs. (4.1) and (4.2). An excitation dichroism factor f is introduced to account for the different amplitudes of the incoming field in its two polarizations states so that $E_Y = fE_X$. This factor, mainly caused by the polarization dependent reflection efficiency of the diffraction grating at the exit of the pulse shaper, is estimated at $f = 1$ in Figure 4.4a and $f = 0.7$ in Figure 4.4b. Moreover, a detection dichroism factor is introduced to account for the detection efficiency difference between the two channels of the spectrometer, 0.8 in the present case. Both factors only affect the overall intensities but not the shape of the orientation dependence curves depicted in Figure 4.4. A good agreement between the measured and expected dependence of the SFG tensorial coefficients with respect to the ϕ macroscopic in-plane crystal orientation

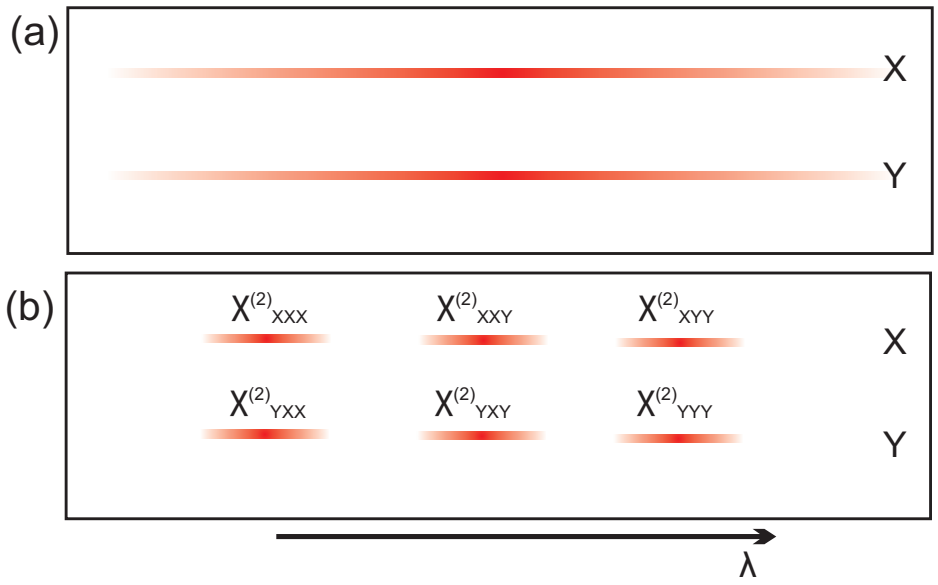

Figure 4.3: Sketch of the spectral detection on the CMOS chip in the spectrometer (see Fig. 2.8). (a) No amplitude shaping is performed, only one signal peak gets detected, separated into its X- and Y-component, which appear as thin horizontal lines on the CMOS chip. (b) SFG excitation with the two-peak profile detailed in the text. Three signal peaks appear, separated along X and Y aligned in horizontal lines on the CMOS chip. The responsible $\chi^{(2)}$-components for each signal part are indicated.

is reached. The excitation laser profile employed in Figure 4.4b shows in particular that six individual coefficients of the crystal nonlinear susceptibility can be retrieved from a spectral filtering, which is based on a single pulse measurement. In contrast the more traditional scheme of Figure 4.4a requires two different measurements involving separate X and Y excitation polarizations. Whatever its direction, this single polarization excitation is unable to retrieve more than two crystalline SFG tensorial components at the same time. The four tensorial components that are accessed in total can also be obtained from a polarimetric measurement as indicated in the polar graphs in Fig. 4.4a.

There is still a disadvantage of the two-peak excitation profile: the generated SFG signal is considerably lower compared to the single-peak excitation. In the latter case the whole pulse energy is used while in the former only a part of it reaches the sample due to the amplitude shaping. Consequently much less coupling possibilities between different wavelengths are available and the signal intensity drops. As a result the spectra get noisier, making a reliable component readout more difficult. This concern can be reduced by employing laser sources that provide more power and those that possess larger bandwidths as then broader amplitude windows can be shaped into the pulse so that the available energy gets used better.

Although it is not visible in the present case where index permutations are valid since

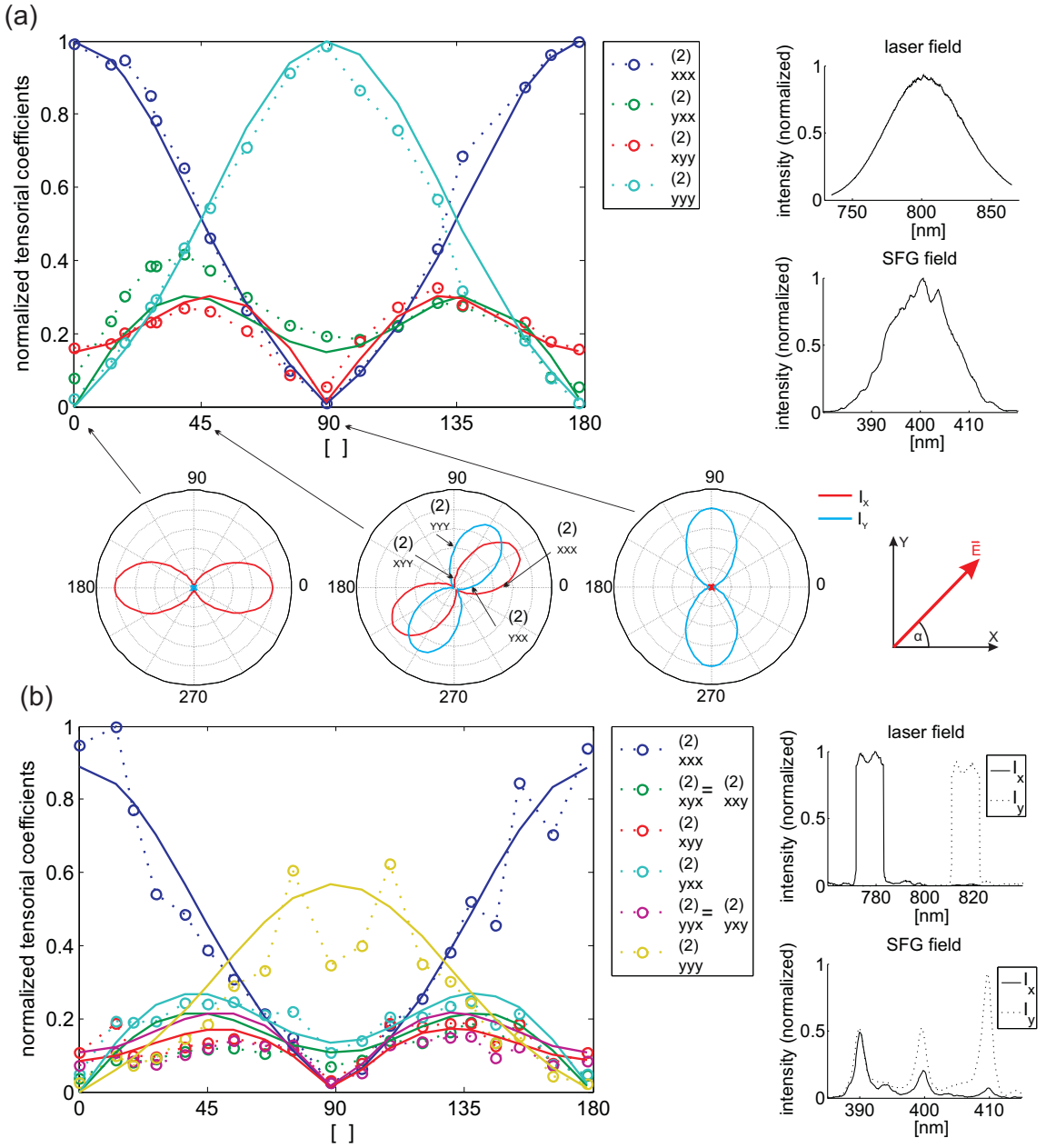

Figure 4.4: Dependence of the measured relative tensorial components of a KTP crystal with respect to its in-plane orientation angle ϕ. Dashed lines: experimental data; solid lines: expected behavior according to the calculations detailed in the text. (a) Whole spectrum polarized in one direction. For various orientation angles ϕ the polarimetric SHG response is given as well, where a linear incident polarization gets turned (theoretical calculations). (b) Two spectral windows with perpendicular polarizations to each other; right hand pictures: incident laser spectrum and corresponding measured SFG spectrum for both cases (the lower SFG spectrum is obtained for a KTP orientation of $\phi = 90°$, with dotted (resp. continuous) lines corresponding to a Y (resp. X) analysis direction.

Kleinman conditions are applicable, this approach shows furthermore that polarization pulse shaping allows the investigation of possible deviations from index permutation conditions since six coefficients are determined independently, which is not the case with a single polarization excitation.

4.3 Effect of the Z-direction coupling under high NA focussing

So far only a planar wave excitation was assumed to retrieve the macroscopic coefficients from the measured data. However, in our work, we aim at applying polarization control schemes to imaging, therefore high NA objectives are used. To collect as much as possible of the so generated nonlinear signal, these objectives are used as well in the detection paths as detailed in section 2.5.2. The strong focussing leads to a substantial change in the polarization state of the field. Not only is a new Z-component introduced but also the lateral components get redistributed for points within the focal volume not lying on the optical axis [208]. While a NA = 0.5 objective hardly modifies the field, an objective with NA = 1.2 leads to a field component in Z that amounts to up to 40% of the in-plane (X, Y) amplitude (see Fig. 3.15). For samples exhibiting strong susceptibility components with Z-indices this contribution may be non-negligible [198, 209]. The actual effect of the Z-coupling is dependent on the symmetry and orientation of the sample under investigation and therefore each case needs to be studied specifically. Appendix C describes our approach that accounts both for excitation effects as well as for those of the collection of the propagated SHG from an assembly of dipoles in the focal volume. Thus the sample rotation dependence as shown in Fig. 4.4 can be modeled including all tensorial components.

Different crystal symmetries are reflected by different $\chi^{(2)}$ structures which makes it difficult to get a general overview of the Z-coupling effect in polarization sensitive measurements. To facilitate this task we introduce the ratio between all tensorial components containing at least one Z-component:

$$\chi^{(2)}_{out} = \sqrt{\sum_{I'J'K'} (\chi^{(2)}_{I'J'K'})^2}\,, \qquad \text{with } I' \vee J' \vee K' = Z \tag{4.8}$$

and the full norm $\chi^{(2)} = \sqrt{\sum_{(I,J,K)=(X,Y,Z)} (\chi^{(2)}_{IJK})^2}$. (For the calculation of these values we do not include index permutations.) This allows the quantification of the out-of-plane nonlinear coupling in any sample symmetry and orientation. $\frac{\chi^{(2)}_{out}}{\chi^{(2)}}$ can range from 0 (no Z-coupling) to 1 (maximum Z-coupling effect). For the above case of KTP with its $(1, 3) = (x, z)$ axes lying in the (X, Y) sample plane $\frac{\chi^{(2)}_{out}}{\chi^{(2)}} = 0.25$. Turning its main axis z along the Z direction increases this ratio to 0.96.

Fig. 4.5 shows the effect of the Z-coupling contributions on the crystal rotation experiment detailed above (Fig. 4.4). In Fig. 4.5a the theoretical root mean squared error

between the situations of NA = 1.2 and the planar wave approximation in such an experiment is shown as a function of the ratio $\frac{\chi^{(2)}_{out}}{\chi^{(2)}}$. This error is seen to lie in a reasonable range (below 4%) for $\frac{\chi^{(2)}_{out}}{\chi^{(2)}} < 0.8$. For larger out-of-plane contributions the error grows rapidly which makes the determination of in-plane tensorial components not reliable anymore. The maximum value reached by this error in the sample rotation dependence for a certain angle ϕ is represented in Fig. 4.5b. In both figures small dots at $\frac{\chi^{(2)}_{out}}{\chi^{(2)}} = 0.25$ indicate the corresponding values for the KTP experiment above. The effect of a high out-of-plane coupling on the sample rotation dependence is exemplified for a case with KTP-like symmetry (crystal class C_{2v}) in Fig. 4.5c and 4.5d, assuming $\frac{\chi^{(2)}_{out}}{\chi^{(2)}} = 0.8$. Strong modifications of the angular dependence are induced by the Z-coupling contribution for high numerical aperture focussing (Fig. 4.5c, NA = 1.2). However, using a lower numerical aperture (NA = 0.5, which still provides reasonable micrometric resolution) is shown to be highly reliable even for samples containing significant Z-coupling contributions (Fig. 4.5d). The use of a high NA objective without taking the Z-coupling into account is therefore justified in the present experiment (assuming that a 4% error margin is acceptable) as long as the Z-coupling contribution to the tensor does not surpass 0.8. In the general case of an unknown Z-contribution, the use of a lower numerical aperture is recommended. Note that similar conclusions could be drawn for any other crystal or sample symmetry by using the $\chi^{(2)}_{out}/\chi^{(2)}$ ratio as a quantification of the Z-components contribution to the nonlinear coupling.

Finally, the Z-coupling in KTP involves only its $\chi^{(2)}_{zyy}$ susceptibility component, which amounts to 30% of the main component $\chi^{(2)}_{zzz}$. Consequently, the Z-coupling efficiency does not significantly affect the results of Fig. 4.4. The maximum error margins are in this situation: 1.8% for $\chi^{(2)}_{XXX}$ (measured at $\phi = 45°$), 3% for $\chi^{(2)}_{XYX}$ (at $\phi = 45°$) and 13% for $\chi^{(2)}_{XYY}$ (at $\phi = 90°$). The high NA focussing is thus seen to have a minor effect on the polarization responses. This estimated error range corresponds to the maximum discrepancy range obtained between the experimental and theoretical SHG angle dependencies shown in Fig. 4.4.

To complete this study, we investigated furthermore the effect of the off-plane tilt angle θ of the sample to determine its possible influence on the retrieved 2D information. As mentioned above, these measurements are essentially 2D projection measurements. θ is defined as the angle between the Z direction and the symmetry axis z of the sample. Numerical simulations performed on KTP show that an off-plane rotation of the crystal can induce deviations to the expected coefficients at high tilt angles (typically θ below $\frac{\pi}{8}$) using a NA of 1.2 (Fig. 4.6a), whereas the use of a lower numerical aperture (NA = 0.5) does not alter the measured data significantly (Fig. 4.6b). This is essentially due to the fact that the projection of the sample in the (X, Y)-plane still keeps an important part of the symmetry information. The same is observed in the simulation of a polarization shaping experiment where 2D coefficients are retrieved for a tilted KTP crystal (Fig. 4.6c): the influence of the tilt angle in this case is seen to be negligible.

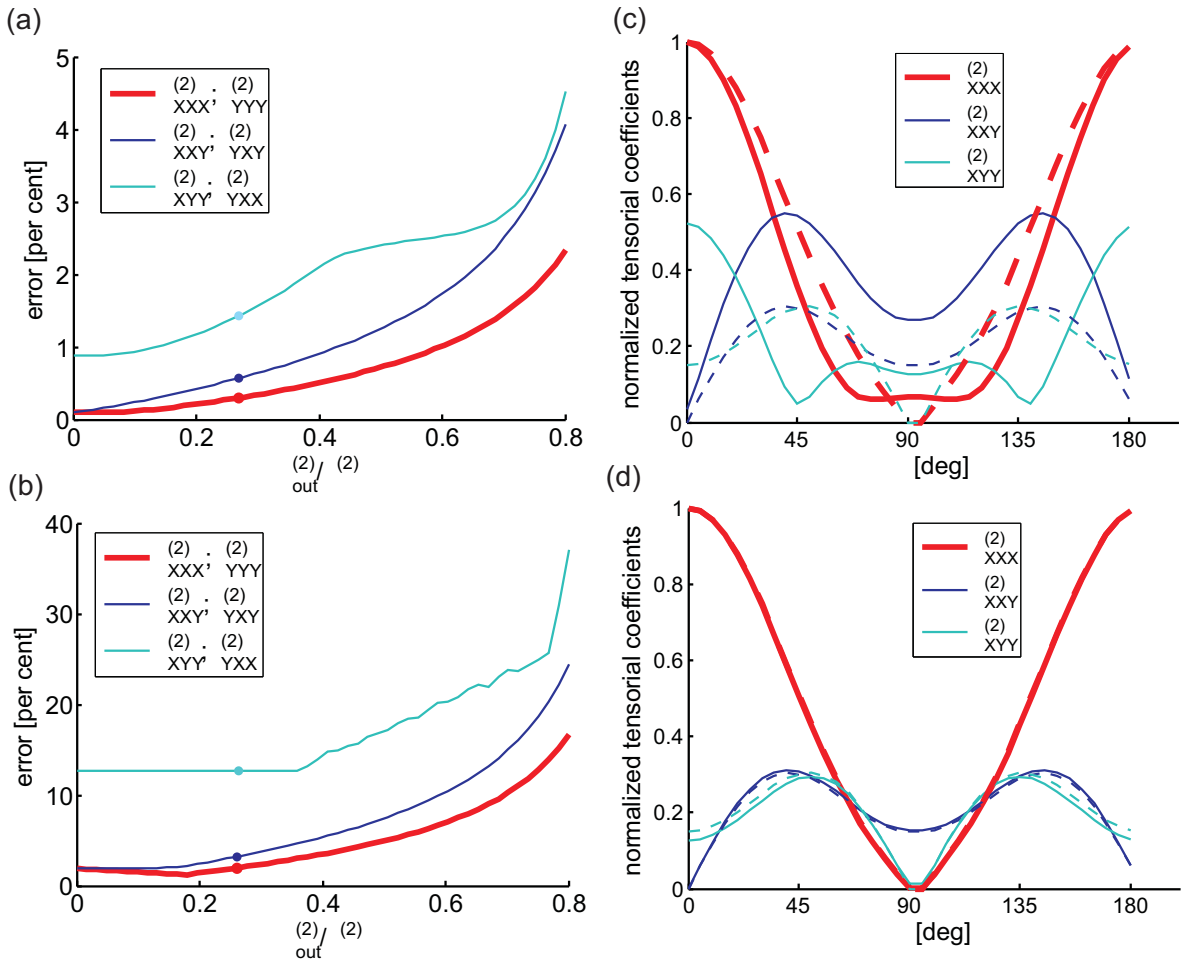

Figure 4.5: Effect of the out-of-plane Z-contribution to the nonlinear coupling on the polarization shaping experiment (numerical simulations). (a) Theoretical root mean squared error between the situation NA = 1.2 and the plane wave approximation, estimated on the crystal rotation dependence (Fig. 4.4) of individual nonlinear tensorial components, as a function of the ratio $\frac{\chi^{(2)}_{out}}{\chi^{(2)}}$ which quantifies the amount of the Z-coupling contribution. The points correspond to the situation of a KTP crystal with its (x, z) axes in the sample plane. Components undergoing a similar dependence are joined in one curve. (b) maximum value reached by the error defined in (a). (c) Calculated crystal rotation dependence of the individual tensorial components in the case of $\frac{\chi^{(2)}_{out}}{\chi^{(2)}} = 0.8$ for NA = 1.2 (continuous line) and a planar wave approximation (dashed line). (d) Same dependencies for NA = 0.5 (continuous line) and a planar wave approximation (dashed line).

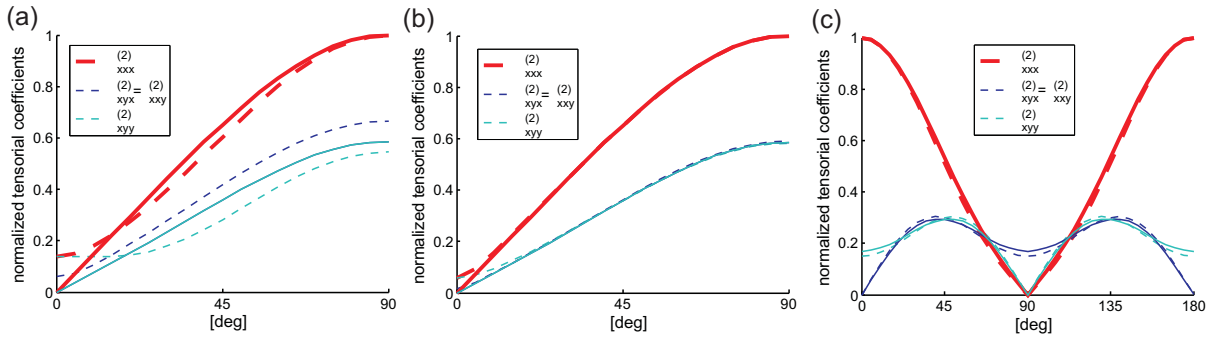

Figure 4.6: Effect of the out-of-plane tilt angle θ of KTP on the polarization shaping experiment (numerical simulations). Components undergoing a similar dependence are joined in one curve such as in Fig. 4.5. All coefficients are normalized to $\chi^{(2)}_{XXX}$ measured at $\left(\phi = 0, \theta = \frac{\pi}{2}\right)$. (a) θ-dependence of the individual KTP macroscopic nonlinear coefficients at $\phi = \frac{\pi}{4}$, for NA $= 1.2$ (dashed line) and in the plane wave approximation (continuous line). (b) same dependence for NA $= 0.5$ (dashed line) compared to the plane wave approximation (continuous line). (c) ϕ rotation dependence of the KTP individual nonlinear tensorial components (such as measured in Fig. 4.4), for $\theta = \frac{\pi}{2}$ (dashed line) and $\theta = \frac{\pi}{4}$ (continuous line) in plane wave approximation.

To further illustrate the power and sensitivity of our tensorial component read-out method, we simulated the SFG response of several other typical crystals. Fig. 4.7a shows again the KTP graphs already seen in Fig. 4.6c together with $Ba_2NaNb_5O_{15}$ (Fig. 4.7b), appertaining to the same crystal class C_{2v}. Fig. 4.7c and 4.7d depict two examples of the crystal class C_{6v}, CdS and CdSe, and finally $BaTiO_3$ (C_{4v}) and Ag_3AsS_3 (C_{3v}) are seen in Fig. 4.7e and 4.7f. The corresponding symmetries and values of the nonlinear tensorial components in the microscopic frame are given in Table 4.1. As before, the individual nonlinear in-plane components are shown as a function of the ϕ angle defining the rotation of the crystals within the sample plane. All crystals are placed with their (x, z)-axes in the (X, Y) macroscopic plane ($\theta = \psi = 90°$). Dashed lines correspond to focussing and detection with an NA $= 0.5$ objective while solid lines refer to a plane wave illumination. It can be seen that the $Z-$coupling of the electric field can be neglected for all shown crystals under these weak focussing conditions. Moreover, the tensorial components of different crystal classes show a very diverse dependencies on ϕ and even within the same crystal class the behavior may change a lot. This confirms that our method can easily distinguish not only between different orientations of a given crystal but also between different crystals.

To summarize the results so far, we have shown that it is possible to directly measure the components of the second-order nonlinear susceptibility tensor $\chi^{(2)}_{IJK}$ in a single-pulse measurement using amplitude and polarization shaping. This method is much faster than standard polarimetry (even if only three linear incident polarizations were used at $\alpha = (0°, 45°, 90°)$) and furthermore avoids the subsequent fitting procedure. Currently there

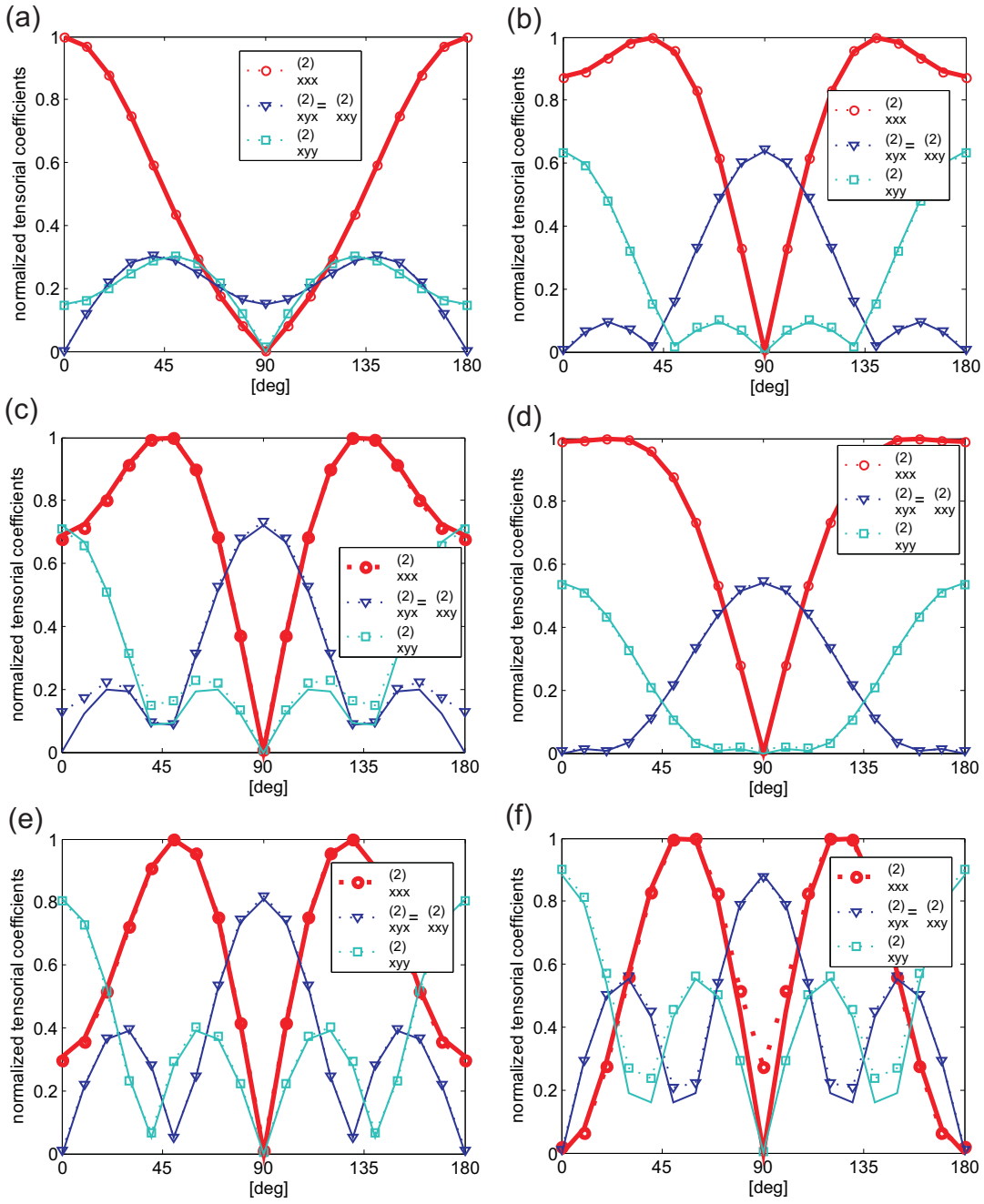

Figure 4.7: Dependence of tensorial components with respect to the in-plane orientation angle ϕ of the crystals. Dashed lines: focussed illumination with NA = 0.5; solid lines: plane wave approximation. (a) KTP; (b) $Ba_2NaNb_5O_{15}$; (c) CdS; (d) CdSe; (e) $BaTiO_3$; (f) Ag_3AsS_3. For clarity, only the X-detected components are shown. The Y-detected dependencies can be deduced from the observed curves by a shift of $\phi = 90°$ so that $\chi^{(2)}_{XXX}$ corresponds to $\chi^{(2)}_{YYY}$, $\chi^{(2)}_{XXY}$ to $\chi^{(2)}_{YXY}$ and $\chi^{(2)}_{XYY}$ to $\chi^{(2)}_{YXX}$. See Table 4.1 for the second-order nonlinear tensors $\chi^{(2)}_{ijk}$ in the crystal frame.

crystal	crystal class	symmetries and $\chi^{(2)}_{ijk}$ [10^{-9} esu]
$Ba_2NaNb_5O_{15}$	C_{2v}	$\chi^{(2)}_{zzz} = -48$
		$\chi^{(2)}_{zxx} = -35$
		$\chi^{(2)}_{zyy} = -35$
CdS	C_{6v}	$\chi^{(2)}_{zzz} = 86$
		$\chi^{(2)}_{zxx} = \chi^{(2)}_{zyy} = 90$
		$\chi^{(2)}_{zxy} = 100$
CdSe	C_{6v}	$\chi^{(2)}_{zzz} = 74$
		$\chi^{(2)}_{zxx} = \chi^{(2)}_{zyy} = 68$
		$\chi^{(2)}_{zxy} = 130$
$BaTiO_3$	C_{4v}	$\chi^{(2)}_{zzz} = -16$
		$\chi^{(2)}_{zxx} = \chi^{(2)}_{zyy} = -43$
		$\chi^{(2)}_{xxz} = \chi^{(2)}_{yyz} = -41$
Ag_3AsS_3	C_{3v}	$\chi^{(2)}_{yyy} = -\chi^{(2)}_{yxx} = -\chi^{(2)}_{xxy} = -\chi^{(2)}_{xyx} = 68$
		$\chi^{(2)}_{zxx} = \chi^{(2)}_{zyy} = 36$

Table 4.1: Second-order nonlinear tensors $\chi^{(2)}_{ijk}$ in the crystal frame for the different crystals shown in Fig. 4.7 [204].

are still some noise issues to solve, but as more intense lasers become available, this should only be a minor problem. Eventually, our method may even be more robust to noise, as the same noise level acts on all SFG signal peaks. This may not be the case in polarimetry where experimental conditions can change during the acquisition of a polarimetric curve. As will be seen later (section 4.5) this amplitude and polarization shaping approach can also be combined with phase shaping to lead to a better contrast in imaging.

4.4 Molecular order imaging using polarization pulse shaping

So far we focussed on the experimental principle by applying it to a crystalline calibration sample. In more complex samples valuable structural information on the nanometric scale is contained in its individual SFG tensorial components. Based on the $\chi^{(2)}$ single component read-out detailed above we propose a single SFG-components imaging as an alternative to retrieve information on molecular order. Due to polarization shaping we do not rely anymore on a variable input polarization but rather employ a single-pulse input excitation. The same scheme as in the previous section can easily be extended to imaging to extract individual SFG tensorial components. Imaging requires fast acquisition times which usually are not reached by spectrometers. In the standard mode of our spectrometer a grating spatially separates the different signal frequencies that are then measured by a

CMOS camera. Its read-out process limits the time resolution of the instrument which is of the order of a few Hertz and consequently ill suited for any imaging purposes. To improve the time resolution an alternative would be to either change to a sensitive EM-CCD camera or to strongly disperse the emission spectrum and measure the corresponding intensities on different sensitive detectors. We chose to show here the demonstration of principle using the capabilities of our spectrometer. The signal is sent after the diffraction grating to a narrow side exit behind which we placed a PMT (see Fig. 2.8c). Due to the spatial separation of frequencies this slit is only passed by a up to $\Delta\lambda \approx 3$ nm broad spectral region whose center wavelength can be tuned by rotating the diffraction grating. The PMT does not only have a much better time resolution so that the limiting factor for imaging speed is now the scanning speed of the sample stage, it also benefits from a much greater sensitivity than the CMOS camera (around one to two orders of magnitude). Single $\chi^{(2)}$ components imaging can now be performed by extracting the corresponding regions of the SFG spectrum. By setting the detected wavelength on $\omega_J + \omega_K$, an image is obtained for the corresponding $I^{(J,K)} = \hat{I}_{XJK} + \hat{I}_{YJK}$ intensity defined above, leading to the measurement of $(4 - 3\delta_{JK})\left(\mid \chi^{(2)}_{XJK} \mid^2 + \mid \chi^{(2)}_{YJK} \mid^2\right)$. The factor $(4 - 3\delta_{JK})$ accounts for the XY permutation in the field coupling. This means we sum over both polarization directions of the SFG signal. This is a choice for the validation of the technique, individual separated intensities could also have been measured by placing an analyzer in front of the spectrometer entrance or by blocking one of the beams after the passage of the Wollaston prism (see Fig. 2.8a).

The imaging of independent components is demonstrated on a crystal with 1D symmetry studied previously [89], and already described on page 105. It is placed with its main z-axis along the X direction, as verified by white light illumination imaging and additional polarimetric measurements (as described in section 3.1). Note that in this symmetry case the Z-contribution discussed in Section 4.3 is of minor influence. This situation allows the identification of possible crystalline disorder as discussed in section 4.1. (X, X)- and (X, Y)-coupling SFG images, depicted respectively in Fig. 4.8a and Fig. 4.8b, show that the main tensorial component present in the crystal involves the (X, X) coupling evidenced by the dominant $I^{(X,X)}$ intensity, as expected from the sample symmetry. The presence of a weak but existing $I^{(X,Y)}$ contribution in several crystal regions is a signature of imperfect 1D alignment along the X-axis at those locations. However note, as described before, that this can be due to an imperfect alignment of the molecules along X (as discussed later). In order to quantify the local orientational disorder present in the crystal, we define the anisotropy factor

$$A = \frac{I^{(X,X)} - I^{(X,Y)}}{I^{(X,X)} + I^{(X,Y)}} \tag{4.9}$$

which does not depend on the incident intensity (Fig. 4.8c). A can be evaluated theoretically using a model where the crystal is made of a collection of microscopic molecular dipoles which are not strictly parallel to the direction of the crystal axis (see Eq. (4.4)). The angular distribution of these dipoles $f(\phi, \theta, \psi)$ is defined as a cone of angular aperture

Ψ lying in the (X, Y) plane, tilted by an angle Φ_0 relative to X (Fig. 4.8d). This distribution is used to calculate an effective macroscopic nonlinear susceptibility $\chi^{(2)}$ according to Eq. (4.4) which is then inserted in Eq.(4.1) to deduce the SFG intensities $I^{(X,X)}$ and $I^{(X,Y)}$. A quantifies the order in the sample, with in the present case $A = 1$ for a pure 1D crystalline orientation along X (high order) and $A = 0$ for a high disorder. For a known cone orientation, the measurement of A leads to an estimation of the degree of disorder (Ψ) of the molecular orientations within the crystal. When Φ_0 increases, the dependence of A relative to the cone aperture is shifted to lower values of A (Fig. 4.8d). Even the lack of knowledge of a possible tilt angle Φ_0 of the orientation cone does not prevent a qualitative estimation of the disorder. The maximum $A = 0.97$ value measured in the present crystal leads to $\Phi_0 < 4°$, and $\Psi < 50°$, meaning that in the "high order" regions, the measured molecular cone aperture angle cannot surpass 50°. As the general crystal orientation Φ_0 is easily seen by white light illumination, we can safely confirm that Φ_0 lies below 10° throughout the whole investigated region. This finding in combination with the minimum A value measured ($A = 0.76$) restricts the "highly disordered" crystal regions to a disorder of $60° < \Psi < 85°$. Such a behavior in the measured crystal has been previously observed in a complete polarimetric analysis [89]. Note that as in the case of crystals discussed above, this indetermination between "disorder" (cone aperture) and "orientation" is due to the fact that we use only A as a reporter of structural information, thus one measurement for two unknown parameters. A measurement of the X- and Y-projections would remove this indetermination.

The example above demonstrates the power of single tensorial component imaging on a molecular crystal. It can also be applied to complex biological media and ultimately be used for dynamic measurements of disorder, which is not accessible using polarimetry. In this work, we apply our technique to collagen, in particular collagen fibers extracted from rat-tail tendons and stretched on a surface with a NaCl containing surrounding medium (sample fabricated at the Exeter University, P. Winlove group). Collagen is the currently most studied bio-molecule in SHG imaging. First, because of the high SHG efficiencies that it provides due to its highly packed intrinsic non-centrosymmetric helix structure; second, because it is the most important constituent of the extra-cellular matrix; and third, because its microscopic structure is strongly related to tissue pathologies [91, 94, 210].

The measurement of the individual tensorial $\chi^{(2)}$ components within a collagen type I fiber laying in the (X, Y)-plane was performed with the two-peak excitation profile explained above. In addition to the situation in Fig. 4.8 we additionally separated the SHG signal along its two polarization directions. This was done by blocking either the X- or the Y-polarized signal after the passage of the Wollaston prism to only detect the non-blocked signal with the PMT (see Fig. 2.8). Thus by blocking one path at a time and centering the spectrum alternately on each of the three peaks, six images of the same collagen region were taken, each corresponding to the signal generated by one specific $\chi^{(2)}$ component. The values of these components are then obtained by forming the square root of the intensity image $\left(\chi^{(2)}_{IJJ} = \sqrt{\hat{I}_{IJJ}}\right)$ for those peaks coupling the field's polarization with itself, or by

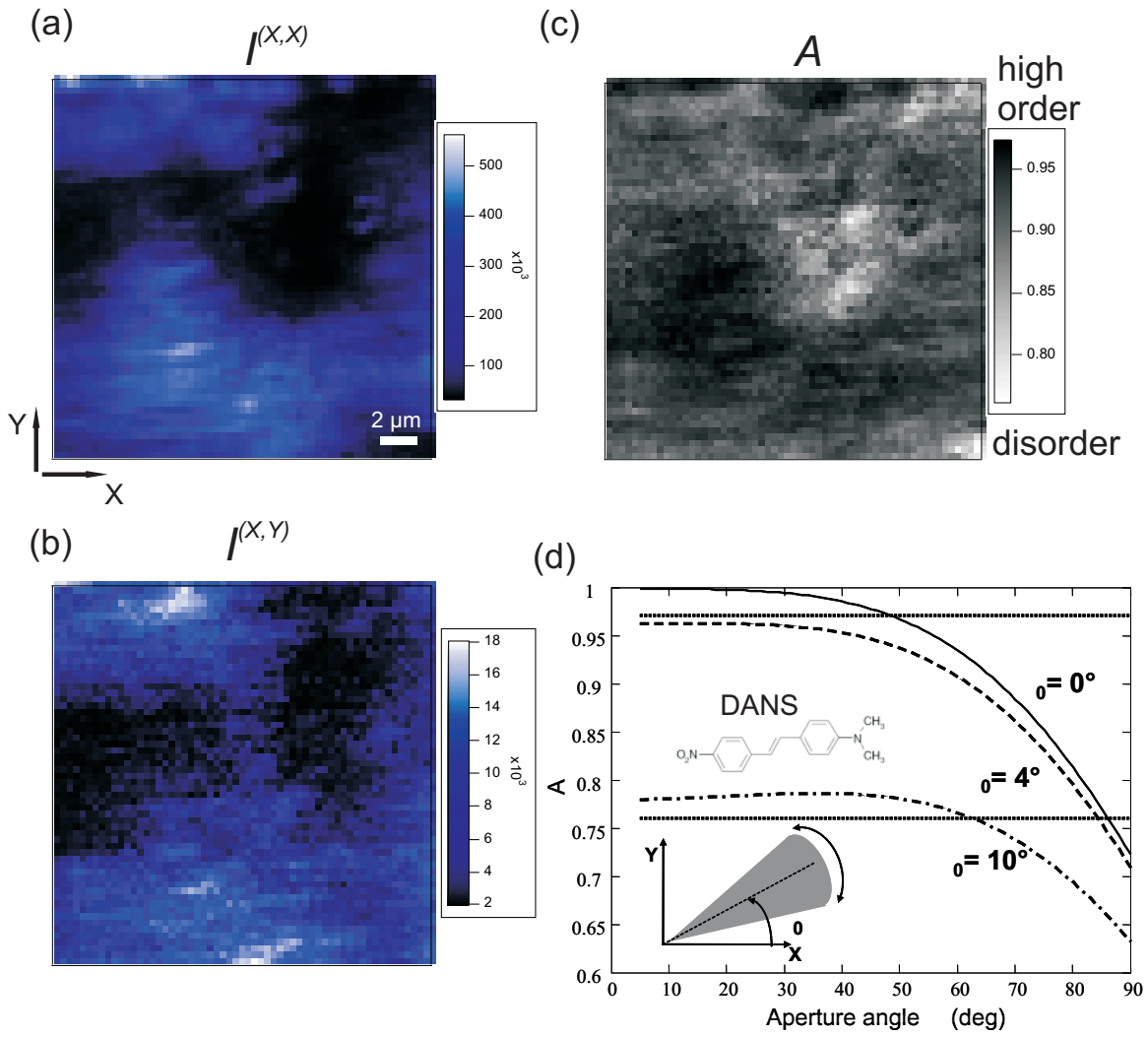

Figure 4.8: Imaging of tensorial components of a 1D symmetry DANS-PHTP crystal. (a) $I^{(X,X)}$ intensity component; (b) $I^{(X,Y)}$ intensity component (both in $\frac{\text{counts}}{\text{s}}$); (c) anisotropy A as described in the text; (d) calculation of the dependence of A on the angular aperture Ψ for several tilt angles Φ_0 of the cone; the chemical structure of the nonlinear DANS molecule is seen as well [89].

taking half of the square root of the intensity image $\left(\chi^{(2)}_{IXY} = \frac{\sqrt{\hat{I}_{IXY}}}{2}\right)$ in the case of the crossed terms due to the fact that $\chi^{(2)}_{IXY} = \chi^{(2)}_{IYX}$. To eliminate the influence on the total SHG intensity created at each point (m, n) within the XY-plane, we normalized the signal at each pixel so that:

$$\sqrt{\sum_{IJK} \chi^{(2)}_{IJK,mn}} = 1 \ , \qquad \forall \ m, n \tag{4.10}$$

The result of this procedure is depicted in the left column of Fig. 4.9. The ensemble of all six images gives the XY-part of the nonlinear $\chi^{(2)}$ for each point within the image.

Additionally we also estimated the tensorial components with a more standard excitation scheme. For this no pulse shaping was performed and the linear polarization of the excitation beam was turned to 0°, 45° and 90° with the help of a $\frac{\lambda}{2}$-waveplate. The generated signals were separated according to their main polarization components and detected by two APDs (see Fig. 2.8). From this procedure we deduced the individual tensorial components with Eqs. (4.5) and (4.7)

The right column of Fig. 4.9 shows the tensorial components of the same collagen sample obtained by this method. The normalization is the same as for the left column. The images show a section within the collagen fiber where the fibrils exhibit a different predominant orientation on the left than on the right. Within the central region different orientations are present. This finding is also confirmed by the polarimetric responses depicted in Fig. 4.10, which are unique for each of these regions. Each region possesses a unique polarimetric response. They can also be simulated by employing a sixth-order symmetry for the microscopic $\chi^{(2)}_{ijk}$-tensor, since many works assigned collagen to a C_6 crystalline point group structure [8, 210, 211]. In region 1 the fiber is oriented close to 45° relative to the X-axis, which is seen in the polar graph (Fig. 4.10b) in the very similar magnitudes of the X- and Y-coupling. In region 2 the fiber is oriented close to 0°, evidenced by the strong X-coupling in Fig. 4.10c. The observed polar graph shows a certain resemblance to the expected one from a C_6 symmetry (small graph). The differences being assigned to signal backscattering within the thick collagen fiber. The fiber in region 3 on the other hand is oriented around 135° with similar I_X and I_Y intensities again (Fig. 4.10d), but a rotated polar graph as compared to region 1.

The $\chi^{(2)}$-values extracted from both methods presented in Fig. 4.9 do not always coincide though they frequently lie within the same value range. Both methods encounter its particular difficulties. The extraction by different angles of the incident polarization (right column in Fig. 4.9) profits from a high signal to noise ratio as the whole pulse spectrum is involved in the signal creation and very sensitive detectors (APDs) are used. On the downside the crossed tensorial components $\chi^{(2)}_{XXY}$ and $\chi^{(2)}_{YXY}$ cannot be determined directly, as one has to take into account several incident polarizations (Eq. (4.7)) and consequently the relative error increases. In this case it is also absolutely necessary that the observation conditions do not change between different polarization measurements. All images shown in Fig. 4.9 consist of 60×60 pixel. For the linear polarization excitation

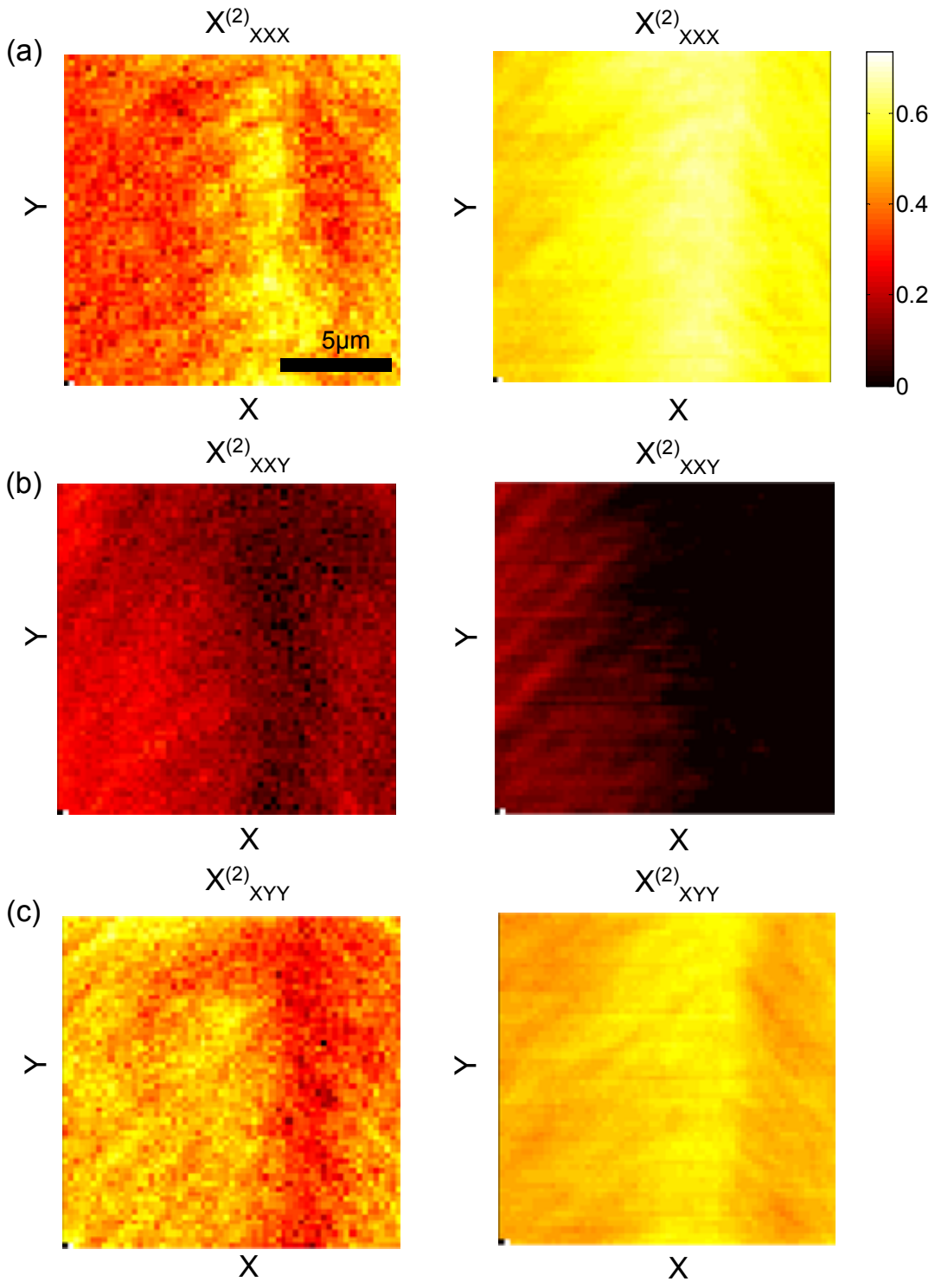
(a)
$X^{(2)}_{XXX}$
$X^{(2)}_{XXX}$
5μm
Y
X
Y
X
0.6
0.4
0.2
0
(b)
$X^{(2)}_{XXY}$
$X^{(2)}_{XXY}$
Y
X
Y
X
(c)
$X^{(2)}_{XYY}$
$X^{(2)}_{XYY}$
Y
X
Y
X

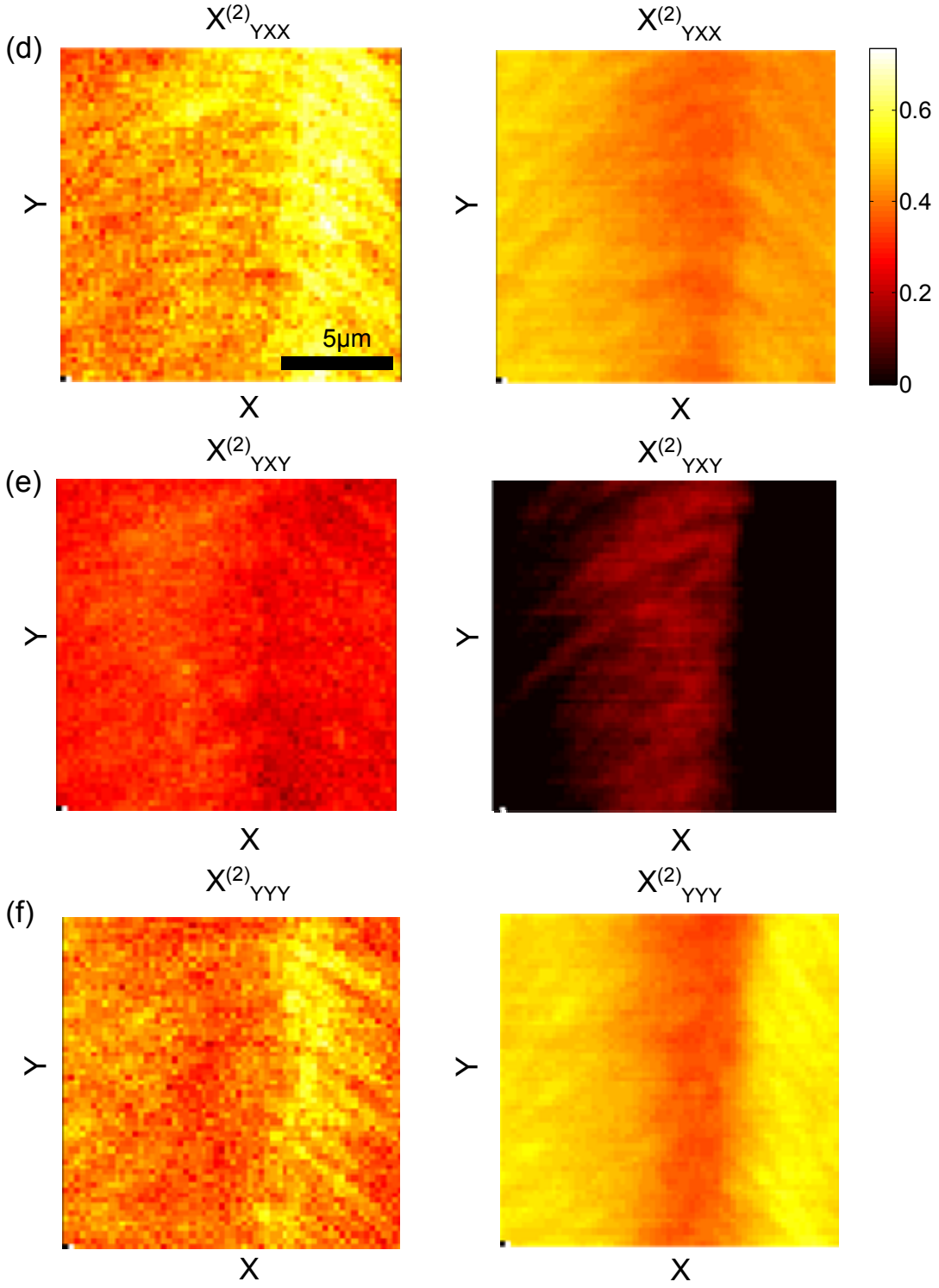

Figure 4.9: Imaging of tensorial components of a collagen fiber. (a) $\chi^{(2)}_{XXX}$; (b) $\chi^{(2)}_{XXY} = \chi^{(2)}_{XYX}$; (c) $\chi^{(2)}_{XYY}$; (d) $\chi^{(2)}_{YXX}$; (e) $\chi^{(2)}_{YXY} = \chi^{(2)}_{YYX}$; (f) $\chi^{(2)}_{YYY}$. Left column: two-peak excitation profile; right column: calculations based on standard excitation with linear polarized light at 0°, 45° and 90°.

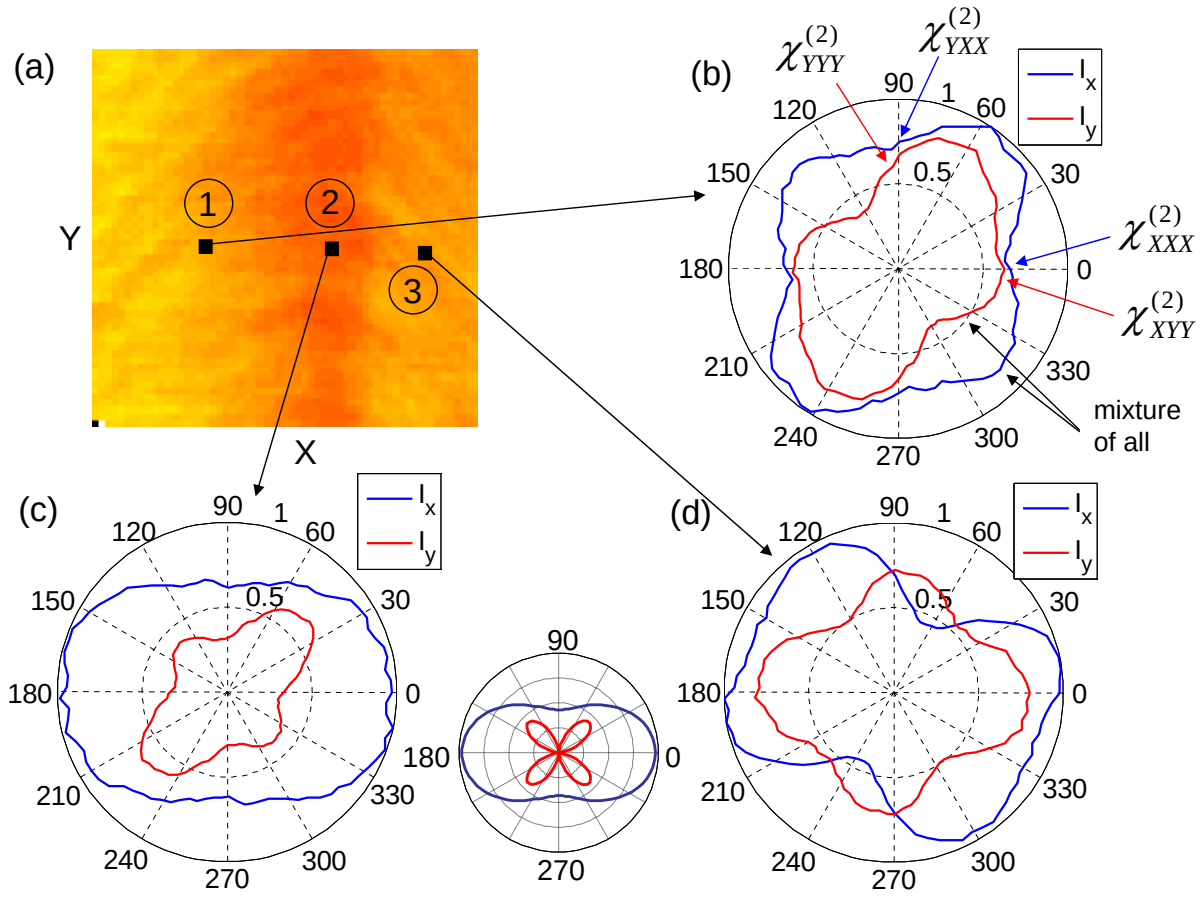

Figure 4.10: Polarimetric SFG response of collagen type I. (a) 2D overview of the investigated region as in Fig. 4.9; (b-d) polar plots of the SFG intensity ([a.u.]) with respect to the incident polarization angle (see Fig. 4.2a) at the points specified in (a). For the graph in (b) the expected polarimetric response based on a C_6 symmetry model is shown as a small graph.

scheme the pixel dwell time was 20 ms, resulting in an image acquisition time of about 70 s. For the two-peak excitation profile on the other hand, a longer pixel dwell time of 50 ms was chosen due to the lower excitation field strength caused by the amplitude shaping, and the less sensitive detector (PMT) (as compared to APDs), both of which reduce the signal. The corresponding image acquisition time was therefore around three minutes, which is clearly limited by the quality of the detection. Within these periods we additionally encountered changes in the vertical sample position of up to a micrometer. In a very thin sample this is easily corrected for as only one sample layer will give the maximal signal and even minimal shifts are immediately noticed. But a collagen fiber is a very thick sample with numerous signal-generating layers that each have their proper orientations. Under these conditions it is much harder to maintain a stable vertical position over a long time. Because collagen fibers are birefringent materials, a vertical shift is prone to alter

the polarimetric SHG response [211] as well as the signal peak heights detected with our two-peak excitation profile.

The consequences of this effect can be observed in the right part of the right column in Fig. 4.9b and Fig. 4.9e where in an extended region the $\chi^{(2)}_{XXY}$ and $\chi^{(2)}_{YXY}$ coefficients were found to be negative - they were set to 0 in the images - which is an inconsistent result. (It should be noted that $\chi^{(2)}$ can very well possess negative elements, these describe a polarization response opposite to the driving fields (see Eq. (1.16), but we only have access to their absolute values with the methods presented here, because they both rely on intensity measurements where no information on the sign is kept.) A consequence of these black or near-black regions is that the associated $\chi^{(2)}$-values for the other four components get increased due to the normalization condition in Eq. (4.10). This leads to less contrasted images in the right column of Fig. 4.9 compared to the left one, even though the signal to noise ratio is much better.

Of course also the $\chi^{(2)}$ extraction method based on a shaped pulse (left column in Fig. 4.9) suffers from sample instabilities, but as each tensorial component depends exclusively on one measurement, within this measurement the values of that particular component can be compared relative to each other. On the other hand the shaped pulse excitation provides a worse signal to noise ratio, for the reasons detailed above. This difference in signal-to-noise ratios is evident in Fig. 4.9 between the left and the right columns. The use of more powerful laser sources and a temporally stable sample should however lead to very reliable results with this method. Another possible solution to circumvent this problem will be discussed in the conclusion of this chapter.

4.5 Single SFG tensorial component contrast by phase and polarization pulse shaping

The possibility to manipulate intra-pulse interferences by the design of specific spectral phase profiles has been exploited in molecular media to enhance nonlinear pathway efficiencies [29] and improve the contrast in two-photon coherent effects [212]. In addition to the polarization control detailed above, phase shaping could therefore provide an additional degree of control to target specific nonlinear processes related to a given symmetry inside a sample. Here we explore the possibility to annihilate polarization coupling pathways by phase shaping, with the perspective of a structural contrast imaging that would avoid the use of the spectral filtering described above. A phase shaping scheme involving the control of the parity of the phase profile in a given spectral window is applied [29, 212, 31]. Let us consider a spectrally broad incident field that has a phase of ϕ_0 at a given frequency ω_0. If we now assume that the phase profile is antisymmetric around that point it follows that $\phi(\omega_0 - \Omega) = -\phi(\omega_0 + \Omega)$. An evaluation of the SFG signal at $2\omega_0$ according to Eq. (4.1)

gives:

$$\begin{aligned} P^{SFG}(2\omega_0) &\propto \int E(\omega_0-\Omega)E(\omega_0+\Omega)\mathrm{d}\Omega \\ &= \int |E(\omega_0-\Omega)||E(\omega_0+\Omega)|e^{i\phi(\omega_0-\Omega)}e^{i\phi(\omega_0+\Omega)}\mathrm{d}\Omega \\ &= \int |E(\omega_0-\Omega)||E(\omega_0+\Omega)|e^{i(\phi(\omega_0-\Omega)-\phi(\omega_0-\Omega))}\mathrm{d}\Omega \\ &= \int |E(\omega_0-\Omega)||E(\omega_0+\Omega)|\mathrm{d}\Omega \end{aligned} \tag{4.11}$$

All possible frequency combinations leading to a SFG signal at $2\omega_0$ therefore have the same phase and thus interfere constructively. If we assume on the other hand a symmetric phase profile around ω_0, meaning $\phi(\omega_0-\Omega)=\phi(\omega_0+\Omega)$, an analogous calculation leads to:

$$P^{SFG}(2\omega_0) \propto \int |E(\omega_0-\Omega)||E(\omega_0+\Omega)|e^{2i\phi(\omega_0-\Omega)}\mathrm{d}\Omega \tag{4.12}$$

Each frequency pair contributing to the SFG signal at $2\omega_0$ has a different phase which amounts to a mostly destructive interference depending on the amount of phase mismatch between each frequency coupling pair and the spectral weight of every one of them. By a controlled distribution of symmetric and antisymmetric phase points it is therefore possible to selectively suppress certain SFG pathways while maintaining others. This is most conveniently done by applying sinusoidal phase profiles, as they possess both symmetric and antisymmetric points and at the same time do not take on huge phase values, qualifying them for use with SLMs (see page 75).

Fig. 4.11 depicts several simulated sinusoidal phase profiles for the same laser spectrum and the corresponding SFG spectra compared to one obtained for a flat phase. For an antisymmetric point at λ_0 the SFG spectrum at $\frac{\lambda_0}{2}$ has a maximum, while it gets suppressed when the phase profile has a symmetric point at λ_0. At other wavelengths the interferences between the different SFG pathways lead to a signal with a more or less destructive interference. For a better contrast between the signal at $\frac{\lambda_0}{2}$ and the surrounding wavelengths, some schemes have been developed based on a "binary" phase shape [31].

Here we use spectrally narrow windows that considerably reduce the second-order coupling possibilities compared to a non-amplitude shaped pulse. Over the remaining coupling subset the control of constructive and destructive interferences for frequencies other than $2\omega_0$ is easily established with a convincing quality by setting an appropriate period of the sine. The amplitude windows are centered respectively on ω_1 and ω_2 (Fig. 4.2c). The resulting SFG efficiency at the coupling polarization component $\omega_1+\omega_2$ is therefore dependent on the spectral phase $\phi_1(\omega)+\phi_2(\omega)$, with $\phi_1(\omega)$ and $\phi_2(\omega)$ being the spectral phase dependencies of both incident field components. By setting the phase dependence so that it presents a symmetric point at both positions ω_1 and ω_2 but with opposite extrema (Fig. 4.12a), the intrapulse interference will be constructive at the SFG position $\omega_1+\omega_2$,

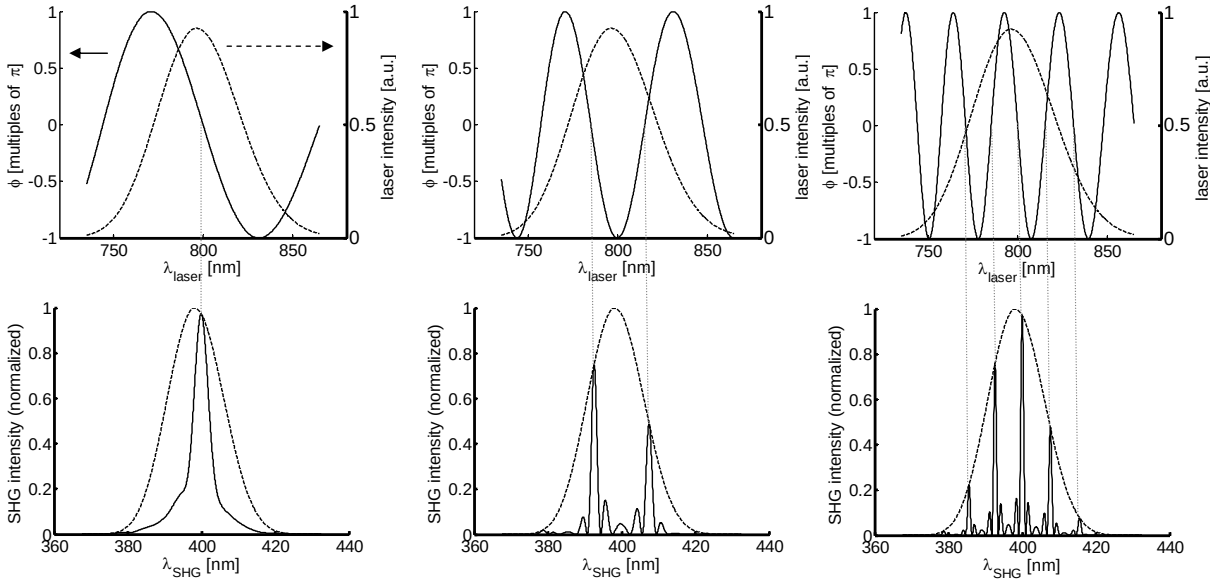

Figure 4.11: SFG response for pulses with sinusoidal phase profiles (simulation). Upper row: sinusoidal phase profiles (solid lines) for the same laser spectrum (dashed lines). Lower row: corresponding SFG signals (solid lines) compared to the SFG response for the same excitation spectrum but with a flat phase (dashed lines). Dotted grey lines connect the antisymmetric phase points at λ_0 to the SFG maxima at $\frac{\lambda_0}{2}$.

while being destructive at $2\omega_1$ and $2\omega_2$ (Fig. 4.12c). Contrariwise, by setting antisymmetric frequency dependencies with opposing slopes at ω_1 and ω_2 (Fig. 4.12b), constructive interference is reached at $2\omega_1$ and $2\omega_2$ while at $\omega_1 + \omega_2$ the signal gets suppressed (Fig. 4.12d). This effect has been observed experimentally on a KTP crystal (Fig. 4.12) with a good agreement with the expected response. Because both spectral windows still have a width of 10 nm there remains a small signal in the SFG peaks with destructive interference, but the contribution of these peaks is nonetheless strongly suppressed compared to the constructive peak. The same reasoning also explain the spectral narrowing of the central peak in Fig. 4.12c where constructive interference is only reached for $\omega_1 + \omega_2$ but not for neighboring frequencies. This approach nevertheless gives a possibility to manipulate two-photon excitation pathways, which could be specifically polarized. It allows in particular working with a complete spectral integration by a detector without the need of spectral filtering, leading to an enhanced structural contrast imaging by accentuating specific tensorial components of the SFG response relative to other ones.

4.6 Conclusion

We demonstrated the possibilities of combined amplitude, phase and polarization shaping of single pulses to obtain information on the second-order nonlinear susceptibility tensor

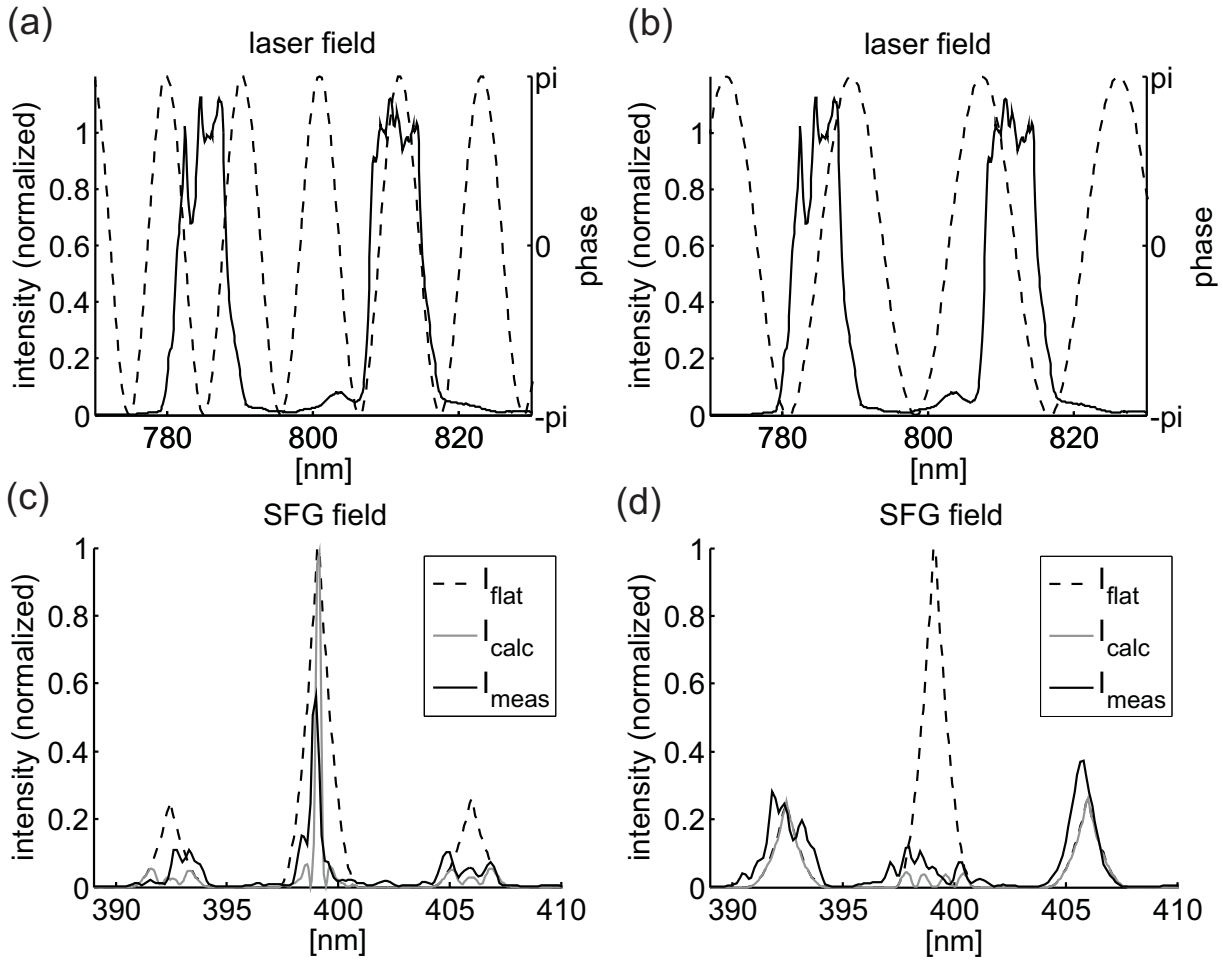

Figure 4.12: Phase control of the different polarization coupling schemes following the design of odd versus even dependencies of the spectral phase in two spectral windows. (a,b) laser field with intensity (continuous line) and phase (dashed line); (c,d) their corresponding SFG spectra with the measured signal (black line), the expected one (light grey line) and the expected signal for a flat spectral phase (dashed line) for comparison; symmetric phases in the spectral windows attenuate the side peaks leaving the one in the center (a,c) while antisymmetric phases in the spectral windows leave the side peaks and attenuate the central peak (b,d).

$\chi^{(2)}$. By shaping two amplitude windows into a broadband pulse that get perpendicularly polarized to each other, the sum frequency signals arising from the different $\chi^{(2)}$ components are spectrally separated. In combination with a polarized detection, all six tensorial components present in the (X, Y)-plane where the sample is located can be read out simultaneously from a single measurement. Thus our scheme is much faster than for example a complete polarimetric study or one consisting of three subsequent measurements with different linear polarizations. For known crystalline samples our method offers the possibility to determine their orientations. And for molecular and biomolecular assemblies the order and disorder can be quantified.

This scheme is particularly adapted to microscopy. The use of high NA objectives in combination with a nonlinear signal generation process leads to high resolutions in imaging. The potential to visualize order and disorder on sub-micrometric length scales is especially interesting for biological applications as the proper functioning of biomolecular assemblies is often closely connected with their spatial configuration. For such investigations a contrast method as we have presented, that does not depend neither on prior sample staining nor on the spatial repartition of different molecular species nor on their concentration, should be of great promise.

Yet there are still a number of issues to be resolved. Due to the high NA focussing tensorial components containing a Z-dependence come into play and may disturb the signal. However, if the symmetry of the studied molecules is known, this Z-contribution can be theoretically quantified and thus removed from the results. Furthermore its effect is only non-negligible when the nonlinear dipoles are preferentially oriented along the propagation direction. And in imaging, where relative measurements between different (X, Y)-positions are performed, this Z-coupling does hardly influence the contrast. In any case, working with lower NA objectives provides an interesting alternative.

A more serious concern is the low signal intensity generated by our method especially in biological media. It is mainly due to two reasons: first, the amplitude shaping reduces considerably the excitation power which has very negative effects especially for nonlinear optical processes like SFG as the signal intensity depends on the square of the incident intensity. Second, a spectral readout is required to separate the contributions of the different tensorial components. Spectrometer cameras are in general much less sensitive than for example avalanche photodiodes. Moreover these cameras are way too slow for imaging purposes.

While this problem could be solved by changing the detection capabilities, we tried to solve it in two different ways. First, we avoided the spectrometer camera and directed a portion of the spectrally dispersed signal to a photomultiplier tube, that offers a much higher sensitivity than the spectrometer camera and a much better time resolution. However, while single tensorial component imaging was possible for crystalline samples it got very challenging for biological media such as collagen because the detected signal was still very weak. An even more sensitive detector like an APD could lead to a further improvement.

A second path taken to obtain more satisfactory results was the addition of phase pulse shaping to the amplitude and polarization shaping. By using a combination of symmetric

and antisymmetric points it is possible to suppress certain SFG pathways while maintaining others. The idea is to maintain only one of the three signal peaks that can then be detected by an APD without the need of a spectral readout leading to a simpler setup and a higher signal. And while it is possible to fix a constructive interference at a certain signal wavelength, it is however not trivial to completely suppress another one. Moreover, even if one succeeds in doing so, signals at neighboring wavelengths are less well controlled. The same is true for the spectral neighborhood of constructive interferences. These residues reduce the possible attainable contrast between the signals from different components.

To really render our method useful for the study of a wide range of materials, especially biological ones, the generated signal needs to be optimized. Unless more intense laser sources are employed the only way to do so is by avoiding the amplitude shaping that reduces the pulse energy. However, the method presented here relies on this shaping to obtain a spectral separation of the signals originating from different tensorial components. It would be worthwhile to study whether a pure combination of phase and polarization shaping could yield a similar contrast.

Fig. 4.13 shows such a possibility. Throughout the excitation spectrum both polarizations are present, but with different phase dependencies, for example sinusoidal profiles (Fig. 4.13a). This scheme would fully exploit the independent tuning of the phase profiles of both polarizations, accessible using a polarization and phase shaper. The corresponding SFG fields then exhibit maxima and minima at different positions. It can be assured that at certain spectral positions only one of the three fundamental polarization couplings is maintained while the other two get suppressed (Fig. 4.13b). In this case a spectral readout or a readout of only a narrow region of the spectrum with a more sensible detector can again provide a single tensorial component contrast. Because in such a phase and polarization shaped pulse the whole pulse energy is used, the obtained signal is much larger than for an amplitude shaped pulse. In Fig. 4.13c we compare the excitation pulse shaped as in Fig. 4.13a with the two-peak excitation profile as used in this chapter, where both amplitude windows are polarized perpendicular to one another and possess a flat phase. The corresponding SHG signals (Fig. 4.13d) reveal the large signal loss due to amplitude shaping. But more work needs to be done to optimize the excitation phase profiles and explore the potential and the limitations of this approach.

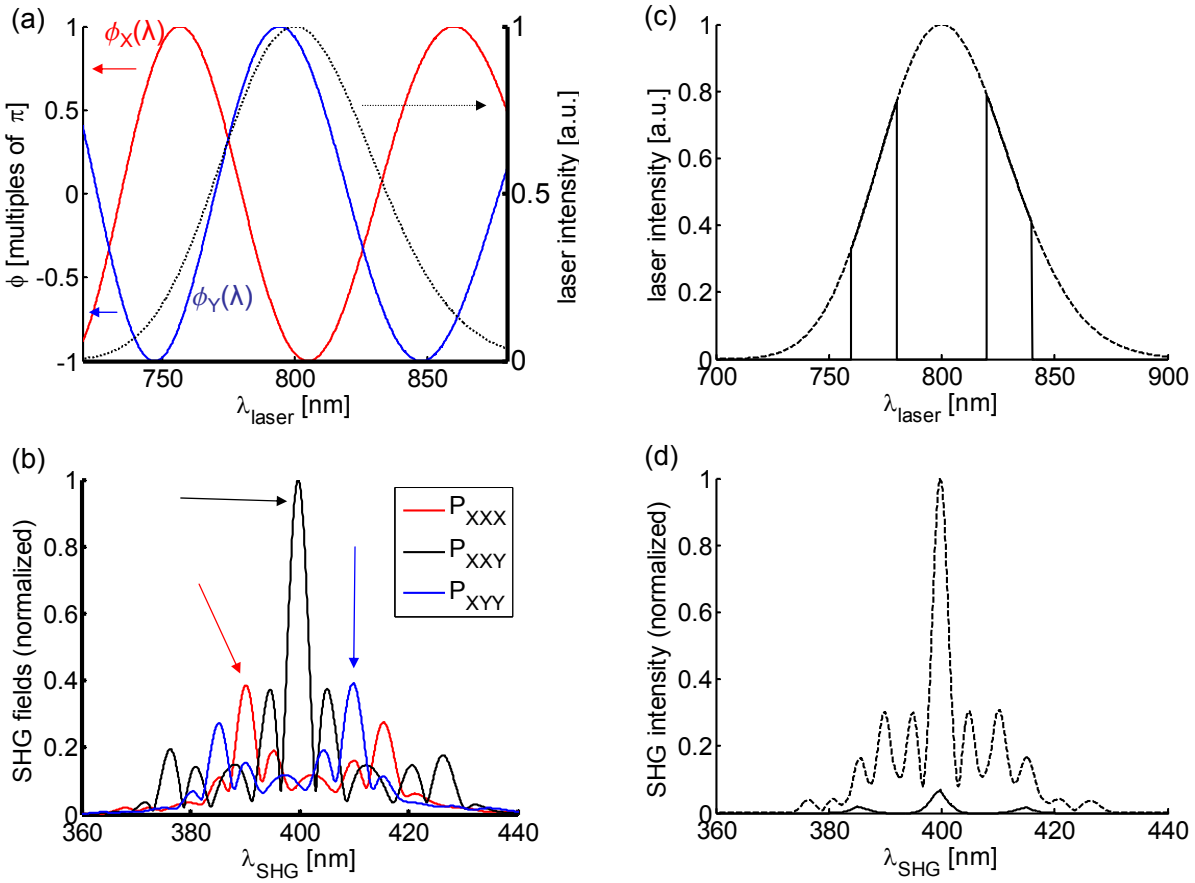

Figure 4.13: Possible pulse shaping scheme for the readout of individual tensorial components without amplitude shaping. (a) Excitation profile: both polarizations are present in the whole pulse but with different phase dependencies (here: sinusoidal phases). (b) Corresponding fields generated by the sum frequency coupling (only shown for X-polarized fields): at certain signal wavelengths (indicated with arrows) one of the three possible polarization couplings is clearly dominant, permitting a single component readout. (c) Comparison of the excitation spectra for the case in (a) (dashed line) and the two-peak profile with a flat phase used in this chapter (solid line). (d) SHG spectra for those two profiles, line styles as in (c).

Chapter 5

Single pulse Coherent anti-Stokes Raman Spectroscopy (CARS)

5.1 Introduction

Coherent anti-Stokes Raman scattering (CARS) is a coherent third-order nonlinear process as already explained in section 1.3.2. It is usually performed by focussing two lasers (the pump at frequency ω_p and the Stokes at frequency ω_S) onto the sample with a frequency difference $\omega_p - \omega_S$ corresponding to the frequency Ω of a molecular vibration of the sample. Thus a coherence is induced in the medium which is further read out by a probe beam (at the same frequency as the pump) to finally radiate an anti-Stokes signal (Fig. 5.1a). CARS is an interesting process to analyze and image vibrational bands in a medium, as the signal generation is much more efficient than in spontaneous Raman scattering [9]. Controlling this process experimentally is however far from trivial. For a maximal signal generation is it mandatory that both laser pulses overlap perfectly in time and space. Due to the third-order nonlinearity of the process even small deviations from these conditions lead to huge signal losses. Furthermore, two fixed laser frequencies ω_p and ω_S only allow to probe one specific anti-Stokes frequency $\omega_{as} = 2\omega_p - \omega_S$. To obtain a whole CARS spectrum at least one of the laser sources must be frequency-tuneable (Fig. 5.1a). For each frequency pair a CARS measurement has to be performed. Therefore it takes a relatively long time to obtain a spectrum.

These restrictions can be removed by using spectrally broad femtosecond lasers. They can replace one of the picosecond lasers in the standard CARS setup (multiplex CARS), allowing for the acquisition of a whole spectrum in a single measurement [105, 121], whose spectral resolution is determined by the bandwidth of the spectrally narrow pulse (Fig. 5.1b). Note that the Raman spectral bands information can then be retrieved accounting for the effect of the non-resonant signal (see section 1.3.2) using maximum entropy methods (MEMS)[213]. It is also possible to employ two broadband lasers. But this leads to numerous resonant coupling possibilities and even more non-resonant combinations, both of which completely blur the CARS spectrum. Additional measures have to be taken

to regain an acceptable spectral resolution. This can be done by linearly chirping both pulses (see section 2.2), as the probed frequency $\omega(t) = \omega_p(t) - \omega_S(t)$ then becomes time-dependent and thus the CARS spectrum is obtained from the time trace on the detector [122, 123, 124, 125].

These schemes still rely on the use of two separate lasers. However, it is also possible to just use one single broadband laser where the same pulse acts as pump, Stokes and probe field simultaneously (Fig. 5.1c), which was pioneered by the Silberberg group. In this

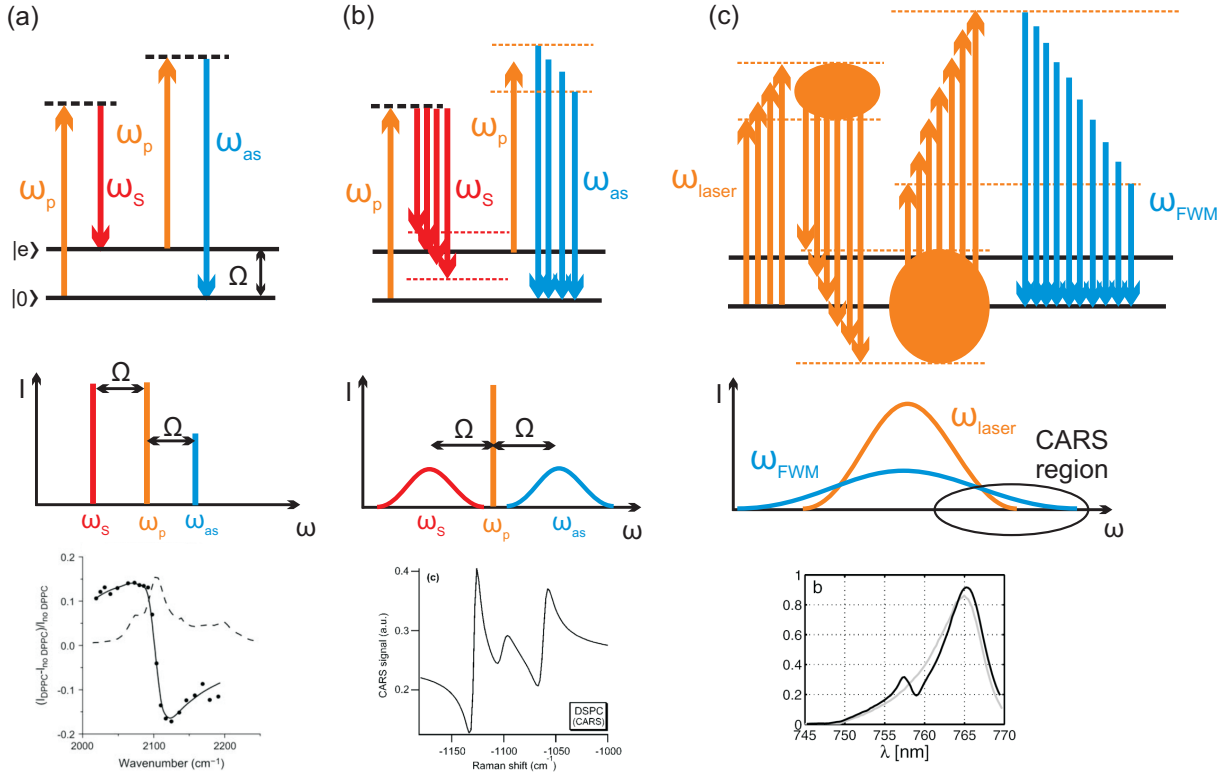

Figure 5.1: CARS schemes. (a) standard configuration with two narrow-band lasers; (b) multiplex CARS with a narrow-band and a broadband laser; (c) single pulse CARS with a broadband laser. Upper row: energy level diagrams; real states are represented by solid lines, virtual states by dashed lines, for (b) and (c) only the boundaries of the traversed virtual state regions are drawn. Lower row: sketches of the spectral positions of the participating lasers and the signal. Ω: energy of the probed vibrational transition; ω_p: pump/probe frequency; ω_S: Stokes frequency. In (c) all four-wave-mixing (FWM) processes occur, only a portion of the total signal can be attributed to CARS as indicated in the lower right corner. For all three cases a typical CARS spectrum is shown as well [214, 105, 39].

case all resonant and non-resonant third-order nonlinear processes occur, that are usually called four-wave-mixing (FWM) - referring to the three generating fields and the signal -, of which CARS is only one example that can be found at the high frequency edge of the

FWM spectrum. The complexity of such a setup is much reduced compared to a two-laser configuration as there is no need anymore for pulse synchronization and beam recombining. Also the focal volume overlap of all fields is perfect. Not surprisingly, these advantages are accompanied by challenges of a different nature, namely assuring the spectral resolution of the resonant signal. For this, pulse shaping has been used to introduce amplitude, phase or polarization features within the excitation spectrum that help to recover the resonant CARS spectrum. By shaping a sinusoidal phase with a short period into the pulse it is possible to selectively excite only certain vibrational transitions [38]. Another scheme is based on setting the high-frequency edge of the excitation pulse to a different polarization (Y - for example) than the rest (X) and introducing additionally a phase jump within the Y-polarized region. The time profile of the Y-polarized pulse is then split in two with no intensity at $t = 0$ when the X-polarized pulse arrives. As a result the Y-polarized resonant CARS signal is almost background-free and has a nanometer spectral resolution [49]. At last, the approach by Oron *et al.* [39] introduces a narrow phase jump into the pulse. This scheme, detailed in the following section, has been chosen in this work. We explored in particular its potential towards polarization-CARS readout, applying the polarization shaping setup developed in chapter 2.

5.2 Principle

For the moment let us assume that the generating fields are all polarized in the same direction. According to Eq. (1.36) the CARS field is then given by:

$$P = \chi_R^{(3)}(\Omega) E_p E_p E_S^* + \chi_{NR}^{(3)} E_p E_p E_S^* \tag{5.1}$$

where $\chi_R^{(3)}$ and $\chi_{NR}^{(3)}$ are the resonant and non-resonant third-order nonlinear susceptibilities (see Fig. 1.8). $\chi_{NR}^{(3)}$ describes the pathways that only involve virtual energy levels, usually far away from any vibrational or electronic molecular energy levels, and can therefore be considered to be frequency independent. $\chi_R^{(3)}$ on the other hand is responsible for the interaction of the fields with the molecular vibrations and thus contains the same frequency dependence as these energy levels themselves:

$$\chi_R^{(3)} = \frac{a}{(\Omega - \Omega_R) + i\Gamma} \tag{5.2}$$

Here, Ω is the beating frequency $\omega_p - \omega_S$ between the pump and the Stokes field, Ω_R the frequency of the vibrational transition, and Γ the HWHM of the Lorentzian shape of the vibrational band. In the case of single pulse CARS, $E_p = E_S = E(\omega) = |E(\omega)|e^{i\phi(\omega)}$. The first part of the CARS process - the generation of the beating frequency Ω - thus becomes [39]:

$$A(\Omega) \propto \int_0^\infty \mathrm{d}\omega E^*(\omega - \Omega) E(\omega) \tag{5.3}$$

where $A(\Omega)$ is a second-order driving polarization. The resonant and non-resonant CARS polarizations P_R and P_{NR} are then calculated through:

$$P_{NR}(\omega) \propto \int_{-\infty}^{\infty} \mathrm{d}\Omega E(\omega-\Omega)A(\Omega) \tag{5.4}$$

$$P_R(\omega) \propto \int_{-\infty}^{\infty} \mathrm{d}\Omega \frac{E(\omega-\Omega)}{\Omega-\Omega_R+i\Gamma}A(\Omega) \tag{5.5}$$

P_R and P_{NR} contain all four-wave-mixing possibilities. For the CARS signal it suffices to perform the integration in Eqs. (5.4) and (5.5) only from 0 to infinity, which corresponds to the case where the Stokes field is of lower frequency than the pump field.

Consider the case where A only has a contribution at Ω_R, meaning that $A(\Omega) = A(\Omega_R)\delta(\Omega-\Omega_R)$ which corresponds to standard CARS with two narrow-band lasers when only one beating frequency gets selected. If this was possible in single pulse CARS the resulting resonant field would be:

$$\begin{aligned} P_R(\omega) &\propto \int_0^{\infty} \mathrm{d}\Omega \frac{E(\omega-\Omega)}{\Omega-\Omega_R+i\Gamma}A(\Omega_R)\delta(\Omega-\Omega_R) \\ &= \frac{E(\omega-\Omega_R)}{i\Gamma}A(\Omega_R) \end{aligned} \tag{5.6}$$

The signal thus has the same form as the exciting laser spectrum $E(\omega)$ and consequently the information from the vibrational transition with Ω_R is spectrally spread. Because in single pulse CARS $A(\Omega)$ is itself a spectrally broad function and by no means a narrow peak, all these different Ω will result in a broad resonant CARS spectrum. Additionally, the numerous non-resonant coupling mechanisms surpass by far the resonant ones. As a result, no information on the molecular vibration can be obtained from such a measurement unless further steps are taken to regain the spectral resolution.

A possibility to do so is the insertion of a change in either amplitude, phase, polarization or any combination of these within a narrow spectral interval, which will therefore "singularize" one resonant coupling among others. We opt, in accordance with Oron *et al.* [39], for a phase jump of π at a certain probe frequency ω_{pr}. This change hardly affects $A(\Omega)$ as the energy contained within this narrow spectral region is negligible compared to that of the whole pulse. It will however affect $P_R(\omega)$ differently from $P_{NR}(\omega)$. The resonant signal of a vibration with Ω_R only arises from a small region Ω around Ω_R. Thus the phase of the resonant signal $P_R(\omega)$ in Eq. (5.5) follows the phase of the probing field $E(\omega-\Omega_R)$. A phase jump in $E(\omega)$ at $\omega=\omega_{pr}$ therefore results in a phase jump in $P_R(\omega)$ around $\omega=\omega_{pr}+\Omega_R$ as well. The non-resonant signal on the other hand arises from all frequency couplings and not only from those where $\Omega \approx \Omega_R$ and consequently the phase jump within P_{NR} will occur at a different position for each frequency coupling. In the coherent sum of all of these, it cannot be seen anymore and the final phase is almost flat.

The total CARS signal comes from the sum of the resonant and the non-resonant

contribution (Eq. (1.38)):

$$\begin{aligned} I_{CARS} &= |P_R + P_{NR}|^2 \propto |P_{NR}|^2 + 2\mathfrak{Re}\{P_{NR}P_R\} + |P_R|^2 \\ &\approx |P_{NR}|^2 + 2|P_{NR}|\mathfrak{Re}\{P_R\} \end{aligned} \tag{5.7}$$

Here we took into account that the non-resonant contribution is a real quantity as only pathways via virtual levels are involved and no absorption occurs. Furthermore the non-resonant signal surpasses by far the resonant one, as much more coupling possibilities exist. Therefore the pure resonant term has been omitted in Eq. (5.7). The first of the two-remaining terms contains the pure non-resonant contribution, but contrary to CARS with two narrow-band lasers, it is not anymore a constant function but follows the form of the pulse spectrum, as the number of coupling possibilities and their spectral weight differs from frequency to frequency. The second term describes the interference between the resonant and the non-resonant signal. Both contributions are coherent with the probe field $E(\omega - \Omega)$ and P_{NR} thus acts as a local oscillator for P_R. As stated earlier the non-resonant signal nearly shows a constant phase while the resonant one exhibits a phase jump around $\omega_{pr} + \Omega_R$. In this region the phase relationship between P_R and P_{NR} quickly changes resulting in successive constructive and destructive interference. Consequently a peak-dip structure, as characteristic for CARS is seen on top of the strong non-resonant background (Fig. 5.2). It should be noted, that contrary to CARS with two narrow-band lasers where

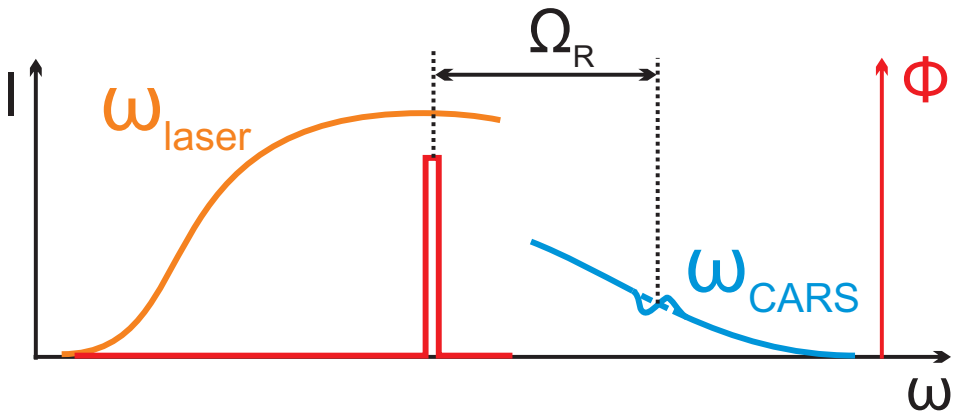

Figure 5.2: Single pulse CARS. A phase step within the laser spectrum leads to a peak-dip structure at a spectral position shifted by Ω_R within the CARS spectrum.

a lot of effort is put into the suppression of the non-resonant background (see page 30), here it is precisely this background that permits the detection of the resonant signal. In itself $|P_R|^2$ is way to weak to be detected because the probe field - the narrow phase jump region within the broad pulse - does not contain much energy. Only the heterodyning with the strong non-resonant field that amplifies the resonant one leads to sufficiently high intensities for spectral detection.

Our laser provides pulses around 800 nm with a FWHM of 60 nm (approximated in Fig. 5.3a, solid line, by a Gaussian with this width). This provides us with a driving polarization A according to Eq. (5.3) with a bandwidth of 55 THz (Fig. 5.3b, solid line) of which only the positive half can lead to a CARS process. As A is centered around 0 it follows that low energetic vibrations are best excited. The frequency values ν are related to wave numbers wn by: $wn = \frac{\nu}{c}$ with c the speed of light. Thus for $A(\nu_{1/2} \approx 28\,\mathrm{THz}) = \frac{1}{2}A_{max}$, $\nu_{1/2}$ corresponds to $wn \approx 930\,\mathrm{cm}^{-1}$. Vibrations with much higher wave numbers are hardly excited by our single pulse CARS laser. Therefore this technique is not suited for the detection of classic CARS bands like the C-H stretching mode ($3000\,\mathrm{cm}^{-1}$) or the C=O stretching mode ($1750\,\mathrm{cm}^{-1}$). It rather addresses the fingerprint region (500-1500 cm^{-1}), where each organic compound has its unique vibrations.

Let us suppose we place the phase step at the center of the laser spectrum around $\lambda_{ph} = 800\,\mathrm{nm}$. The heterodyning term is then visible at a frequency $\nu_{CARS} = \frac{c}{\lambda_{CARS}} = \Omega_R + \nu_{ph} = \Omega_R + \frac{c}{\lambda_{ph}}$, from which follows:

$$\lambda_{CARS} = \frac{1}{wn + \frac{1}{\lambda_{ph}}} \tag{5.8}$$

A vibration with $wn = 930\,\mathrm{cm}^{-1}$ therefore appears around $\lambda = 744\,\mathrm{nm}$, a spectral region where the laser is still present. For vibrations with lower wave numbers the signal is even closer to the phase step position. Due to the extremely small third-order nonlinear cross sections no CARS signal can be extracted as it is many orders of magnitude smaller than the laser intensity at these positions.

It is therefore indispensable to separate the generated signal from the incident light. For this a spectral cut-off is inserted into the beam path to chop all high laser frequencies. This can be done by a high-pass (in the wavelength domain) filter. An even better option is to block high frequencies in the Fourier plane of the $4f$-line (see section 2.3), as it only necessitates a black screen. Furthermore the phase jump has to be placed close to the cut-off frequency to ensure that the signal of low wave numbers appears outside the laser region. Of course this filtering reduces the spectral width of the laser and thus also the accessible wave numbers. The dashed lines in Fig. 5.3 illustrate this change when the spectrum of Fig. 5.3a gets cut at $\lambda_{cut} = 770\,\mathrm{nm}$. Under these conditions the width of $A(\Omega)$ is reduced to 40 THz and $\nu_{1/2}$ only corresponds to $wn \approx 670\,\mathrm{cm}^{-1}$. For the detection of vibrations with small wave numbers it is necessary that the phase step is placed close to the cut-off wavelength λ_{cut}. Even if this high frequency filtering is perfect, which can be assumed using a thick absorbing material as a stopper in the $4f$-line, the excitation light at lower frequencies that reaches the spectrometer quickly saturates the whole detector, because long integration times are needed to detect the small CARS signal. Therefore it is also indispensable to eliminate the laser wavelengths with low-pass or bandpass filters in the detection path (see Fig. 2.8). These filters have to be of very high quality, meaning they have to attenuate the signal in the non-passing spectral regions by at least six orders of magnitude and the cut has to be as sharp as possible to not affect the CARS signal as well.

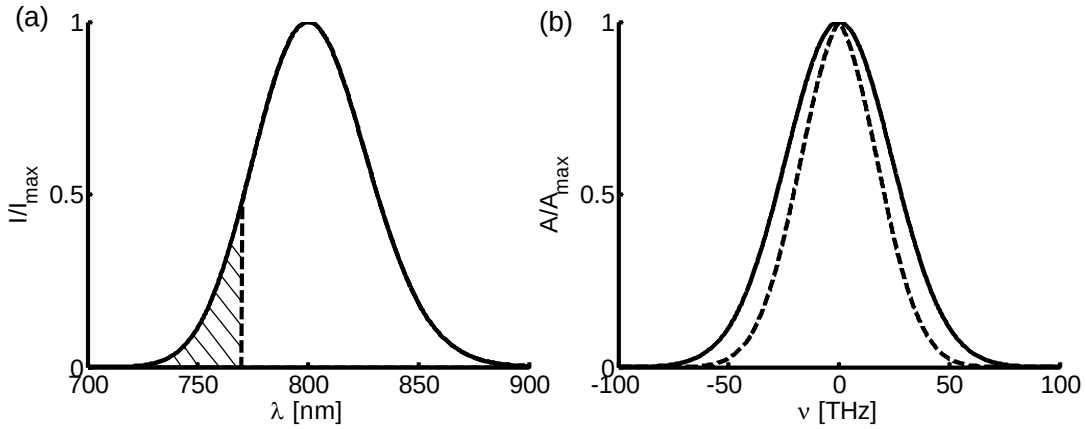

Figure 5.3: Driving polarization $A(\Omega)$ for single pulse CARS. (a) Excitation spectrum: Solid line: Gaussian spectrum; dashed line: high frequencies are chopped (hatched area) to separate the excitation from the emission. (b) $A(\Omega)$ for both cases presented in (a). The high pass filtering reduces the accessible wave numbers.

Thus one can summarize the necessary conditions for single pulse CARS measurements as follows: In a broadband laser pulse the high frequencies must be chopped. Close the this cutting wavelength, a phase step has to be shaped into the pulse (of course other shaping schemes involving amplitude or polarization can be employed as well, but still have to be applied in the same spectral region). Nevertheless the spectral energy within the phase jump region that acts as the probe field needs to be high to generate a sufficiently strong resonant signal. Consequently one has to find a compromise between on the one hand cutting only the very highest pulse frequencies (thus ensuring access to many vibrations but suffering from a low probe field), and on the other hand cutting a more considerable portion of the high-frequency pulse half limiting the maximally attainable vibrations (but probing them with a strong field). The ideal laser spectrum would therefore not be of a Gaussian shape but rather possesses a broad plateau with a steep descent at the high-frequency side. Furthermore low-pass filters need to be placed in the detection path that have a cut-off frequency only slightly below the laser cut-off to detect a maximum of the CARS spectrum while eliminating the excitation light. The spectral difference between both cut-offs determines the lowest accessible wave numbers. Fig. 5.4 illustrates these conditions. Finally, vibrations between $300\,\mathrm{cm}^{-1}$ and $900\,\mathrm{cm}^{-1}$ can be measured with our laser.

5.3 Measurement of basic resonance characteristics

Our experimental setup for single pulse CARS detection is shown in Fig. 5.5. As excitation high-pass we use black cardboard at the SLM exit. The phase distortions introduced by the objective are compensated by a pair of chirped mirrors (see section 2.7.1) and an

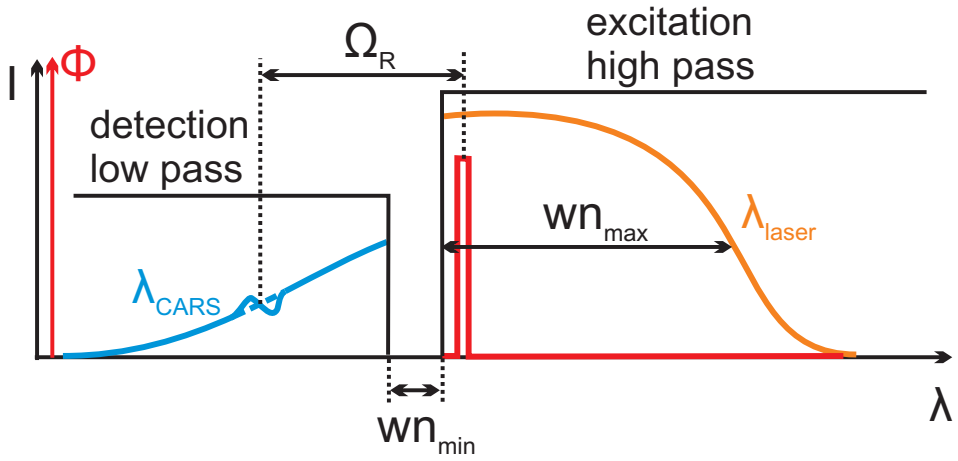

Figure 5.4: Accessible wave number range for single pulse CARS. wn_{max} is limited by the band width of the laser spectrum and wn_{min} depends on the difference between the cut-off wavelengths of the excitation high pass and the detection low pass. It is only achieved when the phase step is located in close spectral proximity to the excitation cut-off.

evolutionary strategy (see section 2.7.3) performed in the SLM in the $4f$-line (see section 2.3). As samples we use the isotropic solvents chloroform ($CHCl_3$) and Dimethyl sulfoxide (DMSO). In solutions the CARS signal is almost exclusively emitted in the forward direction due to phase matching conditions (see page 29). Therefore we use a pair of NA = 0.5 objectives (×20, Nikon, Tokyo, Japan and ×40, Zeiss, Oberkochen, Germany) to focus the incident beam on the sample and to optimally detect the forward generated signal. The relatively low NA is founded on several considerations. First, there are working distance constraints. Higher NA objectives around NA = 1.2 possess reduced working distances that impede to place a sample between two of them that are conjugated (which means that their foci coincide). Replacing only the excitation path objective with a high NA one would allow the positioning of the sample between both objectives and create higher field strengths in the reduced focal volume, but a considerable portion of the generated signal could not be collected because it is created over an angle range that surpasses the collection aperture. Furthermore as forward emitted CARS is phase matched (see section 1.3.2), a long generating length is beneficial for the total signal intensity. This is easily achieved by lower and medium NA objectives that focuss only weakly along the propagation direction while still possessing a quite good lateral focussing capability. On top of the sample another glass slide is placed to provide a planar surface and avoid a lens effect by the sample drop. The detection low pass consists of two FF01-775/SP-25 bandpass filters (Semrock, Rochester, NY) that cut wavelengths above 761 nm. Detection is performed by a spectrometer as detailed in section 2.5.2.

Figure 5.6 shows our excitation laser spectrum and the CARS spectra of $CHCl_3$ and DMSO for several phase step positions λ_{ph}. The laser cut-off is inserted at around 770 nm.

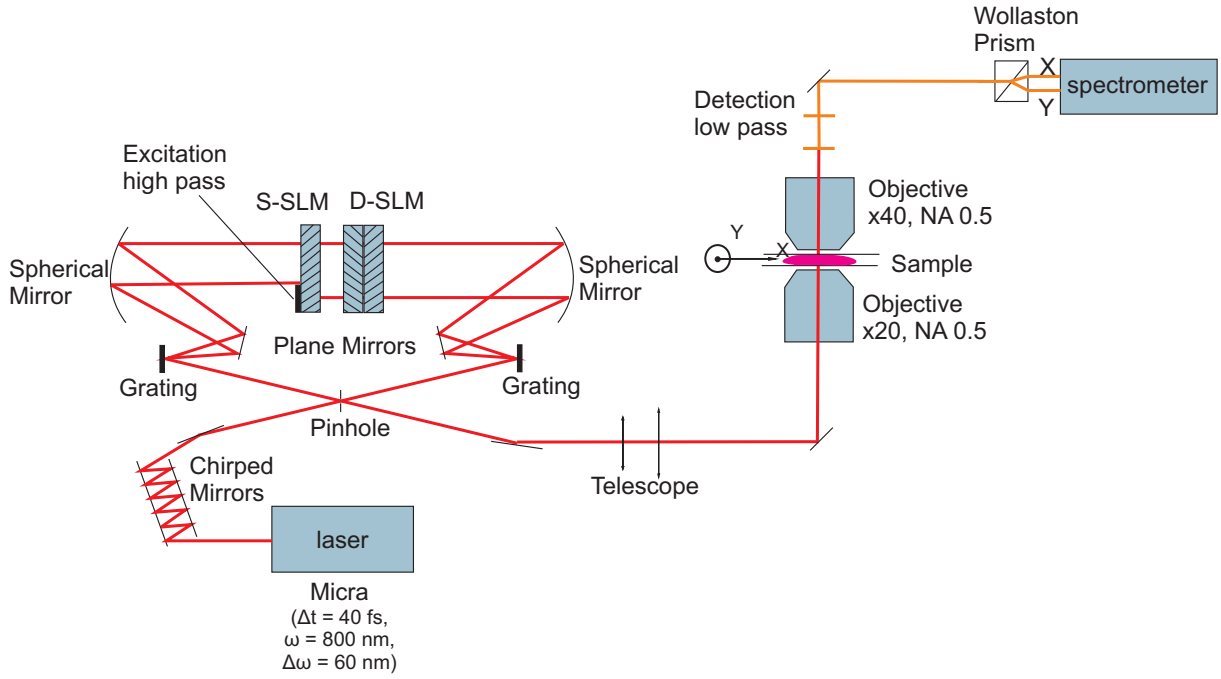

Figure 5.5: Setup for single pulse CARS. The excitation high pass is placed at the exit of the SLM, the detection low pass at the exit of the collecting objective. For details concerning the chirped mirrors, the pulse shaper and the spectrometer see sections 2.3 to 2.7.1.

Under these conditions the incident power amounts to 13 mW. The width of the π phase step is set to 1.5 nm. This choice is based on two considerations: First, for this width five SLM pixel contribute which assures that the π step is indeed reached. For smaller widths the finite SLM resolution would result in a less accurate phase shaping as the affected wavelengths would pass phase-shifted and non-phase-shifted pixels at the same due to the spatial resolution of about three pixels in the Fourier plane of the shaper (see section 2.5.1), leading to a less controlled phase jump. Second, the strongest heterodyne modification of the CARS spectrum is to be expected when the width of the phase jump region corresponds to the width of the resonance that is described by Γ in Eq. (5.2). 1.5 nm around $\lambda = 780$ nm roughly correspond to 25 cm^{-1}, which is in the same region as many resonances of organic solvents. In both cases depicted in Fig. 5.6c and 5.6d a resonance is clearly visible that shifts its position within the CARS spectrum when λ_{ph} changes. The resonances are indicated in the Raman spectra depicted in Fig. 5.6b. Because the resonant signal is much weaker than the non-resonant one, even the heterodyne term only appears as a small modification within the strong non-resonant background. Due to an imperfect alignment along both the excitation and the detection paths and the experimental noise always encountered, it is very difficult to identify a certain resonance within the single pulse CARS spectrum. Only a shift of λ_{ph} reveals its presence as the signal of a particular vibration shifts within the spectrum while other spectral features remain unchanged. Thus

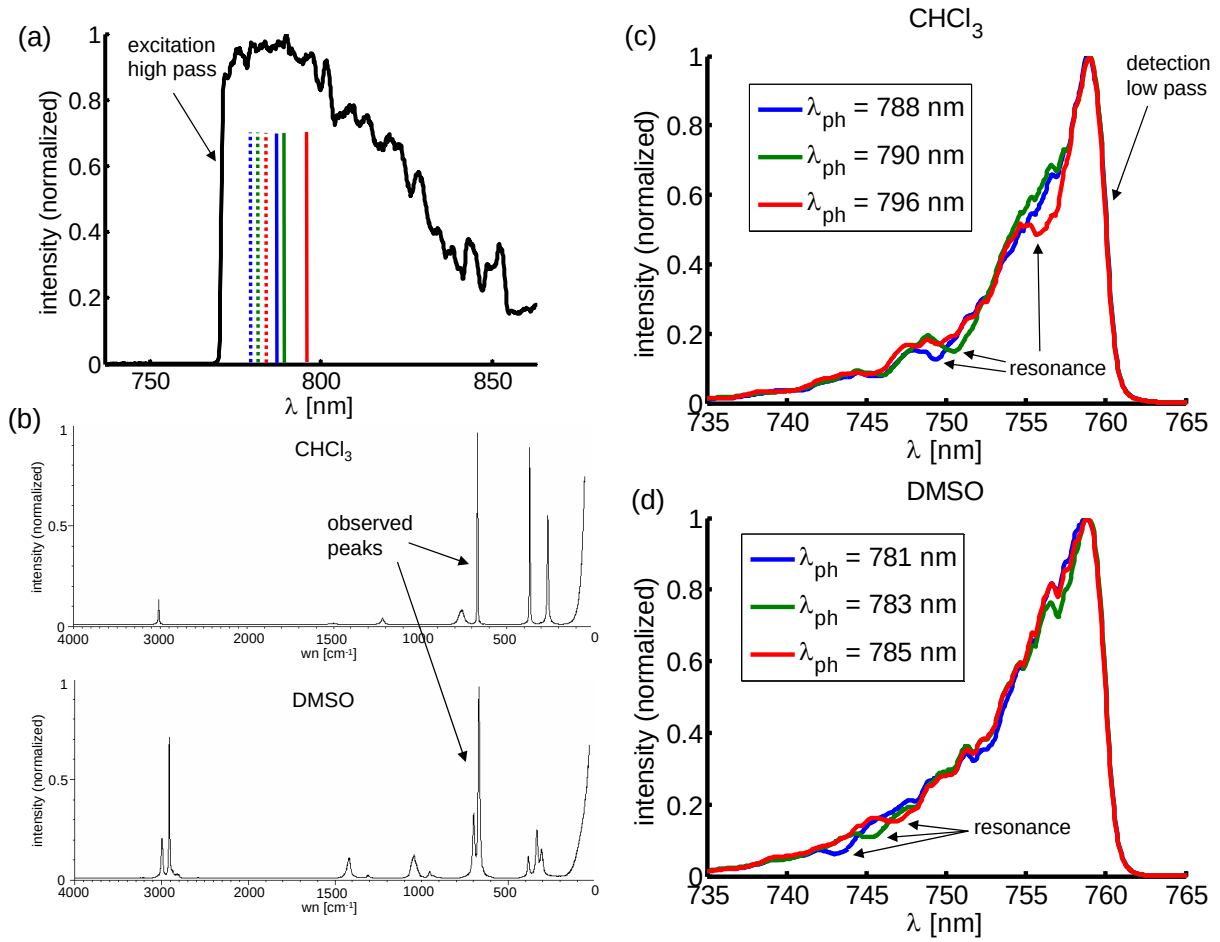

Figure 5.6: Single pulse CARS. (a) Laser spectrum after the application of the excitation high pass; (b) Raman spectra for $CHCl_3$ (top) and DMSO (bottom) [215]; (c) single pulse CARS spectrum of $CHCl_3$, the resonance at $669\,\mathrm{cm}^{-1}$ can be seen at different positions within the CARS spectrum depending on the position of the phase step λ_{ph} as indicated in (a) by solid vertical lines; the cut-off at high wavelengths is due to the detection low pass; (d) single pulse CARS spectrum of DMSO, the resonance at $670\,\mathrm{cm}^{-1}$ is seen, but less pronounced than the one of $CHCl_3$. The corresponding λ_{ph} are shown in (a) by dotted vertical lines.

it is for example possible to differentiate the resonance at $670\,\mathrm{cm}^{-1}$ in the DMSO single pulse CARS spectrum (Fig. 5.6) from the non-resonance dips at 752 nm and 757 nm. These latter are static and do not move when the phase step position is changed. They probably arise from interferences of multiple reflections within the detection path.

Now that individual vibrations can be seen in the single pulse CARS spectra, the question arises whether they can be quantified as well. A resonance is described according to Eq. (5.2) by its resonance frequency Ω_R, its spectral width Γ and its strength a. Ω_R can be approximately determined from the spectra in Fig. 5.6 by Eq. (5.8), but its width and its strength are less easily seen, especially because the strength of the modulation in the CARS background depends on the strength of the non-resonant field as the local oscillator at this spectral position that is not constant with respect to λ. To better visualize the resonance we divide the derivative of the spectrum with respect to λ by the spectrum itself (in accordance with the work at the Weizmann Institute of Science, Rehovot, Israel):

$$\frac{\mathrm{d}I(\lambda)/\mathrm{d}\lambda}{I(\lambda)} \tag{5.9}$$

The division eliminates the scaling dependence on the non-resonant field in the heterodyne term $2|P_{NR}|\mathfrak{Re}\{P_R\}$ in the CARS intensity in Eq. (5.7), and the derivative enhances the modification of I_{CARS} by this heterodyne term. Figure 5.7a shows the results of this treatment for a large number of DMSO CARS spectra with varying phase step positions obtained under the same conditions as in Fig. 5.6d. The resonance is characterized by a dip in the spectrum that moves to higher wavelengths as λ_{ph} gets shifted in the same way. We fitted these results by simulated CARS spectra obtained from Eqs. (5.2) to (5.7) on which the same treatment as in expression (5.9) was performed, with Ω_R, Γ and the ratio between the resonant and non-resonant contribution $\frac{\chi_R^{(3)}}{\chi_{NR}^{(3)}} = \frac{a}{\chi_{NR}^{(3)}\Gamma}$ as fit parameters. Fig. 5.7b and 5.7c depict two fit examples out of all the spectra in Fig. 5.7a. The fit is performed by minimizing the mean square difference χ^2 between the simulated curve $f(\lambda)$ for the triple $\left(\Omega_R, \Gamma, \frac{a}{\chi_{NR}^{(3)}\Gamma}\right)$ and the measured data $g(\lambda)$:

$$\chi^2 = \int \left(g(\lambda) - f\left(\lambda, \Omega_R, \Gamma, \frac{a}{\chi_{NR}^{(3)}\Gamma}\right)\right)^2 \mathrm{d}\lambda \tag{5.10}$$

For this, first the resonance position is varied while the other two parameters are kept constant. Then the same procedure is performed for Γ and $\frac{a}{\chi_{NR}^{(3)}\Gamma}$. The whole cycle is repeated until no further decrease in χ^2 is achieved. From Fig. 5.7b and 5.7c it can be seen that Ω_R gets fitted very nicely, while the other two parameters are expected to show much larger error margins due to the considerable noise in the experimental data.

This fit procedure was applied to all DMSO curves presented in Fig. 5.7a as well as to a similar number of them for a chloroform sample. Table 5.1 summarizes the results. Additionally the values for Ω_R and Γ obtained by Raman spectroscopy are given in paren-

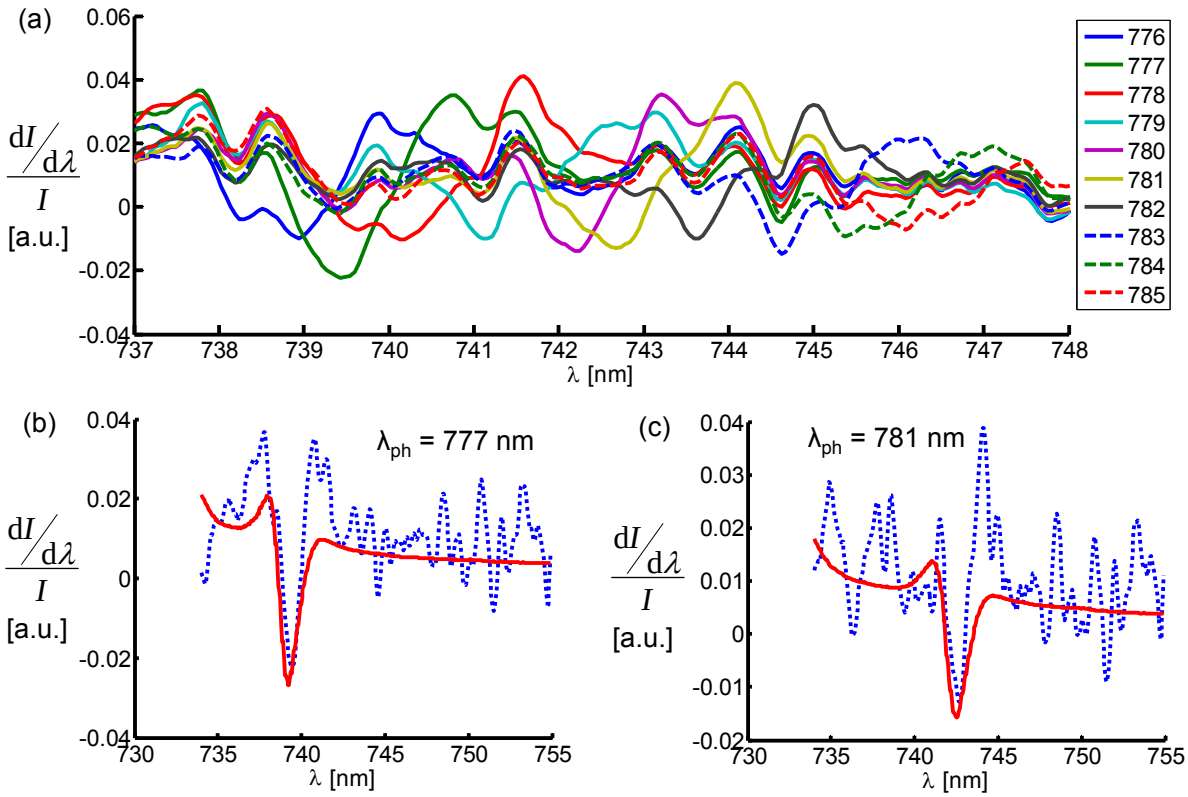

Figure 5.7: Qualitative analysis of single pulse CARS spectra. (a) Treated CARS spectra $\left(\frac{\mathrm{d}I(\lambda)/\mathrm{d}\lambda}{I(\lambda)}\right)$ of DMSO for various phase step positions (see legend, values in nm) of DMSO under the same experimental conditions as in Fig. 5.6d; (b,c) examples of the fit as detailed in the text for two of these curves with λ_{ph} at 777 nm and 781 nm.

theses. As there is no non-resonant background in Raman scattering, this method cannot provide an independent estimation of $\frac{a}{\chi^{(3)}_{NR}\Gamma}$. It can be seen that the chloroform resonance position is retrieved very accurately by our fit. In the case of DMSO there is a slight offset that is probably due to a second resonance at 700 cm^{-1} (see Fig. 5.6b). Both resonances are too close to be resolved by our method considering that our probe field has a width of about 25 cm^{-1}, which limits our spectral resolution to this value. As a consequence our fitted resonance lies somewhere in the middle between both DMSO resonances, but still closer to the one at 670 cm^{-1} as it is the stronger one of the two. Concerning the resonance width we systematically overestimate Γ by a factor of about 2.5. For DMSO this might as well be an effect of the neighboring second resonance, however for chloroform an influence of the closest other resonance at around 760 cm^{-1} seems unlikely as this resonance is relatively far away and not very strong. The Γ-overestimation most likely arises from several causes: the high noise level as evidenced in Fig. 5.7b and 5.7c hinders an accurate fitting and the spectrally large probe field of 25 cm^{-1} probably smears the effect of the heterodyne term in the CARS spectrum leading to a less pronounced modification that is

Sample	Ω_R [cm^{-1}]	Γ [cm^{-1}]	$\frac{a}{\chi^{(3)}_{NR}\Gamma}$
$CHCl_3$	667.5 ± 3.6 (669)	10.5 ± 1.6 (4.3)	3.9 ± 0.6
DMSO	679.1 ± 3.0 (670)	17.6 ± 5.5 (7.3)	4.6 ± 0.86

Table 5.1: Fit values of the resonances for $CHCl_3$ and DMSO. The error margins correspond to the standard deviation of the values obtained for all different phase step positions λ_{ph}. Numbers in parentheses correspond to the values obtained by Raman spectroscopy.

more difficult to fit.

5.4 Determination of the Raman depolarization ratio ρ_R

So far we did not take the tensorial nature of the third-order nonlinear susceptibility $\chi^{(3)}$ into account. This is, however, an additional information that provides interesting ways to quantify - in isotropic media - the depolarization nature of a vibrational band (in other words, its capacity to respond in a more or less directional way to an excitation) [216, 217]. As soon as different polarizations are present in the exciting field or a polarized detection is performed, the different components of the 81-element tensor $\chi^{(3)}$ come into play. In an isotropic solution it possesses only two independent components [218]:

$$\chi^{(3)}_{IJKL} = \chi^{(3)}_{XXYY}\left(\delta_{IJ}\delta_{KL} + \delta_{IK}\delta_{JL}\right) + \chi^{(3)}_{XYYX}\delta_{IL}\delta_{JK} \tag{5.11}$$

Here, δ is the Kronecker delta function and $I, ..., K$ stand for the cartesian coordinates X, Y and Z. Both $\chi^{(3)}_{XXYY}$ and $\chi^{(3)}_{XYYX}$ define the CARS depolarization ratio ρ_{CARS} via [216]:

$$\rho_{CARS} = \frac{\chi^{(3)}_{XYYX}}{\chi^{(3)}_{XXXX}} = \frac{\chi^{(3)}_{XYYX}}{2\chi^{(3)}_{XXYY} + \chi^{(3)}_{XYYX}} \tag{5.12}$$

In analogy to Raman scattering ρ_{CARS} quantifies to which extent linear polarizations in one direction lead to a signal polarized in the orthogonal direction. Decomposition into the resonant and non-resonant susceptibilities $\left(\chi^{(3)} = \chi^{(3)}_R + \chi^{(3)}_{NR}\right)$ results in [217]:

$$\chi^{(3)}_{IJKL} = \chi^{(3)}_{NR}\left(\delta_{IJ}\delta_{KL} + \delta_{IK}\delta_{JL} + \delta_{IL}\delta_{JK}\right) + \chi^{(3)}_R\left(\delta_{IJ}\delta_{KL} + \delta_{IK}\delta_{JL} + \frac{2\rho_R}{1-\rho_R}\delta_{IL}\delta_{JK}\right) \tag{5.13}$$

$\chi^{(3)}_{NR}$ and $\chi^{(3)}_R$ stand for $\chi^{(3)NR}_{XXYY}$ and $\chi^{(3)R}_{XXYY}$ respectively. In the non-resonant pathways no real vibrational levels are involved and thus Kleinman conditions (see page 113) apply and $\chi^{(3)NR}_{XXYY} = \chi^{(3)NR}_{XYYX}$, so there remains only one independent non-resonant component. Once the non-resonant contribution is removed from the CARS depolarization ratio, ρ_{CARS} transforms into the Raman depolarization ratio ρ_R. It assumes values between 0 for a perfectly polarized vibration and $\frac{3}{4}$ for a completely depolarized one [216]. ρ_R can be

obtained from a polarimetric study of the CARS spectrum [217]. Here we attempt to retrieve it with the help of polarization and phase pulse shaping of broadband pulses.

The excitation profile used so far with a high-frequency cut-off and a phase step at a spectral position close to the cut-off is not sufficient to determine ρ_R. As the whole pulse is polarized in the same direction - for sake of simplicity X - the only tensorial components $\chi^{(3)}_{IJKL}$ that can be accessed in a polarized detection are $\chi^{(3)}_{XXXX}$ and $\chi^{(3)}_{YXXX}$. (In $\chi^{(3)}_{IJKL}$, I refers to the polarization direction of the signal, J to the one of the pump field, K to the probe field and L to the Stokes field.) According to Eq. (5.13) these components are:

$$\begin{aligned} \chi^{(3)}_{XXXX} &= 3\chi^{(3)}_{NR} + \left(2 + \frac{2\rho_R}{1-\rho_R}\right)\chi^{(3)}_R \propto 3 + \left(2 + \frac{2\rho_R}{1-\rho_R}\right)\frac{\chi^{(3)}_R}{\chi^{(3)}_{NR}} \\ \chi^{(3)}_{YXXX} &= 0 \end{aligned} \tag{5.14}$$

Thus ρ_R acts as an amplitude factor of the resonant part just in the same way as $\frac{\chi^{(3)}_R}{\chi^{(3)}_{NR}}$. Consequently, as only one tensorial component leads to a signal, ρ_R cannot be determined because an infinite number of $\left(\rho_R, \frac{\chi^{(3)}_R}{\chi^{(3)}_{NR}}\right)$-pairs leads to the same spectral result.

Let us now extend the previous excitation profile by polarizing the high-frequency side of the spectrum along one direction - for example X - and the low-frequency side perpendicular to it (Y) (Fig. 5.8a). In this case the probe field (at the phase step position) is polarized along X, while pump and Stokes fields are formed by the spectrum as a whole. Out of the four fundamental couplings $\chi^{(3)}_{IXXX}$, $\chi^{(3)}_{IXXY}$, $\chi^{(3)}_{IYXX}$, $\chi^{(3)}_{IYXY}$ (with $I = (X, Y)$) only $\chi^{(3)}_{IYXX}$ cannot lead to a CARS signal as in this case the Stokes field has a higher frequency than the pump field and the corresponding signal would not appear in the CARS range but rather at wavelengths above the phase step position λ_{ph}. The resonant contributions to the signal of all remaining components are again determined by Eq. (5.13):

$$\chi^{(3)R}_{XXXX} = \left(2 + \frac{2\rho_R}{1-\rho_R}\right)\chi^{(3)}_R \tag{5.15}$$

$$\begin{aligned} \chi^{(3)R}_{YXXX} &= 0 \\ \chi^{(3)R}_{XXXY} &= 0 \\ \chi^{(3)R}_{YXXY} &= \frac{2\rho_R}{1-\rho_R}\chi^{(3)}_R \\ \chi^{(3)R}_{XYXY} &= \chi^{(3)}_R \\ \chi^{(3)R}_{YYXY} &= 0 \end{aligned} \tag{5.16}$$

In a polarized detection the resonant fields in the X- and Y-channels are therefore:

$$\begin{aligned} P_X = \; & c_{XX}\chi^{(3)R}_{XXXX} + c_{YY}\chi^{(3)R}_{XYXY} \propto c_{XX}\left(2 + \frac{2\rho_R}{1-\rho_R}\right) + c_{YY} \\ P_Y = \; & c_{XY}\chi^{(3)R}_{YXXY} \propto c_{XY}\frac{2\rho_R}{1-\rho_R} \end{aligned} \tag{5.17}$$

The proportionality constants c_{XX}, c_{YY} and c_{XY} reflect the fact that each pump-Stokes polarization coupling results in a different driving polarization $A(\Omega)$ (Fig. 5.8c). Thus by measuring the CARS intensities $I_X = |P_X|^2$ and $I_Y = |P_Y|^2$ it should be possible to retrieve the Raman depolarization ratio ρ_R.

We assess the potential of the method by calculating a single pulse CARS signal based on the excitation profile detailed above as depicted in Fig. 5.8b. This is the actual profile of our laser. We assume a resonance with the parameters specified in Table 5.2. Experimental conditions are simulated by the addition of a normally distributed noise. Afterwards a fitting as described above is performed for the ensemble of all four parameters. Table 5.2 shows the results and Fig. 5.8d the corresponding curve. It can be seen that it is possible to correctly retrieve the CARS depolarization ratio.

resonance parameters	original values	retrieved values
$\Omega_R\,[\mathrm{cm}^{-1}]$	670	670
$\Gamma\,[\mathrm{cm}^{-1}]$	15	15.5
$\frac{\chi_R^{(3)}}{\chi_{NR}^{(3)}}$	4	3.8
ρ_R	0.5	0.5

Table 5.2: Retrieval of resonance parameters Ω_R, Γ, $\frac{\chi_R^{(3)}}{\chi_{NR}^{(3)}}$ and ρ_R by a fit of the CARS intensities I_X and I_Y. Middle column: starting values used in the simulation of a single pulse CARS response (chosen to give a visible band within the CARS spectrum); right column: values retrieved from the fit of said response (see Fig. 5.8d).

Even without a simultaneous fit of all four parameters it is possible to estimate ρ_R. If the resonance position and width are already known - which is the case for many solvents as Raman spectra are readily available [215] - ρ_R can be accessed without having to pass by a simulation of the whole single pulse CARS spectrum. As already stated in Eq. (5.17) the resonance strength R of the CARS signal is expressed by:

$$\begin{aligned} R_X &\propto c_{XX}\chi^{(3)R}_{XXXX} + c_{YY}\chi^{(3)R}_{XYXY} \\ R_Y &\propto c_{XY}\chi^{(3)R}_{YXXY} \end{aligned} \tag{5.18}$$

The factors c_{XX}, c_{YY} and c_{XY} correspond to the strength of the driving polarization $A(\Omega)$ at the resonance position Ω_R. Therefore $c_{JL} = A_{JL}(\Omega = \Omega_R)$ with $A_{JL}(\Omega) \propto \int_0^\infty \mathrm{d}\omega E_L^*(\omega - \Omega)E_J(\omega)$ (see Eq. 5.3). These values are easily obtained once the exciting laser spectrum is known. There remains the question how the resonance strengths R_X and R_Y can be determined from a single pulse CARS spectrum. According to Eq. (5.7) the real part of the resonant CARS signal is expressed as:

$$\mathfrak{Re}\{P_R\} = \frac{I_{CARS} - |P_{NR}|^2}{2\sqrt{|P_{NR}|^2}} \tag{5.19}$$

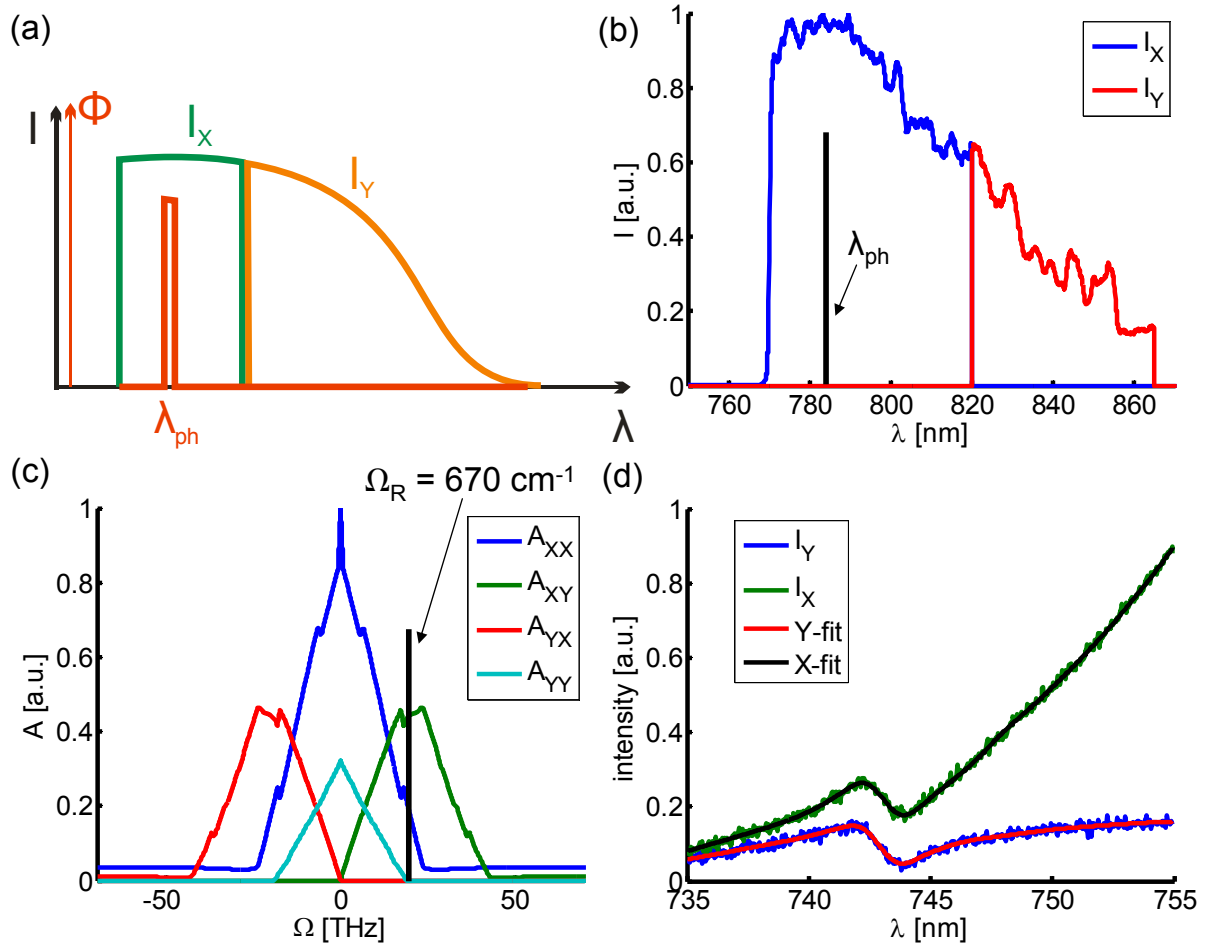

Figure 5.8: Polarized single pulse CARS for the determination of ρ_R. (a) Sketch of the excitation scheme; (b) experimental realization with indication of the phase step position λ_{ph}; (c) driving polarization $A(\Omega)$ for all polarization coupling possibilities for the laser spectrum of (b), with indication of the position of a resonance with $\Omega_R = 670\,\mathrm{cm}^{-1}$. Note that $A_{YX}(\Omega)$ does not lead to a resonant CARS signal because $\lambda_{Stokes} < \lambda_{pump}$. (d) Calculated single pulse CARS spectrum plus added Gaussian noise for the excitation with the spectrum in (b) and the best fit of these curves that led to the resonance parameters in Table 5.2 (right column).

The non-resonant contribution $|P_{NR}|^2$ is estimated by a monotonous fit (e.g. an exponential function) of the ascending portion of the CARS spectrum. $\mathfrak{Re}\{P_R\}$ is maximal around the position where the resonance appears in the spectrum and therefore its maximal value is a measure for the resonance strength R. By forming the quotient:

$$\frac{R_X}{R_Y} = \frac{c_{XX}\chi^{(3)R}_{XXXX} + c_{YY}\chi^{(3)R}_{XYXY}}{c_{XY}\chi^{(3)R}_{YXXY}} = \frac{c_{XX}\left(2 + \frac{2\rho_R}{1-\rho_R}\right) + c_{YY}}{c_{XY}\frac{2\rho_R}{1-\rho_R}} \tag{5.20}$$

ρ_R is retrieved via:

$$\rho_R = \frac{R_Y\left(c_{YY} + 2c_{XX}\right)}{2R_X c_{XY} + R_Y c_{YY}} \tag{5.21}$$

For the same set of starting parameters as in Table 5.2 this rather crude calculation leads to $\rho_R = 0.51$, in very good agreement with the original value of 0.5.

In a next step we tested our method experimentally. The splitting wavelength that separates the X-polarized region from the Y-polarized one was set at 800 nm with a width of 1.5 nm. We targeted again the 670 cm^{-1} vibration of chloroform and the DMSO vibration at 669 cm^{-1}. Each spectrum was obtained over a signal integration time of 5 s. In both cases the modulation of the single-pulse CARS signal by the resonant contribution was only seen in the X-polarized signal but not in the Y-polarized one. This result might be explained by $\rho_R = 0$ for both vibrations. The only tensorial component contributing to the resonant Y-signal ($\chi^{(3)R}_{YXXY}$) is proportional to $\frac{2\rho_R}{1-\rho_R}$ (see Eq. (5.17)) and does not contain any non-ρ_R-dependent terms.

To obtain an independent determination of ρ_R we performed polarized Raman spectroscopy measurements [219] on both samples. For these the sample is excited with a continuous wave laser at $\lambda = 633$ nm with a linear polarization. The generated Raman scattering signal is analyzed along the polarization direction of the incident beam ($I_\parallel$) and perpendicular to it ($I_\perp$). The ratio:

$$\rho_R = \frac{I_\perp}{I_\parallel} \tag{5.22}$$

then gives the Raman depolarization ratio. We obtained the values:

$$\begin{aligned} \rho_{R,\mathrm{CHCl_3}} &= 0.20 \\ \rho_{R,\mathrm{DMSO}} &= 0.21 \end{aligned} \tag{5.23}$$

$\rho_R = 0$ refers to a completely polarized vibration while a completely depolarized one is described by $\rho_R = 0.75$. This means that both vibrations that we observe are strongly polarized and the resonant signal is mainly expected to be in the detection channel that corresponds to the polarization of the phase step region (X in our case). Though there should be a small resonant contribution in the other detection channel as well, it might easily be covered by noise as the overall signal intensity is small due to the polarization splitting.

To avoid this problem of small resonant contributions that might be overlaid by noise we propose a slightly different excitation scheme: Now we also polarize the probe field (the spectral region of the phase jump) in the same direction as the second part of the spectrum - Y in our case - while the first part remains polarized along X as shown in Fig. 5.9a. As above the pump and Stokes fields are formed by the whole of the pulse. Again only three out of the four pump-Stokes polarization couplings can lead to a CARS signal for a vibration around $670\,\mathrm{cm}^{-1}$, namely $A_{XX}(\Omega)$, $A_{YY}(\Omega)$ and $A_{XY}(\Omega)$. Even though with this excitation profile there are certain couplings where the Y-polarized field in the phase jump region has a higher frequency than a portion of the X-polarized one, this frequency difference is too small to excite our vibrations in chloroform and DMSO and consequently the driving polarization $A_{YX}(\Omega)$ can be neglected (Fig. 5.9c). Thus remain the following resonant contributions, evaluated with Eq. (5.13):

$$\begin{aligned}
\chi^{(3)R}_{XXYX} &= 0 \\
\chi^{(3)R}_{YXYX} &= \chi^{(3)}_R \\
\chi^{(3)R}_{XXYY} &= \chi^{(3)}_R \\
\chi^{(3)R}_{YXYY} &= 0 \\
\chi^{(3)R}_{XYYY} &= 0 \\
\chi^{(3)R}_{YYYY} &= \left(2 + \frac{2\rho_R}{1-\rho_R}\right)\chi^{(3)}_R
\end{aligned} \tag{5.24}$$

The corresponding fields in a polarized detection setup are:

$$\begin{aligned}
P_X = &\quad c_{XY}\chi^{(3)R}_{XXYY} &&\propto c_{XY} \\
P_Y = &\quad c_{XX}\chi^{(3)R}_{YXYX} + c_{YY}\chi^{(3)R}_{YYYY} &&\propto c_{XX} + c_{YY}\left(2 + \frac{2\rho_R}{1-\rho_R}\right)
\end{aligned} \tag{5.25}$$

The proportionality constants c_{XX}, c_{YY} and c_{XY} again reflect the different strengths of the corresponding driving polarizations $A(\Omega)$ (Fig. 5.9c). With this excitation scheme only the detection channel for the polarization of the phase step region measures a ρ_R-dependent signal, but both channels also have a contribution that is independent of the depolarization ratio. Thus the resonance should be seen in both channels no matter which value ρ_R assumes.

As for the previous excitation profile we first test its performance numerically based on the measured laser profile (Fig. 5.9b). The same resonance is tested: $\Omega_R = 670\,\mathrm{cm}^{-1}$, $\Gamma = 15\,\mathrm{cm}^{-1}$. We calculate the single pulse CARS spectrum, add a normally distributed noise to mirror experimental conditions and attempt to retrieve the Raman depolarization ratio and the ratio between the resonant and non-resonant contributions $\frac{\chi^{(3)}_R}{\chi^{(3)}_{NR}}$ by fitting these two parameters. The results of this procedure are presented in Table 5.3 and Fig. 5.9d. Both parameters are determined correctly. Ω_R and Γ are considered to be known.

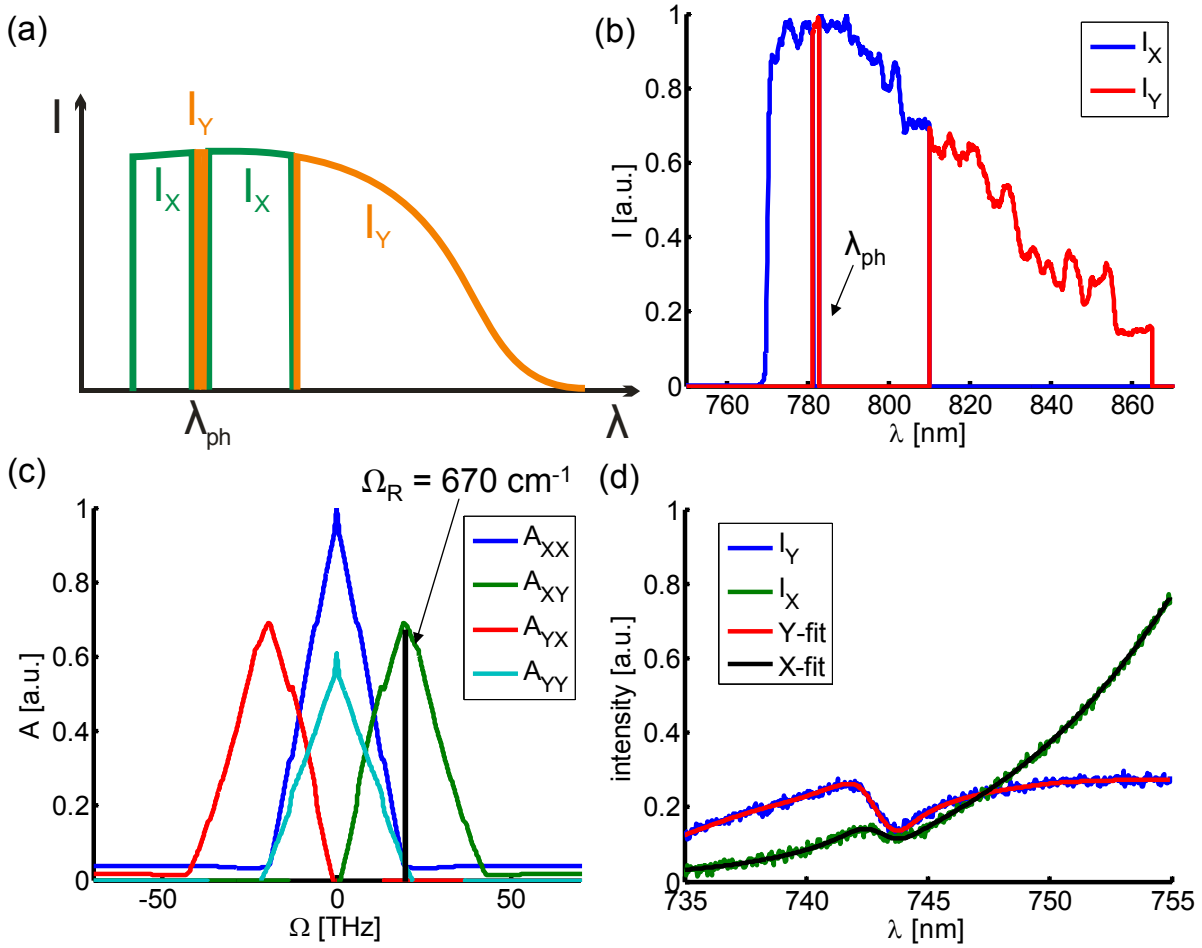

Figure 5.9: Polarized single pulse CARS for the determination of ρ_R. (a) sketch of the modified excitation scheme; (b) experimental realization with indication of the phase step position λ_{ph}; (c) driving polarization $A(\Omega)$ for all polarization coupling possibilities within the laser spectrum of (b), with indication of the position of a resonance with $\Omega_R = 670\,\mathrm{cm}^{-1}$. Note that $A_{YX}(\Omega)$ does not lead to a resonant CARS signal because the necessary frequency differences are not available. (d) Calculated single pulse CARS spectrum plus added Gaussian noise for the excitation with the spectrum in (b) and the best fit of these curves that led to the resonance parameters in Table 5.3 (right column).

resonance parameters	original values	retrieved values
$\frac{\chi_R^{(3)}}{\chi_{NR}^{(3)}}$	4	3.86
ρ_R	0.5	0.51

Table 5.3: Retrieval of resonance parameters $\frac{\chi_R^{(3)}}{\chi_{NR}^{(3)}}$ and ρ_R by a fit of the CARS intensities I_X and I_Y. Middle column: starting values used in the simulation of a single pulse CARS response; right column: values retrieved from the fit of said response (see Fig. 5.9d).

In a second step we attempt to obtain ρ_R by a direct calculation based on the single pulse CARS spectrum without the need for a multidimensional fit.

The resonance strength R is expressed in analogy to Eqs. (5.18) and (5.25) as:

$$\begin{aligned} R_X &\propto c_{XY} \\ R_Y &\propto c_{XX} + c_{YY}\left(2 + \frac{2\rho_R}{1-\rho_R}\right) \end{aligned} \tag{5.26}$$

from which ρ_R is obtained by:

$$\rho_R = 1 - \frac{2c_{YY}}{\frac{R_Y}{R_X}c_{XY} - c_{XX}} \tag{5.27}$$

The factors c_{JL} are again calculated by $c_{JL} = A_{JL}(\Omega = \Omega_R)$ with $A_{JL}(\Omega) \propto \int_0^\infty \mathrm{d}\omega E_L^*(\omega - \Omega)E_J(\omega)$ (see Eq. 5.3), and the resonance strength R is estimated according to the procedure detailed on page 154. This leads us to a value of $\rho_R = 0.93$ for the starting parameters of Table 5.3. This is not only far away from the original value of 0.5, but even outside the interval for possible Raman depolarization ratios $\left(\rho_R \,\epsilon\, \left[0\ \frac{3}{4}\right]\right)$. The reason lies most likely in an insufficient determination of the resonance strength R which we only crudely extracted from the amplitude of the resonant feature within the single pulse CARS spectrum. Thus the complete two-dimensional fit over $\frac{\chi_R^{(3)}}{\chi_{NR}^{(3)}}$ and ρ_R has to be performed to reliably extract the Raman depolarization ratio in this case.

We tested this excitation profile experimentally for both chloroform and DMSO to detect the two resonances mentioned above. The excitation high pass was placed at 770 nm and the splitting wavelength separating the X- and Y-polarized parts was fixed at 800 nm. To see the resonance feature within the CARS spectrum we varied the phase step position λ_{ph} from 771 nm to 791 nm, the step region always having a width of 1.5 nm. All CARS spectra were integrated over a time of 5 s. However, the resonance could not be identified neither in the resulting raw spectra (Fig. 5.10a), nor in the ones treated according to the procedure $\left(\frac{\mathrm{d}I/\mathrm{d}\lambda}{I}\right)$ explained on page 150. A more refined treatment is necessary to visualize a shifting feature within the spectra when λ_{ph} changes. To separate this very weak resonant feature from other constant spectral fluctuations a singular value decomposition

(SVD) is useful. For this the spectra for all λ_{ph} are joined in one matrix (T) of dimension (n_{ph}, n_λ) where n_{ph} denotes the number of phase step positions and n_λ the size of one spectrum. The SVD then computes $T = USV$, where U and V are unitary matrices of dimension (n_{ph}, n_{ph}) and (n_λ, n_λ) respectively, and S a matrix of singular values. While $S(1,1)$ contains the information that is shared by all spectra contained in T the other singular values $S(2,2), S(3,3), ...$ describe the differences between them. Therefore $T_{ref} = US_0V$ - with S_0 as a matrix of the size of S but only containing the first singular value $S(1,1)$ - is a matrix of reference spectra $I_{ref}(\lambda)$ that ideally contains all spectral features independent of the resonance. $I(\lambda) - I_{ref}(\lambda)$ thus enhances the resonant feature compared to all other ones. A division by the non-resonant part has still to be performed to eliminate this contribution from the heterodyne term. The non-resonant signal is approximated by a fit (I_{fit}) of the CARS spectrum with a monotonous curve like an exponential function. The modified signal $M(\lambda)$ thus calculates as:

$$M(\lambda) = \frac{I(\lambda) - I_{ref}(\lambda)}{I_{fit}(\lambda)} \tag{5.28}$$

Fig. 5.10b and Fig. 5.10c show $M(\lambda)$ of DMSO for a number of phase step positions λ_{ph}. Though they are still very noisy, there clearly is one feature that shifts when λ_{ph} changes. The resonance can thus be recovered. However, due to the manifold oscillations within $M(\lambda)$ it is not possible to retrieve the resonance's parameters, in particular ρ_R, by a fitting procedure similar to the one explained above.

5.5 Conclusion

Single pulse CARS allows the measurement of CARS spectra with a much simpler setup than in standard CARS with two narrow-band lasers. But this advantage is accompanied by problems in the spectral resolution of the signal. It can however be reestablished to a certain degree by the insertion of spectral features into the excitation beam. A narrow phase step that acts as a probe field is such a means. The range of wave numbers that can be explored by single pulse CARS are limited on the upper side by the spectral width of the pulse and on the lower one by the difference of the cut-off wavelengths between the excitation high pass and the detection low pass that are essential to separate the CARS signal from the incident light. An analysis of the CARS spectra allows determining the spectral position of a resonance, its width and the ratio between the resonant and non-resonant CARS contributions. We have implemented such a technique and showed some of its limitations. The next step of our study was to extend this "simple pulse" information readout to polarization-resolved excitation and detection, since the depolarization ratio is an important structural parameter in CARS imaging [216, 217]. To measure the Raman depolarization ratio of the resonance, polarization shaping of the incident beam has to be performed and a polarized readout is necessary. Several excitation profiles are proposed for this purpose of which numerical calculations demonstrate the potential. However, there are problems encountered in the experimental realization that for the moment do not permit

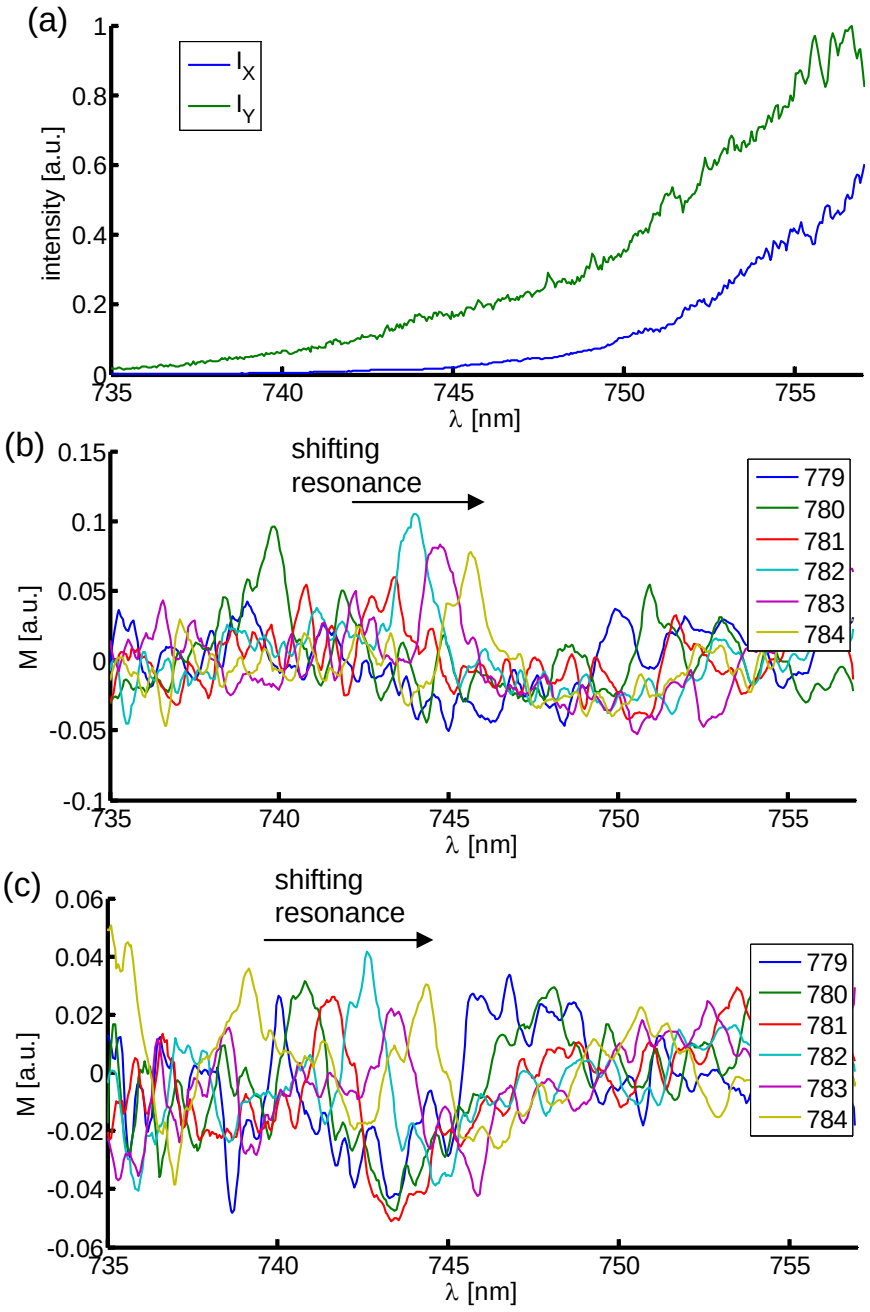

Figure 5.10: Experimental realization of the excitation scheme of Fig. 5.9. (a) single pulse CARS spectra of DMSO for $\lambda_{ph} = 782\,\text{nm}$ and a polarization splitting wavelength of 800 nm (X- and Y-polarized light). It is not possible to identify the resonant feature within the spectrum. (b) Modified signal $M(\lambda)$ (see text for details) of the X-polarized spectrum in (a) and several others with different λ_{ph} (see legend, values in nanometer). A shifting resonant feature is clearly visible. (c) $M(\lambda)$ as in (b), but for the Y-polarized signal. Again the resonance can be seen.

a measurement of the Raman depolarization ratio. In particular, polarization shaped excitation fields couple with all the components of the third-order nonlinear susceptibility of the sample. As a consequence the generated resonant signal of a single component is much smaller than in the case of only one exciting polarization. This problem should however be easy to overcome by the use of lasers with greater bandwidth and power as much more resonant pathways become available and the different resonant couplings as indicated in Fig. 5.9 are more efficiently excited.

Chapter 6

Enhancement of nonlinear signals by photonic structures

6.1 Introduction

All effects described so far were based on the interaction of a focussed laser beam with a sample. But the focussing itself was considered to be independent of the investigated sample, which were of dielectric nature and quite homogeneous within the focal volume. We assumed indeed a fixed electric field distribution within the focal volume that is only determined by the objective, as well as a collection and detection process of the nonlinear optical signal, not any longer influenced by the medium itself. The only exception to this rule considered so far are phase matching constraints which require that CARS signals are detected in the forward direction, and that backward emitted SHG can only be used in the investigation of interfaces and thin objects (see chapter 1). This is a valid description when extended samples like fluorescent solutions, macroscopic crystals or biological fibers are observed. But as soon as objects with sizes from the nanometric up to the low micrometric range are concerned, additional effects arise. In particular the distribution of the incident field depends on the object itself. This capability to influence the state of the electric field in their vicinity has led to the name of photonic structures for these objects. Here, we investigate two different classes of them: metallic nanostructures and dielectric microspheres. This chapter is a description of attempts to investigate photonic structures for future applications including phase, amplitude and polarization pulse shaping.

Metallic nanostructures encounter an increasing interest in the research community. Since metallic structures reduced to nanometric sizes are known to considerably confine electromagnetic fields, significant enhancements in the linear regime are expected, which can be even stronger in the nonlinear regime due to their higher-power dependence. The understanding and optimization of their nonlinear optical properties is a major issue for future applications in nanophotonics. Quadratic nonlinear effects arising from interfaces between a metal and the outer medium have already been described by Guyot-Sionnest *et al.* in 1986 [220], and were later on experimentally quantified [221]. This led to a wide range

of studies on nonlinear responses from metallic nanoparticles. Applied to metal spherical particles this has led to large hyper-Rayleigh scattering signals [222, 223] which can be explained by quadrupolar-type SHG (dipolar SHG being canceled from centrosymmetry reasons), enhanced by plasmon resonances [224]. Plasmons - which are at the origin of field enhancements - are collective oscillations of the free electron density in metals against the fixed ions [225]. Metal nanostructures cannot only enhance their nonlinear intrinsic responses, but also signals from molecules placed in their vicinity. Two-photon fluorescence enhancement has been observed on surfaces (when the effect is confined in a 2D environment, the collective electron oscillations are called surface plasmon polaritons) in a TIRF (total internal reflection fluorescence) setup [226, 227]. The characteristics of the plasmons strongly depends on the shape and the physical environment of the nanoparticles [228].

Many structures have been proposed for nanoplasmonics. Nanometric metal tips have been successfully employed to perform near-field TPF imaging due to the spatial confinement of very strong fields at the tip [229]. Other geometries to profit from plasmon resonances are fractal shaped periodic metal nanostructures where the exact location of the field's hot spots depends on the incident wavelength and polarization [230]. Thus one can fabricate nano-antennas that are resonant at certain optical frequencies [231]. Under broadband ultrashort excitation, the appearance of hot spots in metal nanostructures is a dynamic process, since specific localizations will enhance electromagnetic fields only at specific wavelength combination conditions. In an array of gold nanoparticles with increasing sizes on top of a silica substrate Lévêque *et al.* created a hot spot sweeping across the structure at femtosecond time scales [232].

Another possibility are nano-apertures within a metal film [233] which are able to significantly enhance the electric field in the nano-volume they define [234, 235]. The actual form of the electric field strongly depends on the shape and size of the nano-apertures. In triangular ones the hot spots position is controlled by the polarization of the incident field [236, 237]. For simple photonic structures like isolated spherical nano-apertures in a metal film the field distribution within and around the aperture can be theoretically calculated by a rigorous differential theory of diffraction [238] while this is not anymore the case for more complicated shapes. Nano-apertures have been exploited to detect the fluorescence of single molecules with high sensitivity in very dilute systems [239, 240, 241]. This enhancement effect has been explained by an increase of the state density of the electromagnetic field around the cut-off of the fundamental propagative mode within the aperture [242].

Other groups focussed more on both regular and disordered arrays of nanoparticles [243, 244] or nano-apertures [245, 246] where the transmission coefficient and the generated nonlinear signals not only depend on the shape of the photonic structures but also on the incident angle of the electric field due to surface plasmon resonances. Onuta *et al.* probed the field enhancement of bow-tie structures larger than the diffraction limit by an analysis of the SHG signal arising from them [247]. Because the structures itself could be resolved by light microscopy, a field map over the whole structure was retrieved so that hot spots - very confined areas with huge field strengths - could be identified. For bow-tie structures below the diffraction limit and for closely related double holes an enhancement in the

two-photon photoluminescence and the SHG signal was observed as well [248, 249]. Apart from this general enhancement no in-depth studies have been performed to understand the characteristics of nonlinear signals emitted by single metal nano-apertures with sizes below the diffraction limit.

In the first part of this chapter we attempt to close this gap. We will explore the ability of metallic nano-apertures with sizes below the diffraction limit to enhance SHG signals. SHG is an interesting probe for interface effects. As all other nonlinear optical effects it can probe field enhancements due to the square dependence on the field intensity. Moreover, its dependence on the symmetry of the nonlinear medium (see section 1.2.1) predestines it as a morphology probe. Furthermore, SHG can also be used as a sensor for optical field characteristics such as the spectral and temporal pulse profile. Unlike linear signals it arises in a spectral region far away from the excitation and therefore contains a surface-specific response over a dark background. It is a unique contrast to both investigate nanostructures - as shown in this chapter -, and to manipulate and control optical fields at the nano-scale, which is a future perspective of our work.

Dielectric microspheres are a different class of photonic structures. As opposed to metallic nanostructures they do not alter the distribution of the electric field in their vicinity by the interaction with surface plasmons but by the refractive index change between the sphere and its surrounding. Under a plane wave illumination such a sphere focusses the beam on the sphere's shadow side into what is called a photonic nanojet [250, 251]. Therein the field attains high intensities. The nanojet is moreover characterized by sub-wavelength transverse dimensions and a low divergence, which recently has been observed directly using fluorescence from a surrounding solution [252]. These microspheres offer a low-cost alternative to complex objectives commonly used in microscopy [253]. In combination with high NA objectives an even better confinement is reached well below the diffraction limit [254, 255]. Nanoparticles placed within the photonic nanojet experience an enhanced backscattering of light [256]. Such microspheres were also used in nonlinear optics to enhance the TPF signal of a Rhodamine B dye solution [257].

In the second part of this chapter we investigate the use of dielectric microspheres to increase CARS signals. The choice of this different kind of photonic structures is due to conclusions coming from a first try on CARS-enhancement in nano-apertures, which was unsuccessful, because CARS detection has to be performed in the forward direction due to phase matching considerations (see section 1.3.2), but the electric field enhancement only occurs on the excitation side of the aperture, as shown in the next section. Only very little intensity gets transmitted through the nano-aperture where the CARS-active medium is located.

6.2 SHG enhancement from metallic nano-apertures

In the case of a nano-aperture in a metallic film all nonlinear signals arise from the metal itself. Second-order nonlinear effects like SHG only occur in non-centrosymmetric media

(see page 15). Thus - except in nanoparticles of sizes below 40 nm, when quadrupolar decompositions play a role in the SHG induced effect [223] - the bulk of the metal does not contribute and SHG is created at the interface between the metal and the outer medium. In our geometry two different interfaces exist: The circumference of the aperture itself and the plane between the metal layer and the outer medium (Fig. 6.1a). In both cases the nonlinear dipole is characterized by a strong diagonal coefficient $\chi^{(2)}_{nnn}$ - with n designating the normal direction to the interface - and off-diagonal contributions $\chi^{(2)}_{ntt}$, $\chi^{(2)}_{tnt}$ and $\chi^{(2)}_{ttn}$ - t refers to the tangential direction relative to the interface - that are typically smaller by a factor of ten [221]. The generated SHG field $P^{2\omega}_I$ polarized along the direction $I = (X, Y, Z)$ is expressed as (see Eq. (1.16)):

$$P^{2\omega}_I = \sum_{\mathbf{r}} p^{2\omega}_I(\mathbf{r}) = \sum_{\mathbf{r}} \sum_{JK} \chi^{(2)}_{IJK}(\mathbf{r}) E^{\omega}_J(\mathbf{r}) E^{\omega}_K(\mathbf{r}) \tag{6.1}$$

It arises from the coupling of a field E polarized along direction J with another one polarized along K, summed over all dipole positions $\mathbf{r}$. Contrary to the previous sections dealing with bulk media, we account here for the spatial repartition of the nonlinear induced dipoles, since it plays a key role in the global SHG response (see below). It can be split into the two contributions $P^{2\omega}_{a,I}$ from the aperture circumference and $P^{2\omega}_{s,I}$ from the surface of the metal layer.

We excite and detect the SHG signal with the same setup as already used in chapter 3 (see Fig. 3.4). A tunable Ti:Sapphire laser providing pulses of 150 fs with a repetition rate of 80 MHz is operated at a wavelength of 800 nm with a typical averaged power of a few mWs. The axis of the beam's linear polarization is controlled by an achromatic half waveplate mounted on a step rotation motor at the entrance of the microscope. A high NA objective ($\times$60, NA = 1.2) focusses the beam on the sample. The backward emitted SHG signal is collected by the same objective and is separated from the incident laser by a dichroic beam splitter. After the subsequent passage of a polarization beam splitter the signal is detected by two avalanche photodiodes. As samples we use circular and triangular nano-apertures that are formed by focussed ion beams in a 200 nm thick gold film which adheres to a glass coverslip by an intermediate chromium layer with a thickness of 20 nm. Their diameters, respectively side lengths, vary between 140 nm and 470 nm. These structures have been fabricated in the T. Ebbesen group (ISIS, Université de Strasbourg, France). A piezoelectric stage on which the sample is fixed allows a 3D scan of the nano-apertures.

Under this configuration the normal direction n of the nonlinear dipoles along the circumference of the aperture lies in the (X, Y)-plane of the macroscopic frame while the dipoles of the layer surface are aligned along Z (Fig. 6.1a). Due to the high NA focussing (see section 4.3 and appendix C) the latter can still couple with the incident electric field, but the weight of their contribution is expected to be lower than of those dipoles formed by the aperture itself, as even for strong focussing the field components within the (X, Y)-plane surpass the one along Z (Fig. 6.1c).

Because the aperture size is below or at the diffraction limit a typical SHG scanning image of theses structures only shows a feature resembling a diffraction-limited spot (Fig.

6.1b). The effect of the surrounding metal layer is evidenced in a weak non-vanishing

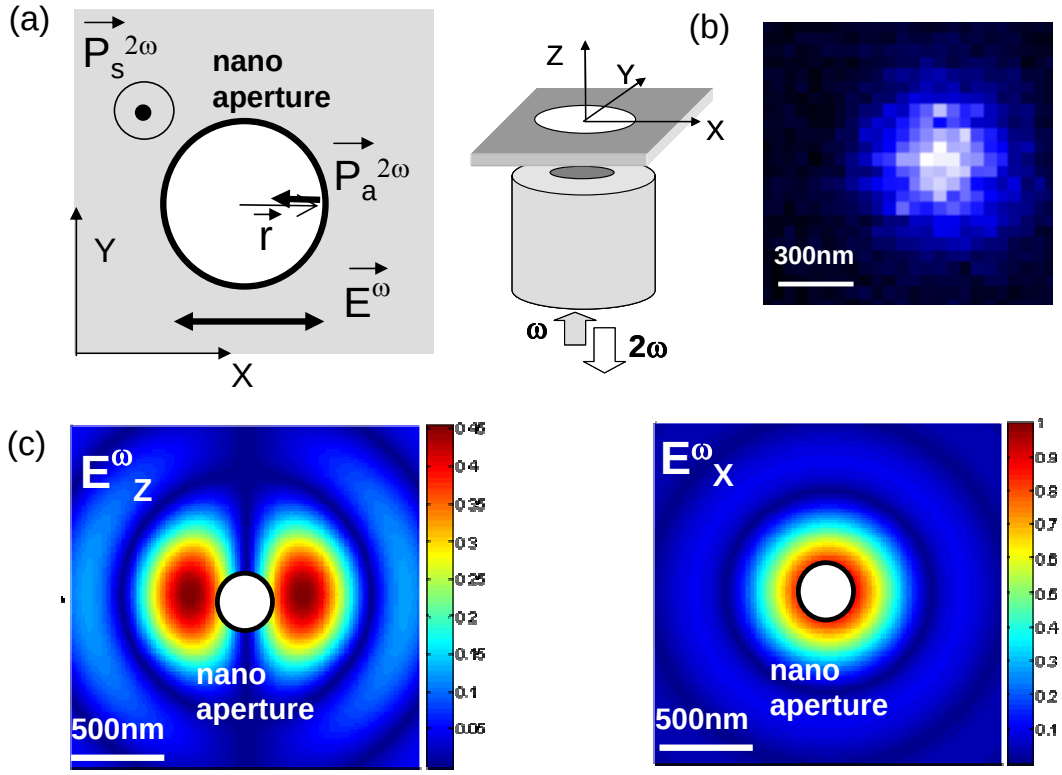

Figure 6.1: (a) Schematic representation of the nonlinear dipoles in a metal nano-aperture at the aperture circumference ($\mathbf{P}_a^{2\omega}$) and and at the metal surface ($\mathbf{P}_s^{2\omega}$), and sketch of the experimental scheme for nonlinear microscopy imaging; (b) SHG image of a circular nano-aperture with a diameter of 195 nm; (c) intensity maps of the E_X^ω and E_Z^ω excitation fields in the focal plane under strong focussing conditions (NA = 1.2). At the objective's back aperture, $\mathbf{E}^\omega$ is polarized along X (see Fig. 3.15). A schematic nano-aperture is superimposed as a white disk.

background signal. A spectral analysis of the total blue-shifted signal as shown in Fig. 6.2 reveals the presence of a dominant SHG peak and of a spectrally broad two-photon luminescence signal which originates from interband excitations within the gold layer. To reject the luminescence we use a bandpass filter around 400 nm (HQ400/40m-2p, Chroma Technology, Bellows Falls, VT) that only keeps the SHG signal. Overall, both image (Fig. 6.1b) and spectrum (Fig. 6.2) show a significant response of the nano-aperture compared to the bare metal surrounding surface.

In order to quantify the SHG enhancement from the nano-aperture as well as its size dependence, the polarization dependence of the SHG signal needs to be understood since it plays an important role in the nonlinear coupling process. Moreover, polarization responses

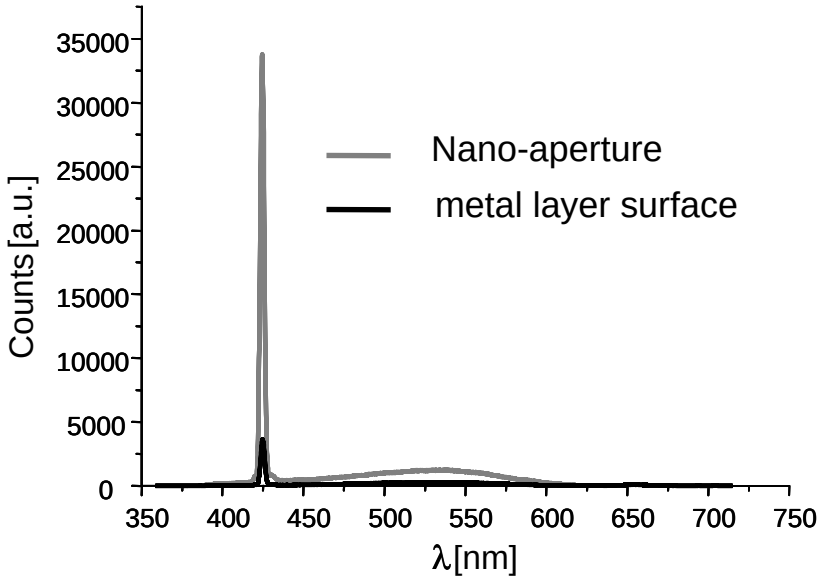

Figure 6.2: Spectra of the blue shifted signals emitted by the nano-aperture (grey) and the metal film (black). A strong SHG peak (here at 425 nm, because the excitation was fixed at 850 nm) is accompanied by a spectrally broad but smaller luminescence peak red-shifted compared to the SHG signal.

are an interesting way to extract information on the shape and size of metal nanostructures, as we will see in the following part. For this we rotate the linear polarization of the excitation field $\mathbf{E}$ in the (X, Y)-plane and measure the signal generated for each of these orientations α of the incident field as depicted in Fig. 6.3. This approach is identical to the one used previously to study structural information in crystals and molecular samples (see section 3.1). The SHG trace is recorded for both fundamental polarization directions of the signal. These polarimetric responses are compared with numerical calculations based on Eq. (6.1), where the high NA focussing is taken into account both for the excitation field in the focal volume and the collection by the same objective following the formalism detailed in appendix C. The total calculated signal arises from an assembly of dipoles around the aperture's circumference. In circular apertures they are placed every $\frac{10\pi}{3}$ nm and in triangular ones every 10 nm. In this calculation, for each nonlinear induced dipole the nonlinear radiated field is calculated in all wave vector directions and integrated over the angular aperture of the collection objective. A further rotation of the wave vectors is required to compute the response after the objective (see appendix C). Fig. 6.3 shows the measured and calculated polarimetric responses of several circular and triangular nano-apertures together with the corresponding transmission electron microscopy (TEM) images [258].

In the case of a triangular aperture a SHG signal is generated - whatever the size of the structure - due to the non-centrosymmetry of the structure. For an equilateral triangle

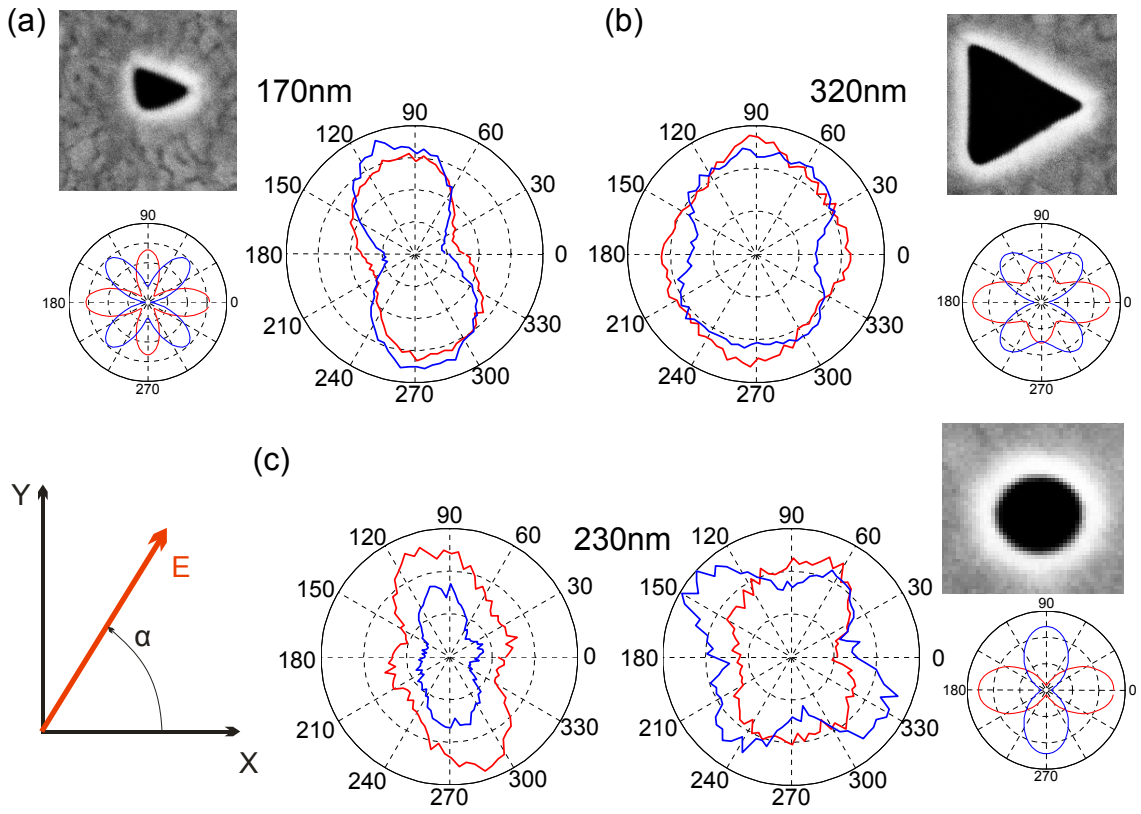

Figure 6.3: Polarimetric responses of nano-apertures. The exciting polarization $\mathbf{E}(\alpha)$ turns around the angle α in the (X, Y)-plane. SHG signal (radius) as a function of α for a triangular aperture with a side length of 170 nm (a), for a triangular aperture with a side length of 320 nm (b), and for two circular apertures with a diameter of 230 nm (c). In all cases the expected polarimetric response (small polar graph) and the corresponding TEM image are depicted (measured in the ISIS lab, Université de Strasbourg, France). Red curves correspond to a X-polarized signal and blue curves to a Y-polarized one.

where one side is parallel to the Y-axis the X-polarized signal $I_X = |P_X^{2\omega}|^2$ is expected to exhibit four lobes at $\alpha = (0°, 90°, 180°, 270°)$ while the Y-polarized one shows a similar four-lobe pattern but shifted by 45° [259]. The larger the triangular aperture gets, the more dissimilar these two pattern become (small theoretical polar graphs in Fig. 6.3a and 6.3b). This is primarily due to the occurrence of phase retardation effects between dipoles at different positions of the interface, whose emission can enter in constructive or destructive interference. This feature is only visible in structures above sizes of about 50-100 nm [223]. To a certain extent this pattern is seen in the experimental polar graph in Fig. 6.3b though there also is a strong background masking it partially. But for smaller apertures the SHG response is found to be more dipole-shaped. Partially this can be explained by the imperfect form of these triangular apertures that arise from the impossibility to mill accurate shapes with focussed ion beams which is evidenced by the TEM image in Fig.

6.3a.

Circular apertures on the other hand are centrosymmetric structures which is highly unfavorable for SHG. That there arises any SHG signal at all is due to phase retardation effects between the nonlinear emitters at the perimeter of the aperture [222, 223]. This means that the signals of two dipoles with opposing orientations do not cancel each other completely because a phase shift is acquired linked to the spatial separation between them. Our calculations predict a polarimetric response with two lobes around $\alpha = (0°, 180°)$ for I_X and the same pattern turned by 90° for I_Y. However this is not seen in our experiments. Moreover the polarimetric response of different circular apertures with the same diameter may differ strongly (Fig. 6.3c). We attribute this to the fact that the SHG response of such apertures is extremely sensitive to defects breaking the intrinsic centrosymmetry of the object, as was already observed in metallic nanospheres [223]. Phase retardation effects can lead to a SHG signal of centrosymmetric structures but it will still be small compared to non-centrosymmetric ones. Thus the phase retardation signal as predicted in our calculations can quickly be completely overlaid by small defects in the aperture that are much more favorable for SH generation.

Although our model is only a crude simplification because we do not account for the scattered contribution from the aperture that leads to a field enhancement at certain regions around the photonic structure (which could also probably explain the deviations observed in the polarimetric data), we are nonetheless able to recover some of the features of the SHG signal especially for SHG favorable symmetries like triangular apertures.

For a better comparison of the SHG efficiency from different structure shapes and sizes we sum the signals over all incident polarization angles α and over both detection directions. We define an enhancement factor by the ratio between this averaged SHG signal and the averaged SHG response of the metal layer without an aperture. Fig. 6.4 combines the results for both circular and triangular nano-apertures as a function of their size. As expected the enhancement for triangular apertures is much larger than for circular ones due to symmetry considerations. Moreover while a strong enhancement is observed for all studied sizes of triangular apertures, circular ones only show an enhancement for diameters between 170 nm and 250 nm. For larger diameters the field intensities at the aperture perimeter are most likely too small to generate a considerable SH field as most of the energy is focused inside the aperture where there are no nonlinear dipoles, and additionally for larger sizes the enhancement of the incident field caused by the photonic structure itself only plays a minor role. On the other hand for smaller sizes where there is considerable energy focussed on the nonlinear dipoles at the circumference the phase retardation effects are very small because of the proximity of the dipoles and the whole structure behaves more and more as a purely centrosymmetric object not generating any SH signal.

We also calculated in collaboration with N. Bonod (CLARTE group at Institut Fresnel) the field inside circular apertures by a rigorous differential method that solves Maxwell's equations in single sub-wavelength apertures drilled in real metals [242]. The field is developed in a Fourier-Bessel basis reducing the Maxwell equations to a new set of differential

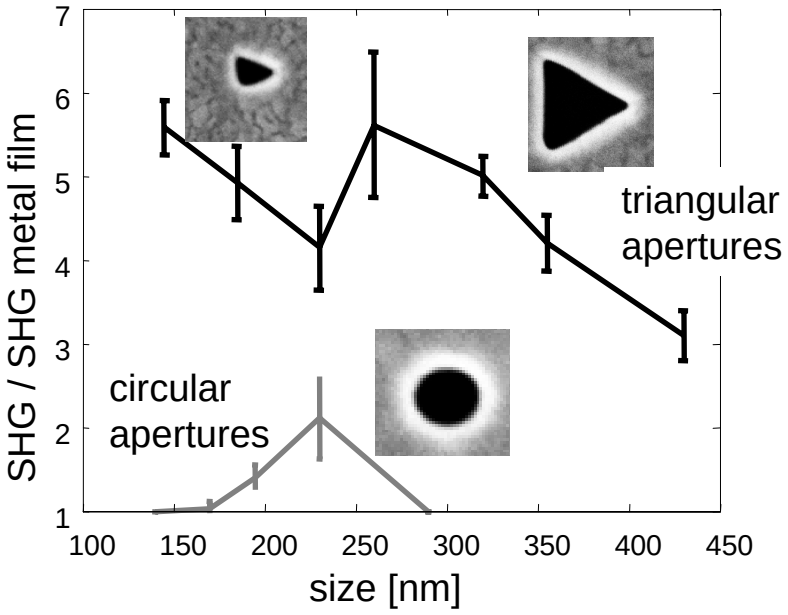

Figure 6.4: SHG enhancement factor relative to the signal from the aperture-free metal layer of circular (grey) and triangular (black) nano-apertures, averaged over all incident polarizations α. For circular apertures the size refers to the diameter and for triangular ones to the side length. Error bars correspond to the standard deviation of the enhancement factors obtained from several apertures of the same type and size. Circular apertures with diameters of 290 nm and more could not be identified anymore within the gold layer.

equations. The nano-aperture is illuminated at normal incidence by a linearly polarized plane wave (Fig. 6.5a). The electromagnetic field in the substrate and the superstrate is obtained by a first integration and a second one leads to the knowledge of the field components at the interface of the aperture (Fig. 6.5b). This field is introduced at two levels into our calculations: First, the normal components $E_n^\omega(\mathbf{r}_n)$ at the field's frequency ω and the dipole positions $\mathbf{r}_n$ is directly inserted into Eq. 6.1 to determine the induced dipoles. Second, the enhancement of the field at frequency 2ω is taken into account as a scaling factor for the radiated nonlinear field. The nano-apertures behave very differently at these two frequencies: at the excitation wavelength of 800 nm they are metal like with a cut-off diameter of about 280 nm. Apertures with larger sizes transmit some of the incident light while no propagative modes exist for smaller diameters. But at the emission wavelength of 400 nm they behave like a lossy dielectric-like waveguide. This model still only approximates our experimental conditions because it is based on a plane wave illumination rather than on a focussed field, and moreover the enhancement of the 2ω field is treated in a linear diffraction regime that does not account for higher order-couplings between the fields at ω and 2ω. Nonetheless it provides already a good agreement with the observed size dependence of the SHG emission as seen in Fig. 6.5c.

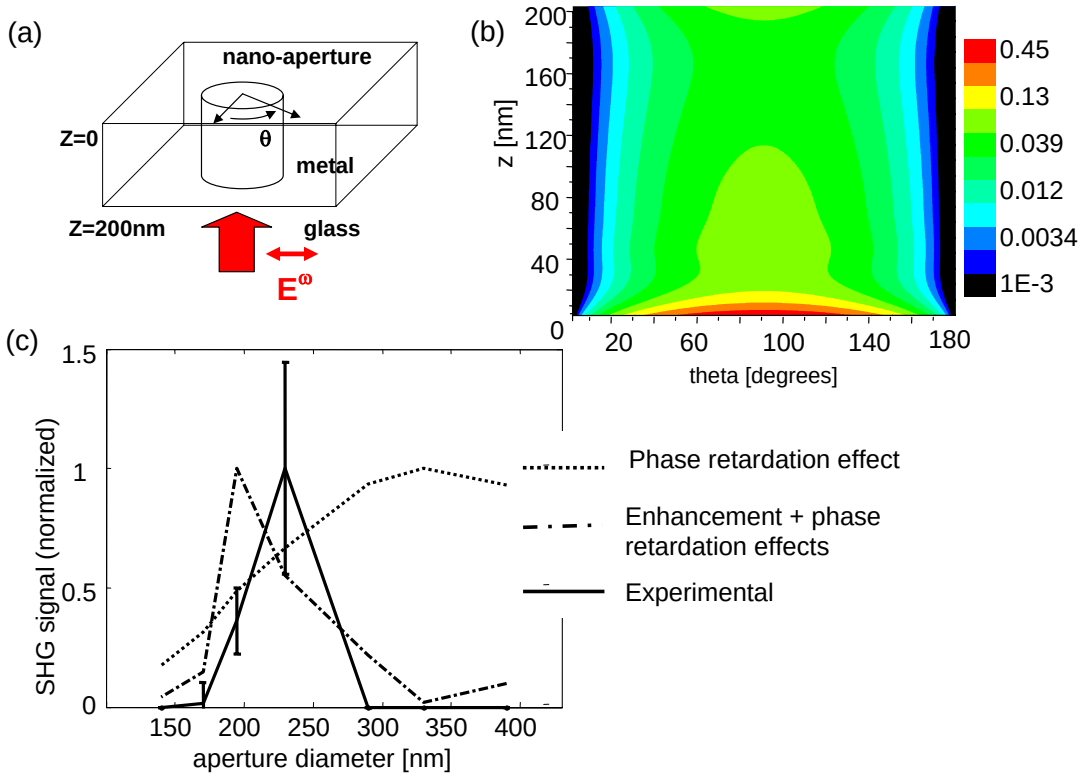

Figure 6.5: (a) Geometry used for the calculation of the scattered electric field. (b) Map of the calculated radial component $|E_n^\omega|$ of the field normal to the aperture surface as a function of the angle θ around the surface and the height Z relative to the glass substrate. (c) Size dependence of the emitted SHG signal (normalized to the maximal value). Continuous line: experimental signal as in Fig. 6.4; dotted line: simple dipole model taking only the phase retardation effects into account but not the contribution of the scattered field by the aperture itself; dashed line: calculated SHG signal including the field enhancement factors.

This indicates that the SHG enhancement observed from nano-apertures originates mainly from their interface, which acts advantageously for both the generation of nonlinear dipoles, and the enhancement of the exciting and the radiated optical fields. For triangular nano-apertures a similar approach could be used which would, however, have to include a more complex spatial distribution of the diffracted fields [237]. Since this structure is not of cylindrical symmetry anymore, Fourier-Bessel decompositions cannot be used, so we did not pursue this calculation.

SHG was used here to probe the two-photon enhancement effects originating from the metal-air interface in nano-apertures. This approach has also been developed in metallic nanoparticles isolated on a glass substrate, in collaboration with the Université Technologique de Troyes (UTT). This study is not described here since the understanding of SHG responses is still under work, nevertheless we have shown the interesting potential of

both metal nanostructure approaches to monitor and ultimately manipulate SHG responses by an adequate optimization of phase, polarization and amplitude profiles of the excitation field as described in this thesis. Indeed, any resonance in the structure can strongly affect the phase profile of a diffracted field, which could advantageously be measured using the SHG from the structure itself.

6.3 CARS enhancement from dielectric microspheres

The nanostructures described above could serve as interesting enhancement substrates for any kind of nonlinear optical contrast. Their application to CARS was therefore envisioned. The apertures and the metallic layer were covered with a solution of neocyanine dye. Unfortunately, in a forward detection setup, no CARS signal was seen. This is most likely due to the fact, that the field enhancement occurs almost exclusively on the excitation side of the nano-aperture (see Fig. 6.5b), and only very little of the incident intensity gets transmitted to the other side of the aperture. Moreover, due to the fact that the aperture is filled with a liquid, the refractive index jump between the metal and the surrounding medium is smaller than compared with an air-filled aperture. Because this refractive index jump is a key factor in the field enhancement process, it is to be expected that for a liquid-filled aperture this enhancement is less pronounced than for an air-filled one studied so far.

Consequently, we switched to a different class of photonic structures: dielectric microspheres. As opposed to metallic nanostructures in which the nonlinear signal arises from the metal itself, dielectric microspheres only serve to enhance a signal from a nonlinear material in their vicinity. The underlying mechanism is the creation of a photonic jet on the shadow side of the microsphere [254]. In this region the incident field assumes higher strengths in a smaller volume than under normal focussing conditions without the presence of the microsphere (Fig. 6.6). Because processes like SHG or CARS depend quadratically or cubically on the incident field, their generation within the photonic jet is highly favored and even though the generating volume is reduced the total signal can surpass that of a bead-less focussing.

We tested the enhancing capability of dielectric microspheres by measuring the single pulse CARS signals generated in their vicinity. The setup is the same as in Fig. 5.5. Additionally we use the detection by a photomultiplier tube (PMT) as depicted in Fig. 2.8c to only detect a narrow region of the whole CARS spectrum in order to transpose this experiment to imaging. As a sample we use polystyrene beads with a diameter of $5\,\mu$m dispersed onto a glass cover slip. The beads are easily seen by white light illumination and we verify that only a single one is present within the focal region of the excitation beam. The spatial resolution of our microscope when using an objective with NA = 0.5 is 800 nm in the lateral dimensions (X, Y) and $6.4\,\mu$m in the axial direction Z according to Eq. 2.23. The microspheres are surrounded by dimethyl sulfoxide (DMSO) whose resonance at $\Omega_R = 670\,\mathrm{cm}^{-1}$ has already been characterized in chapter 5. On top another glass

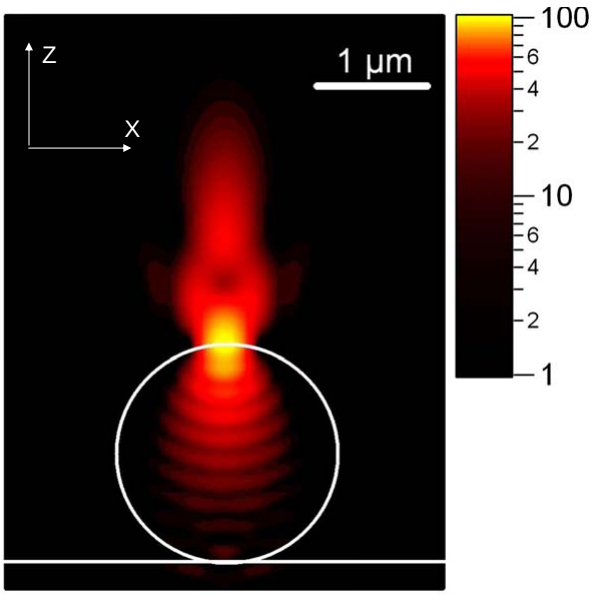

Figure 6.6: Electric field intensity of the nanojet forming on the shadow side of the microsphere, when it gets illuminated by a strongly focussed Gaussian beam (here from below) [260]. The actual form of the nanojet depends on the incident wavelength, the focussing conditions, the microsphere size and the diffractive index difference between the microsphere and the surrounding medium.

slide is placed to provide a planar surface and avoid a lens effect of the DMSO drop. When no narrow spectral features like phase steps or polarization switches are inserted into the excitation profile, the CARS spectrum does not show any spectral resolution and only the non-resonant contribution is seen (Fig. 6.7b). The various oscillation in the spectrum are not caused by vibrational resonances, because they do change in position when a phase step is shaped into the excitation spectrum at different λ. They are stable and would therefore not hinder the retrieval of a resonance. They probably arise from interferences between signal fields reflected multiple times within the detection path. The overall strength of this non-resonant signal is a measure of the strength of the electric fields involved in the nonlinear optical coupling. Thus by scanning the microsphere on a piezoelectric stage through the focal volume of the objective the CARS enhancement due to the presence of the sphere can in principle be assessed. Because a complete spectral measurement for each scanning point would take an enormous amount of time, we select a narrow spectral region where the non-resonant CARS signal is very high. Fig. 6.7c shows the XY- and the XZ-scan of such a sphere. The signal is normalized to the one arising from DMSO without the presence of the microsphere.

One might argue that the stronger CARS signal under the presence of the microsphere is not caused by an increased emission of the DMSO but by the non-resonant CARS signal

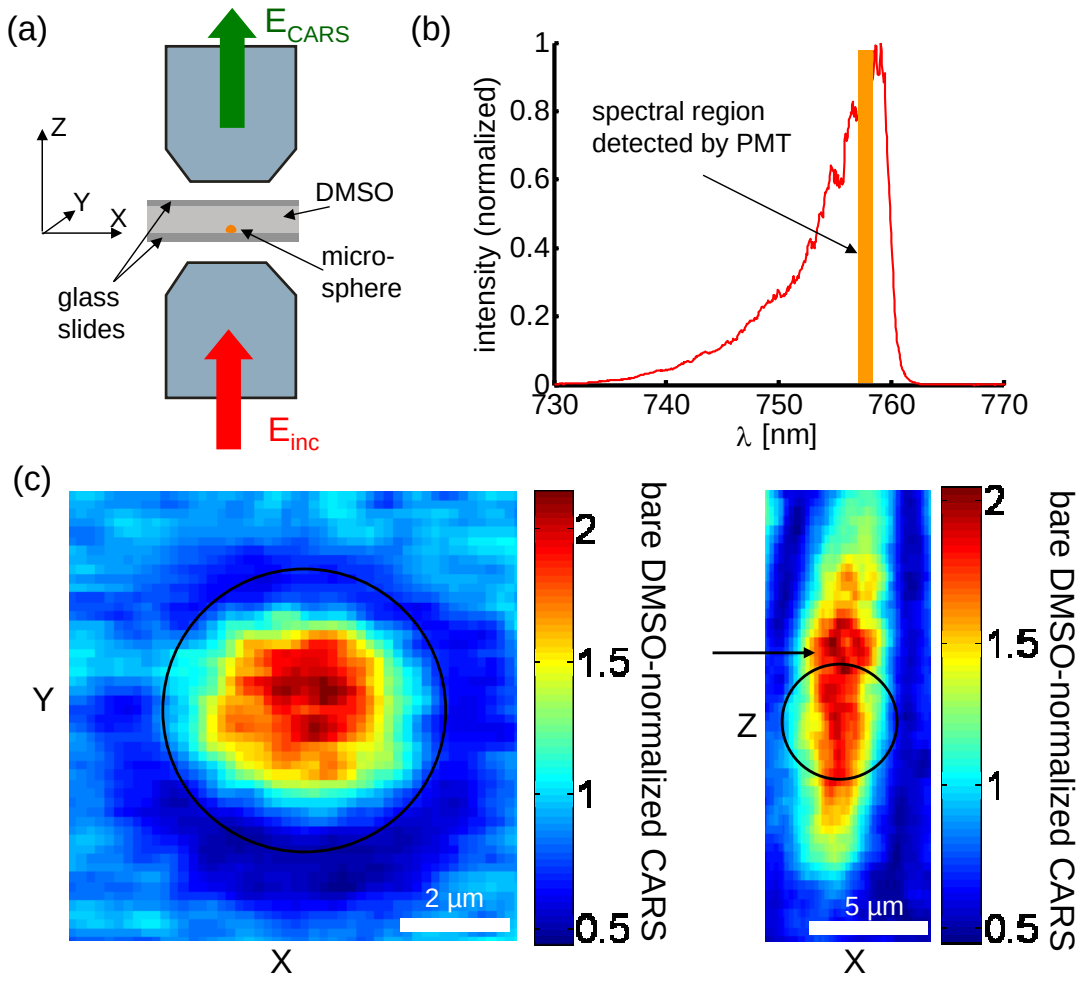

Figure 6.7: CARS enhancement of polystyrene microspheres. (a) Scheme of the experiment. (b) Typical DMSO CARS spectrum when no spectrally narrow feature is inserted into the excitation profile. The drop at 760 nm is due to the detection low pass (see page 145). (c) XY- and XZ-scans of the CARS signal under the presence of the microsphere, with a drawing of the sphere's position. The signal is normalized by the signal in pure DMSO without the presence of the microsphere. An arrow in the XZ-scan denotes the Z-position at which the XY-scan was taken. The detected signal comes from the spectral region indicated in (b).

of the sphere itself. And indeed, as all media possess a third-order nonlinear susceptibility $\chi^{(3)}$ a contribution of the bead to the total signal is expected. Thus the question arises how to quantify the contribution of the different media. The non-resonant contributions of both DMSO and polystyrene have the same spectral shape, because the non-resonant part of the susceptibility $\chi^{(3)}_{NR}$ is nearly wavelength independent and therefore the spectral behavior of the corresponding CARS signal is governed by the excitation spectrum which is identical for both materials.

As a consequence only the resonant contribution to the total signal can permit a separation between polystyrene and DMSO. While DMSO possesses the well-known resonance at $\Omega_R = 670\,\mathrm{cm}^{-1}$, polystyrene is resonance-free in the whole wave number range observable with single pulse CARS. As explained in chapter 5 a spectrally narrow phase jump at position ω_{ph} leads to a peak-dip structure in the CARS spectrum at frequency $\omega_{ph} + \Omega_R$. The amplitude of this structure is a measure for the strength of the resonance at Ω_R which is expressed by the ratio between the resonant and non-resonant third-order nonlinear susceptibilities $\frac{\chi^{(3)}_R}{\chi^{(3)}_{NR}}$. In the case of a mixture of two media A and B where only medium A has a resonance this ratio is written as:

$$\frac{\chi^{(3)}_R}{\chi^{(3)}_{NR}} = \frac{x\chi^{(3)}_{R,A}}{x\chi^{(3)}_{NR,A} + (1-x)\chi^{(3)}_{NR,B}} \tag{6.2}$$

where x is the fraction of medium A within the CARS generating volume and $1 - x$ that of medium B. Thus once the resonance strength of medium A is known, its fraction can be obtained from the resonance feature in a CARS spectrum.

We use this approach to estimate the contribution of the polystyrene to the signals in Fig. 6.7c. We insert a phase jump at $\lambda_{ph} = 782\,\mathrm{nm}$ which results in a resonance feature around 744 nm. From this we deduce the resonance strength by calculating the ratio:

$$r = \frac{I_{peak}}{I_{dip}} \tag{6.3}$$

where I_{peak} and I_{dip} are the intensity values at the peak and the dip of the resonance feature. Fig. 6.8a shows the spectra of the two limiting cases where either only DMSO or polystyrene is present. In a theoretical calculation we verify that r varies monotonously - almost linearly - when the resonant contribution increases relative to the non-resonant one (Fig. 6.8b). We thus perform a spectral measurement of the CARS signal at different positions Z in the XZ-scan in Fig. 6.7c and determine r. The result is shown in Fig. 6.8c where the two limiting cases of only DMSO (resonant) or polystyrene (non-resonant) are indicated as well. For the whole Z-range observed in Fig. 6.7c, r stays between both limiting cases confirming that a portion of the CARS signal is indeed due to the polystyrene microsphere. As Z increases the focal volume is more and more leaving the microsphere and the signal comes predominantly from the DMSO. But because there is not any photonic jet being formed anymore, no CARS enhancement can be seen. In the region of $Z \approx 12\,\mu\mathrm{m}$ where the highest CARS signal is observed, r reaches about three quarters of the DMSO-only value (compared to the polystyrene-only case). As the relationship between r and

$\frac{\chi_R^{(3)}}{\chi_{NR}^{(3)}}$ is almost linear it is safe to assume that at these Z about three quarters of the whole signal originate in the DMSO and one quarter in the microsphere. Thus the CARS DMSO-normalized factor drops from around 2 to 1.5.

This low value is quite surprising because the electric field in the photonic jet region is expected to be around a factor two times stronger than the field under bead-free focussing conditions. For CARS as a third-order nonlinear process enhancement factors around $2^3 = 8$ are therefore expected. The reason for this discrepancy probably lies in the fact that CARS as a coherent process depends on a coherent build-up over a certain signal-generating propagation length to lead to measurable intensities (for more on phase matching rules see chapter 1). The photonic jet behind the microsphere, however, is very localized in all three dimensions and thus the build-up distance gets reduced and with it the generated signal. This unsuccessful attempt exposes nevertheless the crucial parameters to access CARS-enhancement signatures in nanostructures. Other works have shown other difficulties in metallic nanostructures [261].

6.4 Conclusions

Photonic structures are a possible means to enhance nonlinear signals. Metallic nanostructures like nano-apertures locally enhance electric fields in the vicinity of the structure. These hot spots are ideally suited for the generation of nonlinear optical fields as they depend on large field strengths. The actual enhancement is however strongly dependent on the shape and size of the nanostructure and on the used wavelength and polarization direction. This chapter has shown the delicate monitoring and interpretation of the data in this field, since nonlinear optical signals are coherent processes, where the spatial expansion of the structures can be an issue (either from apparition of new phase-retardation effects, or from changes in propagation rules in reduced excitation volumes).

We presented a formalism that can predict the best size-wavelength combinations for second harmonic generation in circular nano-apertures. For triangular and other shapes that are much more efficient in the SH generation due to their non-centrosymmetry a model has still to be developed that takes the field enhancement by the aperture into account. In principle it should be possible to use the polarimetric response of the SHG signal from a nano-aperture to deduce the aperture's size and shape in a sort of "diagnostic" measurement at the nano-scale. However, this is quite a challenge because tiny defects can strongly alter the SHG response, especially in circular apertures as their intrinsic signal is relatively low due to symmetry considerations. Thus SHG polarimetry might be used to assess the quality of such nano-apertures, but before that more work has to be done to characterize the responses for different sizes, shapes and defects.

Dielectric microspheres have also been proposed to enhance nonlinear signals due to the photonic nanojet that is formed on their shadow side when they get illuminated. For CARS they only lead to a minimal gain because the strong light confinement impedes the

full use of the long coherence length for an efficient coherent buildup of the CARS signal. For other nonlinear processes that possess shorter coherence lengths, these microspheres might prove to be more useful. The use of dielectric microspheres is also accompanied by experimental difficulties as the positioning of the laser focus on the microsphere is very crucial for an optimal enhancement.

At last, we applied dielectric microspheres to enhance the two-photon fluorescence from single molecules in a fluorescence correlation spectroscopy (FCS) setup, which appeared to be successful [262]. The easier implementation in fluorescence is again probably due to the incoherent nature of this signal.

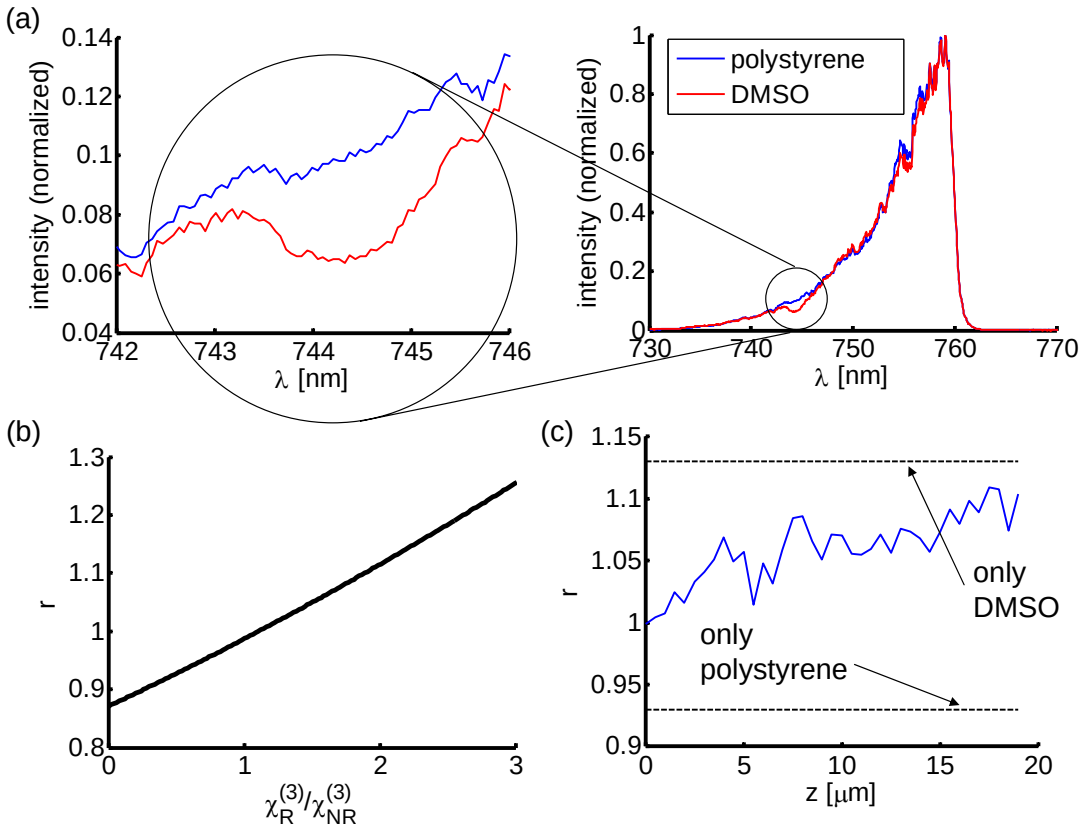

Figure 6.8: Peak-dip ratio of the resonant feature in single pulse CARS spectra. (a) CARS spectra for DMSO and polystyrene generated from an excitation profile with a phase jump inserted at $\lambda_{ph} = 782\,\text{nm}$ (on the left side is a close-up of the spectrum on the right). The peak-dip is visible for DMSO while polystyrene does not possess a resonance there, its spectrum being like that of DMSO when no phase jump is inserted in the excitation beam. (b) Dependence of the peak-dip ratio r on the resonance strength $\frac{\chi_R^{(3)}}{\chi_{NR}^{(3)}}$ (calculation). (c) r for different Z-positions in Fig. 6.7c; horizontal lines refer to the limiting cases of only DMSO or only polystyrene.

Conclusion and perspectives

In this thesis we assessed the potential of the shaping of femtosecond pulses for the readout of structural information in nonlinear microscopy. A pulse shaper was set up consisting of a $4f$-line in which three liquid crystal masks are placed to allow independent control of amplitude, phase and polarization for each spectral component within the broadband pulse.

Before this device can be employed for nonlinear microscopy applications, the distortions - both in phase and amplitude - to which the pulse is subject, between the Fourier plane of the pulse shaper (where its spectral state can be controlled) and the focal spot of the objective (where the nonlinear signal is generated) need to be quantified and possibly corrected for. While phase distortions arise predominantly from the objective, polarization distortions have their origin mostly in reflection optics.

For the measurement and correction of phase distortions we presented two approaches in detail: evolutionary strategies and single-beam homodyne SPIDER. Evolutionary strategies can remove most of the phase distortions and are well suited when the general nonlinear signal output of an experiment needs to be maximized. They reach their limits when a more accurate control of the spectral phase is needed, especially when the found pulse shaper configuration - presumably leading to a flat phase - forms the basis on top of which specific phase profiles need to be created. Single-beam homodyne SPIDER can directly measure these phase profiles, even in a much shorter time than needed for an evolutionary strategy and with a simple setup. However, the spectral resolution is limited as well as the accessible phase profiles. For a better control of the evolution of the phase state between the pulse shaper and the focal spot of the objective, a collinear FROG method should be implemented, even though this will result in a more complicated setup as an interferometer is needed.

We have shown that polarization distortions can be reliably characterized by two-photon fluorescence polarimetry measurements in a dye solution. In our setup their correction is not possible at the current stage, because the main polarization axes turn within the beam path. Nevertheless in this work we limited ourselves to linear polarizations perpendicular to one another that are well controlled. To fully profit from our polarization shaping capabilities, for example in creating circular polarizations at specific spectral positions, further control of the direction of the main polarization axes has to be obtained.

We demonstrated the potential of combined amplitude and polarization shaping by

reading out the individual components of the second-order nonlinear susceptibility tensor simultaneously. This information is a key component in the understanding of structural properties in molecular and bio-molecular samples. Our scheme works much faster than those used previously based on more traditional polarimetry measurements. In particular it allows single-component tensorial imaging with sub-micrometric resolution. From the obtained images local order and disorder can be deduced. This contrast mechanism does neither require prior sample staining, nor the presence of different molecular species, nor concentration variations. It should therefore be of great interest to the biological community for the imaging of order and disorder of cellular and extracellular components whose functionality depends on their organization.

Before this stage is reached further improvements are needed, especially an increase in signal intensity. We suggested a possible path towards this goal by replacing the amplitude pulse shaping with phase shaping to profit from the complete pulse energy provided by the laser source.

Polarization pulse shaping, in combination with phase shaping, also allowed measuring vibrational signatures of solvents by CARS microscopy, in the fingerprint region with a single pulse. Beyond the simple determination of the spectral position of a vibrational resonance, also the Raman depolarization ratio can be retrieved, at least theoretically. In practice, there are still some difficulties to resolve, in particular the insufficient addressing of the resonance, but this should be more accessible as soon as laser sources providing a broader spectrum are employed.

Finally we assessed the enhancement of nonlinear signals by photonic structures. Nanoapertures in a metallic film seem especially promising to provide molecular signature enhancements, as they enhance the incident electric field in their vicinity. The SHG polarimetric signature of such an aperture is characteristic of its size and shape and should thus allow in principle a structure identification even when its size is below the diffraction limit. Because SHG is very sensitive to surface defects, this might however be difficult to achieve unless the fabrication techniques improve, which is nowadays progressively the case. We have nevertheless shown that such polarimetric responses can provide a diagnostic tool for the quality of nanostructures, be they apertures or particles.

Furthermore these structures (and more specifically nanoparticles-based metallic substrates) can serve as nanometric light sources which could be used in high resolution imaging applications. Together with polarization pulse shaping it should be possible to control the exact position and polarization characteristics of these sources, an interesting perspective that theoretical works and only a few experimental demonstrations have recently investigated.

Dielectric microspheres can serve to enhance nonlinear signals emitted by materials in their vicinity by better focussing the incident beam in a photonic nanojet. We demonstrated however, that this is not beneficial for all nonlinear contrasts. In the case of CARS almost no enhancement is achieved, while for an incoherent process like two-photon fluorescence, their potential is much greater.

Overall, this PhD was mostly dedicated to the construction of an instrument and its application to original nonlinear imaging approaches. More work will definitely be required to take a complete advantage of its capabilities and circumvent the limitations that have been identified. Future investigations have already started, on one side in bio-imaging for fibril-based structures investigations, on another side in nanophotonics applied to the coherent control of the localization of optical fields at the nano-scale on metallic nanostructures.

Appendix A

Weighted linear fit

To assure a proper functioning of the single-beam homodyne SPIDER (see section 2.8) the linear component of the retrieved phase $\phi(\omega)$ has to be removed as the method is not sensitive to it. However, subtracting a simple linear fit does not succeed as the fit would be dominated by the huge values of ϕ on the spectral fringes that are caused by the small signal-to-noise ratios in these regions. This problem can be avoided by subtracting a weighted linear fit.

If one wants to fit a function $f(\omega)$ by another function $g(\omega, p_1, p_2, ..., p_n)$, containing n fit parameters $p_1, p_2, ..., p_n$, the difference between both functions, for example expressed by the mean squared error χ^2

$$\chi^2 = \int \left(f(\omega) - g(\omega, p_1, p_2, ..., p_n)\right)^2 \mathrm{d}\omega \tag{A.1}$$

needs to be minimized. Thus follows the set of conditions:

$$\frac{\partial \chi^2}{\partial p_i} = 0 \quad , \quad \text{for } \; i = 1, ..., n \tag{A.2}$$

A weighted fit is achieved by multiplying the mean squares with a weighting function $h(\omega)$, that can for example be a Gaussian distribution around a central frequency ω_0. Eq. (A.1) then becomes:

$$\chi^2 = \int \left(f(\omega) - g(\omega, p_1, p_2, ..., p_n)\right)^2 h(\omega)\mathrm{d}\omega \tag{A.3}$$

For a linear fit $g(\omega, m, n) = m\omega + n$ Eqs. (A.2) resolve to:

$$\begin{aligned} \frac{\partial \chi^2(m,n)}{\partial m} &= \frac{\partial}{\partial m}\left(\int \left(f(\omega) - m\omega - n\right)^2 h(\omega)\mathrm{d}\omega\right) = -2\int \left(f(\omega) - m\omega - n\right) h(\omega)\omega\mathrm{d}\omega \\ &= 2\left[m\int \omega^2 h(\omega)\mathrm{d}\omega + n\int \omega h(\omega)\mathrm{d}\omega - \int \omega f(\omega)h(\omega)\mathrm{d}\omega\right] = 0 \end{aligned} \tag{A.4}$$

$$\begin{aligned} \frac{\partial \chi^2(m,n)}{\partial n} &= \frac{\partial}{\partial n}\left(\int \left(f(\omega) - m\omega - n\right)^2 h(\omega)\mathrm{d}\omega\right) = -2\int \left(f(\omega) - m\omega - n\right) h(\omega)\mathrm{d}\omega \\ &= 2\left[m\int \omega h(\omega)\mathrm{d}\omega + n\int h(\omega)\mathrm{d}\omega - \int f(\omega)h(\omega)\mathrm{d}\omega\right] = 0 \end{aligned} \tag{A.5}$$

This is a system of linear equations that can be easily solved for m and n, resulting in:

$$m = \frac{\left(\int \omega h(\omega)\mathrm{d}\omega\right)\left(\int f(\omega)h(\omega)\mathrm{d}\omega\right) - \left(\int h(\omega)\mathrm{d}\omega\right)\left(\int \omega f(\omega)h(\omega)\mathrm{d}\omega\right)}{\left(\int \omega h(\omega)\mathrm{d}\omega\right)^2 - \left(\int \omega^2 h(\omega)\mathrm{d}\omega\right)\left(\int h(\omega)\mathrm{d}\omega\right)} \quad \text{(A.6)}$$

$$n = \frac{\left(\int \omega h(\omega)\mathrm{d}\omega\right)\left(\int \omega f(\omega)h(\omega)\mathrm{d}\omega\right) - \left(\int \omega^2 h(\omega)\mathrm{d}\omega\right)\left(\int f(\omega)h(\omega)\mathrm{d}\omega\right)}{\left(\int \omega h(\omega)\mathrm{d}\omega\right)^2 - \left(\int \omega^2 h(\omega)\mathrm{d}\omega\right)\left(\int h(\omega)\mathrm{d}\omega\right)} \quad \text{(A.7)}$$

By adapting the center and the width of the weighting function $h(\omega)$ it can be assured that the fitting function $g(\omega) = m\omega + n$ fits well in the frequency regions of highest reliability. See Fig. A.1 for an illustration of this effect.

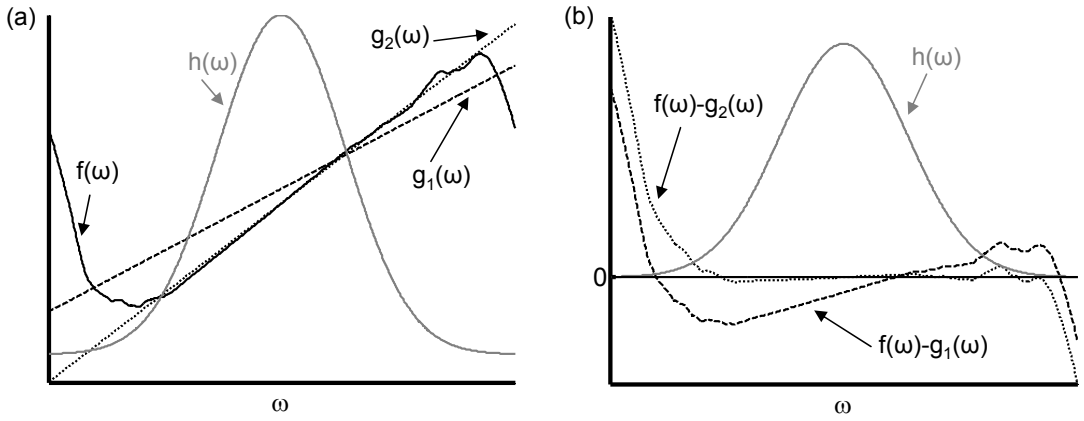

Figure A.1: Weighted fit. (a) Two linear fits of a function $f(\omega)$ (black solid line); one without a weighting function ($g_1(\omega)$ - dashed line) and another one ($g_2(\omega)$ - dotted line) with the weighting function $h(\omega)$ (grey line). (b) Effect of the substraction of these fits from $f(\omega)$: while for the weighted fit $f(\omega) - g_2(\omega)$ (dotted line) lies close to the baseline (solid black line) in the region where the weighting function (grey line) is not negligible, this is not achieved with the non-weighted fit (dashed line).

Appendix B

Orientation measurement with fluorescence anisotropy

To better understand the limits of fluorescence anisotropy for measuring molecular orientations let us consider the following situation: Suppose we have an ensemble of fluorescence dipoles with fixed orientations. If the are embedded in an ordered structure their dipole moments $\boldsymbol{\mu}$ will be oriented around a preferential direction ρ (Fig. B.1). For the sake of simplicity we restrict this study to the case where ρ lies in the (X, Y)-plane. In the molecular coordinate system (x', y', z') the dipole moment $\boldsymbol{\mu}'$ is expressed as a radial unit vector:

$$\boldsymbol{\mu}' = \begin{pmatrix} \mu_{x'} \\ \mu_{y'} \\ \mu_{z'} \end{pmatrix} = \begin{pmatrix} \sin\theta\cos\phi \\ \sin\theta\sin\phi \\ \cos\theta \end{pmatrix} \tag{B.1}$$

where θ designates the angle between $\boldsymbol{\mu}'$ and the z'-axis and ϕ the one between the x'-axis and the projection of $\boldsymbol{\mu}'$ in the (x', y')-plane. Within the macroscopic frame (X, Y, Z) a rotation of the coordinate system has to be performed so that [184]:

$$\boldsymbol{\mu} = \begin{pmatrix} \mu_X \\ \mu_Y \\ \mu_Z \end{pmatrix} = \begin{pmatrix} \cos\rho & 0 & \sin\rho \\ -\sin\rho & 0 & \cos\rho \\ 0 & 1 & 0 \end{pmatrix} \begin{pmatrix} \sin\theta\cos\phi \\ \sin\theta\sin\phi \\ \cos\theta \end{pmatrix} \tag{B.2}$$

But as long as the embedding structure is not a perfect crystal the individual dipoles may take on orientations somewhat different from ρ. We model this with a Heavyside function of the form:

$$f(\theta) = \begin{cases} 1 & \text{if } \theta \leq v \\ 0 & \text{if } \theta > v \end{cases} \tag{B.3}$$

resulting in a cone around ρ with an opening angle $2v$ wherein all orientations are equiprobable. A small v then corresponds to a sample where the dipole moments are strongly aligned as would be expected in a crystal. A large v on the other hand indicates a much higher degree of disorder.

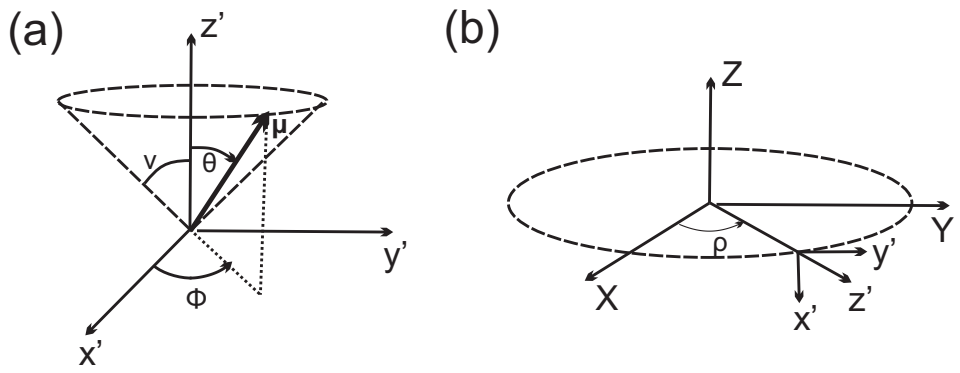

Figure B.1: Geometry of the dipole ensemble. (a) Within a cone of aperture v the orientation of the dipole moments $\boldsymbol{\mu}$ is given by (θ, ϕ), defined in the molecular frame (x', y', z'); (b) orientation of the cone within the macroscopic frame (X, Y, Z).

Further assuming that absorption and emission dipole moments are identical, and that no focussing of the incident field $\mathbf{E}$ is performed, it follows from Eq. (1.50) that the TPF intensity emitted along the direction j can be written as:

$$I_j(\rho, v) = \int_0^{2\pi} \int_0^{\pi} |\boldsymbol{\mu}(\theta, \phi, \rho) \cdot \mathbf{E}|^4 |\mu_j(\theta, \phi, \rho)|^2 f(\theta, v) \sin\theta \mathrm{d}\theta \mathrm{d}\phi \tag{B.4}$$

To assure that the total TPF response does not depend on the orientation ρ of the dipoles we choose a circular polarized laser:

$$\mathbf{E} = \frac{1}{\sqrt{2}} \begin{pmatrix} 1 \\ i \end{pmatrix} \tag{B.5}$$

From the evaluation of Eq. (B.4) it is possible to calculate the anisotropy A of the fluorescence signal via:

$$A = \frac{I_Y - I_X}{I_Y + I_X} \tag{B.6}$$

Fig. B.2 shows the anisotropy with respect to v for several cone orientations ρ. It can be seen that from a standard anisotropy measurement it is possible to deduce the cone aperture v and thus determine the degree of order within the sample as long as the dipoles are oriented around one of the major axes and this orientation ρ is known. But as soon as ρ lies around 45°, no such information can be obtained from this scheme.

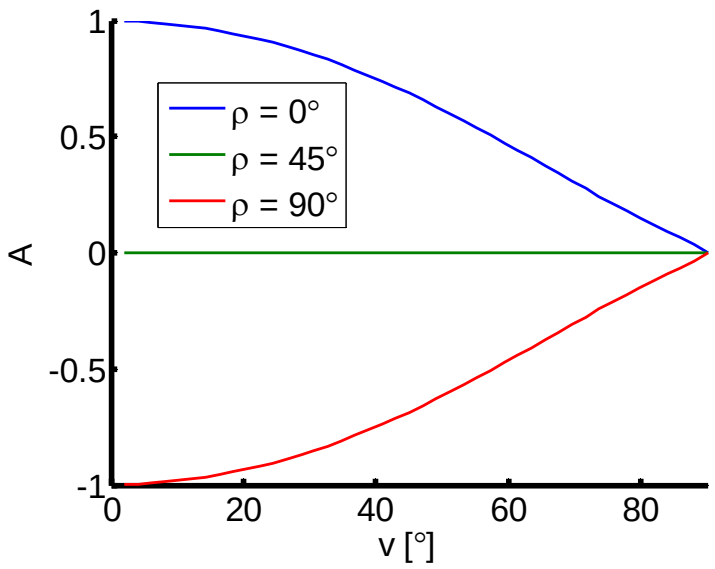

Figure B.2: Dependence of the anisotropy A on the cone aperture v for different cone orientations ρ.

Appendix C

Field propagation in high NA optics

For nonlinear optical microscopy high spatial resolutions are required in imaging. This has led to the widespread use of objectives with high numerical apertures (NA) that strongly focus the excitation laser beam. But this is paid for by an alteration of the polarization and phase profile of the exciting laser which is unique for each point within the focal volume. Consequently the generated nonlinear signals are influenced by this change and if they are collected by the same objective - which is the case for backward detection setups - they suffer as well from this focussing effect. This may lead to serious data misinterpretations if the effect has not been taken into account.

In this appendix we consider the objective as a perfect lens. This is justified even though in reality an objective is a highly sophisticated lens array, because all elements therein serve to reduce the numerous aberrations present in each lens to approach a perfect lens as much as possible. The goal of this appendix is to provide the field expression to be used in an development of a rigorous model for nonlinear optical excitation and radiation.

C.1 Focussing of the exciting field

Before passing an objective the incident beam is most frequently a collimated parallel beam with a 2D Gaussian profile:

$$E_p(\rho) \propto e^{-\left(\frac{\rho}{\sigma}\right)^2} \tag{C.1}$$

with width σ. ρ denotes the radial coordinate normal to the propagation direction. It is related to the focal length f via $\rho = f \sin\theta$ (Fig. C.1a). f in turn can be expressed by the numerical aperture:

$$\mathrm{NA} = n \sin\theta_{max} = \frac{nd}{2f} \tag{C.2}$$

where θ_{max} is the maximal collection angle that is given by the diameter of the lens d. By introducing the objective's coverage parameter $\beta = \frac{d}{2\sigma}$ Eq.(C.1) transforms to:

$$E_p(\theta) \propto e^{-\left(\frac{n\beta \sin\theta}{\mathrm{NA}}\right)^2} \tag{C.3}$$

When an unfocussed laser beam traverses an objective it passes from a plane p to a sphere s whose center is the focal point F. During this process the energy is conserved. The power P transported by a field E is the mean time value of its Poynting vector, thus $P = \frac{1}{2}\sqrt{\frac{\varepsilon_0\varepsilon}{\mu_0\mu}}|E|^2$ [263]. Here ε_0 and μ_0 are the vacuum permittivity and magnetic permeability and ε and μ those of the medium. As at optical frequencies almost all media have $\mu = 1$ the refractive index $n = \sqrt{\varepsilon\mu}$ becomes $n = \sqrt{\varepsilon}$. Assuming that there is no absorption involved when the beam passes from p to s it follows that [208, 264, 209]:

$$P_p \mathrm{d}S_p = P_s \mathrm{d}S_s \tag{C.4}$$

where P_p and P_s is the energy of the field at p and s and $\mathrm{d}S_p$ and $\mathrm{d}S_s$ are infinitesimal area elements of p and s. As these are related via $\mathrm{d}S_p = \mathrm{d}S_s \cos\theta$ the fields on both sides of a focussing objective are related via:

$$E_s = E_p \sqrt{\frac{n_p}{n_s}} \sqrt{\cos\theta} \tag{C.5}$$

Usually there will be air at the entrance of the objective ($n_p = 1$) while at the exit there might be an immersion liquid with a refractive n. Eq. (C.5) then becomes:

$$E_s = E_p \sqrt{\frac{\cos\theta}{n}} \tag{C.6}$$

Before the objective the incident field $\mathbf{E}_p$ has components along the radial and azimuthal directions of a cylindrical coordinate system, denoted by the unit vectors $\mathbf{n}_\rho$ and $\mathbf{n}_\phi$. $\mathbf{E}_p$ can then be decomposed along these two directions:

$$\mathbf{E}_p = (\mathbf{E}_p \cdot \mathbf{n}_\phi)\, \mathbf{n}_\phi + (\mathbf{E}_p \cdot \mathbf{n}_\rho)\, \mathbf{n}_\rho \tag{C.7}$$

After the passage of the objective $\mathbf{E}_s$ is best described in spherical coordinates where its components are along the azimuthal and polar directions ($\mathbf{n}_\phi$ and $\mathbf{n}_\theta$) while it propagates along the radial direction. The azimuthal component is thus not affected by the objective while the radial component gets mapped into $\mathbf{n}_\theta$. Thus the field after the objective $\mathbf{E}_s$ becomes:

$$\mathbf{E}_s = \left[(\mathbf{E}_p \cdot \mathbf{n}_\phi)\, \mathbf{n}_\phi + (\mathbf{E}_p \cdot \mathbf{n}_\rho)\, \mathbf{n}_\theta\right] \sqrt{\frac{\cos\theta}{n}} \tag{C.8}$$

Here we assume that both field components have the same transmission coefficients when passing the objective. In cases where this is not true, each summand has to be multiplied with the corresponding factor. The unit vectors $\mathbf{n}_\rho$, $\mathbf{n}_\phi$ and $\mathbf{n}_\theta$ can be decomposed in terms of the conventional Cartesian unit vectors $\mathbf{n}_x$, $\mathbf{n}_y$ and $\mathbf{n}_z$, using the spherical coordinates θ and ϕ as shown in Fig. C.1b:

$$\begin{aligned} \mathbf{n}_\rho &= \cos\phi\, \mathbf{n}_x + \sin\phi\, \mathbf{n}_y \\ \mathbf{n}_\phi &= -\sin\phi\, \mathbf{n}_x + \cos\phi\, \mathbf{n}_y \\ \mathbf{n}_\theta &= \cos\theta\cos\phi\, \mathbf{n}_x + \cos\theta\sin\phi\, \mathbf{n}_y - \sin\theta\, \mathbf{n}_z \end{aligned} \tag{C.9}$$

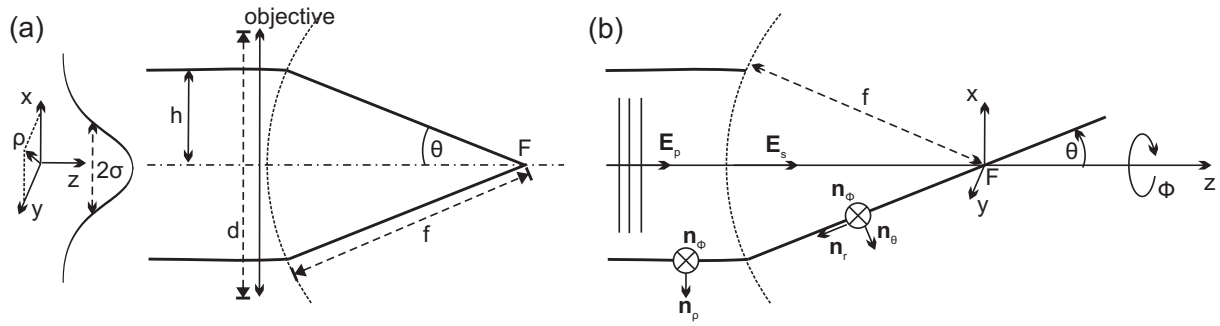

Figure C.1: Focussing of an incident collimated beam. (a) 2D Gaussian beam with variance σ^2 traverses an objective of size d, getting focused by it onto point F, separated from from the reference sphere by the focal distance f; (b) coordinate definitions: Before the objective $\mathbf{E}_p$ has components along $\mathbf{n}_\rho$ and $\mathbf{n}_\phi$ while after the objective $\mathbf{E}_s$ lies along $\mathbf{n}_\theta$ and $\mathbf{n}_\phi$ and propagates against $\mathbf{n}_r$, all of which can be expressed in terms of a Cartesian system centered on F by the spherical coordinates θ and ϕ.

Thus:

$$\begin{aligned}\mathbf{E}_s(\theta,\phi) &= \left[\mathbf{E}_p(\theta,\phi)\cdot\begin{pmatrix}-\sin\phi\\ \cos\phi\\ 0\end{pmatrix}\right]\begin{pmatrix}-\sin\phi\\ \cos\phi\\ 0\end{pmatrix}\sqrt{\frac{\cos\theta}{n}}\\ &+ \left[\mathbf{E}_p(\theta,\phi)\cdot\begin{pmatrix}\cos\phi\\ \sin\phi\\ 0\end{pmatrix}\right]\begin{pmatrix}\cos\theta\cos\phi\\ \cos\theta\sin\phi\\ -\sin\theta\end{pmatrix}\sqrt{\frac{\cos\theta}{n}}\end{aligned} \tag{C.10}$$

Under the assumption that the beam propagates in a homogeneous medium from the exit of the objective to the focal point F - which is justified because this space will be either occupied by air or by a homogeneous immersion liquid - we can decompose the field in plane waves:

$$\mathrm{E}(x,y,z) = \int\int_{-\infty}^{\infty}\hat{\mathrm{E}}(k_x,k_y,0)\,e^{i(k_x x+k_y y\pm k_z z)}\mathrm{d}k_x\mathrm{d}k_y \tag{C.11}$$

with the wave vector

$$\mathbf{k} = k\mathbf{n}_r = \frac{2\pi}{\lambda}\begin{pmatrix}\sin\theta\cos\phi\\ \sin\theta\sin\phi\\ \cos\theta\end{pmatrix} \tag{C.12}$$

along the propagation direction $\mathbf{n}_r$. $\hat{\mathrm{E}}$ is related to $\mathbf{E}_s$ via:

$$\hat{\mathrm{E}}(k_x,k_y,0) = \frac{ire^{-ikr}}{2\pi k_z}\mathbf{E}_s(k_x,k_y) \tag{C.13}$$

when placing the coordinate origin at F and r being the distance from this point. Replacing the differentials by $\frac{1}{k_z}\mathrm{d}k_x\mathrm{d}k_y = k\sin\theta\,\mathrm{d}\theta\mathrm{d}\phi$ and performing the integration only over the

numerical aperture of the objective Eq. (C.11) then transforms to:

$$\mathbf{E}(x,y,z) \propto \int_0^{2\pi} \int_0^{\theta_{max}} \mathbf{E}_s(\theta,\phi) e^{i(\mathbf{k}\cdot\mathbf{r})} \sin\theta \mathrm{d}\theta \mathrm{d}\phi \tag{C.14}$$

with

$$\mathbf{k}\cdot\mathbf{r} = \frac{2\pi}{\lambda}\left[\sin\theta(x\cos\phi + y\sin\phi) + z\cos\theta\right] \tag{C.15}$$

C.2 Collection of the generated signal

Each nonlinear dipole in the vicinity of the focus $\mathbf{r} = (x,y,z)$ radiates a field $\mathbf{P}$ dependent on the incident field $\mathbf{E}$ at its location, calculated with Eq. (C.14). In the case of epi-detected signals, only those parts of the radiation are collected that fall within the numerical aperture of the objective, that is only those $\mathbf{k}(\theta,\phi)$ for which $\theta \leq \theta_{max}$. The radiation follows the normal dipole radiation pattern:

$$\mathbf{P}_s(\theta,\phi,\mathbf{r}) \propto -\frac{k^2}{r_d} e^{iknr_d}\left[\mathbf{n}_{rd}(\mathbf{n}_{rd}\cdot\mathbf{P}(\mathbf{r})) - \mathbf{P}(\mathbf{r})\right] \tag{C.16}$$

Here, r_d is the distance from the location of a dipole at $\mathbf{r}$ to a certain point $f\mathbf{n}_r$ on the reference sphere at the entrance of the objective and $\mathbf{n}_{rd}$ the unit vector in that direction.

$$\mathbf{n}_{rd} = \frac{f\mathbf{n}_r - \mathbf{r}}{|f\mathbf{n}_r - \mathbf{r}|} = \frac{f\mathbf{n}_r - \mathbf{r}}{r_d} \tag{C.17}$$

$k = \frac{2\pi}{\lambda_{signal}}$ may be different from the wave vector of the excitation as in nonlinear optics the generated signal often has a different wavelength than the generating field.

If the nonlinear process is a coherent one all these fields originating from the different dipole positions $\mathbf{r}$ have to be propagated independently towards the reference sphere. From there the field traverses again the objectives and the unit vector $\mathbf{n}_\theta$ gets mapped into the unit vector $\mathbf{n}_\rho$ and in analogy to Eq. (C.8) one obtains:

$$\mathbf{P}_p(\theta,\phi,\mathbf{r}) = \left[(\mathbf{P}_s\cdot\mathbf{n}_\phi)\,\mathbf{n}_\phi + (\mathbf{P}_s\cdot\mathbf{n}_\theta)\,\mathbf{n}_\rho\right]\sqrt{\frac{n}{\cos\theta}} \tag{C.18}$$

resulting in:

$$\begin{aligned}\mathbf{P}_p(\theta,\phi,\mathbf{r}) &= \left[\mathbf{P}_s(\theta,\phi,\mathbf{r})\cdot\begin{pmatrix}-\sin\phi\\ \cos\phi\\ 0\end{pmatrix}\right]\begin{pmatrix}-\sin\phi\\ \cos\phi\\ 0\end{pmatrix}\sqrt{\frac{n}{\cos\theta}} \\ &+ \left[\mathbf{P}_s(\theta,\phi,\mathbf{r})\cdot\begin{pmatrix}\cos\theta\cos\phi\\ \cos\theta\sin\phi\\ -\sin\theta\end{pmatrix}\right]\begin{pmatrix}\cos\phi\\ \sin\phi\\ 0\end{pmatrix}\sqrt{\frac{n}{\cos\theta}}\end{aligned} \tag{C.19}$$

This can present a considerable computational effort especially when a large number of radiating dipoles are considered. In many cases, however, this is not necessary. The focal

volume when using high NA objectives is of the order of $0.3 \times 0.3 \times 1\,\mu\mathrm{m}^3$. Dipoles far outside this region do not radiate, especially not in a nonlinear way as the field strengths are too small there. On the other hand the focal length of such objectives is of the order of 0.5 cm, thus $\frac{|\mathbf{r}_i|}{f} < 10^{-4}$. Thus $r_d \approx f$, which means that all dipoles are considered to be located at the same position. This allows the summation of all the fields $\mathbf{P}(\mathbf{r}_i)$ before the total field gets radiated according to Eqn. (C.16) and (C.18).

Bibliography

[1] C. H. Townes, *A Century of Nature: Twenty-One Discoveries that Changed Science and the World: The first laser.* (University of Chicago Press, 2003).

[2] F. Krausz and M. Ivanov, "Attosecond physics." Rev. Mod. Phys. **81**, 163–234 (2009).

[3] J. J. Hopfield, J. M. Worlock, and K. Park, "Two-Quantum Absorption Spectrum of KI." Phys. Rev. Lett. **11**, 414–417 (1963).

[4] J. J. Hopfield and J. M. Worlock, "Two-Quantum Absorption Spectrum of KI and CsI." Phys. Rev. **137**, A1455–A1464 (1965).

[5] R. F. Begley, A. B. Harvey, and R. L. Byer, "Coherent anti-Stokes Raman spectroscopy." Appl. Phys. Lett. **25**, 387–390 (1974).

[6] R. Hellwarth and P. Christensen, "Nonlinear optical microscopic examination of structure in polycrystalline ZnSe." Opt. Commun. **12**, 318–322 (1974).

[7] J. N. Gannaway and C. J. R. Sheppard, "Second-harmonic imaging in the scanning optical microscope." Opt. Quantum. Electron. **10**, 435–439 (1978).

[8] I. Freund, M. Deutsch, and A. Sprecher, "Optical Second-harmonic Microscopy, Crossed-beam Summation, and Small-angle Scattering in Rat-tail Tendon." Biophys. J. **50**, 693–712 (1986).

[9] A. Zumbusch, G. R. Holtom, and X. S. Xie, "Three-dimensional vibrational imaging by coherent anti-Stokes Raman scattering." Phys. Rev. Lett. **82**, 4142–4145 (1999).

[10] W. Denk, J. H. Strickler, and W. W. Webb, "2-Photon Laser Scanning Fluorescence Microscopy." Science **248**, 73–76 (1990).

[11] L. Moreaux, O. Sandre, S. Charpak, M. Blanchard-Desce, and J. Mertz, "Coherent Scattering in Multi-Harmonic Light Microscopy." Biophys. J. **80**, 1568–1574 (2001).

[12] F. Helmchen and W. Denk, "Deep tissue two-photon microscopy." Nat. Methods **2**, 932–940 (2005).

[13] W. Supatto, D. Débarre, B. Moulia, E. Brouzés, J.-L. Martin, E. Farge, and E. Beaurepaire, "*In vivo* modulation of morphogenetic movements in Drosophila embryos with femtosecond laser pulses." Proc. Natl. Acad. Sci. U. S. A. **102**, 1047–1052 (2005).

[14] T. Boulesteix, A.-M. Pena, N. Pagès, G. Godeau, M.-P. Sauviat, E. Beaurepaire, and M.-C. Schanne-Klein, "Micrometer scale *Ex Vivo* multiphoton imaging of unstained arterial wall structure." Cytometry **69A**, 20–26 (2006).

[15] A. J. Radosevich, M. B. Bouchard, S. A. Burgess, B. R. Chen, and E. M. C. Hillman, "Hyperspectral *in vivo* two-photon microscopy of intrinsic contrast." Opt. Lett. **33**, 2164–2166 (2008).

[16] R. Trebino, K. W. DeLong, D. N. Fittinghoff, J. N. Sweetser, M. A. Krumbügel, B. A. Richman, and D. J. Kane, "Measuring ultrashort laser pulses in the time-frequency domain using frequency-resolved optical gating," Rev. Sci. Instrum. **68**, 3277–3295 (1997).

[17] C. Iaconis and I. A. Walmsley, "Spectral phase interferometry for direct electric-field reconstruction of ultrashort optical pulses." Opt. Lett. **23**, 792–794 (1998).

[18] C. Dorrer, B. de Beauvoir, C. L. Blanc, S. Ranc, J.-P. Rousseau, P. Rousseau, J.-P. Chambaret, and F. Salin, "Single-shot real-time characterization of chirped-pulse amplification systems by spectral phase interferometry for direct electric-field reconstruction." Opt. Lett. **24**, 1644–1646 (1999).

[19] L. Gallmann, D. H. Sutter, N. Matuschek, G. Steinmeyer, U. Keller, C. Iaconis, and I. A. Walmsley, "Characterization of sub-6-fs optical pulses with spectral phase interferometry for direct electric-field reconstruction." Opt. Lett. **24**, 1314–1316 (1999).

[20] J. M. D. Cruz, I. Pastirk, V. V. Lozovoy, K. A. Walowicz, and M. Dantus, "Multiphoton Intrapulse Interference 3: Probing Microscopic Chemical Environments." J. Phys. Chem. A **108**, 53–58 (2004).

[21] V. V. Lozovoy, I. Pastirk, and M. Dantus, "Multiphoton intrapulse interference. IV. Ultrashort laser pulse spectral phase characterization and compensation," Opt. Lett. **29**, 775–777 (2004).

[22] D. J. Tannor, R. Kosloff, and S. A. Rice, "Coherent pulse sequence Induced control of selectivity of reactions: Exact quantum mechanical calculations." J. Chem. Phys. **85**, 5805–5820 (1986).

[23] A. M. Weiner, J. P. Heritage, and E. M. Kirschner, "High-resolution femtosecond pulse shaping." J. Opt. Soc. Am. B **5**, 1563–1572 (1988).

[24] C. W. Hillegas, J. X. Tull, D. Goswami, D. Strickland, and W. S. Warren, "Femtosecond laser pulse shaping by use of microsecond radio-frequency pulses." Opt. Lett. **19**, 737–739 (1994).

[25] M. A. Dugan, J. X. Tull, and W. S. Warren, "High-resolution acousto-optic shaping of unamplified and amplified femtosecond laser pulses." J. Opt. Soc. Am. B **14**, 2348–2358 (1997).

[26] Y. Ding, R. M. Brubaker, D. D. Nolte, M. R. Melloch, and A. M. Weiner, "Femtosecond pulse shaping by dynamic holograms in photorefractive multiple quantum wells." Opt. Lett. **22**, 718–720 (1997).

[27] W. S. Warren, H. Rabitz, and M. Dahleh, "Coherent Control of Quantum Dynamics: The Dream Is Alive." Science **259**, 1581–1589 (1993).

[28] E. Zeek, K. Maginnis, S. Backus, U. Russek, M. Murnane, G. Mourou, H. Kapteyn, and G. Vdovin, "Pulse compression by use of deformable mirrors." Opt. Lett. **24**, 493–495 (1999).

[29] D. Meshulach and Y. Silberberg, "Coherent quantum control of two-photon transitions by a femtosecond laser pulse," Nature **396**, 239–242 (1998).

[30] M. Dantus and V. V. Lozovoy, "Experimental Coherent Laser Control of Physicochemical Processes," Chem. Rev. **104**, 1813–1859 (2004).

[31] V. V. Lozovoy and M. Dantus, "Systematic control of nonlinear optical processes using optimally shaped femtosecond pulses." Chem. Phys. Chem. **6**(10), 1970–2000 (2005).

[32] M. I. Stockman, D. J. Bergman, and T. Kobayashi, "Coherent control of nanoscale localization of ultrafast optical excitation in nanosystems," Phys. Rev. B **69**, 54,202 (2004).

[33] T. Baumert, T. Brixner, V. Seyfried, M. Strehle, and G. Gerber, "Femtosecond pulse shaping by an evolutionary algorithmwith feedback," Appl. Phys. B **65**, 779–782 (1997).

[34] T. Brixner, M. Strehle, and G. Gerber, "Feedback-controlled optimization of amplified femtosecond laser pulses," Appl. Phys. B **68**, 281–284 (1999).

[35] T. Brixner, A. Oehrlein, M. Strehle, and G. Gerber, "Feedback-controlled femtosecond pulse shaping," Appl. Phys. B **70**, S119–S124 (2000).

[36] P. Xi, Y. Andegeko, L. R. Weisel, V. V. Lozovoy, and M. Dantus, "Greater signal, increased depth, and less photobleaching in two-photon microscopy with 10 fs pulses." Opt. Commun. **281**, 1841–1849 (2008).

[37] N. Dudovich, D. Oron, and Y. Silberberg, "Single-pulse coherently controlled nonlinear Raman spectroscopy and microscopy." Nature **418**, 512–514 (2002).

[38] N. Dudovich, D. Oron, and Y. Silberberg, "Single-pulse coherent anti-Stokes Raman spectroscopy in the fingerprint spectral region." J. Chem. Phys. **118**, 9208–9215 (2003).

[39] D. Oron, N. Dudovich, and Y. Silberberg, "Single-Pulse Phase-Contrast Nonlinear Raman Spectroscopy," Phys. Rev. Lett. **89**, 273,001 (2002).

[40] B.-C. Chen and S.-H. Lim, "Optimal Laser Pulse Shaping for Interferometric Multiplex Coherent Anti-Stokes Raman Scattering Microscopy." J. Phys. Chem. B **112**, 3653–3661 (2008).

[41] W. Min, S. Lu, G. R. Holtom, and X. S. Xie, "Triple-Resonance Coherent Anti-Stokes Raman Scattering Microspectroscopy." ChemPhysChem **10**, 344–347 (2009).

[42] W. Min, S. Lu, M. Rueckel, G. R. Holtom, and X. S. Xie, "Near-Degenerate Four-Wave-Mixing Microscopy." Nano Letters **9**, 2423–2426 (2009).

[43] T. Brixner and G. Gerber, "Femtosecond polarization pulse shaping," Opt. Lett. **26**, 557–559 (2001).

[44] T. Brixner, G. Krampert, P. Niklaus, and G. Gerber, "Generation and characterization of polarization-shaped femtosecond laser pulses," Appl. Phys. B **74**, S133–S144 (2002).

[45] T. Brixner, "Poincaré representation of polarization-shaped femtosecond laser pulses," Appl. Phys. B **76**, 531–540 (2003).

[46] G. Krampert, "Femtosecond Quantum Control and Adaptive Polarization Pulse Shaping," Ph.D. thesis, Julius-Maximilians-Universität Würzburg (2004).

[47] T. Brixner, G. Krampert, T. Pfeifer, R. Selle, G. Gerber, M. Wollenhaupt, O. Graefe, C. Horn, D. Liese, and T. Baumert, "Quantum control by ultrafast polarization shaping," Phys. Rev. Lett. **92**, 208,301 (2004).

[48] T. Suzuki, S. Minemoto, T. Kanai, and H. Sakai, "Optimal control of multiphoton ionization processes in aligned I-2 molecules with time-dependent polarization pulses," Phys. Rev. Lett. **92**, 133,005 (2004).

[49] D. Oron, N. Dudovich, and Y. Silberberg, "Femtosecond Phase-and-Polarization Control for Background-Free Coherent Anti-Stokes Raman Spectroscopy," Phys. Rev. Lett. **90**, 213,902 (2003).

[50] S.-H. Lim, A. G. Caster, O. Nicolet, and S. R. Leone, "Chemical Imaging by Single Pulse Interferometric Coherent Anti-Stokes Raman Scattering Microscopy." J. Phys. Chem. B **110**, 5196–5204 (2006).

[51] N. Dudovich, D. Oron, and Y. Silberberg, "Quantum Control of the Angular Momentum Distribution in Multiphoton Absorption Processes," Phys. Rev. Lett. **92**, 103,003 (2004).

[52] L. Polachek, D. Oron, and Y. Silberberg, "Full control of the spectral polarization of ultrashort pulses," Opt. Lett. **31**, 631–633 (2006).

[53] M. Plewicki, F. Weise, S. M. Weber, and A. Lindinger, "Phase, amplitude, and polarization shaping with a pulse shaper in a Mach-Zehnder interferometer." Appl. Opt. **45**, 8354–8359 (2006).

[54] S. M. Weber, F. Weise, M. Plewicki, and A. Lindinger, "Interferometric generation of parametrically shaped polarization pulses," Appl. Opt. **46**, 5987–5990 (2007).

[55] M. Ninck, A. Galler, T. Feurer, and T. Brixner, "Programmable common-path vector field synthesizer for femtosecond pulses." Opt. Lett. **32**, 3379–3381 (2007).

[56] T. Brixner, F. G. de Abajo, J. Schneider, and W. Pfeiffer, "Nanoscopic Ultrafast Space-Time-Resolved Spectroscopy," Phys. Rev. Lett. **95**, 93,901 (2005).

[57] T. Brixner, F. G. de Abajo, C. Spindler, and W. Pfeiffer, "Adaptive ultrafast nanooptics in a tight focus," Appl. Phys. B **84**, 89–95 (2006).

[58] T. Brixner, F. G. de Abajo, J. Schneider, C. Spindler, and W. Pfeiffer, "Ultrafast adaptive optical near-field control," Phys. Rev. B **73**, 125,437 (2006).

[59] M. Aeschlimann, M. Bauer, D. Bayer, T. Brixner, F. J. G. de Abajo, W. Pfeiffer, M. Rohmer, C. Spindler, and F. Steeb, "Adaptive subwavelength control of nanooptical fields." Nature **446**(7133), 301–304 (2007).

[60] J. C. Maxwell, *A Treatise on Electricity and Magnetism.* (Clarendon Press, Oxford, 1873).

[61] Y. R. Shen, *The Principles of Nonlinear Optics.* (Wiley Interscience, 2003).

[62] F. Sanchez, *Optique non-linéaire.* (ellipses, 1999).

[63] P. N. Butcher and D. Cotter, *The Elements of Nonlinear Optics.* (Cambridge University Press, 1990).

[64] "Refractive Indix Database." URL `http://refractiveindex.info/`.

[65] L. G. Gouy, "Sur une propriété nouvelle des ondes lumineuses." Compt. Rendue Acad. Sci. Paris **110**, 1251 (1890).

[66] L. G. Gouy, "Sur la propagation anormale des ondes." Compt. Rendue Acad. Sci. Paris **111**, 33 (1890).

[67] J. Squier and M. Müller, "High resolution nonlinear microscopy: A review of sources and methods for achieving optimal imaging." Rev. Sci. Instrum. **72**, 2856–2867 (2001).

[68] J. Mertz, "Nonlinear microscopy," C. R. Acad. Sci. Paris **2**, 1153–1160 (2001).

[69] M. Strupler, M. Hernest, C. Fligny, J.-L. Martin, P.-L. Tharaux, and M.-C. Schanne-Klein, "Second harmonic microscopy to quantify renal interstitial fibrosis and arterial remodeling." J. Biomed. Opt. **13**, 054,041 (2008).

[70] P. A. Franken, A. E. Hill, C. W. Peters, and G. Weinreich, "Generation of optical harmonics." Phys. Rev. Lett. **7**, 118–119 (1961).

[71] C. K. Chen, T. F. Heinz, D. Ricard, and Y. R. Shen, "Equilibrium and transient study of adsorption of pyridine on silver in an electrolytic solution," Chem. Phys. Lett. **83**, 455–458 (1981).

[72] S. Roth and I. Freund, "Optical second-harmonic scattering in rat-tail tendon." Biopolymers **20**, 1271–1290 (1981).

[73] P. J. Campagnola, M. D. Wei, A. Lewis, and L. M. Loew, "High-resolution nonlinear optical imaging of live cells by second harmonic generation." Biophys. J. **77**(6), 3341–3349 (1999).

[74] L. Moreaux, O. Sandre, and J. Mertz, "Membrane imaging by second harmonic generation," J. Opt. Soc. Am. B **17**, 1685–1694 (2000).

[75] M. Flörsheimer, M. Bösch, C. Brillert, M. Wierschem, and H. Fuchs, "Second-Harmonic Microscopy - A Quantitative Probe for Molecular Surface Order," Adv. Mater. **9**, 1061–1065 (1997).

[76] C. Anceau, S. Brasselet, and J. Zyss, "Local orientational distribution of molecular monolayers probed by nonlinear microscopy," Chem. Phys. Lett. **411**, 98–102 (2005).

[77] M. Flörsheimer, R. Paschotta, U. Kubitscheck, C. Brillert, D. Hofmann, L. Heuer, G. Schreiber, C. Verbeek, W. Sohler, and H. Fuchs, "Second-harmonic imaging of ferroelectric domains in LiNbO3 with micron resolution in lateral and axial directions." Appl. Phys. B **67**, 593–599 (1998).

[78] Y. Shen, P. Markowicz, J. Winiarz, J. Swiatkiewicz, and P. N. Prasad, "Nanoscopic study of second-harmonic generation in organic crystals with collection-mode near-field scanning optical microscopy," Opt. Lett. **26**, 725–727 (2001).

[79] S. Brasselet, V. L. Floc'h, F. Treussart, J.-F. Roch, J. Zyss, E. Botzung-Appert, and A. Ibanez, "*In Situ* Diagnostics of the Crystalline Nature of Single Organic Nanocrystals by Nonlinear Microscopy," Phys. Rev. Lett. **92**, 207,401 (2004).

[80] R. LaComb, O. Nadiarnykh, and P. J. Campagnola, "Quantitative second harmonic generation imaging of the diseased state osteogenesis imperfecta: experiment and simulation." Biophys. J. **94**(11), 4504–4514 (2008).

[81] T. Yasui, Y. Takahashi, M. Ito, S. Fukushima, and T. Araki, "*Ex vivo* and *in vivo* second-harmonic-generation imaging of dermal collagen fiber in skin: comparison of imaging characteristics between mode-locked Cr:forsterite and Ti:sapphire lasers," Appl. Opt. **48**, D88–D95 (2009).

[82] D. A. Dombeck, K. A. Kasischke, H. D. Vishwasrao, M. Ingelsson, B. T. Hyman, and W. W. Webb, "Uniform polarity microtubule assemblies imaged in native brain tissue by second-harmonic generation microscopy." Proc. Natl. Acad. Sci. U. S. A. **100**(12), 7081–7086 (2003).

[83] E. Ralston, B. Swaim, M. Czapiga, W.-L. Hwu, Y.-H. Chien, M. G. Pittis, B. Bembi, O. Schwartz, P. Plotz, and N. Raben, "Detection and imaging of non-contractile inclusions and sarcomeric anomalies in skeletal muscle by second harmonic generation combined with two-photon excited fluorescence." J. Struct. Biol. **162**(3), 500–508 (2008).

[84] K. Yoshiki, M. Hashimoto, and T. Araki, "Second-harmonic-generation microscopy using excitation beam with controlled polarization pattern to determine three-dimensional molecular orientation." Jap. J. Appl. Phys. **44**, L1066–L1068 (2005).

[85] K. Yoshiki, K. Ryosuke, M. Hashimoto, N. Hashimoto, and T. Araki, "Second-harmonic-generation microscope using eight-segment polarization-mode converter to observe three-dimensional molecular orientation." Opt. Lett. **32**, 1680–1682 (2007).

[86] E. Yew and C. Sheppard, "Second harmonic generation polarization microscopy with tightly focused linearly and radially polarized beams." Opt. Commun. **275**, 453–457 (2007).

[87] S. Brasselet and J. Zyss, "Nonlinear polarimetry of molecular crystals down to the nanoscale," C. R. Phys. **8**, 165–179 (2007).

[88] V. L. Floc'h, S. Brasselet, J. Zyss, B. Cho, S. Lee, S. Jeon, M. Cho, K. Min, and M. Suh, "High efficiency and quadratic nonlinear optical properties of a fully optimized 2-D octupolar crystal by nonlinear microscopy." Adv. Mater. **17**, 196–200 (2005).

[89] K. Komorowska, S. Brasselet, J. Zyss, L. Pourlsen, M. Jazdzyk, H. J. Egelhaaf, J. Gierschner, and M. Hanack, "Nanometric scale investigation of the nonlinear efficiency of perhydrotriphynylene inclusion compounds," Chem. Phys. **318**, 12–20 (2005).

[90] V. L. Floc'h, S. Brasselet, J.-F. Roch, and J. Zyss, "Monitoring of Orientation in Molecular Ensembles by Polarization Sensitive Nonlinear Microscopy," J. Phys. Chem. B **107**, 12,403–12,410 (2003).

[91] P. Stoller, K. M. Reiser, P. M. Celliers, and A. M. Rubenchik, "Polarization-modulated second harmonic generation in collagen." Biophys. J. **82**(6), 3330–3342 (2002).

[92] T. Yasui, Y. Tohno, and T. Araki, "Determination of collagen fiber orientation in human tissue by use of polarization measurement of molecular second-harmonic-generation light ." Appl. Opt. **43**, 2861–2867 (2004).

[93] T. Yasui, K. Sasaki, Y. Tohno, and T. Araki, "Tomographic imaging of collagen fiber orientation in human tissue using depth-resolved polarimetry of second-harmonic-generation light." Opt. Quantum. Electron. **37**, 1397–1408 (2005).

[94] R. M. Williams, W. R. Zipfel, and W. W. Webb, "Interpreting second-harmonic generation images of collagen I fibrils." Biophys. J. **88**(2), 1377–1386 (2005).

[95] C. Odin, Y. L. Grand, A. Renault, L. Gailhouste, and G. Baffet, "Orientation fields of nonlinear biological fibrils by second harmonic generation microscopy." J. Microsc. **229**(Pt 1), 32–38 (2008).

[96] E. J. Gualtieri, L. M. Haupert, and G. J. Simpson, "Interpreting nonlinear optics of biopolymer assemblies: Finding a hook," Chem. Phys. Lett. **465**, 167–174 (2008).

[97] D. Débarre, W. Supatto, and E. Beaurepaire, "Structure sensitivity in third-harmonic generation microscopy." Opt. Lett. **30**, 2134–2136 (2005).

[98] D. Débarre, W. Supatto, A.-M. Pena, A. Fabre, T. Tordjmann, L. Combettes, M.-C. Schanne-Klein, and E. Beaurepaire, "Imaging lipid bodies in cells and tissues using third-harmonic generation microscopy." Nat. Methods **3**, 47–53 (2006).

[99] D. Oron, D. Yelin, E. Tal, S. Raz, R. Fachima, and Y. Silberberg, "Depth-resolved structural imaging by third-harmonic generation microscopy." J. Struct. Biol. **147**, 3–11 (2004).

[100] D. Oron, E. Tal, and Y. Silberberg, "Depth-resolved multiphoton polarization microscopy by third-harmonic generation." Opt. Lett. **28**, 2315–2317 (2003).

[101] O. Masihzadeh, P. Schlup, and R. A. Bartels, "Enhanced spatial resolution in third-harmonic microscopy through polarization switching." Opt. Lett. **34**, 1240–1242 (2009).

[102] G. Landsberg and L. Mandelstam, "Eine neue Erscheinung bei der Lichtzerstreuung in Krystallen." Naturwissenschaften **16**, 557 (1928).

[103] C. Raman and K. Krishnan, "A New Type of Secondary Radiation." Nature **121**, 501–502 (1928).

[104] D. Gachet, "Microscopie CARS (Coherent anti-Stokes Raman scattering). Génération du signal au voisinage d'interfaces et à l'intérieur d'une cavité Fabry-Pérot." Ph.D. thesis, Université Paul Cézanne - Aix-Marseille III (2007).

[105] M. Müller and J. M. Schins, "Imaging the thermodynamic state of lipid membranes with multiplex CARS microscopy." J. Phys. Chem. B **106**, 3715–3723 (2002).

[106] P. D. Maker and R. W. Terhune, "Study of Optical Effects Due to an Induced Polarization Third Order in the Electric Field Strength." Phys. Rev. **137**, A801–A818 (1965).

[107] P. R. Régnier and J. P.-E. Taran, "On the possibility of measuring gas concentrations by stimulated anti-Stokes scattering." Appl. Phys. Lett. **23**, 240–242 (1973).

[108] M. D. Duncan, J. Reintjes, and T. J. Manuccia, "Scanning coherent anti-Stokes Raman microscope." Opt. Lett. **7**, 350–352 (1982).

[109] E. O. Potma and X. S. Xie, "Direct visualization of lipid phase segregation in single lipid bilayers with coherent anti-Stokes Raman scattering microscopy." ChemPhysChem **6**, 77–79 (2005).

[110] H. Wang, Y. Fu, P. Zickmund, R. Shi, and J.-X. Cheng, "Coherent Anti-Stokes Raman Scattering Imaging of Axonal Myelin in Live Spinal Tissues." Biophys. J. **89**, 581–591 (2005).

[111] X. L. Nan, J. X. Cheng, and X. S. Xie, "Vibrational imaging of lipid droplets in live fibroblast cells with coherent anti-Stokes Raman scattering microscopy." J. Lipid Res. **44**, 2202–2208 (2003).

[112] C. L. Evans, E. O. Potma, M. Puoris'haag, D. Cote, C. P. Lin, and X. S. Xie, "Chemical imaging of tissue in vivo with video-rate coherent anti-Stokes Raman scattering microscopy." Proc. Natl. Acad. Sci. U. S. A. **102**, 16,807–16,812 (2005).

[113] X. Nan, E. O. Potma, and X. S. Xie, "Nonperturbative Chemical Imaging of Organelle Transport in Living Cells with Coherent Anti-Stokes Raman Scattering Microscopy ." Biophys. J. **91**, 728–735 (2006).

[114] J. J. Song, G. L. Eesley, and M. D. Levenson, "Background suppression in coherent Raman spectroscopy." Appl. Phys. Lett. **29**, 567–569 (1976).

[115] J.-X. Cheng, L. D. Book, and X. S. Xie, "Polarization coherent anti-Stokes Raman scattering microscopy." Opt. Lett. **26**, 1341–1343 (2001).

[116] F. M. Kamga and M. G. Sceats, "Pulse-sequenced coherent anti-Stokes Raman scattering spectroscopy: a method for suppression of the nonresonant background." Opt. Lett. **5**, 126–128 (1980).

[117] A. Volkmer, L. D. Book, and X. S. Xie, "Time-resolved coherent anti-Stokes Raman scattering microscopy: Imaging based on Raman free induction decay." Appl. Phys. Lett. **80**, 1505–1507 (2002).

[118] C. L. Evans, E. O. Potma, and X. S. Xie, "Coherent anti-Stokes Raman scattering spectral interferometry: determination of the real and imaginary components of nonlinear susceptibility $\chi^{(3)}$ for vibrational microscopy." Opt. Lett. **29**, 2923–2935 (2004).

[119] E. O. Potma, C. L. Evans, and X. S. Xie, "Heterodyne coherent anti-Stokes Raman scattering (CARS) imaging." Opt. Lett. **31**, 241–243 (2006).

[120] D. L. Marks, C. Vinegoni, J. S. Bredfeldt, and S. A. Boppart, "Interferometric differentiation between resonant coherent anti-Stokes Raman scattering and nonresonant four-wave-mixing processes." Appl. Phys. Lett. **85**, 5787–5789 (2004).

[121] J.-X. Cheng, A. Volkmer, L. D. Book, and X. S. Xie, "Multiplex Coherent anti-Stokes Raman Scattering Microspectroscopy and Study of Lipid Vesicles." J. Phys. Chem. B **106**, 8493–8498 (2002).

[122] T. Hellerer, A. M. K. Enejder, and A. Zumbusch, "Spectral focusing: High spectral resolution spectroscopy with broad-bandwidth laser pulses." Appl. Phys. Lett. **85**, 25–27 (2004).

[123] K. P. Knutsen, J. C. Johnson, A. E. Miller, P. B. Petersen, and R. J. Saykally, "High spectral resolution multiplex CARS spectroscopy using chirped pulses." Chem. Phys. Lett. **387**, 436–441 (2004).

[124] K. P. Knutsen, B. M. Messer, R. M. Onorato, and R. J. Saykally, "Chirped coherent anti-Stokes Raman scattering for high spectral resolution spectroscopy and chemically selective imaging." J. Phys. Chem. B **110**, 5854–5864 (2006).

[125] E. R. Andresen, H. N. Paulsen, V. Birkedal, J. Thøgersen, and S. R. Keiding, "Broadband multiplex coherent anti-Stokes Raman scattering microscopy employing photonic-crystal fibers." J. Opt. Soc. Am. B **22**, 1934–1938 (2005).

[126] D. Oron, N. Dudovich, D. Yelin, and Y. Silberberg, "Quantum control of coherent anti-Stokes Raman processes." Phys. Rev. A **65**, 043,408 (2002).

[127] D. Oron, N. Dudovich, D. Yelin, and Y. Silberberg, "Narrow-Band Coherent Anti-Stokes Raman Signals from Broad-Band Pulses." Phys. Rev. Lett. **88**, 063,004 (2002).

[128] J. R. Lakowicz, *Principles of Fluorescence Spectroscopy.* (Kluwer Academic, 1999).

[129] J. Franck and E. G. Dymond, "Elementary processes of photochemical reactions." Trans. Faraday Soc. **21**, 536–542 (1926).

[130] E. Condon, "A Theory of Intensity Distribution in Band Systems." Phys. Rev. **28**, 1182–1201 (1926).

[131] M. Kasha, "Characterization of Electronic Tansitions in Complex Molecules." Discuss. Faraday Soc. **9**, 14–19 (1950).

[132] W. Kaiser and C. G. B. Garrett, "Two-photon Excitation in CaF_2:Eu^{2+}." Phys. Rev. Lett. **7**, 229–232 (1961).

[133] R. K. P. Benninger, B. Önfelt, M. A. A. Neil, D. M. Davis, and P. M. W. French, "Fluorescence Imaging of Two-Photon Linear Dichroism: Cholesterol Depletion Disrupts Molecular Orientation in Cell Membranes." Biophys. J. **88**, 609–622 (2005).

[134] A.-M. Pena, T. Boulesteix, T. Dartigalongue, M. Strupler, E. Beaurepaire, and M.-C. Schanne-Klein, "Chiroptical Effects in the Second Harmonic Generation from Collagens I and IV: Applications in Nonlinear Microscopy." Nonlinear Opt. Quantum Opt. **35**, 235–240 (2006).

[135] O. E. Martinez, "Grating and prism compressors in the case of finite beam size." J. Opt. Soc. Am. B **3**, 929–934 (1986).

[136] M. Kakehata, R. Ueda, H. Takada, K. Torizuka, and M. Obara, "Combination of high-intensity femtosecond laser pulses for generation of time-dependent polarization pulses and ionization of atomic gas," Appl. Phys. B **70**, S207–S213 (2000).

[137] D. Oron, E. Tal, and Y. Silberberg, "Scanningless depth-resolved microscopy." Opt. Express **13**, 1468–1476 (2005).

[138] O. Masihzadeh, P. Schlup, and R. A. Bartels, "Complete polarization state control of ultrafast laser pulses with a single linear spatial light modulator," Opt. Express **15**, 18,025–18,032 (2007).

[139] O. Masihzadeh, P. Schlup, and R. A. Bartels, "Control and measurement of spatially inhomogeneous polarization distributions in third-harmonic generation microscopy." Opt. Lett. **34**, 1090–1092 (2009).

[140] F. Weise, S. M. Weber, M. Plewicki, and A. Lindinger, "Application of phase, amplitude, and polarization shaped pulses for optimal control on molecules," Chem. Phys. **332**, 313–317 (2007).

[141] C. G. Slater, D. E. Leaird, and A. M. Weiner, "Programmable polarization-independent spectral phase compensation and pulse shaping by use of a single-layer liquid-crystal modulator," Appl. Opt. **45**, 4858–4863 (2006).

[142] R. Selle, P. Nuernberger, F. Langhojer, F. Dimler, S. Fechner, G. Gerber, and T. Brixner, "Generation of polarization-shaped ultraviolet femtosecond pulses." Opt. Lett. **33**, 803–805 (2008).

[143] C. Froehly, B. Colombeau, and M. Vampouille, *Progress in Optics*, vol. 20 (North-Holland, Amsterdam, 1983).

[144] G. Steinmeyer, "A review of ultrafast optics and optoelectronics." J. Opt. A: Pure Appl. Opt. **5**, R1–R15 (2003).

[145] A. M. Weiner, "Femtosecond pulse shaping using spatial light modulators." Rev. Sci. Instrum. **71**, 1929–1960 (2000).

[146] A. Monmayrant, S. Weber, and B. Chatel, "A newcomer's guide to ultrashort pulse shaping and characterization." J. Phys. B: At. Mol. Opt. Phys. **43**, 103,001 (2010).

[147] F. Verluise, V. Laude, Z. Cheng, C. Spielmann, and P. Tournois, "Amplitude and phase control of ultrashort pulses by use of an acousto-optic programmable dispersive filter: pulse compression and shaping." Opt. Lett. **25**, 575–577 (2000).

[148] C. Lupulescu, "Femtosecond Analysis and Feedback Control of Molecular Processes in Organometallic and Alkaline Systems." Ph.D. thesis, Freie Universität Berlin (2004).

[149] A. Monmayrant, "Façonnage et caractérisation d'impulsions ultracourtes. Contrôle cohérent de systémes simples." Ph.D. thesis, Université Paul Sabatier Toulouse III (2005).

[150] B. J. Sussman, R. Lausten, and A. Stolow, "Focusing of light following a 4-f pulse shaper: Considerations for quantum control," Phys. Rev. A **77**, 043,416 (2008).

[151] M. M. Wefers and K. A. Nelson, "Analysis of programmable ultrashort waveform generation using liquid-crystal spatial light-modulators." J. Opt. Soc. Am. B **12**, 1343–1362 (1995).

[152] P. Aubourg, J. P. Huignard, M. Hareng, and R. A. Mullen, "Liquid crystal light valve using bulk monocrystalline $Bi_{12}SiO_{20}$ as the photoconductive material." Appl. Opt. **21**, 3706–3712 (1982).

[153] Y. Igasaki, F. Li, N. Yoshida, H. Toyoda, T. Inoue, N. Mukohzaka, Y. Kobayashi, and T. Hara, "High Efficiency Electrically Addressable Phase-Only Spatial Light Modulator." Opt. Rev. **6**, 339–344 (1999).

[154] C. Dorrer, F. Salin, F. Verluise, and J. P. Huignard, "Programmable phase control of femtosecond pulses by use of a nonpixelated spatial light modulator." Opt. Lett. **23**, 709–711 (1998).

[155] E. Abbe, "Beiträge zur Theorie des Mikroskops und der mikroskopischen Wahrnehmung." Archiv für mikroskopische Anatomie **9**, 413–468 (1873).

[156] "Ultrafast Laser Mirrors." URL `https://www.cvimellesgriot.com/Products/Documents/GeneralInfo/Ultrafast_mirrors_discussion.pdf`.

[157] URL `http://www.femtolasers.com/Dispersion-management.117\+M54a708de802.0.html`.

[158] M. Müller, J. Squier, and G. J. Brakenhoff, "Measurement of femtosecond pulses in the focal point of a high-numerical-aperture lens by two-photon absorption," Opt. Lett. **20**, 1038–1040 (1995).

[159] T. Mindl, P. Hefferle, S. Schneider, and F. Dörr, "Characterisation of a Train of Subpicosecond Laser Pulses by Fringe Resolved Autocorrelation Measurements." Appl. Phys. B **31**, 201–207 (1983).

[160] R. Trebino and D. J. Kane, "Using phase retrieval to measure the intensity and phase of ultrashort pulses: frequency-resolved optical gating." J. Opt. Soc. Am. A **10**, 1101–1111 (1993).

[161] J. Paye, M. Ramaswamy, J. G. Fujimoto, and E. P. Ippen, "Measurement of the amplitude and phase of ultrashort light pulses from spectrally resolved autocorrelation." Opt. Lett. **18**, 1946–1948 (1993).

[162] D. N. Fittinghoff, J. A. Squier, C. P. J. Barty, J. N. Sweetser, R. Trebino, and M. Müller, "Collinear type II second-harmonic-generation frequency-resolved optical gating for use with high-numerical-aperture objectives." Opt. Lett. **23**, 1046–1048 (1998).

[163] I. Amat-Roldán, I. G. Cormack, P. Loza-Alvarez, E. J. Gualda, and D. Artigas, "Ultrashort pulse characterisation with SHG collinear-FROG." Opt. Express **12**, 1169–1178 (2004).

[164] J. Extermann, L. Bonacina, F. Courvoisier, D. Kiselev, Y. Mugnier, R. L. Dantec, C. Galez, and J.-P. Wolf, "Nano-FROG: Frequency Resolved Optical Gating by a nanometric object," Opt. Express **16**, 10,405–10,411 (2008).

[165] B. Chatel, "Caractérisation d'une impulsion ultra-courte par des méthodes non linéaires." in *Impulsions femtosecondes: des concepts fondamentaux aux applications.* (2009).

[166] A. Baltuska, M. S. Pshenichnikov, and D. A. Wiersma, "Second-harmonic generation frequency-resolved optical gating in the single-cycle regime." IEEE J. Quantum. Electron. **35**, 459–478 (1999).

[167] I. Rechenberg, *Evolutionsstrategie: Optimierung Technischer Systeme nach Prinzipien der Biologischen Evolution.* (Frommann-Holzboog Verlag, Stuttgart, 1973).

[168] H.-P. Schwefel, "Kybernetische Evolution als Strategie der experimentellen Forschung in der Strömungstechnik." Master's thesis, Technische Universität Berlin (1965).

[169] H. J. Lichtfuß, "Evolution eines Rohrkrümmers." Master's thesis, Technische Universität Berlin (1965).

[170] J. Kunde, B. Baumann, S. Arlt, F. Morier-Genoud, U. Siegner, and U. Keller, "Optimization of adaptive feedback control for ultrafast semiconductor spectroscopy," J. Opt. Soc. Am. B **18**, 872–881 (2001).

[171] T. Bäck, D. B. Fogel, and Z. Michalewicz, *Evolutionary Computation* (Taylor and Francis, 2000).

[172] D. Zeidler, "Coherent Control of Molecular Dynamics with Shaped Femtosecond Pulses," Ph.D. thesis, Ludwig-Maximilians-Universität München (2001).

[173] A. Monmayrant, M. Joffre, T. Oksenhendler, R. Herzog, D. Kaplan, and P. Tournois, "Time-domain interferometry for direct electric-field reconstruction by use of an acousto-optic programmable filter and a two-photon detector." Opt. Lett. **28**, 278–280 (2003).

[174] C. Ventalon, J. M. Fraser, and M. Joffre, "Time-domain interferometry for direct electric field reconstruction of mid-infrared femtosecond pulses." Opt. Lett. **28**, 1826–1828 (2003).

[175] B. von Vacano, T. Buckup, and M. Motzkus, "*In situ* broadband pulse compression for multiphoton microscopy using a shaper-assisted collinear SPIDER." Opt. Lett. **31**, 1154–1156 (2006).

[176] B. Xu, J. M. Gunn, J. M. D. Cruz, V. V. Lozovoy, and M. Dantus, "Quantitative investigation of the multiphoton intrapulse interference phase scan method for simultaneous phase measurement and compensation of femtosecond laser pulses," J. Opt. Soc. Am. B **23**, 750–759 (2006).

[177] V. V. Lozovoy, B. Xu, Y. Coello, and M. Dantus, "Direct measurement of spectral phase for ultrashort laser pulses." Opt. Express **16**, 592–597 (2008).

[178] B.-C. Chen and S.-H. Lim, "Characterization of a broadband pulse for phase controlled multiphoton microscopy by single beam SPIDER." Opt. Lett. **32**, 2411–2413 (2007).

[179] J. Sung, B.-C. Chen, and S.-H. Lim, "Single-beam homodyne SPIDER for multiphoton microscopy." Opt. Lett. **33**, 1404–1406 (2008).

[180] L. Lepetit, G. Chériaux, and M. Joffre, "Linear techniques of phase measurement by femtosecond spectral interferometry for applications in spectroscopy." J. Opt. Soc. Am. B **12**, 2467–2474 (1995).

[181] C. Dorrer, P. Londero, and I. A. Walmsley, "Homodyne detection in spectral phase interferometry for direct electric-field reconstruction." Opt. Lett. **26**, 1510–1512 (2001).

[182] N. Forget, V. Crozatier, and T. Oksenhendler, "Pulse-measurement techniques using a single amplitude and phase spectral shaper." J. Opt. Soc. Am. B **27**, 742–756 (2010).

[183] P. Schön and S. Brasselet, "Control of complex spectral phase profiles by single beam homodyne SPIDER." Opt. Lett. (submitted).

[184] A. Gąsecka, T.-J. Han, C. Favard, B. R. Cho, and S. Brasselet, "Quantitative Imaging of Molecular Order in Lipid Membranes Using Two-Photon Fluorescence Polarimetry." Biophys. J. **97**, 2854–2862 (2009).

[185] J. A. Dix and A. S. Verkman, "Mapping of fluorescence anisotropy in living cells by ratio imaging. Application to cytoplasmic viscosity." Biophys. J. **57**, 231–240 (1990).

[186] T. H. Foster, B. D. Pearson, S. Mitra, and C. E. Bigelow, "Fluorescence Anisotropy Imaging Reveals Localization of *meso*-Tetrahydroxyphenyl Chlorin in the Nuclear Envelope." Photochem. Photobiol. **81**, 1544–1547 (2005).

[187] J. Borejdo and S. Burlacu, "Measuring Orientation of Actin Filaments within a Cell: Orientation of Actin in Intestinal Microvilli." Biophys. J. **65**, 300–309 (1993).

[188] D. Axelrod, "Carbocyanine dye orientation in red cell membrane studied by microscopic fluorescence polarization." Biophys. J. **26**(3), 557–573 (1979).

[189] K. Florine-Casteel, "Phospholipid order in gel- and fluid-phase cell-size liposomes measured by digitized video fluorescence polarization microscopy." Biophys. J. **57**, 1199–1215 (1990).

[190] R. E. Dale, S. C. Hopkins, U. A. an der Heide, T. Marszałek, M. Irving, and Y. E. Goldman, "Model-Independent Analysis of the Orientation of Fluorescent Probes with Restricted Mobility in Muscle Fibers." Biophys. J. **76**, 1606–1618 (1999).

[191] A. M. Vrabioiu and T. J. Mitchison, "Structural insights into yeast septin organization from polarized fluorescence microscopy." Nature **443**, 466–469 (2006).

[192] T. E. Schaus, E. W. Taylor, and G. G. Borisy, "Self-organization of actin filament orientation in the dendritic-nucleation/array-treadmilling model." Proc. Natl. Acad. Sci. U. S. A. **104**, 7086–7091 (2007).

[193] D. Lara and C. Dainty, "Axially resolved complete Mueller matrix confocal microscopy." Appl. Opt. **45**, 1917–1930 (2006).

[194] C. E. Bigelow and T. H. Foster, "Confocal fluorescence polarization microscopy in turbid media: effects of scattering-induced depolarization." J. Opt. Soc. Am. A **23**, 2932–2943 (2006).

[195] P. Schön, F. Munhoz, A. Gasecka, S. Brustlein, and S. Brasselet, "Polarization distortion effects in polarimetric two-photon microscopy." Opt. Express **16**, 20,891–20,901 (2008).

[196] F. Roma, F. Nieto, E. E. Vogel, and A. J. Ramírez-Pastor, "Ground-state entropy of +/- J Ising lattices by Monte Carlo simulations." Journal of Statistical Physics **114**, 1325–1341 (2004).

[197] B. Castellon, Sopralab document.

[198] E. Y. S. Yew and C. J. R. Sheppard, "Effects of axial field components on second harmonic generation microscopy." Opt. Express **14**, 1167–1174 (2006).

[199] F. Munhoz, Ph.D. thesis (to be published).

[200] J. L. Oudar and D. S. Chemla, "Hyperpolarizabilities of the nitroanilines and their relations to the excited state dipole moment." J. Chem. Phys. **66**, 2664–2668 (1977).

[201] N. Dudovich, B. Dayan, S. M. G. Faeder, and Y. Silberberg, "Transform-Limited Pulses Are Not Optimal for Resonant Multiphoton Transitions." Phys. Rev. Lett. **86**, 47–50 (2001).

[202] N. Dudovich, D. Oron, and Y. Silberberg, "Coherent Transient Enhancement of Optically Induced Resonant Transitions." Phys. Rev. Lett. **88**, 123,004 (2002).

[203] D. A. Kleinman, "Nonlinear Dielectric Polarization in Optical Media." Phys. Rev. **126**, 1977–1979 (1962).

[204] R. W. Boyd, *Nonlinear Optics* (Academic Press, 1992).

[205] M. Zielinski, D. Oron, D. Chauvat, and J. Zyss, "Second-Harmonic Generation from a Single Core/Shell Quantum Dot." Small **5**, 2835–2840 (2009).

[206] P. Schön, M. Behrndt, D. Aït-Belkacem, H. Rigneault, and S. Brasselet, "Polarization and Phase Pulse Shaping applied to Structural Contrast in Nonlinear Microscopy Imaging." Phys. Rev. A **81**, 013,809 (2010).

[207] H. Vanherzeele and J. D. Bierlein, "Magnitude of the nonlinear-optical coefficients of $KTiOPO_4$," Opt. Lett. **17**, 982–984 (1992).

[208] B. Richards and E. Wolf, "Electromagnetic diffraction in optical systems. II. Structure of the image field in an aplanetic system." Proc. R. Soc. London Ser. A. **153**, 358–579 (1959).

[209] N. Sandeau, L. L. Xuan, D. Chauvat, C. Zhou, J.-F. Roch, and S. Brasselet, "Defocused imaging of second harmonic generation from a single nanocrystal," Opt. Express **15**, 16,051–16,060 (2007).

[210] S. Psilodimitrakopoulos, S. I. C. O. Santos, I. Amat-Roldán, A. K. N. Thayil, D. Artigas, and P. Loza-Alvarez, "*In vivo*, pixel-resolution mapping of thick filaments' orientation in nonfibrilar muscle using polarization-sensitive second harmonic generation microscopy." J. Biomed. Opt. **14**(1), 014,001 (2009).

[211] D. Aït-Belkacem, A. Gąsecka, F. Munhoz, S. Brustlein, and S. Brasselet, "Influence of birefringence on polarization resolved nonlinear microscopy and collagen SHG structural imaging." Opt. Express **18**, 14,859–14,870 (2010).

[212] V. V. Lozovoy, I. Pastirk, K. A. Walowicz, and M. Dantus, "Multiphoton intrapulse interference. II. Control of two- and three-photon laser induced fluorescence with shaped pulses," J. Chem. Phys. **118**, 3187–3196 (2003).

[213] E. M. Vartiainen, H. A. Rinia, M. Müller, and M. Bonn, "Direct extraction of Raman line-shapes from congested CARS spectra." Opt. Express **14**(8), 3622–3630 (2006).

[214] L. Li, H. Wang, and J.-X. Cheng, "Quantitative Coherent Anti-Stokes Raman Scattering Imaging of Lipid Distribution in Coexisting Domains." Biophys. J. **89**, 3480–3490 (2005).

[215] "Spectral Database for Organic Compounds SDBS." URL `http://riodb01.ibase.aist.go.jp/sdbs/cgi-bin/direct_frame_top.cgi`.

[216] C. Otto, A. Voroshilov, S. G. Kruglik, and J. Greve, "Vibrational bands of luminescent zinc(II)-octaethylporphyrin using a polarization-sensitive 'microscopic' multiplex CARS technique." J. Raman Spectrosc. **32**, 495–501 (2001).

[217] F. Munhoz, S. Brustlein, D. Gachet, F. Billard, S. Brasselet, and H. Rigneault, "Raman depolarization ratio of liquids probed by linear polarization Coherent Anti-Stokes Raman spectroscopy," J. Raman Spectrosc. **40**, 775–780 (2009).

[218] S. Popov, Y. Svirko, and N. N. Zheludev, *Susceptibility Tensors for Nonlinear Optics.* (Institute of Physics Publishing: London, UK, 1995).

[219] A. B. Kudryavtsev, S. B. Mirov, L. J. DeLucas, C. Nicolete, M. van der Woerd, T. L. Bray, and T. T. Basiev, "Polarized Raman Spectroscopic Studies of Tetragonal Lysozyme Single Crystals." Acta Cryst. **D54**, 1216–1229 (1998).

[220] P. Guyot-Sionnest, W. Chen, and Y. R. Shen, "General considerations on optical second-harmonic generation from surfaces and interfaces," Phys. Rev. B **33**, 8254–8263 (1986).

[221] D. Krause, C. W. Teplin, and C. T. Rogers, "Optical surface second harmonic measurements of isotropic thin-film metals: Gold, silver, copper, aluminum, and tantalum," J. Appl. Phys. **96**, 3626–3634 (2004).

[222] F. W. Vance, B. I. Lemon, and J. T. Hupp, "Enormous Hyper-Rayleigh Scattering from Nanocrystalline Gold Particle Suspensions." J. Phys. Chem. B **102**, 10,091–10,093 (1998).

[223] I. Russier-Antoine, C. Jonin, E. B. Jé rôme Nappa, and P.-F. Brevet, "Wavelength dependence of the hyper Rayleigh scattering response from gold nanoparticles." J. Chem. Phys. **120**, 10,748–10,752 (2004).

[224] J. I. Dadap, J. Shan, and T. F. Heinz, "Theory of optical second-harmonic generation from a sphere of centrosymmetric material: small-particle limit," J. Opt. Soc. Am. B **21**, 1328–47 (2004).

[225] C. Kittel, *Introduction to Solid State Physics.* (Wiley Interscience, 2005).

[226] C.-Y. Lin, K.-C. Chiu, C.-Y. Chang, S.-H. Chang, T.-F. Guo, and S.-J. Chen, "Surface plasmon-enhanced and quenched twophoton excited fluorescence." Opt. Express **18**, 12,807–12,817 (2010).

[227] E. Fort and S. Grésillon, "Surface enhanced fluorescence." J. Phys. D: Appl. Phys. **41**, 013,001 (2008).

[228] C. Noguez, "Surface Plasmons on Metal Nanoparticles: The Influence of Shape and Physical Environment," J. Phys. Chem. **111**, 3806–3819 (2007).

[229] E. J. Sánchez, L. Novotny, and X. S. Xie, "Near-Field Fluorescence Microscopy Based on Two-Photon Excitation with Metal Tips." Phys. Rev. Lett. **82**, 4014–4017 (1999).

[230] J. Beermann, A. Evlyukhin, A. Boltasseva, and S. I. Bozhevolnyi, "Nonlinear microscopy of localized field enhancements in fractal shaped periodic metal nanostructures," J. Opt. Soc. Am. B **25**, 1585–1592 (2008).

[231] P. Mühlschlegel, H.-J. Eisler, O. J. F. Martin, B. Hecht, and D. W. Pohl, "Resonant Optical Antennas." Science **308**, 1607–1609 (2005).

[232] G. Lévêque and O. J. F. Martin, "Narrow-Band Multiresonant Plasmon Nanostructure for the Coherent Control of Light: An Optical Analog of the Xylophone," Phys. Rev. Lett. **100**, 117,402 (2008).

[233] T. W. Ebbesen, H. J. Lezec, H. F. Ghaemi, T. Thio, and P. A. Wolff, "Extraordinary optical transmission through sub-wavelength hole arrays." Nature **391**, 667–669 (1998).

[234] M. J. Levene, J. Korlach, S. W. Turner, M. Foquet, H. G. Craighead, and W. W. Webb, "Zero-Mode Waveguides for Single-Molecule Analysis at High Concentrations." Science **299**, 682–686 (2003).

[235] S.-H. Chang, S. K. Gray, and G. C. Schatz, "Surface plasmon generation and light transmission by isolated nanoholes and arrays of nanoholes in thin metal films," Opt. Express **13**, 3150–3165 (2005).

[236] G. C. des Francs, D. Molenda, U. C. Fischer, and A. Naber, "Enhanced light confinement in a triangular aperture: Experimental evidence and numerical calculations," Phys. Rev. B **72**, 165,111 (2005).

[237] D. Molenda, G. C. des Francs, U. Fischer, N. Rau, and A. Naber, "High-resolution mapping of the optical near-field components at a triangular nano-aperture," Opt. Express **13**, 10,688–10,696 (2005).

[238] E. Popov, M. Nevière, A. Sentenac, N. Bonod, A.-L. Fehrembach, J. Wenger, P.-F. Lenne, and H. Rigneault, "Single-scattering theory of light diffraction by a circular subwavelength aperture in a finitely conducting screen," J. Opt. Soc. Am. A **24**, 339–358 (2007).

[239] H. Rigneault, J. Capoulade, J. Dintinger, J. Wenger, N. Bonod, E. Popov, T. W. Ebbesen, and P.-F. Lenne, "Enhancement of Single-Molecule Fluorescence Detection in Subwavelength Apertures," Phys. Rev. Lett. **95**, 117,401 (2005).

[240] H. Aouani, J. Wenger, D. Gérard, H. Rigneault, E. Devaux, T. W. Ebbesen, F. Mahdavi, T. Xu, and S. Blair, "Crucial Role of the Adhesion Layer on the Plasmonic Fluorescence Enhancement." ACS Nano **3**, 2043–2048 (2009).

[241] J. Wenger, J. Dintinger, N. Bonod, E. Popov, P.-F. Lenne, T. W. Ebbesen, and H. Rigneault, "Raman scattering and fluorescence emission in a single nanoaperture: Optimizing the local intensity enhancement," Opt. Commun. **267**, 224–228 (2006).

[242] E. Popov, M. Nevière, J. Wenger, P.-F. Lenne, H. Rigneault, P. Chaumet, N. Bonod, J. Dintinger, and T. Ebbesen, "Field enhancement in single subwavelength apertures," J. Opt. Soc. Am. A **23**, 2342–2348 (2006).

[243] M. Airola, Y. Liu, and S. Blair, "Second-harmonic generation from an array of subwavelength metal apertures," J. Opt. A: Pure Appl. Opt. **7**, 118–123 (2005).

[244] T. Xu, X. Jiao, G. P. Zhang, and S. Blair, "Second-harmonic emission from subwavelength apertures: Effects of aperture symmetry and lattice arrangement." Opt. Express **15**, 13,894–13,906 (2007).

[245] J. A. H. van Nieuwstadt, M. Sandtke, R. H. Harmsen, F. B. Segerink, J. C. P. S. Enoch, and L. Kuipers, "Strong Modification of the Nonlinear Optical Response of Metallic Subwavelength Hole Arrays," Phys. Rev. Lett. **97**, 146,102 (2006).

[246] S. J. Paradise, "Effects of Aperture Shape on Optical Second-Harmonic Generation from Arrays of Metallic Sub-wavelength Apertures," Master's thesis, University of Utah (2006).

[247] T.-D. Onuta, M. Waegele, C. C. DuFort, W. L. Schaich, and B. Dragnea, "Optical Field Enhancement at Cusps between Adjacent Nanoapertures," Nano Lett. **7**, 557–564 (2007).

[248] P. J. Schuck, D. P. Fromm, A. Sundaramurthy, G. S. Kino, and W. E. Moerner, "Improving the Mismatch between Light and Nanoscale Objects with Gold Bowtie Nanoantennas." Phys. Rev. Lett. **94**, 017,402 (2005).

[249] A. Lesuffleur, L. K. S. Kumar, and R. Gordon, "Enhanced second harmonic generation from nanoscale double-hole arrays in a gold film," Appl. Phys. Lett. **88**, 261,104 (2006).

[250] Z. Chen, A. Taflove, and V. Backman, "Photonic nanojet enhancement of backscattering of light by nanoparticles: a potential novel visible-light ultramicroscopy technique." Opt. Express **12**, 1214–1220 (2004).

[251] X. Li, Z. Chen, A. Taflove, and V. Backman, "Optical analysis of nanoparticles via enhanced backscattering facilitated by 3-D photonic nanojets." Opt. Express **13**, 526–533 (2005).

[252] P. Ferrand, J. Wenger, A. Devilez, M. Pianta, B. Stout, N. Bonod, E. Popov, and H. Rigneault, "Direct imaging of photonic nanojets." Opt. Express **16**, 6930–6940 (2008).

[253] J. Wenger, D. Gérard, H. Aouani, and H. Rigneault, "Disposable Microscope Objective Lenses for Fluorescence Correlation Spectroscopy Using Latex Microspheres." Anal. Chem. **80**, 6800–6804 (2008).

[254] D. Gérard, J. Wenger, A. Devilez, D. Gachet, B. Stout, N. Bonod, E. Popov, and H. Rigneault, "Strong electromagnetic confinement near dielectric microspheres to enhance single-molecule fluorescence." Opt. Express **16**, 15,297–15,303 (2008).

[255] A. Devilez, N. Bonod, J. Wenger, D. Gérard, B. Stout, H. Rigneault, and E. Popov, "Three-dimensional subwavelength confinement of light with dielectric microspheres." Opt. Express **17**, 2089–2094 (2009).

[256] A. Heifetz, K. Huang, A. V. Sahakian, X. Li, A. Taflove, and V. Backman, "Experimental confirmation of backscattering enhancement induced by a photonic jet." Appl. Phys. Lett. **89**, 221,118 (2006).

[257] S. Lecler, S. Haacke, N. Lecong, O. Crégut, J.-L. Rehspringer, and C. Hirlimann, "Photonic jet driven non-linear optics: example of two-photon fluorescence enhancement by dielectric microspheres." Opt. Express **15**, 4935–4942 (2007).

[258] P. Schön, N. Bonod, J. Wenger, H. Rigneault, E. Devaux, T. Ebbesen, and S. Brasselet, "Second Harmonic Generation enhancement from metallic nano-apertures." Opt. Lett. (submitted).

[259] S. Brasselet and J. Zyss, "Multipolar molecules and multipolar fields: probing and controlling the tensorial nature of nonlinear molecular media." J. Opt. Soc. Am. B **15**, 257–288 (1998).

[260] D. Gérard, A. Devilez, H. Aouani, B. Stout, N. Bonod, JérômeWenger, E. Popov, and H. Rigneault, "Efficient excitation and collection of singlemolecule fluorescence close to a dielectric microsphere." J. Opt. Soc. Am. B **26**, 1473–1478 (2009).

[261] H. Kim, D. K. Taggart, C. Xiang, R. M. Penner, and E. O. Potma, "Spatial control of coherent anti-Stokes emission with height-modulated gold zig-zag nanowires." Nano Lett. **8**(8), 2373–2377 (2008).

[262] H. Aouani, P. Schön, S. Brasselet, H. Rigneault, and JérômeWenger, "Two-photon fluorescence correlation spectroscopy with high count rates and low background using dielectric microspheres." Opt. Express (submitted).

[263] L. Novotny and B. Hecht, *Principles of Nano-Optics.* (Cambridge University Press, 2006).

[264] N. Sandeau, "4π-microscopie : Applications à la localisation axiale de luminophores et à l'amélioration de la résolution latérale." Ph.D. thesis, Université Paul Cézanne Aix-Marseille III (2005).

Abstract

The amplitude, spectral phase and polarization shape of ultrashort laser pulses in the femtosecond regime can strongly influence the outcome of nonlinear optical experiments. In this PhD thesis we present a pulse shaping setup based on two spatial light modulators (SLM) to control these three properties simultaneously for all frequencies present in the pulse. A method is developed to read out the individual components of the second-order nonlinear susceptibility of crystalline and biomolecular media based on second-harmonic generation (SHG). A similar approach is developed for coherent anti-Stokes Raman scattering (CARS). On this basis local orientational order of molecules can be determined by single pulse measurements. A polarimetric approach based on two-photon fluorescence (TPEF) is presented to quantify the polarization distortions that are introduced by all optical elements in the beam path. Spectral phase distortions are determined and corrected either by an evolutionary strategy or a single-beam homodyne SPIDER (spectral phase interferometry for direct-electric field reconstruction) method. Furthermore, nonlinear signal enhancements by photonic structures are characterized by SHG for nano-apertures in a metallic film and by single pulse CARS with amplitude, phase and polarization shaping for dielectric microspheres.

Keywords : pulse shaping, polarization, nonlinear optics, SHG, CARS, microscopy, photonic structures.

Résumé

La mise en forme en amplitude, phase spectrale et polarisation des impulsions laser ultracourtes dans le régime femtoseconde peut fortement influencer le résultat d'une expérience d'optique non-linéaire. Dans cette thèse nous présentons un dispositif de façonnage d'impulsions basé sur l'utilisation de deux modulateurs spatiaux de lumière (SLM) pour contrôler ces trois propriétés simultanément et ce pour toutes les fréquences présentes dans l'impulsion. Une méthode basée sur la génération de second harmonique (SHG) est développée pour lire individuellement les composantes de la susceptibilité non-linéaire du deuxième ordre dans les milieux cristallins et biomoléculaires. Une approche similaire a été utilisée pour la diffusion Raman anti-Stokes cohérente (CARS). Pour cette étude, l'ordre d'orientation des molécules peut être déterminé par des mesures d'impulsion unique. Une approche polarimétrique basée sur la fluorescence à deux photons (TPEF) est présentée pour quantifier les distorsions introduites par tous les éléments optiques dans le trajet du faisceau. Des distorsions de la phase spectrale sont déterminées et corrigées soit par une stratégie évolutive ou par une méthode SPIDER (interférométrie de phase spectrale pour la reconstruction directe du champ électrique) homodyne d'impulsion unique. De plus, l'exaltation des signaux non-linéaires par des structures photoniques est caractérisée par SHG pour des nano-ouvertures dans un film métallique et par impulsion unique CARS pour des microsphères diélectriques avec un façonnage en amplitude, phase et polarisation.

Mots clefs : mise en forme d'impulsions, polarisation, optique non-linéaire, SHG, CARS, microscopie, structures photoniques